

**Appendix PA**

**Attachment TFIELD**

This page intentionally left blank

**Table of Contents**

1

2 TFIELD-1.0 OVERVIEW OF T-FIELD DEVELOPMENT, CALIBRATION, AND  
3 MODIFICATION PROCESS .....1

4 TFIELD-2.0 DEVELOPMENT OF MAPS OF GEOLOGIC FACTORS .....2

5 TFIELD-3.0 DEVELOPMENT OF MODEL RELATING CULEBRA T TO  
6 GEOLOGIC FACTORS .....8

7 TFIELD-3.1 Fracture Interconnection ..... 10

8 TFIELD-3.2 Overburden Thickness ..... 10

9 TFIELD-3.3 Salado Dissolution ..... 10

10 TFIELD-3.4 Halite Overlying the Culebra ..... 11

11 TFIELD-3.5 Halite Bounding the Culebra ..... 11

12 TFIELD-3.6 High-T Zones ..... 12

13 TFIELD-3.7 Linear Transmissivity Model ..... 12

14 TFIELD-3.8 Linear-Regression Analysis ..... 12

15 TFIELD-4.0 CALCULATION OF BASE T FIELDS .....14

16 TFIELD-4.1 Definition of Model Domain ..... 15

17 TFIELD-4.2 Reduction of Geologic Map Data ..... 16

18 TFIELD-4.3 Indicator Variography ..... 17

19 TFIELD-4.4 Conditional Indicator Simulation ..... 17

20 TFIELD-4.5 Construction of Base Transmissivity Fields ..... 19

21 TFIELD-5.0 CONSTRUCTION OF SEED REALIZATIONS .....19

22 TFIELD-6.0 T-FIELD CALIBRATION TO STEADY-STATE AND TRANSIENT  
23 HEADS .....26

24 TFIELD-6.1 Modeling Assumptions ..... 27

25 TFIELD-6.2 Initial Heads ..... 28

26 TFIELD-6.3 Boundary Conditions ..... 33

27 TFIELD-6.4 Observed Steady-State and Transient Head Data Used in Model  
28 Calibration ..... 33

29 TFIELD-6.5 Spatial Discretization ..... 39

30 TFIELD-6.6 Temporal Discretization ..... 41

31 TFIELD-6.7 Weighting of Observation Data ..... 47

32 TFIELD-6.8 Assignment of Pilot Point Geometry ..... 49

33 TFIELD-6.9 Stochastic Inverse Calibration ..... 56

34 TFIELD-7.0 T-FIELD ACCEPTANCE CRITERIA .....62

35 TFIELD-7.1 Candidate Acceptance Criteria ..... 63

36 TFIELD-7.1.1 RMSE Values ..... 63

37 TFIELD-7.1.2 Fit to Steady-State Heads ..... 63

38 TFIELD-7.1.3 Phi Values ..... 64

39 TFIELD-7.1.4 Fit to Transient Heads ..... 64

40 TFIELD-7.2 Application of Criteria to T Fields ..... 66

41 TFIELD-7.2.1 RMSE Values ..... 66

42 TFIELD-7.2.2 Fit to Steady-State Heads ..... 66

43 TFIELD-7.2.3 Phi Values ..... 66

44 TFIELD-7.2.4 Fit to Transient Heads ..... 69

45 TFIELD-7.3 Final Acceptance Criteria ..... 69

46 TFIELD-8.0 INVERSE MODELING RESULTS .....78

1	TFIELD-8.1	Particle Tracking.....	78
2	TFIELD-8.2	Fit to Steady-State Heads.....	79
3	TFIELD-8.3	Pilot-Point Sensitivity.....	81
4	TFIELD-8.4	Ensemble Average T Field.....	81
5	TFIELD-9.0	MODIFICATION OF T FIELDS FOR MINING SCENARIOS.....	87
6	TFIELD-9.1	Determination of Potential Mining Areas.....	88
7	TFIELD-9.2	Scaling of Transmissivity.....	88
8	TFIELD-9.3	Forward Runs.....	89
9	TFIELD-9.4	Results.....	91
10	TFIELD-9.4.1	Travel Times.....	91
11	TFIELD-9.4.2	Travel Directions.....	96
12	TFIELD-9.4.3	Extreme Values.....	101
13	TFIELD-10.0	SUMMARY.....	101

14 **List of Figures**

15	Figure TFIELD-1.	Structure Contour Map for the Top of the Culebra.....	5
16	Figure TFIELD-2.	Salado Dissolution Margin.....	6
17	Figure TFIELD-3.	Rustler Halite Margins. See Figure TFIELD-4 for key to	
18		stratigraphic column.....	7
19	Figure TFIELD-4.	Stratigraphic Subdivisions of the Rustler Formation.....	9
20	Figure TFIELD-5.	Histogram of Log <sub>10</sub> Culebra T. Data from DOE (1996), Beauheim	
21		and Ruskauff (1998), and Beauheim (2002c).....	11
22	Figure TFIELD-6.	Well Locations and Log <sub>10</sub> Culebra Transmissivities.....	13
23	Figure TFIELD-7.	Regression Fit to Observed Culebra Log <sub>10</sub> T Data.....	15
24	Figure TFIELD-8.	Zones for Indicator Grids.....	18
25	Figure TFIELD-9.	High-T Indicator Model and Experimental Variograms.....	18
26	Figure TFIELD-10.	Soft Data Around Wells.....	19
27	Figure TFIELD-11.	Example Base T Field.....	20
28	Figure TFIELD-12.	Conceptual Cross Section Showing the Updating of the Residual	
29		Field and the Base T Field into the Seed T Field.....	22
30	Figure TFIELD-13.	Omnidirectional Variogram Model Fit to the Experimental	
31		Variogram of the Transmissivity Residuals.....	25
32	Figure TFIELD-14.	An Example of the Creation of a Seed T Field. The base T field	
33		(left image) is combined with the initial residual field created	
34		through geostatistical simulation (center image) to produce the	
35		seed T field (right image). That field is then used as the initial	
36		field for the first iteration of the inverse calibration procedure. All	
37		three color scales denote the log <sub>10</sub> T (m <sup>2</sup> /s) value.....	25
38	Figure TFIELD-15.	Experimental and Model Variograms for the Raw-Space (Not	
39		Normal-Score Transformed) Transmissivity Residual Data.....	26
40	Figure TFIELD-16.	Locations and Values of the 2000 Head Measurements Considered	
41		in the Steady-State Calibrations. The approximate extent of the	
42		numerical model domain is shown by the black rectangle in the	
43		image.....	28
44	Figure TFIELD-17.	Gaussian Trend Surface Fit to the 2000 Observed Heads.....	31

1 Figure TFIELD-18. Locations and Values of the Residuals Between the Gaussian  
2 Trend Surface Model and the Observed Head Data. The  
3 approximate boundary of the flow model is shown as a black  
4 rectangle in the image. ....32  
5 Figure TFIELD-19. Omnidirectional Experimental (Straight-Line Segments) and  
6 Model Variograms of the Head Residuals (Curves) for the 2000  
7 Heads. The numbers indicate the number of pairs of values that  
8 were used to calculate each point and the horizontal dashed line  
9 denotes the variance of the residual data set. ....32  
10 Figure TFIELD-20. Map of Initial Heads Created Through Kriging and Used to Assign  
11 Fixed-Head Boundary Conditions .....34  
12 Figure TFIELD-21. Values of Fixed Heads Along the Eastern Boundary of the Model  
13 Domain.....35  
14 Figure TFIELD-22. Values of Fixed Heads Along the Northern and Southern  
15 Boundaries of the Model Domain. Note that not all locations along  
16 the boundaries are active cells. ....35  
17 Figure TFIELD-23. Locations of the H-3b2 Hydraulic Test Well and Observation  
18 Wells .....38  
19 Figure TFIELD-24. Observed Drawdowns for the H-3b2 Hydraulic Test .....39  
20 Figure TFIELD-25. Locations of the WIPP-13 Hydraulic Test Well and Observation  
21 Wells .....40  
22 Figure TFIELD-26. Observed Drawdowns for the WIPP-13 Hydraulic Test. Note the  
23 change in the scale of the Y-axis from the upper to the lower  
24 image.....41  
25 Figure TFIELD-27. Locations of the P-14 Hydraulic Test Well and Observation Wells.....42  
26 Figure TFIELD-28. Observed Drawdowns for the P-14 Hydraulic Test.....43  
27 Figure TFIELD-29. Locations of the WQSP-1 Hydraulic Test Well and Observation  
28 Wells .....44  
29 Figure TFIELD-30. Observed Drawdowns for the WQSP-1 Hydraulic Test.....45  
30 Figure TFIELD-31. Locations of the WQSP-2 Hydraulic Test Well and Observation  
31 Wells .....46  
32 Figure TFIELD-32. Observed Drawdowns from the WQSP-2 Hydraulic Test.....47  
33 Figure TFIELD-33. Locations of the H-11 Hydraulic Test Well and Observation Wells .....48  
34 Figure TFIELD-34. Observed Drawdowns for the H-11 Hydraulic Test .....49  
35 Figure TFIELD-35. Locations of the H-19 Hydraulic Test Well and Observation Wells .....50  
36 Figure TFIELD-36. Observed Drawdowns From the H-19 Hydraulic Test .....51  
37 Figure TFIELD-37. Temporal Discretization and Pumping Rates for the Fifth Call to  
38 MODFLOW-2000. A total of 17 stress periods (SPs) are used to  
39 discretize this model call.....53  
40 Figure TFIELD-38. Locations of the Adjustable and Fixed Pilot Points Within the  
41 Model Domain .....55  
42 Figure TFIELD-39. Close-Up View of the Pilot-Point Locations in the Area of the  
43 WIPP Site. The colored (solid) lines connect the pumping and  
44 observation wells. The legend for this figure is the same as that for  
45 Figure TFIELD-38.....56

1 Figure TFIELD-40. Conceptual Cross-Section Showing the Addition of Pilot Points to  
2 the Optimization Process .....58  
3 Figure TFIELD-41. Flow Chart of the Stochastic Inverse Calibration Process Used to  
4 Create the Final Calibrated Transmissivity Fields.....59  
5 Figure TFIELD-42. Flow Chart of the Core of the Inversion Process Highlighting the  
6 Connection Between PEST and MODFLOW-2000.....60  
7 Figure TFIELD-43. Example Final Steps in the Creation of a Calibrated T Field. The  
8 calibrated residual field (left image) is added to the base T field  
9 (middle image) to get the final calibrated T field (right image). All  
10 color scales are in units of  $\log_{10} T$  ( $m^2/s$ ).....61  
11 Figure TFIELD-44. Steady-State RMSE Values for 146 T Fields .....67  
12 Figure TFIELD-45. Steady-State RMSE Values and Associated Travel Times.....67  
13 Figure TFIELD-46. Travel Times for Fields with Steady-State RMSE <6 m (20 ft) .....68  
14 Figure TFIELD-47. Measured Versus Modeled Steady-State Heads for T Field d21r10.....68  
15 Figure TFIELD-48. Steady-State-Fit Slope Versus Travel Time for All Fields.....70  
16 Figure TFIELD-49. Steady-State-Fit Slope Versus Travel Time for Slopes >0.5.....70  
17 Figure TFIELD-50. Transient Phi Versus Travel Time for All Fields.....71  
18 Figure TFIELD-51. Transient Phi Versus Travel Time for Phi <8,000  $m^2$  .....71  
19 Figure TFIELD-52. Example of Passing Well Response from T Field d21r10.....72  
20 Figure TFIELD-53. Example of Failing Well Response from T Field d21r10.....72  
21 Figure TFIELD-54. Transient Phi Versus Number of Failed Well Responses.....76  
22 Figure TFIELD-55. Number of Failed Well Responses Versus Travel Time .....76  
23 Figure TFIELD-56. Travel-Time CDFs for Different Sets of T Fields .....77  
24 Figure TFIELD-57. Travel-Time CDFs for CCA and CRA-2004 T Fields.....78  
25 Figure TFIELD-58. All Particle Tracks Within the WIPP LWB. The bold lines show  
26 the boundaries of the high-T (left side) and low-T (right side)  
27 zones. ....79  
28 Figure TFIELD-59. All Particle Tracks Within the Model Domain. The bold lines  
29 show the boundaries of the high-T (left) and low-T (right) zone  
30 boundaries. The no-flow and WIPP site boundaries are also  
31 shown. ....80  
32 Figure TFIELD-60. Percentage of T Fields in which Pilot Points Hit Maximum  
33 Allowable Values. Corners of WIPP LWB are shown by  
34 unlabeled black dots.....82  
35 Figure TFIELD-61. Percentage of T Fields in which Pilot Points Hit Minimum  
36 Allowable Values. Corners of WIPP LWB are shown by  
37 unlabeled black dots.....83  
38 Figure TFIELD-62. Ensemble Average of 121 Calibrated T Fields .....84  
39 Figure TFIELD-63. Close-Up View of the Ensemble Average T Field Near the WIPP  
40 Site. Note the different  $\log_{10}$  color scale from Figure TFIELD-64.....85  
41 Figure TFIELD-64. Scatterplot of Measured Versus Modeled Steady-State Heads.....86  
42 Figure TFIELD-65. Histogram of Differences Between Measured and Modeled Steady-  
43 State Heads.....86  
44 Figure TFIELD-66. Leased Potash Resources Near the WIPP Site.....89  
45 Figure TFIELD-67. Potential Potash Distribution Within the WIPP LWB. The  
46 repository excavations are shown in the center. ....90

1 Figure TFIELD-68. Comparison of CRA-2004 and CCA Areas Affected by Mining .....91  
2 Figure TFIELD-69. CDFs of Travel Times for the Full-, Partial-, and No-Mining  
3 Scenarios .....94  
4 Figure TFIELD-70. CDFs of Partial-Mining Travel Times for Three CRA-2004  
5 Replicates and One CCA Replicate .....94  
6 Figure TFIELD-71. Normalized Pore Velocities for the Full-Mining Case. Red  
7 indicates zones of high velocity. The black outline shows the full-  
8 mining zones and the red box is the WIPP LWB. The T field used  
9 to produce the velocity profile is averaged across all T  
10 field/replicate combinations for the full-mining scenario (300 T  
11 fields in total). .....95  
12 Figure TFIELD-72. CDFs of Full-Mining Travel Times for Three CRA-2004  
13 Replicates and One CCA Replicate .....97  
14 Figure TFIELD-73. Particle Tracks for Replicate 1 for the Partial-Mining Scenario.....98  
15 Figure TFIELD-74. Particle Tracks for Replicate 2 for the Partial-Mining Scenario.....98  
16 Figure TFIELD-75. Particle Tracks for Replicate 3 for the Partial-Mining Scenario.....99  
17 Figure TFIELD-76. Particle Tracks for Replicate 1 for the Full-Mining Scenario.....99  
18 Figure TFIELD-77. Particle Tracks for Replicate 2 for the Full-Mining Scenario.....100  
19 Figure TFIELD-78. Particle Tracks for Replicate 3 for the Full-Mining Scenario.....100  
20 Figure TFIELD-79. Correlation Between the Random Mining Factor and Log<sub>10</sub> of  
21 Travel Time.....102  
22 Figure TFIELD-80. Head Contours and Particle Track for the Maximum-Travel-Time  
23 T Field (d04r01-R2) for the Partial-Mining Case. The WIPP LWB  
24 is the red box in the center of the figure and the particle track is the  
25 blue track originating from the approximate center of the WIPP. ....103  
26 Figure TFIELD-81. Head Contours and Particle Track for the Minimum-Travel-Time T  
27 Field (d08r01-R3) for the Partial-Mining Case. The WIPP LWB is  
28 the red box in the center of the figure and the particle track is the  
29 blue track originating from the approximate center of the WIPP. ....104  
30 Figure TFIELD-82. Head Contours and Particle Track for the Median-Travel-Time T  
31 Field (d01r04-R1) for the Partial-Mining Case. The WIPP LWB is  
32 the red box in the center of the figure and the particle track is the  
33 blue track originating from the approximate center of the WIPP. ....105  
34 Figure TFIELD-83. Head Contours and Particle Track for the Maximum-Travel-Time  
35 T Field (d04r01-R2) for the Full-Mining Case. The WIPP LWB is  
36 the red box in the center of the figure and the particle track is the  
37 blue track originating from the approximate center of the WIPP. ....106  
38 Figure TFIELD-84. Head Contours and Particle Track for the Minimum-Travel-Time T  
39 Field (d01r07-R2) for the Full-Mining Case. The WIPP LWB is  
40 the red box in the center of the figure and the particle track is the  
41 blue track originating from the approximate center of the WIPP. ....107  
42 Figure TFIELD-85. Head Contours and Particle Track for the Median-Travel-Time T  
43 Field (d10r09-R1) for the Full-Mining Case. The WIPP LWB is  
44 the red box in the center of the figure and the particle track is the  
45 blue track originating from the approximate center of the WIPP. ....108

1 **List of Tables**

2 Table TFIELD-1. Regression Coefficients for Equations (2) and (3) .....14

3 Table TFIELD-2. Coordinates of the Numerical Model Domain Corners .....16

4 Table TFIELD-3. Log<sub>10</sub> Transmissivity Data Used in Inverse Calibrations .....22

5 Table TFIELD-4. Statistical Parameters Describing the Distributions of the Raw and

6 Normal-score Transformed Residual Data .....24

7 Table TFIELD-5. Well Names and Locations of the 37 Head Measurements

8 Obtained in Late 2000 Used to Define Boundary and Initial Heads .....30

9 Table TFIELD-6. Parameters for the Gaussian Trend Surface Model Fit to the 2000

10 Heads.....31

11 Table TFIELD-7. Model Variogram Parameters for the Head Residuals .....33

12 Table TFIELD-8. Transient Hydraulic Test and Observation Wells for the

13 Drawdown Data .....36

14 Table TFIELD-9. Discretization of Time into 29 Stress Periods and 127 Time Steps

15 with Pumping Well Names and Pumping Rates .....52

16 Table TFIELD-10. Observation Weights for Each of the Observation Wells.....54

17 Table TFIELD-11. Summary Information on T Fields.....73

18 Table TFIELD-12. T-Field Transmissivity Multipliers for Mining Scenarios .....92

19 Table TFIELD-13. Travel Time Statistics for the Full- and Partial-Mining Scenarios as

20 Compared to the No-Mining Scenario .....97



1                   ***TFIELD-1.0 OVERVIEW OF T-FIELD DEVELOPMENT, CALIBRATION, AND***  
2                   **MODIFICATION PROCESS**

3 Modeling the transport of radionuclides through the Culebra Dolomite Member of the Rustler  
4 Formation is one component of the Performance Assessment (PA) performed for the Waste  
5 Isolation Pilot Plant (WIPP) Compliance Recertification Application (CRA). This transport  
6 modeling requires a model of groundwater flow through the Culebra. This Attachment describes  
7 the process used to develop and calibrate the transmissivity (T) fields for the Culebra, and then  
8 modify them for the possible effects of potash mining for use in flow modeling for the CRA-  
9 2004.

10 The work described in this attachment was performed under two Sandia National Laboratories  
11 Analysis Plans (APs): AP-088 (Beauheim 2002a) and AP-100 (Leigh et al. 2003). AP-088  
12 (Analysis Plan for the Evaluation of the Effects of Head Changes on Calibration of Culebra  
13 Transmissivity Fields) dealt with the development, calibration, and modification for potash  
14 mining of the T fields. AP-100 (Analysis Plan for Calculations of Culebra Flow and Transport:  
15 Compliance Recertification Application) included the development of T-field acceptance criteria,  
16 as well as radionuclide-transport calculations not described herein.

17 The starting point in the T-field development process was to assemble information on geologic  
18 factors that might affect Culebra T (Section 2.0 of this attachment). These factors include  
19 dissolution of the upper Salado Formation, the thickness of overburden above the Culebra, and  
20 the spatial distribution of halite in the Rustler Formation above and below the Culebra. Geologic  
21 information is available from hundreds of oil and gas wells and potash exploration holes in the  
22 vicinity of the WIPP site, while T values are available from only 46 well locations. Details of  
23 the geologic data compilation are given in Powers (2002a, 2002b, 2003), and summarized below  
24 in Section 2.0 of this attachment.

25 A two-part “geologically based” approach was then used to generate Culebra base T fields. In  
26 the first part (Section 3.0 of this attachment), a conceptual model for geologic controls on  
27 Culebra T was formalized, and the hypothesized geologic controls were regressed against  
28 Culebra T data to determine linear regression coefficients. The regression includes one  
29 continuously varying function, Culebra overburden thickness, and three indicator functions that  
30 assume values of 0 or 1 depending on the occurrence of open, interconnected fractures, Salado  
31 dissolution, and the presence or absence of halite in units bounding the Culebra.

32 In the second part (Section 4.0 of this attachment), a method was developed for applying the  
33 linear regression model to predict Culebra T across the WIPP area. The regression model was  
34 combined with the maps of geologic factors to create 500 stochastically varying Culebra base T  
35 fields. Details about the development of the regression model and the creation of the base T  
36 fields are given in Holt and Yarbrough (2002, 2003a, 2003b).

37 By the nature of regression models, the base T fields do not honor the measured T values at the  
38 measurement locations. Therefore, before these base T fields could be used in a flow model,  
39 they had to be conditioned to the measured T values. This conditioning is described in McKenna  
40 and Hart (2003a, 2003b) and summarized in Section 5.0 of this attachment. Section 6.0 of this  
41 attachment presents details on the modeling approach used to calibrate the T fields to both

1 steady-state heads and transient drawdown measurements. Heads measured in late 2000 were  
2 used to represent steady-state conditions in the Culebra, and drawdown responses in 40 wells to  
3 pumping in 7 wells were used to provide transient calibration data. Details on the heads and  
4 drawdown data used are described in Beauheim (2002b; 2003a). Assumptions made in  
5 modeling, the definition of an initial head distribution, assignment of boundary conditions,  
6 discretization of the spatial and temporal domain, weighting of the observations, and the use of  
7 PEST in combination with MODFLOW-2000 to calibrate the T fields using a pilot-point method  
8 are described in McKenna and Hart (2003a, 2003b) and summarized in Section 6.0 of this  
9 attachment.

10 Section 7.0 of this attachment addresses the development and application of acceptance criteria  
11 for the T fields. Acceptance was based on a combination of objective fit to the calibration data  
12 and providing travel time results consistent with the cumulative distribution function (CDF) of  
13 travel times from the 23 best-calibrated T fields (Beauheim 2003b). Of the 146 T fields that  
14 went through the calibration process, 121 T fields were judged adequate for further use, with the  
15 100 best T fields selected for use in the CRA-2004 transport calculations.

16 Section 8.0 of this attachment provides summary statistics and other information for the 121 T  
17 fields that were judged to be acceptably calibrated. Particle tracks from a point above the center  
18 of the WIPP disposal panels to the land withdrawal boundary are shown, along with information  
19 on the model fits to steady-state heads, identification of the most sensitive pilot point locations,  
20 and characteristics of an ensemble average T field. This information is summarized from  
21 McKenna and Hart (2003b).

22 Section 9.0 of this attachment discusses the modification of the T fields to account for the effects  
23 of potash mining both within and outside the WIPP land withdrawal boundary. Mining-affected  
24 areas were delineated, random transmissivity multipliers were applied to Ts in those areas, and  
25 particle tracks and travel times were determined (Lowry 2003). The flow fields produced by  
26 these mining-affected T fields are input to SECOTP2D for the CRA-2004 radionuclide-transport  
27 calculations.

28 Section 10.0 of this attachment provides a brief summary of this attachment.

## 29 ***TFIELD-2.0 DEVELOPMENT OF MAPS OF GEOLOGIC FACTORS***

30 Beauheim and Holt (1990), among others, suggested three geologic factors that might be related  
31 to the transmissivity of the Culebra in the vicinity of the WIPP site:

- 32 1. thickness (or erosion) of overburden above the Culebra,
- 33 2. dissolution of the upper Salado , and
- 34 3. spatial distribution of halite in the Rustler Formation below and above the Culebra.

35 Culebra transmissivity is inversely related to thickness of overburden because stress relief  
36 associated with erosion of overburden leads to fracturing and opening of preexisting fractures.  
37 Culebra transmissivity is high where dissolution of the upper Salado has occurred and the

1 Culebra has subsided and fractured. Culebra transmissivity is observed to be low where halite is  
2 present in overlying and/or underlying mudstones. Presumably, high Culebra T leads to  
3 dissolution of nearby halite (if any). Hence, the presence of halite in mudstones above and/or  
4 below the Culebra can be taken as an indicator for low Culebra transmissivity.

5 Maps were developed for each of these factors using drillhole data of different types. The  
6 general area for the geologic study comprised 12 townships, located in townships T21S to T24S,  
7 ranges R30-32E (the WIPP site lies in T22S, R31E). The original sources of geologic data for  
8 this analysis are mainly Powers and Holt (1995) and Holt and Powers (1988) and new  
9 information derived by log interpretation by Powers (2002a, 2003b, 2003). All of the data are  
10 either included or summarized in the references cited above, and can be independently checked;  
11 basic data reports are available for WIPP drillholes, geophysical logs for oil and gas wells are  
12 available commercially or at offices of the Oil Conservation Division (New Mexico) in Artesia  
13 and Hobbs, and potash drillhole information is in files that can be accessed for stratigraphic  
14 information at the Bureau of Land Management (BLM), Carlsbad, NM. No proprietary data are  
15 included.

16 Factor A is represented by a structure contour map of the elevation of the top of the Culebra  
17 (Figure TFIELD-1) that can be digitized and then subtracted from a digital elevation model  
18 (DEM) of the land surface to obtain the thickness of overburden. Factor B is represented on a  
19 map as an approximate margin of the area beginning to be affected by dissolution of the upper  
20 Salado (Figure TFIELD-2). Factor C is delineated on a map by lines that represent as nearly as  
21 possible the boundaries of the occurrence of halite in the Los Medaños, Tamarisk, and Forty-  
22 niner Members of the Rustler Formation in the study domain (Figure TFIELD-3).

23 With respect to Factor B, the upper Salado has been dissolved, and presumably is still dissolving,  
24 along the eastern margin of Nash Draw. On the basis of limited core information, Holt and  
25 Powers (1988) suggested that formations overlying the dissolving upper Salado in Nash Draw  
26 are affected in proportion to the amount of Salado dissolution. The most direct way to estimate  
27 the spatial distribution of dissolution is to have cores of the upper Salado and basal Rustler and  
28 knowledge of the thickness to marker beds (MBs) in the upper Salado. The upper Salado has not  
29 been cored frequently, but geophysical logs from oil and gas wells, and descriptive logs of cores  
30 or cuttings from potash drillholes, provide a considerable amount of evidence of the thickness of  
31 the lower Rustler and upper Salado, even though cores and cuttings are no longer available from  
32 potash industry drillholes.

33 Potash industry geological logs examined at the BLM in Carlsbad, NM are quite variable in the  
34 quality of description and the stratigraphic interval described. Drillhole logs from the 1930s and  
35 1950s typically are the most descriptive; recent drillhole logs are commonly useless for this  
36 project because no strata are described above portions of the McNutt potash zone of the Salado,  
37 near the middle of the formation.

38 The top of the Culebra and the base of the Vaca Triste Sandstone Member in the upper Salado  
39 are the most consistent stratigraphic markers spanning the upper Salado that are recognizable  
40 across various types of records. As a guide to the limits or bounds of upper Salado dissolution, a  
41 map of the thickness from top of Culebra to base of Vaca Triste was prepared (Powers 2003). In  
42 conjunction with previous work by Powers and Holt (1995) and the evidence of the structure of

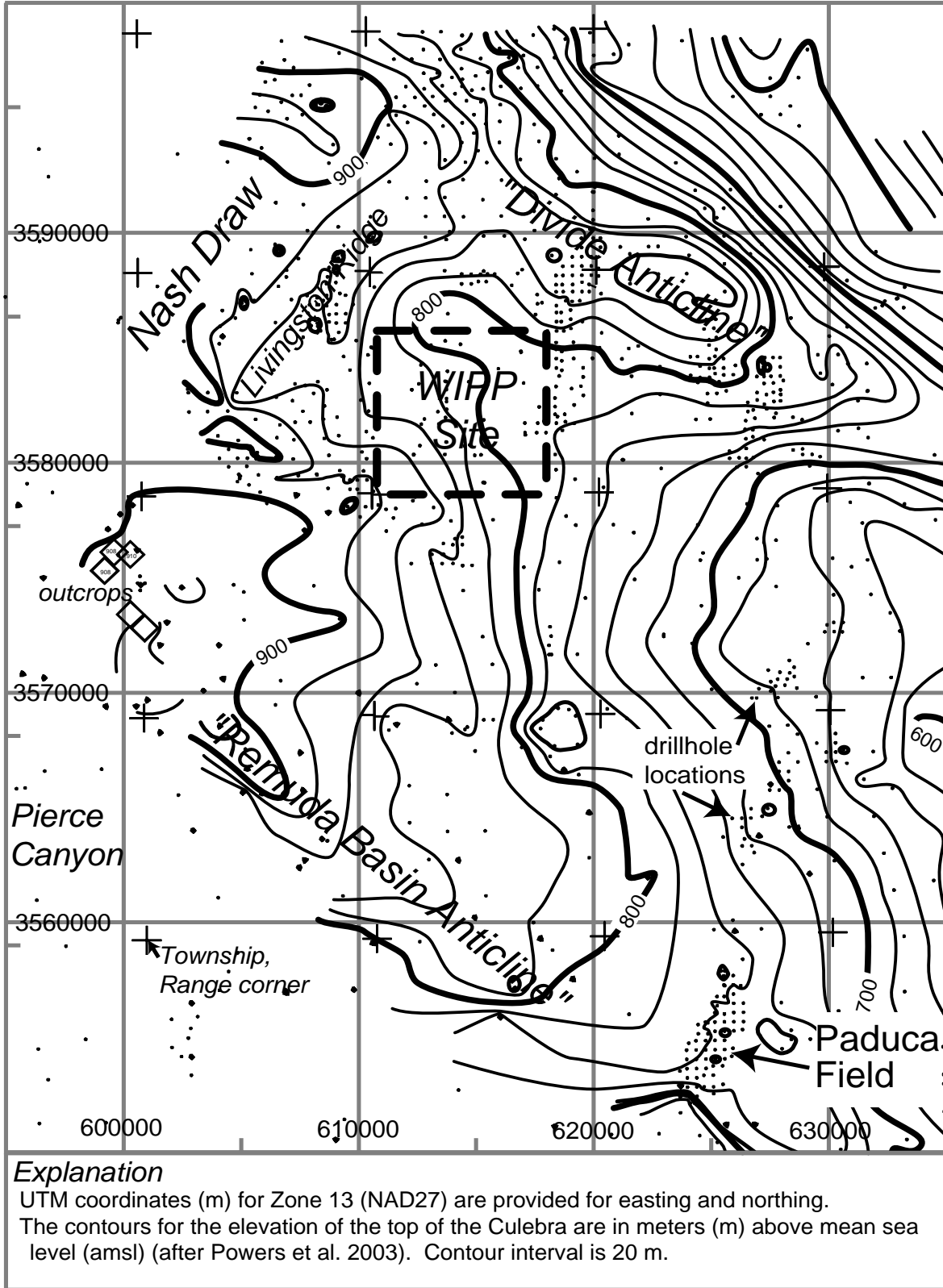
1 the top of Culebra (see Figure TFIELD-1), an approximate boundary of dissolution was drawn as  
2 shown in Figure TFIELD-2.

3 With respect to Factor C, the boundaries of where halite is found in the three non-carbonate  
4 members of the Rustler have been drawn several times on the basis of different borehole data  
5 sets and different data types (e.g., core data and geophysical logs). For the most part, the  
6 different versions of the boundaries do not vary significantly. In the map shown in Figure  
7 TFIELD-3, the margins are based principally on the work of Powers and Holt (1995), which is a  
8 continuation of work reported by Holt and Powers (1988). As discussed in Powers and Holt  
9 (1995), the boundaries drawn here vary slightly from those drawn by Snyder (1985) based on  
10 core data for two reasons: (1) the Los Medaños Member (Powers and Holt 1999; formerly called  
11 the unnamed lower member) is here divided into two separate halite-bearing units (Powers and  
12 Holt 2000), and (2) geophysical log signatures are now used to identify halite in areas where  
13 cores are not available. Figure TFIELD-3 includes a stratigraphic sketch showing the  
14 relationship of halite-bearing strata to other strata in the Rustler. Following the convention  
15 established by Holt and Powers (1988), the mudstone/halite (M/H) strata are numbered  
16 consecutively starting at the base of the Rustler.

17 The margins for halite have now been drawn in the area north of the WIPP site around the  
18 northeastern arm of Nash Draw based on the descriptions of halite encounters in the Rustler  
19 Formation in potash drillholes. In addition, a few areas have been modified (from Powers and  
20 Holt 1995) to the south and west of the WIPP based on the records from potash drillholes as well  
21 as the records of drilling H-12 and H-17 for the WIPP.

22 In 12 potash drillholes, halite was reported above the upper contacts of the Culebra or Magenta  
23 Dolomite Members. The boundaries for M3/H3 and M4/H4 margins (i.e., the spatial limits of  
24 where halite is found in the mudstone intervals) have been drawn north of the WIPP based on  
25 these data. The depth below the Culebra at which halite was reported has also been used to draw  
26 the boundaries of the lower (M1/H1) or the upper (M2/H2) halite-bearing units of the Los  
27 Medaños in this area. Anhydrite A1 divides the M1/H1 (below) and M2/H2 (above) intervals.  
28 M2 (no halite) is about 3 m (10 ft) thick. If halite is reported within about 3 m (10 ft) of the base  
29 of Culebra or is clearly above A1, H2 is considered to be present. The M1/H1 interval is about  
30 33-37 m (110-120 ft) thick at the WIPP site. In potash drillholes north of the WIPP site, where  
31 halite was reported less than 33 m (110 ft) below the Culebra, H1 is present. Within the zone for  
32 H1, other drillholes frequently reveal halite less than 33 m (110 ft) below the Culebra.

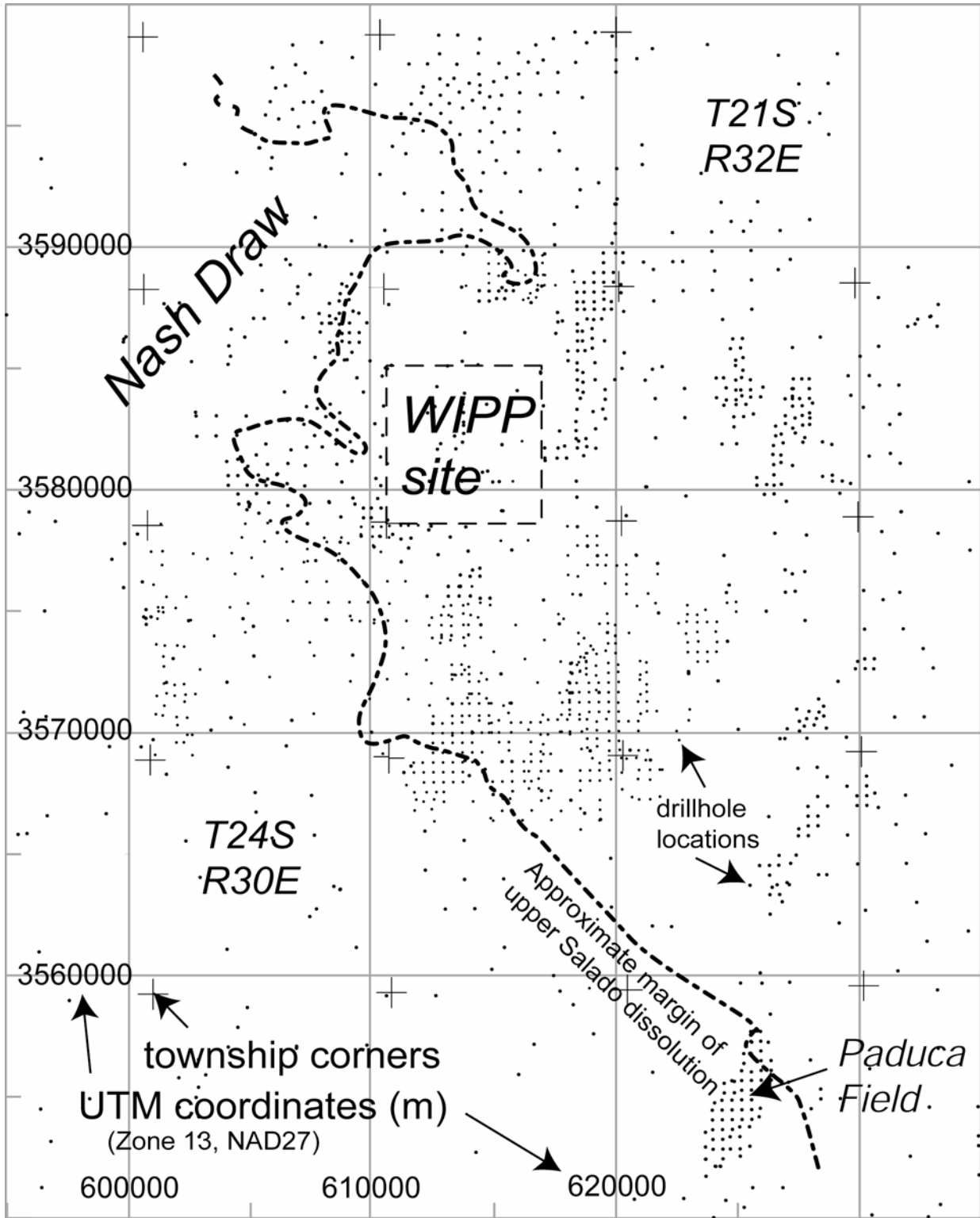
33 It should be noted that the report of "top of salt" or first salt in records for potash drillholes does  
34 not consistently mean the same thing and is frequently not the uppermost halite. It may instead  
35 mean the first halite that is encountered after coring begins or the first unit that is dominantly  
36 halite. Detailed inspection of logs sometimes shows halite described from cuttings, with a  
37 summary report of "top of salt" much deeper. In some cases, it appears "top of salt" is an  
38 estimate of where the Salado-Rustler contact should be.



1

2

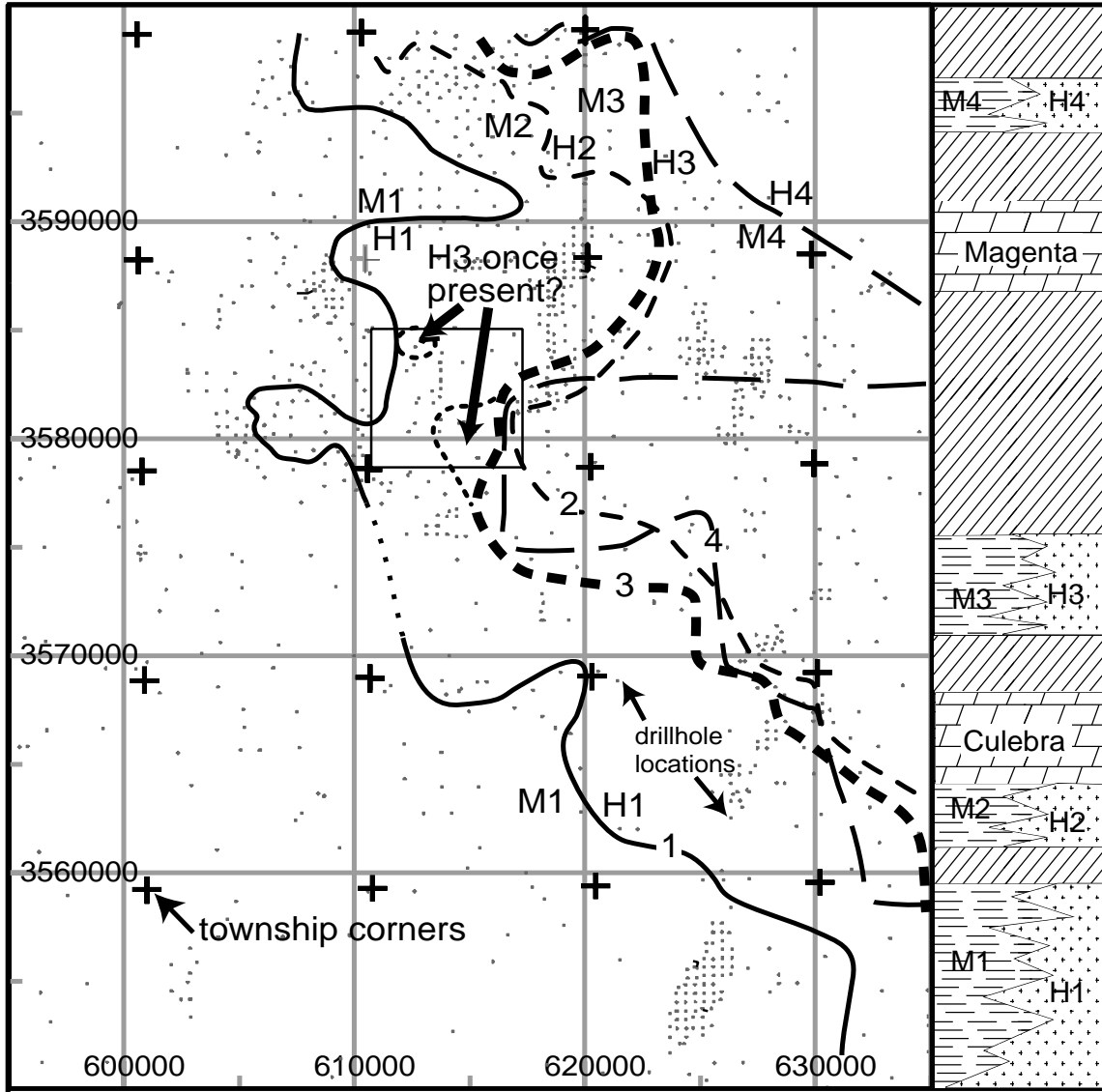
**Figure TFIELD-1. Structure Contour Map for the Top of the Culebra**



1

2

Figure TFIELD-2. Salado Dissolution Margin



**Explanation**

M#, H# indicate mudstone and halitic facies on each side of estimated halite margin (numbered line on map) for stratigraphic intervals as indicated in the column to the right (key on Figure TFIELD-4).

UTM coordinates (m) for Zone 13 (NAD27) are provided for easting and northing.

Two zones within the WIPP site boundary ("H3 once present?") indicate where halite may have been present west of the current boundary of H3 (marked by - - - - -).

1

2 **Figure TFIELD-3. Rustler Halite Margins. See Figure TFIELD-4 for key to stratigraphic**  
 3 **column.**

1 Halite margins in the Rustler Formation are interpreted as mainly due to depositional limits of  
2 saltpan environments and syndepositional removal of some halite exposed in saline mud flat  
3 deposits (Holt and Powers 1988). The halite margins are expected to be the locus of halite  
4 dissolution, if any, since the Rustler was deposited. Facies including halite beds or halite  
5 cements are expected to be less permeable than the equivalent mudstone facies. As a  
6 consequence, the margin is more likely to be attacked by advection and diffusion at the margin,  
7 from the mudstone facies side of the margin. In addition, removing halite along the margin as  
8 the saltpan margin fluctuates is likely to introduce some vertical and horizontal discontinuities  
9 that persist after lithification and are not created where the saltpan persisted. Water in adjacent  
10 units or in the mudstone unit likely has more pathways along these margins, increasing the  
11 likelihood that the margins will be the locus of dissolution. Recent findings of a narrow margin  
12 along which halite is dissolved from the upper Salado (Powers et al. 2003) are consistent with  
13 the expectation that halite margins in the Rustler would be the locus of dissolution.

14 Two areas have been identified where halite appears to have been dissolved from the M3/H3  
15 interval after deposition of the Rustler. These areas are shown with the annotation "H3 once  
16 present?" on Figure TFIELD-3. In the vicinity of drillhole H-19b0 and south (the southern area  
17 shown), cores of several WIPP drillholes show brecciation of the upper Tamarisk Member  
18 anhydrite in response to dissolution. Another area of dissolution, previously discussed in Holt  
19 and Powers (1988), Powers and Holt (1995), and Beauheim and Holt (1990), is around WIPP-13  
20 (the northern area shown), and may represent an outlier of salt left behind during syndepositional  
21 removal of halite from the M3 areas west of the WIPP site (Powers and Holt 2000). These areas  
22 have not been extended interpretively on Figure TFIELD-3 as was done in Beauheim and Holt  
23 (1990), but are limited to the vicinities of the locations at which evidence of dissolution has been  
24 directly observed.

25 Because of the position of M2/H2 directly beneath the Culebra, dissolution of H2 might be  
26 expected to have a strong influence on Culebra T. However, the H2 depositional margin is  
27 largely east of the WIPP site, barely crossing the southern portion of the eastern WIPP site  
28 boundary (Figure TFIELD-3). H2 dissolution does not appear to be a factor affecting Culebra T  
29 in any hydrology test well for WIPP, but there are no direct observations along the H2 margin.

### 30 ***TFIELD-3.0 DEVELOPMENT OF MODEL RELATING*** 31 ***CULEBRA T TO GEOLOGIC FACTORS***

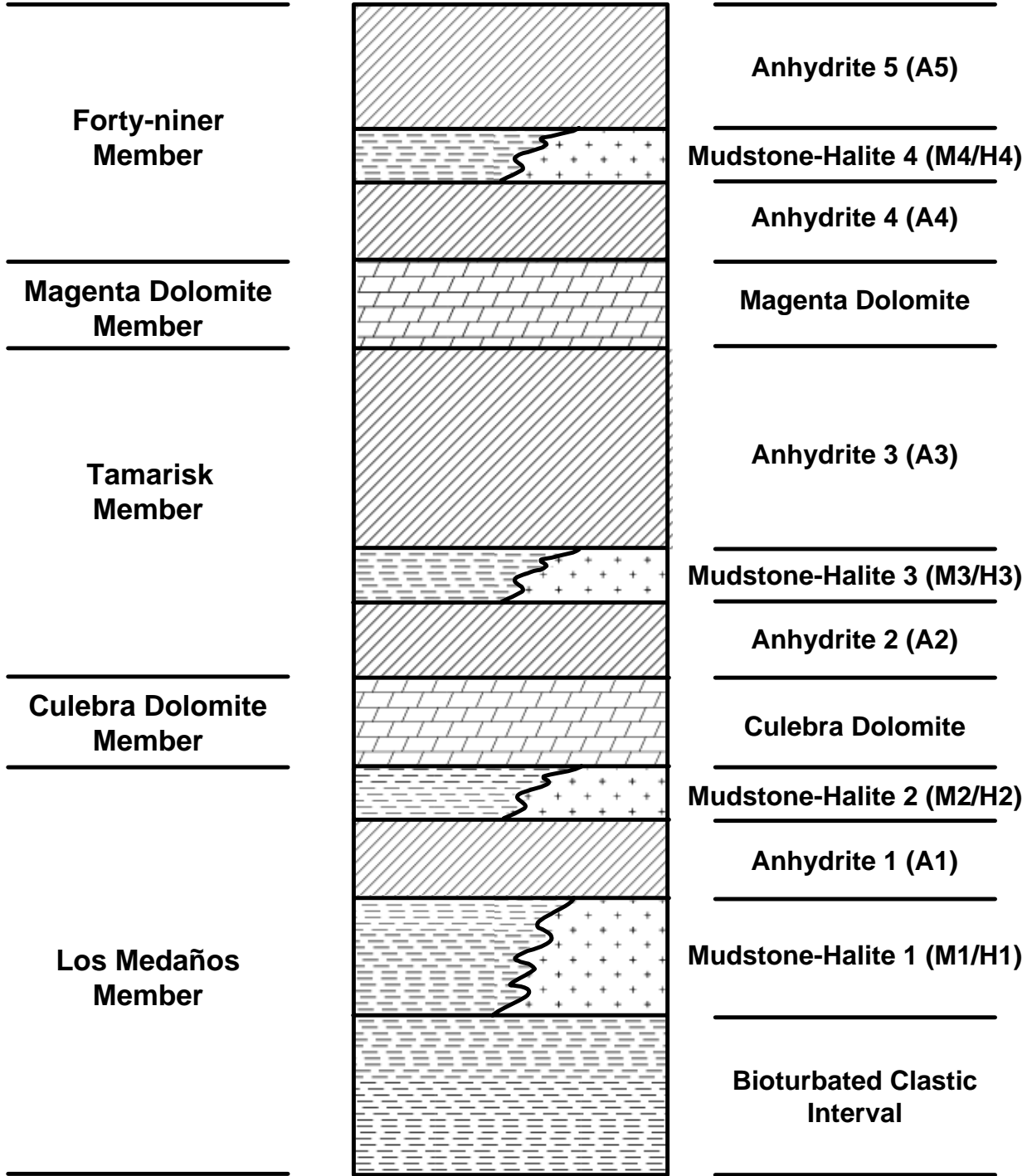
32 Holt and Powers (1988), Powers and Holt (1990), Beauheim and Holt (1990), and Holt (1997)  
33 have described the geology and geologic history of the Culebra. The following model is  
34 developed from their work and is consistent with their interpretations. It is important to note that  
35 this work follows Holt (1997) and assumes that variability in Culebra T is due strictly to post-  
36 depositional processes. Throughout the following discussion, the informal stratigraphic  
37 subdivisions of Holt and Powers (1988) are used to identify geologic units within the Rustler  
38 Formation (Figure TFIELD-4).

39 The spatial distribution of Culebra T on a regional scale is a function of a series of deterministic  
40 geologic controls, including Culebra overburden thickness, dissolution of the upper Salado  
41 Formation, and the occurrence of halite in units above or below the Culebra. Each of these



**Formal Stratigraphy  
After  
Lang (1935) and  
Powers and Holt (1999)**

**Informal Stratigraphy  
of  
Holt and Powers (1988)**



1

2

**Figure TFIELD-4. Stratigraphic Subdivisions of the Rustler Formation**

1 geologic controls can be determined at any location using geological map data. In the region  
 2 between the margin of upper Salado dissolution and the margin of halite occurrence above the  
 3 Culebra, which includes the WIPP site, however, high-T regions occur that cannot be predicted  
 4 using geologic data. These high-T zones are treated stochastically, using what is termed a  
 5 fracture-interconnectivity indicator.

6 In the following paragraphs, the fracture-interconnectivity indicator is defined, and then the  
 7 specifics of each hypothesized control on Culebra T are outlined. Finally, a linear model relating  
 8 these controls to Culebra T is presented that provides an excellent fit to the available data, is  
 9 testable, and is consistent with our understanding of Culebra geology.

### 10 ***TFIELD-3.1 Fracture Interconnection***

11 Culebra T data show a bimodal distribution (Figure TFIELD-5). Interpretations of hydraulic  
 12 tests (e.g., Beauheim and Ruskauff 1998) and observations of the presence or absence of open  
 13 fractures in core show the bimodal T distribution to be the result of hydraulically significant  
 14 fractures. Some degree of fracturing is evident in all Culebra cores, but the fractures tend to be  
 15 filled with gypsum at locations where the T inferred from hydraulic tests is less than  
 16 approximately  $4 \times 10^{-6} \text{ m}^2/\text{s}$  ( $\log_{10} = -5.4$ ). Where  $\log_{10} T \text{ (m}^2/\text{s)}$  is greater than  $-5.4$ , hydraulic  
 17 tests show double-porosity responses and open fractures are observed in core. Therefore, a  
 18 fracture-interconnectivity indicator is defined based on a cutoff of  $\log_{10} T \text{ (m}^2/\text{s)} = -5.4$ :

$$19 \quad I_f = \begin{cases} 1 & \log_{10} T \text{ (m}^2/\text{s)} > -5.4 \\ 0 & \log_{10} T \text{ (m}^2/\text{s)} \leq -5.4 \end{cases} \quad (1)$$

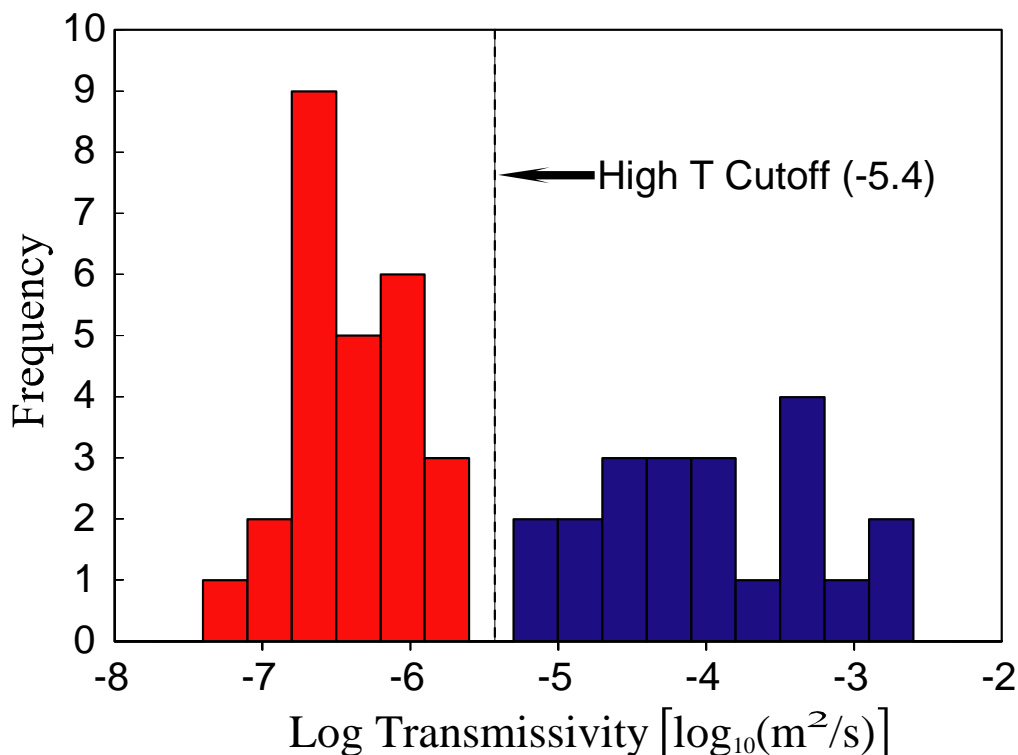
20 Open, interconnected fractures and high Ts occur in regions affected by Salado dissolution (e.g.,  
 21 Nash Draw) and in areas west of the M3/H3 margin where gypsum fracture fillings are absent.

### 22 ***TFIELD-3.2 Overburden Thickness***

23 An inverse relationship exists between Culebra overburden thickness and T. At the WIPP wells  
 24 for which T data are available, the Culebra overburden thickness ranges from 3.7 m (at  
 25 WIPP-29) to 414.5 m (at H-10) (Mercer 1983), increasing from west to east. Overburden  
 26 thickness is a metric for two different controls on Culebra T. First, fracture apertures are limited  
 27 by overburden thickness (e.g., Currie and Nwachukwu 1974), which should lead to lower T  
 28 where Culebra depths are great (Beauheim and Holt 1990; Holt 1997). Second, erosion of  
 29 overburden leads to changes in stress fractures, and the amount of Culebra fracturing increases as  
 30 the overburden thickness decreases (Holt 1997). Holt (1997) estimates that at least 350 m of  
 31 overburden has been eroded at the center of the WIPP site (where the Culebra is at a depth of  
 32 approximately 214 m) since the end of the Triassic, with more erosion occurring west of the site  
 33 center where overburden (chiefly the Dewey Lake) is thinner and less erosion occurring to the  
 34 east where Triassic deposits are thicker.

### 35 ***TFIELD-3.3 Salado Dissolution***

36 In regions north, south, and west of the WIPP site, Cenozoic dissolution has affected the upper  
 37 Salado Formation (Figure TFIELD-2). Where this dissolution has occurred, the rocks overlying  
 38 the Salado, including the Culebra, are strained (leading to larger apertures in existing fractures),



1  
2 **Figure TFIELD-5. Histogram of Log<sub>10</sub> Culebra T. Data from DOE (1996), Beauheim and**  
3 **Ruskauff (1998), and Beauheim (2002c)**

4 fractured, collapsed, and brecciated (e.g., Beauheim and Holt 1990; Holt 1997). All WIPP wells  
5 within the upper-Salado-dissolution zone fall within the high-T population, and all regions  
6 affected by Salado dissolution are expected to have well-interconnected fractures and high T.

#### 7 ***TFIELD-3.4 Halite Overlying the Culebra***

8 All wells (e.g., H-12 and H-17) located where halite occurs in the M3/H3 interval of the  
9 Tamarisk (Figure TFIELD-3) show low T. T data are limited in this region, but it is unlikely that  
10 halite would survive in M3/H3, only several meters from the Culebra, in regions of high T where  
11 Culebra flow rates are relatively high. High-T zones, therefore, are assumed to not occur in  
12 regions where halite is present in the M3/H3 interval.

#### 13 ***TFIELD-3.5 Halite Bounding the Culebra***

14 In regions where halite is present in the M2/H2 interval directly below the Culebra, no reliable  
15 quantitative estimates of Culebra T are available. Beauheim (1987) estimates T at P-18, the only  
16 tested well at which halite is present in the M2/H2 interval, to be less (probably much less) than  
17  $4 \times 10^{-9}$  m<sup>2</sup>/s (log<sub>10</sub> = -8.4). In much of the area where halite is present in the M2/H2 interval  
18 (including the P-18 location), halite is also present in the M3/H3 interval. Based upon geologic  
19 observations of halite-bound units elsewhere within the WIPP area, Holt (1997) suggests that  
20 porosity within the Culebra may contain abundant halite cements in these areas. Beauheim and  
21 Holt (1990) and Holt (1997) indicate that Culebra porosity shows increasing amounts of pore-  
22 filling cement east of the WIPP site. Consequently, Culebra T is assumed to be much lower in

1 the region where halite occurs both above (M3/H3 interval) and below (M2/H2 interval) the  
 2 Culebra. Much lower T is also assumed in the area northeast of the WIPP site where halite is  
 3 present in the M2/H2 interval but absent in the M3/H3 interval (see Figure TFIELD-3).

#### 4 ***TFIELD-3.6 High-T Zones***

5 In addition to the high T that occurs everywhere dissolution of the upper Salado has occurred,  
 6 high-T zones also occur in the Culebra in the region bounded by the limit of upper Salado  
 7 dissolution to the west and by the margin of where halite is present in the M2/H2 and M3/H3  
 8 intervals to the east (see Figures TFIELD-2 and TFIELD-3). Fracture openness and  
 9 interconnectivity in these high-T zones are controlled by a complicated history of fracturing with  
 10 several episodes of cement precipitation and dissolution (Beauheim and Holt 1990; Holt 1997).  
 11 No geologic metric has yet been defined that allows prediction of where fractures are filled or  
 12 open, hence our knowledge of this indicator east of the Salado dissolution margin is limited to  
 13 the test well locations shown in Figure TFIELD-6. Consequently, the spatial location of high-T  
 14 zones between the Salado dissolution margin and the M2/H2 and M3/H3 margins is treated  
 15 stochastically.

#### 16 ***TFIELD-3.7 Linear Transmissivity Model***

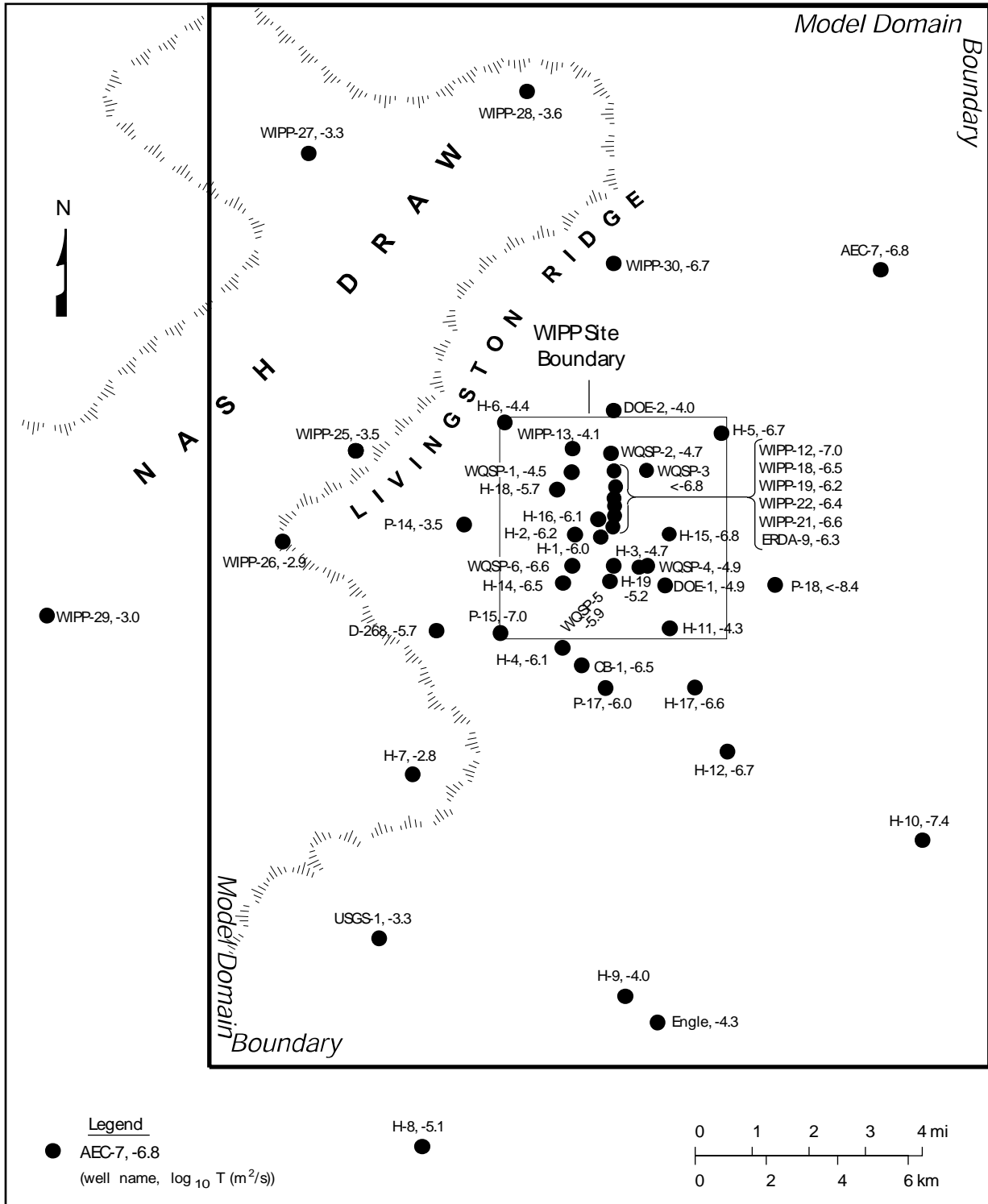
17 Using the hypothesized geologic controls on Culebra T, the following linear model for  $Y(\mathbf{x}) =$   
 18  $\log_{10} T(\mathbf{x})$  was constructed:

$$19 \quad Y(\mathbf{x}) = \beta_1 + \beta_2 d(\mathbf{x}) + \beta_3 I_f(\mathbf{x}) + \beta_4 I_D(\mathbf{x}) \quad (2)$$

20 where  $\beta_i$  ( $i = 1, 2, 3, 4$ ) are regression coefficients,  $\mathbf{x}$  is a two-dimensional location vector  
 21 consisting of UTM X and UTM Y coordinates,  $d(\mathbf{x})$  is the overburden thickness,  $I_f(\mathbf{x})$  is the  
 22 fracture-interconnectivity indicator given in Equation (1) that assumes the value of 1 if fracturing  
 23 and high T have been observed at point  $\mathbf{x}$  and 0 otherwise, and  $I_D(\mathbf{x})$  is a dissolution indicator  
 24 function that assumes the value of 1 if Salado dissolution has occurred at point  $\mathbf{x}$  and 0  
 25 otherwise. In this model, regression coefficient  $\beta_1$  is the intercept value for the linear model.  
 26 Coefficient  $\beta_2$  is the slope of  $Y(\mathbf{x})/d(\mathbf{x})$ . Coefficients  $\beta_3$  and  $\beta_4$  represent adjustments to the  
 27 intercept for the occurrence of interconnected fractures and Salado dissolution, respectively.  
 28 Although other types of linear models could be developed, this model is consistent with the  
 29 conceptual model relating T to geologic controls and can be tested using published WIPP  
 30 geologic and T data. Note that the regression model does not explicitly contain terms relating  
 31 Culebra T to zones where the Culebra is bounded by halite in both the M2/H2 and M3/H3  
 32 intervals because of lack of data from these areas. Therefore, it cannot be used to predict T east  
 33 of the M2/H2 margin.

#### 34 ***TFIELD-3.8 Linear-Regression Analysis***

35 A linear-regression model was written using the Windows-based program Mathcad 7  
 36 Professional<sup>®</sup> specifically for this application. Although other variables are input, this model  
 37 requires only  $\log_{10} T$  data from tested wells, the depth of the Culebra at those wells, and an  
 38 estimate of whether dissolution of the upper Salado has or has not occurred at each location. The  
 39 fracture interconnectivity indicator is defined from the  $\log_{10} T$  data, and a Salado dissolution  
 40 indicator is defined using the Salado dissolution data. These data are then used in a standard  
 41 linear regression algorithm to determine the regression coefficients for Equation (2).



TRI-6115-192-1

1  
2  
3

**Figure TFIELD-6. Well Locations and  $\log_{10}$  Culebra Transmissivities**

1 The regression coefficients for Equation (2) derived from this analysis are presented in Table  
 2 TFIELD-1. The regression has a multiple correlation coefficient ( $R^2$ ) of 0.941 and a Regression  
 3 ANOVA F statistic of 222. The number of degrees of freedom about the regression (n) equals  
 4 the number of observations (46) minus the number of parameters (4). The number of degrees of  
 5 freedom due to the regression (m) equals the number of parameters (4) minus 1. With  $n = 42$  and  
 6  $m = 3$ , the regression is significant above the 0.999 level. Residuals show no anomalous  
 7 behavior. Accordingly, the regression model provides an accurate and reasonable description of  
 8 the data. The fit of the regression to the  $\log_{10}$  T data is shown in Figure TFIELD-7.

9 **Table TFIELD-1. Regression Coefficients for Equations (2) and (3)**

$\beta_1$	$\beta_2$	$\beta_3$	$\beta_4$
-5.441	$-4.636 \times 10^{-3}$	1.926	0.678

10 The regression model does not predict T in the regions where the Culebra is underlain by halite  
 11 in the M2/H2 interval because no quantitative data were available from these regions to be used  
 12 in deriving the regression. In these regions, the following modified version of the regression  
 13 model of Equation (2) is applied:

$$14 \quad Y(\mathbf{x}) = \beta_1 + \beta_2 d(\mathbf{x}) + \beta_3 I_f(\mathbf{x}) + \beta_4 I_D(\mathbf{x}) + \beta_5 I_H(\mathbf{x}) \quad (3)$$

15 where  $I_H(\mathbf{x})$  is a halite indicator function. This indicator is assigned a value of 1 in locations  
 16 where halite occurs in the M2/H2 interval and 0 otherwise. The coefficient  $\beta_5$  is set equal to  $-1$   
 17 so that Equation (3) reduces the predicted T values by one order of magnitude where halite  
 18 occurs in the M2/H2 interval, to accord qualitatively with the expected transmissivity reduction  
 19 discussed in Section 3.5 of this attachment. With knowledge (or stochastic estimations) of the  
 20 values of the geologic controls (e.g., Culebra depth, fracture-interconnectivity indicator,  
 21 dissolution indicator, and halite indicator), Culebra T values can be predicted at unobserved  
 22 locations in the WIPP Culebra model domain using Equation (3).

#### 23 **TFIELD-4.0 CALCULATION OF BASE T FIELDS**

24 In this section, a method is developed for applying the linear regression model from Section 3.0  
 25 of this attachment to predict Culebra T across a model domain encompassing the WIPP area.  
 26 Culebra overburden thickness, Salado dissolution, and the presence or absence of halite in units  
 27 bounding the Culebra can be deterministically evaluated across the WIPP region using maps  
 28 constructed from subsurface data (Section 2.0 of this attachment). The presence of open,  
 29 interconnected fractures, however, cannot be deterministically assessed across the WIPP area  
 30 using maps. A geostatistical approach, conditional indicator simulation, is used to generate 500  
 31 equiprobable realizations of zones with hydraulically significant fractures in the WIPP region.  
 32 These simulations are parameterized using the frequency of occurrence of WIPP wells with  
 33 hydraulically significant fractures and a fit to a variogram constructed using data from those  
 34 same wells. The regression model is then applied to the entire WIPP area by:

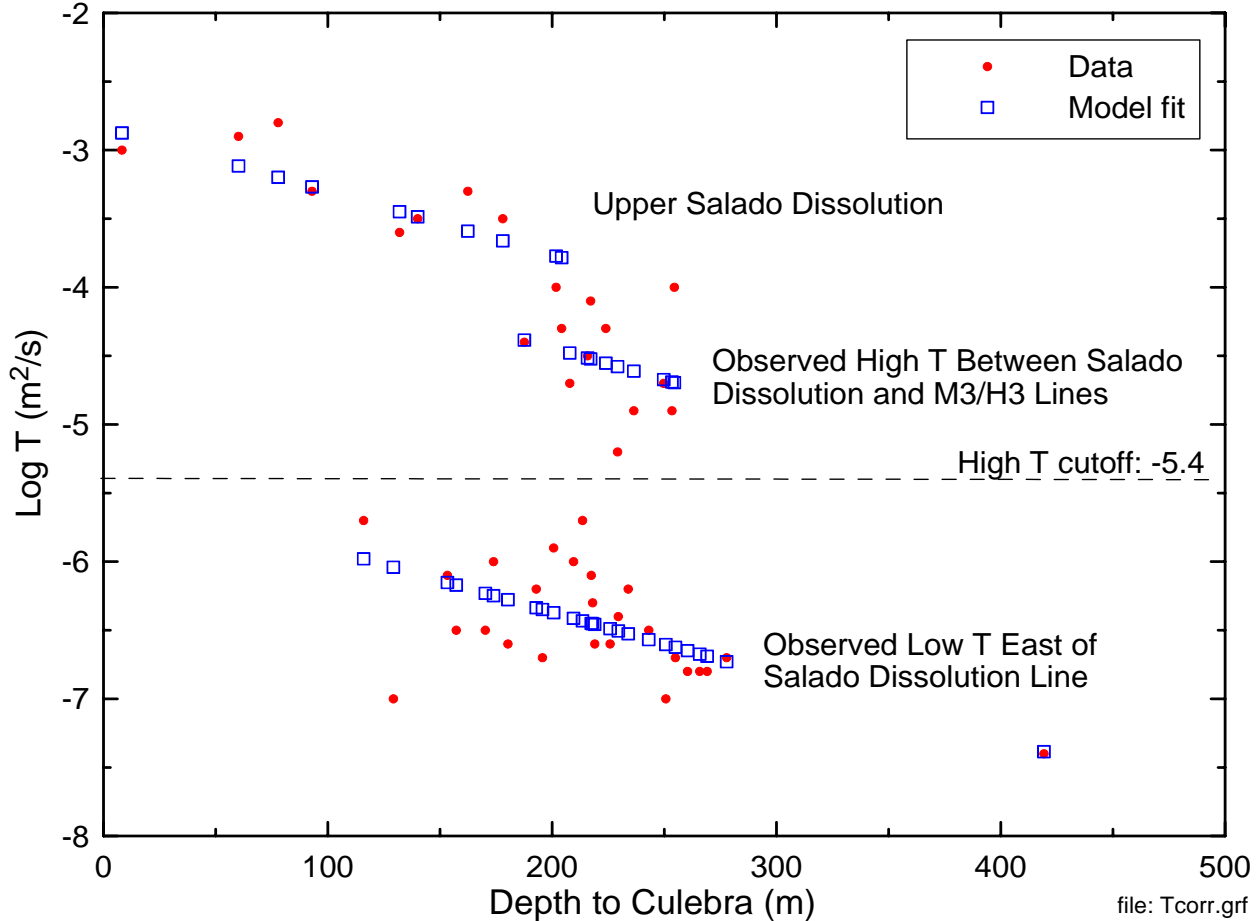


**Figure TFIELD-7. Regression Fit to Observed Culebra Log<sub>10</sub> T Data**

1. Overlaying the geologic map data for Culebra overburden thickness, Salado dissolution, and the presence or absence of halite in units bounding the Culebra with each of the 500 equiprobable realizations of zones containing open, interconnected fractures.
2. Sampling each grid point within the model domain to determine the overburden thickness and the indicator values for Salado dissolution, overlying or underlying halite, and fracture interconnectivity.
3. Using the sampled data at each grid point with the regression model coefficients to estimate Culebra T.

When applied to the 500 equiprobable realizations of zones containing open, interconnected fractures, this procedure generates 500 stochastically varying Culebra base T fields. Details about the creation of the base T fields are given in Holt and Yarbrough (2002, 2003a, 2003b).

**TFIELD-4.1 Definition of Model Domain**

Two principal factors were considered in selecting the boundaries for the Culebra model domain. First, model boundaries should coincide with natural groundwater divides where feasible, or be far enough from the southern portion of the WIPP site, where transport will be modeled, to have

1 minimal influence in that area. Second, the model domain should encompass known features  
 2 with the potential to affect Culebra water levels at the WIPP site (e.g., potash tailings ponds).  
 3 The modeling domain selected is 22.4 km (13.9 mi) east-west by 30.7 km (19.1 mi) north-south,  
 4 aligned with the compass directions (Figure TFIELD-6). This is the same as the domain used by  
 5 LaVenue et al. (1990) except that the current domain extends 1 km (0.62 mi) farther to the west  
 6 than the 1990 domain. The modeling domain is discretized into 68,768 uniform 100-m (328-ft)  
 7 by 100-m (328-ft) cells. The northern model boundary is slightly north of the northern end of  
 8 Nash Draw, 12 km (7.5 mi) north of the northern WIPP site boundary and about 1 km (0.62 mi)  
 9 north of Mississippi Potash Incorporated's east tailings pile. The eastern boundary lies in a low-  
 10 T region that contributes little flow to the modeling domain. The southern boundary lies 12.2 km  
 11 (7.6 mi) south of the southern WIPP site boundary, 1.7 km (1.5 mi) south of our southernmost  
 12 well (H-9) and far enough from the WIPP site to have little effect on transport rates on the site.  
 13 The western model boundary passes through the IMC tailings pond (Laguna Uno of Hunter  
 14 [1985]) due west of the WIPP site in Nash Draw. Boundary conditions assigned for the model  
 15 are discussed in Section 6.2 of this attachment. The coordinates of each corner of the domain are  
 16 given in Table TFIELD-2, in NAD 27 UTM coordinates.

17 **Table TFIELD-2. Coordinates of the Numerical Model Domain Corners**

Domain Corner	UTM X Coordinate (m)	UTM Y Coordinate (m)
Northeast	624,050	3,597,150
Northwest	601,650	3,597,150
Southeast	624,050	3,566,450
Southwest	601,650	3,566,450

18 ***TFIELD-4.2 Reduction of Geologic Map Data***

19 To create useable data sets for conditional simulation of high-T zones and prediction of Culebra  
 20 T, the geological maps described above in Section 2.0 of this attachment were imported into a  
 21 GIS environment and digitized. A uniform 100-m (328-ft) grid was then created over the  
 22 Culebra model domain. Using the Culebra structure contour map data (Figure TFIELD-1) and  
 23 surface elevation data obtained from the United States Geological Survey (USGS) National  
 24 Elevation Dataset (NED) (<http://edcnts12.cr.usgs.gov/ned>), an isopach map of the Culebra  
 25 overburden on the 100-m (328-ft) model grid was created.

26 Using maps showing occurrence of halite in the units above and below the Culebra and well  
 27 locations, soft data files were created for conditional indicator simulations. T within 120 m (374  
 28 ft) of each well is assumed to be from the same population (e.g., high or low T reflecting open,  
 29 interconnected fractures or filled (poorly interconnected) fractures, respectively), and regions  
 30 where the Culebra is overlain by halite in M3/H3 or underlain by halite in M2/H2 are assumed to  
 31 be low-T regions.

32 Using maps of Salado dissolution and the occurrence of halite in the units above and below the  
 33 Culebra, 100-m (328-ft) indicator grids were created over the model domain. These indicator  
 34 grids were created for regions affected by Salado dissolution, regions where the Culebra is



1 underlain by halite in the M2/H2 interval, and a middle zone in which the Culebra is neither  
2 overlain nor underlain by halite where high-T zones occur stochastically (Figure TFIELD-8).

### 3 ***TFIELD-4.3 Indicator Variography***

4 Excluding data where Salado dissolution occurs, Culebra T data are indicator transformed (1 for  
5  $\log_{10} T \text{ (m}^2/\text{s)} > -5.4$ , 0 otherwise). A high-T indicator variogram is then constructed for the  
6 indicator data in the region not affected by Salado dissolution using the GSLIB program gamv  
7 (Deutsch and Journel 1998). The lag spacing for this variogram is selected to maximize  
8 variogram resolution. The resulting indicator variogram is then fit with an isotropic spherical  
9 variogram model:

$$10 \quad \gamma(h) = \begin{cases} s[1.5(h/\lambda) - 0.5(h/\lambda)^3] & \text{if } h \leq \lambda \\ s & \text{if } h \geq \lambda \end{cases} \quad (4)$$

11 where  $\gamma(h)$  is the variogram as a function of lag spacing  $h$ ,  $s$  is the sill value of the indicator  
12 variogram, and  $\lambda$  is the correlation length. This variogram model minimizes the mean squared  
13 error between the experimental and modeled variogram. The sill value was determined using:

$$14 \quad s = P[\log_{10} T \text{ (m}^2/\text{s)} > -5.4] - \{P[\log_{10} T \text{ (m}^2/\text{s)} > -5.4]\}^2 \quad (5)$$

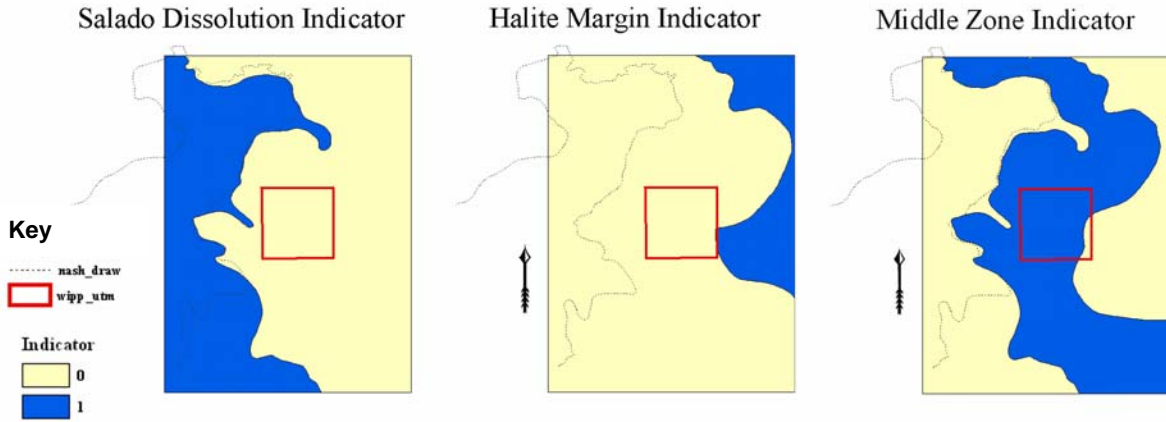
15 For the Culebra data set, excluding wells where dissolution has occurred,  $s = 0.201$ . The  
16 correlation length  $\lambda$  was estimated to be 1,790 m (5,873 ft). No nugget effect was included in  
17 the variogram model (Figure TFIELD-9). Variogram model parameters were then used in  
18 conditional indicator simulations of Culebra high-T zones.

### 19 ***TFIELD-4.4 Conditional Indicator Simulation***

20 “Soft” indicator data were created for the indicator simulations. To ensure that no high-T  
21 regions develop in areas where halite occurs in M2/H2 or M3/H3, soft data points, indicating low  
22 T, were placed on a 200-m (656-ft) grid east of the M2/H2 and M3/H3 salt margins. This 200-m  
23 (656-ft) grid used the original 100-m (328-ft) grid excluding every other node to assure the  
24 200-m (656-ft) soft data grid spatially overlay the 100-m (328-ft) grid. Soft data were also  
25 specified for every 100-m (328-ft) node along the combined lines of the M2/H2 and M3/H3 salt  
26 margins.

27 Additional soft data were created near well locations establishing a 120-m (394-ft) buffer around  
28 each well (Figure TFIELD-10). All 100-m (328-ft) grid nodes lying within the 120-m (394-ft)  
29 buffer were selected and assigned the transmissivity attribute of the well. Because all the nodes  
30 within 120 m (394 ft) of the well and the node corresponding to the block containing the well  
31 were selected as soft data, there was duplication in the input files. Only one data point can  
32 occupy a 100-m (328-ft) grid space during a realization. Therefore, the node closest to the well  
33 was eliminated from the soft data file.

1

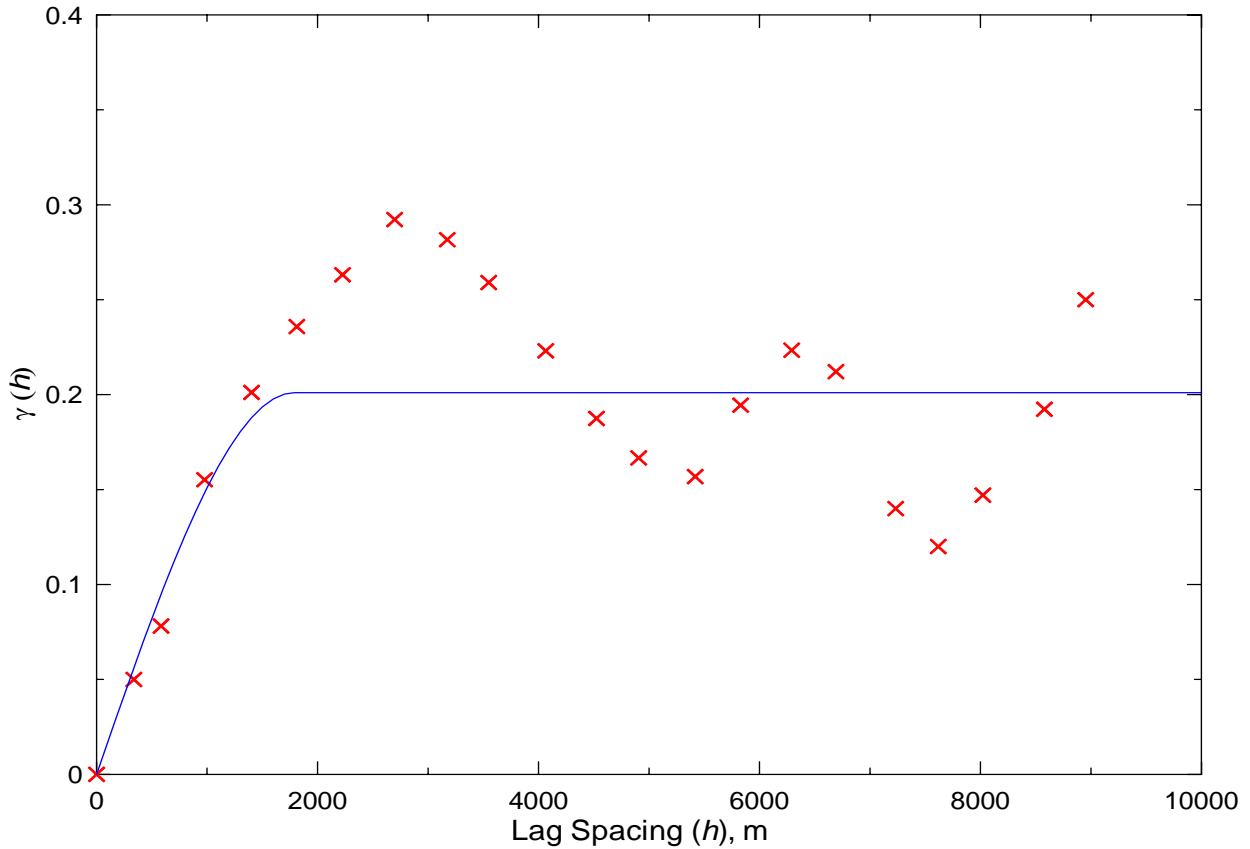


2

3

4

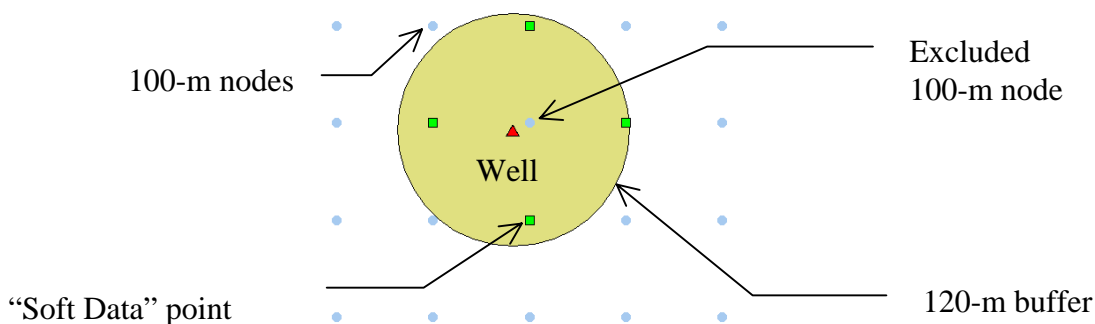
**Figure TFIELD-8. Zones for Indicator Grids**



5

6

**Figure TFIELD-9. High-T Indicator Model and Experimental Variograms**



1  
2 **Figure TFIELD-10. Soft Data Around Wells**

3 Five hundred conditional indicator simulations were generated on the 100-m (328-ft) model grid  
4 using the GSLIB program sisim (Deutsch and Journel 1998) with Culebra high-T indicator data,  
5 soft data for regions around wells and regions where halite underlies and overlies the Culebra,  
6 and the variogram parameters. The resulting indicator simulations were used in the construction  
7 of base T fields.

#### 8 ***TFIELD-4.5 Construction of Base Transmissivity Fields***

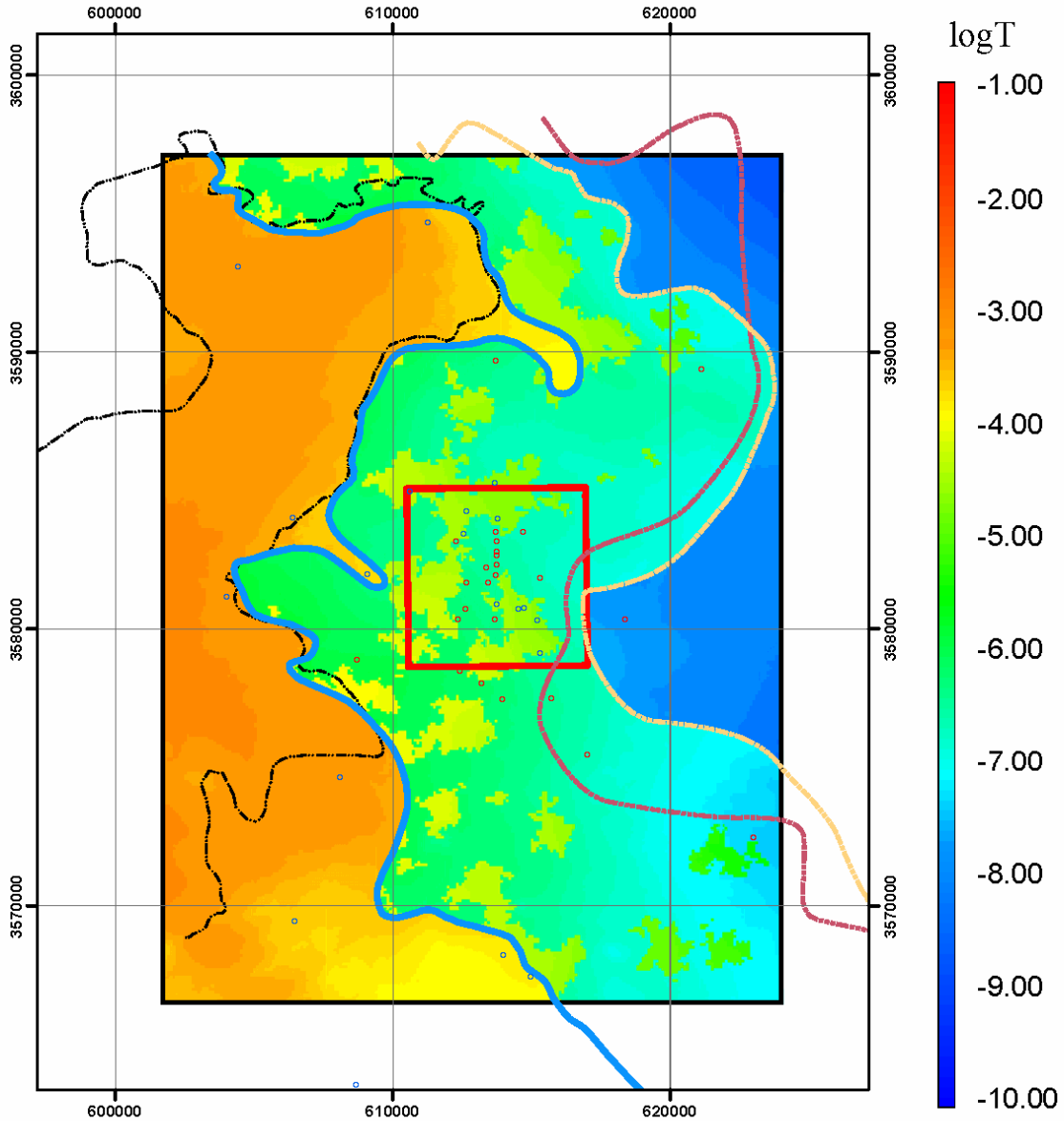
9 The linear predictor (Equation (3)) was used to generate 500 equally probable realizations of the  
10 T distribution in the Culebra model domain. This calculation required the regression coefficients  
11 discussed in Section 3.8 of this attachment, Culebra depth data (Section 3.9 of this attachment), a  
12 Salado dissolution indicator function, an indicator for where halite occurs in M2/H2, and the 500  
13 realizations of high-T indicators discussed in Section 4.4 of this attachment.

14 The 500 base T fields were created in five sets. Each set consists of ten groups of ten  
15 realizations given d##r## designations. The “d” counter ranges from 01 to 50, while the “r”  
16 counter ranges from 01 to 10. An example base T field is shown in Figure TFIELD-11.  
17 Stochastically located patches of relatively high T (yellowish-green) can be clearly seen in the  
18 middle zone of the model domain. (Note: On black and white copy, these patches appear as the  
19 lightest shade of gray.)

#### 20 ***TFIELD-5.0 CONSTRUCTION OF SEED REALIZATIONS***

21 The base T fields described in Section 4.5 of this attachment rely on a regression model to estimate  
22 T at every location. By the nature of regression models, the estimated T values will not honor the  
23 measured T values at the measurement locations. Therefore, before using these base T fields in a  
24 flow model, they must be conditioned to the measured T values. This conditioning is performed  
25 with a Gaussian geostatistical simulation algorithm to generate a series of 500 spatially correlated  
26 residual fields where each field has a mean value of zero. These fields are conditional such that the  
27 residual value at each measurement location, when added to the value provided by the regression  
28 model (which is the same for all 500 fields), provides the known T value at that location. The  
29 result of adding the simulated residual field to the base T field is the “seed” realization.

### D21R10 -- Uncalibrated



**Explanation**

- Well (transmissivity)**
- Low
- High
- Salt Margin m3/h3
- Salt Margin m2/h2
- Nash Draw
- Salado Dissolution
- WIPP Site



1

2

**Figure TFIELD-11. Example Base T Field**

1 This process is shown conceptually along a west-to-east cross section of the Culebra in Figure  
 2 TFIELD-12. The upper image shows the value of the residuals at five T measurement locations  
 3 across the cross section. These residuals are calculated as the observed (measured) T value  
 4 minus the base field T value at the same locations. Positive residuals are where the measured T  
 5 value is greater than that of the base T field. To create a T field from these residuals, there needs  
 6 to be a way to tie the base field to the measured T values. This tie is accomplished by creating a  
 7 spatial simulation of the residual values, a “residual field.” The middle image of Figure  
 8 TFIELD-12 is an example residual field as a (red) dashed line along the cross section. This  
 9 residual field is constructed through geostatistical simulation using a variogram model fit to the  
 10 residual data. The residual field honors the measured residuals at their measurement locations  
 11 and returns to a mean value of zero at distances far away from the measurement locations.  
 12 Finally, this residual field is added to the base T field to create the seed T field. The base T field  
 13 is represented by the solid (blue) line in the bottom image of Figure TFIELD-12 and the seed T  
 14 field is shown by the dotted line. The seed T field corresponds to the base T field except at those  
 15 locations where it must deviate to match the measured T data. The large discontinuity shown in  
 16 the base T field at the bottom of Figure TFIELD-12 is due to the stochastic simulation of high-T  
 17 zones within the Culebra.

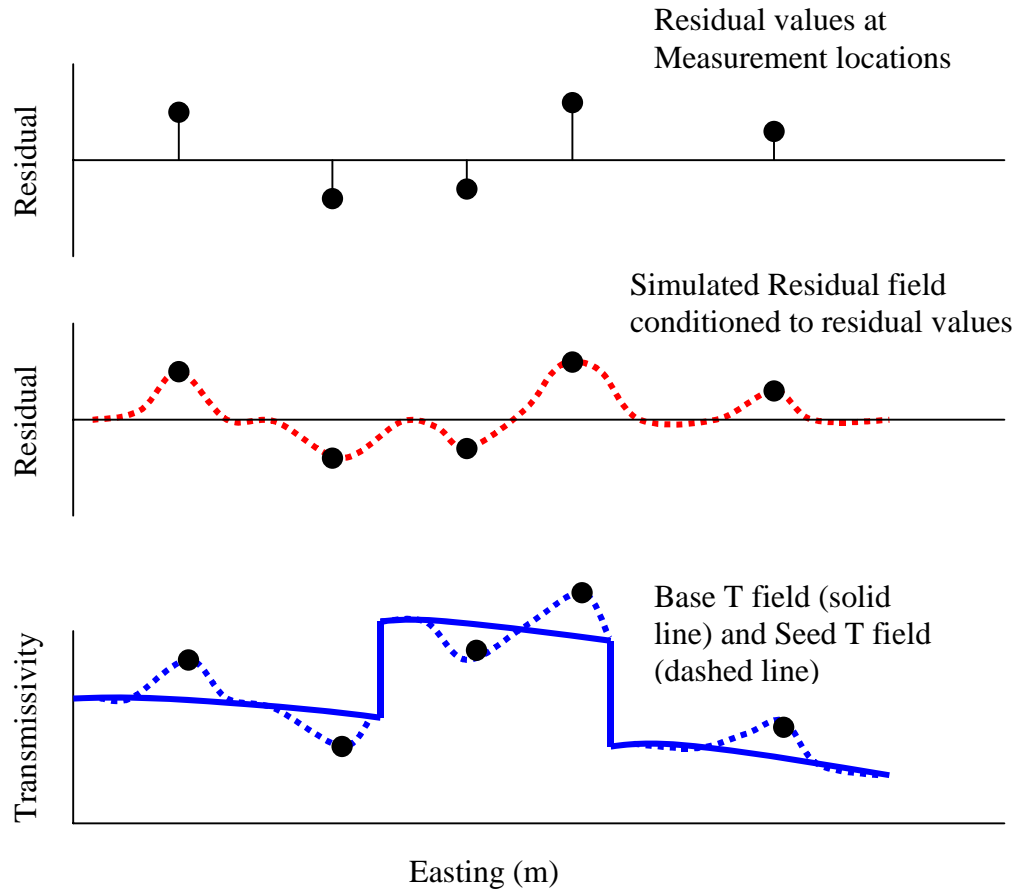
18 A total of 46 measured T values and corresponding residual data, both in units of  $\log_{10}(\text{m}^2/\text{s})$ ,  
 19 are available (Table TFIELD-3). For each pair of  $\log_{10} T$  and residual data, the well name and  
 20 the easting (X) and northing (Y) UTM coordinates are also given (for multiwell hydropads, a  
 21 single well’s coordinates were used).

22 The process of creating the residual fields is to use the residual data to generate variograms in the  
 23 VarioWin<sup>®</sup> software package and to then create conditional stochastic Gaussian geostatistical  
 24 simulations of the residual field within the GSLIB program gsim (Deutsch and Journel 1998).

25 To use the data in a Gaussian simulation algorithm, it is first necessary to transform the  
 26 distribution of the raw residual data to a standard normal distribution. This is accomplished  
 27 through a process called the “normal-score transform” where each transformed residual value is  
 28 the “normal-score” of each original datum. The normal-score transform is a relatively simple  
 29 two-step process. First the cumulative frequency of each original residual value,  $cdf(i)$ , is  
 30 determined as:

$$31 \quad cdf(i) = \frac{R(i) - 0.5}{N} \quad (6)$$

32 where  $R(i)$  is the rank (smallest to largest) of the  $i^{\text{th}}$  residual value and  $N$  is the total number of  
 33 data (46 in this case). Then for each cumulative frequency value, the corresponding normal-  
 34 score value is calculated from the inverse of the standard normal distribution. By definition, the  
 35 standard normal distribution has a mean of 0.0 and a standard deviation of 1.0. Further details of  
 36 the normal-score transform process can be found in Deutsch and Journel (1998).



1  
 2 **Figure TFIELD-12. Conceptual Cross Section Showing the Updating of the Residual Field**  
 3 **and the Base T Field into the Seed T Field**

**Table TFIELD-3.  $\log_{10}$  Transmissivity Data Used in Inverse Calibrations**

Well ID	Easting (UTM, m)	Northing (UTM, m)	$\log_{10} T$ ( $m^2/s$ )	$\log_{10} T$ residual ( $m^2/s$ )
AEC-7	621126	3589381	-6.8	-0.11078
CB-1	613191	3578049	-6.5	-0.32943
D-268	608702	3578877	-5.7	0.27914
DOE-1	615203	3580333	-4.9	-0.21004
DOE-2	613683	3585294	-4.0	0.69492
Engle	614953	3567454	-4.3	-0.51632
ERDA-9	613696	3581958	-6.3	0.15250
H-1	613423	3581684	-6.0	0.41295
H-2c	612666	3581668	-6.2	0.13594
H-3b1	613729	3580895	-4.7	-0.22131
H-4c	612406	3578499	-6.1	0.05221
H-5c	616903	3584802	-6.7	0.02946

**Table TFIELD-3. Log<sub>10</sub> Transmissivity Data Used in Inverse Calibrations — Continued**

Well ID	Easting (UTM, m)	Northing (UTM, m)	log <sub>10</sub> T (m <sup>2</sup> /s)	log <sub>10</sub> T residual (m <sup>2</sup> /s)
H-6c	610610	3584983	-4.4	-0.01524
H-7c	608095	3574640	-2.8	0.39794
H-9c	613974	3568234	-4.0	-0.22763
H-10b	622975	3572473	-7.4	-0.01484
H-11b4	615301	3579131	-4.3	0.25314
H-12	617023	3575452	-6.7	-0.07647
H-14	612341	3580354	-6.5	-0.26934
H-15	615315	3581859	-6.8	-0.12631
H-16	613369	3582212	-6.1	0.34962
H-17	615718	3577513	-6.6	-0.14310
H-18	612264	3583166	-5.7	0.73159
H-19b0	614514	3580716	-5.2	-0.62242
P-14	609084	3581976	-3.5	0.16212
P-15	610624	3578747	-7.0	-0.95938
P-17	613926	3577466	-6.0	0.24762
USGS-1	606462	3569459	-3.3	0.28998
WIPP-12	613710	3583524	-7.0	-0.39627
WIPP-13	612644	3584247	-4.1	0.42180
WIPP-18	613735	3583179	-6.5	0.06840
WIPP-19	613739	3582782	-6.2	0.32598
WIPP-21	613743	3582319	-6.6	-0.11148
WIPP-22	613739	3582653	-6.4	0.10549
WIPP-25	606385	3584028	-3.5	-0.01378
WIPP-26	604014	3581162	-2.9	0.21598
WIPP-27	604426	3593079	-3.3	-0.03209
WIPP-28	611266	3594680	-3.6	-0.15124
WIPP-29	596981	3578694	-3.0	-0.12497
WIPP-30	613721	3589701	-6.7	-0.35131
WQSP-1	612561	3583427	-4.5	0.01540
WQSP-2	613776	3583973	-4.7	-0.02729
WQSP-3	614686	3583518	-6.8	-0.15139
WQSP-4	614728	3580766	-4.9	-0.28895
WQSP-5	613668	3580353	-5.9	0.47178
WQSP-6	612605	3580736	-6.6	-0.32261

1

1 The two-step normal-score transformation process is conducted in Microsoft Excel<sup>®</sup> (see details  
2 in McKenna and Hart 2003b). The resulting normal-score values are the distance from the mean  
3 as measured in standard deviations. The parameters describing the residual and normal-score  
4 transformed distributions are presented in Table TFIELD-4.

5 **Table TFIELD-4. Statistical Parameters Describing the Distributions of the Raw and**  
6 **Normal-score Transformed Residual Data**

Parameter	Raw Residual	Normal-Score Transformed Residual Data
Mean	0.000	0.000
Median	-0.015	0.000
Standard Deviation	0.330	0.997
Minimum	-0.959	-2.295
Maximum	0.732	2.295

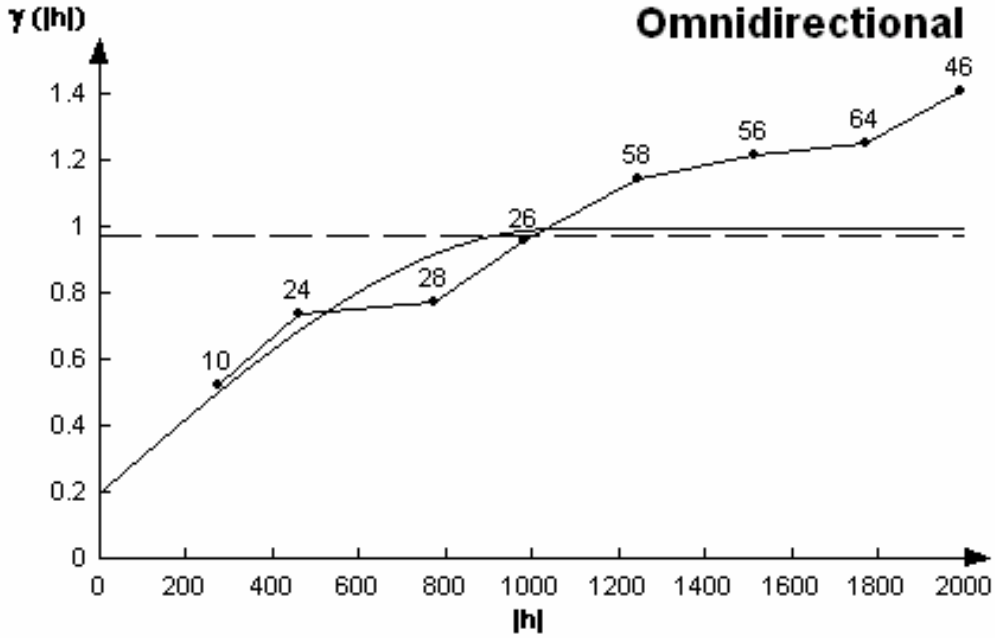
7 The omnidirectional variogram is calculated with a 250-m (820-ft) lag spacing. The  
8 experimental variogram is shown in Figure TFIELD-13. The model fit to this experimental  
9 variogram is Gaussian with a nugget of 0.2, a sill of 0.8, and a range of 1,050 m (3,445 ft). The  
10 sum of the nugget and sill values is constrained to equal the theoretical variance of 1.0 by the  
11 sgsim software that is used to create the spatially correlated residual fields.

12 The variogram parameters for the normal-score transformed residuals are used directly in the  
13 sgsim program to create 500 conditional realizations of the residual field. Each of these 500  
14 residual fields is used as an initial residual field and each one is assigned to an individual base T  
15 field. An example of a realization of the residual field and its combination with a base T field is  
16 shown in Figure TFIELD-14. From Figure TFIELD-14, the effect of the residual field on the  
17 base T field can be seen. The residual field perturbs the Ts to match the measured Ts at the well  
18 locations. The discrete features that are part of the original base T field (e.g., high-T zones in the  
19 middle of the domain) are retained when the residual field is added to the base field, although T  
20 values within those features may be altered to a degree.

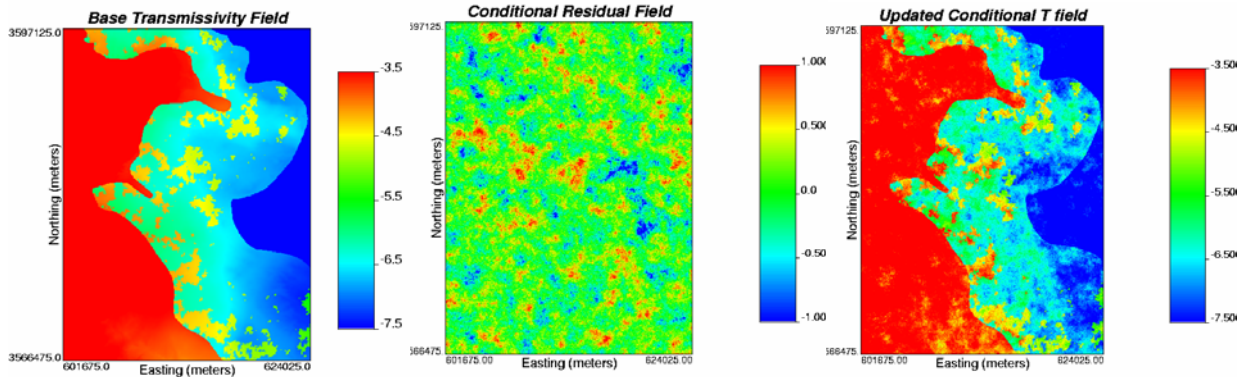
21 A number of distributed locations within the modeling domain are selected and designated as  
22 “pilot points.” PEST adjusts the T value at each of these pilot points to achieve a better match  
23 between the groundwater flow model results and the observed steady-state and transient head  
24 data. The adjustments in T at each pilot point cannot be made independently of surrounding T  
25 values and, therefore, these surrounding T values must be updated in a manner consistent with  
26 the change made at the pilot point. This updating is done by applying a change at each of the  
27 surrounding points that is a weighted fraction of the change made at the pilot point. The weights  
28 are calculated from the residual variogram.

29 These updates are necessary to create a final T field that honors all observed T measurements  
30 and matches the observed heads when used as input to a groundwater flow model. Therefore, it  
31 is also necessary to calculate and model a variogram on the raw, not normal-score transformed,



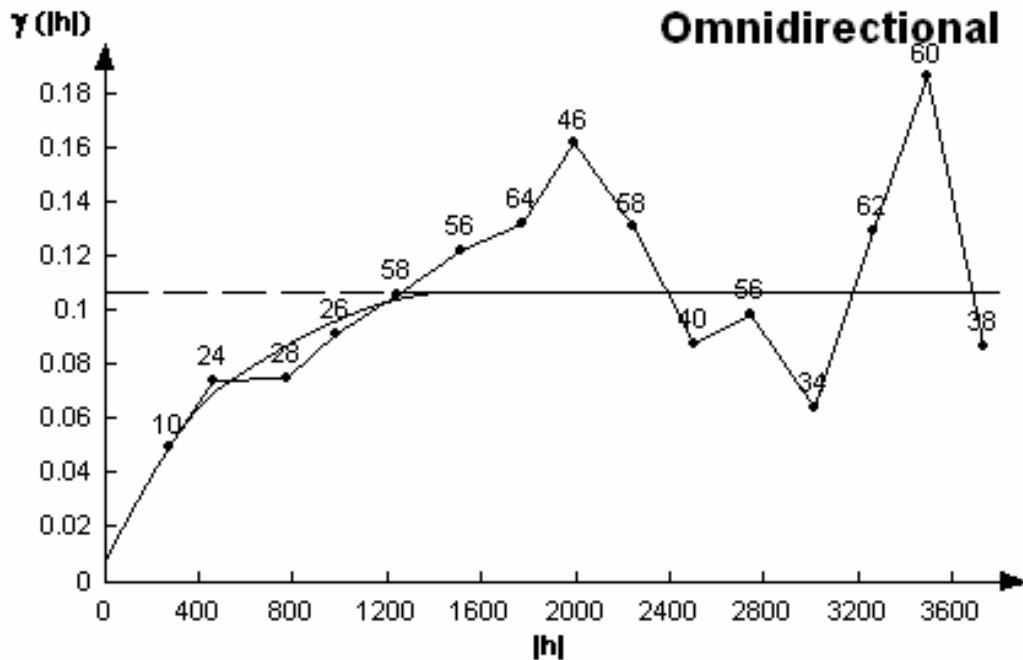


1  
2 **Figure TFIELD-13. Omnidirectional Variogram Model Fit to the Experimental**  
3 **Variogram of the Transmissivity Residuals**



4  
5 **Figure TFIELD-14. An Example of the Creation of a Seed T Field. The base T field (left**  
6 **image) is combined with the initial residual field created through geostatistical simulation**  
7 **(center image) to produce the seed T field (right image). That field is then used as the**  
8 **initial field for the first iteration of the inverse calibration procedure. All three color scales**  
9 **denote the  $\log_{10} T$  ( $m^2/s$ ) value.**

10 residuals for use in this kriging process. This variogram was also calculated with a 250-m (820-  
11 ft) lag and is omnidirectional. A doubly nested spherical variogram model was fit to the  
12 experimental variogram. The variogram parameters are a nugget of 0.008, a first sill and range  
13 of 0.033 and 500 m (1,640 ft), respectively, and a second sill and range of 0.067 and 1,500 m  
14 (4,921 ft), respectively (Figure TFIELD-15).



1

2

3

**Figure TFIELD-15. Experimental and Model Variograms for the Raw-Space (Not Normal-Score Transformed) Transmissivity Residual Data**

4

5

***TFIELD-6.0* T-FIELD CALIBRATION TO STEADY-STATE AND TRANSIENT HEADS**

6

7

8

This section presents details on the modeling approach used to calibrate the T fields to both the 2000 steady-state heads and 1,332 transient drawdown measurements. This section is divided into the following subsections:

9

10

1. Assumptions made in the modeling and the implications of these assumptions are provided.

11

12

13

2. The initial heads used for each calibration are estimated at each location in the domain using the heads measured in 2000 using kriging and accounting for the regional trend in the head values.

14

15

3. The initial heads are used to assign fixed-head boundaries to three sides of the model. The fourth side, the western edge, is set as a no-flow boundary for the model.

16

17

18

4. The transient head observations for each hydraulic test and each observation well are selected from the database. These heads are shown as a function of time for each hydraulic test.

19

5. The spatial and temporal discretization of the model domain are presented.

- 1       6. The transient head observations are given relative weights based on the inverse of the  
2       maximum observed drawdown in each hydraulic test. The relative weights assigned to  
3       the steady-state observations are also discussed.
- 4       7. The locations of the adjustable pilot points are determined using a combination of  
5       approaches.

6 All of these steps can be considered as preprocessing aspects of the stochastic inverse calibration  
7 procedure. The actual calibrations are done using an iterative coupling of the MODFLOW-2000  
8 and PEST codes. The details of this process are covered in McKenna and Hart (2003a, 2003b),  
9 and are briefly summarized in this section.

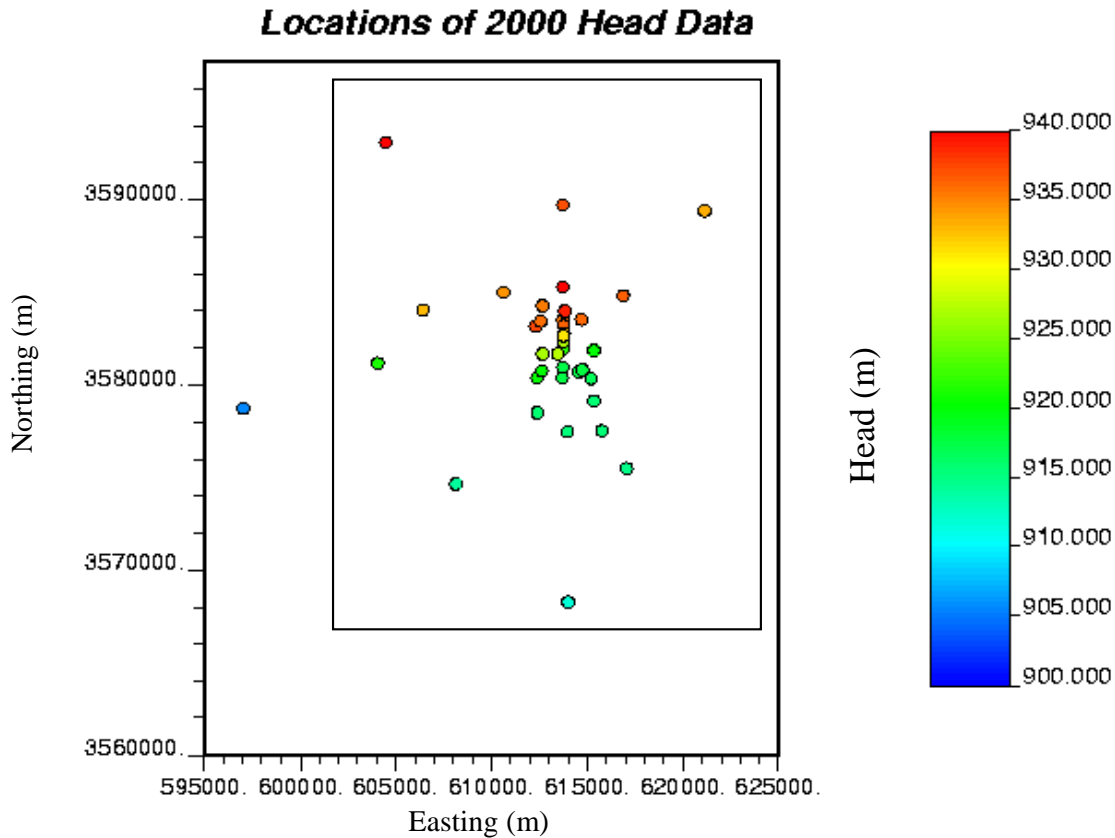
## 10 ***TFIELD-6.1* Modeling Assumptions**

11 The major assumptions that apply to this set of model calculations are:

- 12       1. The boundary conditions along the model domain boundary are known and do not change  
13       over the time frame of the model. This assumption applies to both the no-flow boundary  
14       along the western edge of the domain as well as to the fixed-head boundaries that were  
15       created to be consistent with the 2000 head measurements in the model domain. Implicit  
16       in this assumption is that the fixed-head boundary conditions do not have a significant  
17       impact on the transient tests that were simulated in the interior of the model at times other  
18       than the 2000 period.
- 19       2. The fracture permeability of the Culebra can be adequately modeled as a continuum at  
20       the 100-m (328-ft) × 100-m (328-ft) grid block scale and the measured T values used to  
21       condition the model are representative of the T in the 100-m (328-ft) × 100-m (328-ft)  
22       grid block in which the well test was performed. Implicit in this assumption is the prior  
23       assumption that the hydraulic test interpretations were done correctly and used the correct  
24       conceptual model.
- 25       3. Variable fluid densities in the Culebra can be adequately represented by casting the  
26       numerical solution in terms of freshwater head. Davies (1989) investigated the effects of  
27       variable fluid density on the directions of flow calculated in the Culebra using a  
28       freshwater-head approach. As the Culebra flow system was conceptualized and modeled  
29       by Davies, most of the water flowing in the Culebra in the vicinity of the WIPP site  
30       ultimately discharged to the Pecos River southwest of WIPP. When variable fluid  
31       density was taken into account, the only locations within the model domain where the  
32       flow direction changed by more than 10 degrees were regions 1.1 to 14.3 km (0.7 to 8.9  
33       mi) south of the WIPP site, where the flow direction shifted as much as 70 degrees to the  
34       east toward a more downdip direction (but still primarily to the south) (Davies, 1989,  
35       Figures 35 and 36). As currently conceptualized, flow in the Culebra in the vicinity of  
36       WIPP does not discharge to the Pecos to the southwest, but instead goes to the  
37       southsoutheast toward the Paduca oilfield where extensive dissolution of the Salado and  
38       collapse of the Culebra has occurred (see Figure TFIELD-1). Hence, taking variable  
39       fluid density into account would have little effect on the flow direction.

1 **TFIELD-6.2 Initial Heads**

2 A set of initial head values was estimated across the flow model domain based on water-level  
 3 measurements made in late 2000 (Beauheim 2002b). The water-level measurements were  
 4 converted to freshwater heads using fluid-density data collected from pressure-density surveys  
 5 performed in the wells and/or from water-quality sampling. The head values estimated at the  
 6 cells in the interior of the domain were used as initial values of the heads and were subsequently  
 7 updated by the groundwater flow model until the final solution was achieved. The head values  
 8 estimated for the fixed-head cells along the north, east, and south boundaries of the model  
 9 domain remained constant for the groundwater flow calculation. The estimation of the initial  
 10 and boundary heads was done by kriging. Observed heads both within and outside of the flow  
 11 model domain (Figure TFIELD-16) were used in the kriging process.



12  
 13 **Figure TFIELD-16. Locations and Values of the 2000 Head Measurements Considered in**  
 14 **the Steady-State Calibrations. The approximate extent of the numerical model domain is**  
 15 **shown by the black rectangle in the image.**

16 Kriging is a geostatistical estimation technique that uses a variogram model to estimate values of  
 17 a sampled property at unsampled locations. Kriging is designed for the estimation of stationary  
 18 fields (see Goovaerts 1997); however, the available head data show a significant trend (non-  
 19 stationary behavior) from high head in the northern part of the domain to low head in the  
 20 southern part of the domain. This behavior is typical of groundwater head values measured  
 21 across a large area with a head gradient. To use kriging with this type of non-stationary data, a

1 Gaussian polynomial function is fit to the data, and the differences between the polynomial and  
 2 the measured data (the “residuals”) are calculated and a variogram of the residuals is constructed.  
 3 This variogram and a kriging algorithm are then used to estimate the value of the residual at all  
 4 locations within a domain. The final step in the process is to add the trend from the previously  
 5 defined polynomial to the estimated residuals to get the final head estimates. This head  
 6 estimation process is similar to that used in the Culebra calculations done for the CCA (Lavenue  
 7 1996).

8 The available head data from late 2000, comprising 37 measurements, are listed in Table  
 9 TFIELD-5. In general, these head measurements show a trend from high head in the north to  
 10 low head in the south. The trend was modeled with a bivariate Gaussian function. The use of  
 11 this Gaussian function with five estimated parameters allows considerable flexibility in the shape  
 12 of the trend that can be fit through the observed data. The value of the Gaussian function,  $Z$ , is:

$$13 \quad Z = a \exp \left[ -\frac{1}{2} \left( \left( \frac{X - X_0}{b} \right)^2 + \left( \frac{Y - Y_0}{c} \right)^2 \right) \right] \quad (7)$$

14 where  $X_0$  and  $Y_0$  are the coordinates of the center of the function and  $b$  and  $c$  are the standard  
 15 deviations of the function in the  $X$  (east-west) and  $Y$  (north-south) directions, respectively. The  
 16 parameter  $a$  controls the height of the function. The Gaussian function was fit to the data using  
 17 the regression wizard tool in the SigmaPlot 2001 graphing software. The parameters estimated  
 18 for the Gaussian function are presented in Table TFIELD-6. The fit of the Gaussian trend  
 19 surface to the 2000 heads is shown in Figure TFIELD-17. The locations and values of the  
 20 residuals (observed value – trend surface estimate) are shown in Figure TFIELD-18.

21 The next step in estimating the initial head values is to calculate an experimental variogram for  
 22 each set of residuals and then fit a variogram model to each experimental variogram. Due to the  
 23 rather limited number of data points, anisotropy in the spatial correlation of the residuals was not  
 24 examined and an omnidirectional variogram was calculated. These calculations were done using  
 25 the VarioWin<sup>®</sup> (version 2.21) software (Pannatier 1996). The Gaussian variogram model is:

$$26 \quad \gamma(h) = C \left[ 1 - \exp \left( -\frac{3h^2}{a^2} \right) \right] \text{ for } h > 0 \quad (8)$$

27 where  $C$  is the sill of the variogram,  $h$  is the distance between any two samples, or the lag  
 28 spacing, and  $a$  is the practical range of the variogram, or the distance at which the model reaches  
 29 95 percent of the value of  $C$ . In addition to the sill and range, the variogram model may also  
 30 have a non-zero intercept with the gamma ( $\gamma$ ) axis of the variogram plot known as the nugget.  
 31 Due to numerical instabilities in the kriging process associated with the Gaussian model without  
 32 a nugget value, a small nugget was used in fitting each of the variogram models. The model  
 33 variogram was fit to the experimental data (Figure TFIELD-19) and the parameters of this model  
 34 are given in Table TFIELD-7.

1 **Table TFIELD-5. Well Names and Locations of the 37 Head Measurements Obtained in**  
 2 **Late 2000 Used to Define Boundary and Initial Heads**

Well	UTM X (Easting) (m)	UTM Y (Northing) (m)	2000 Freshwater Head (m amsl)
AEC-7	621126	3589381	933.19
DOE-1	615203	3580333	916.55
DOE-2	613683	3585294	940.03
ERDA-9	613696	3581958	921.59
H-1	613423	3581684	927.19
H-2b2	612661	3581649	926.62
H-3b2	613701	3580906	917.16
H-4b	612380	3578483	915.55
H-5b	616872	3584801	936.26
H-6b	610594	3585008	934.20
H-7b1	608124	3574648	913.86
H-9b	613989	3568261	911.57
H-11b4	615301	3579131	915.47
H-12	617023	3575452	914.66
H-14	612341	3580354	920.24
H-15	615315	3581859	919.87
H-17	615718	3577513	915.37
H-18	612264	3583166	937.22
H-19b0	614514	3580716	917.13
P-17	613926	3577466	915.20
WIPP-12	613710	3583524	935.30
WIPP-13	612644	3584247	935.17
WIPP-18	613735	3583179	936.08
WIPP-19	613739	3582782	932.66
WIPP-21	613743	3582319	927.00
WIPP-22	613739	3582653	930.96
WIPP-25	606385	3584028	932.70
WIPP-26	604014	3581162	921.06
WIPP-27	604426	3593079	941.01
WIPP-29	596981	3578701	905.36
WIPP-30	613721	3589701	936.88
WQSP-1	612561	3583427	935.64
WQSP-2	613776	3583973	938.82
WQSP-3	614686	3583518	935.89
WQSP-4	614728	3580766	917.49
WQSP-5	613668	3580353	917.22
WQSP-6	612605	3580736	920.02

3

1 **Table TFIELD-6. Parameters for the Gaussian Trend Surface Model Fit to the 2000 Heads**

Trend Surface Parameters	Value
$X_0$	611011.89
$Y_0$	3780891.50
$a$	1134.61
$b$	73559.35
$c$	313474.40

2

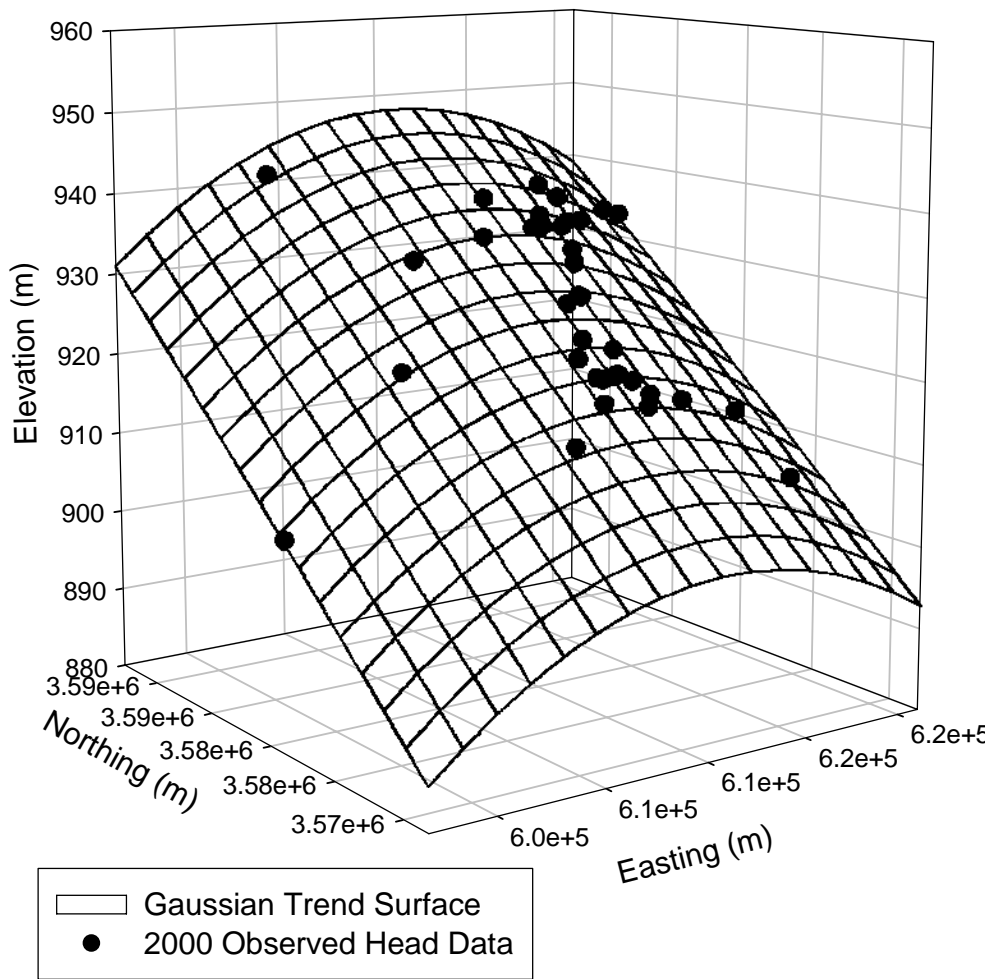
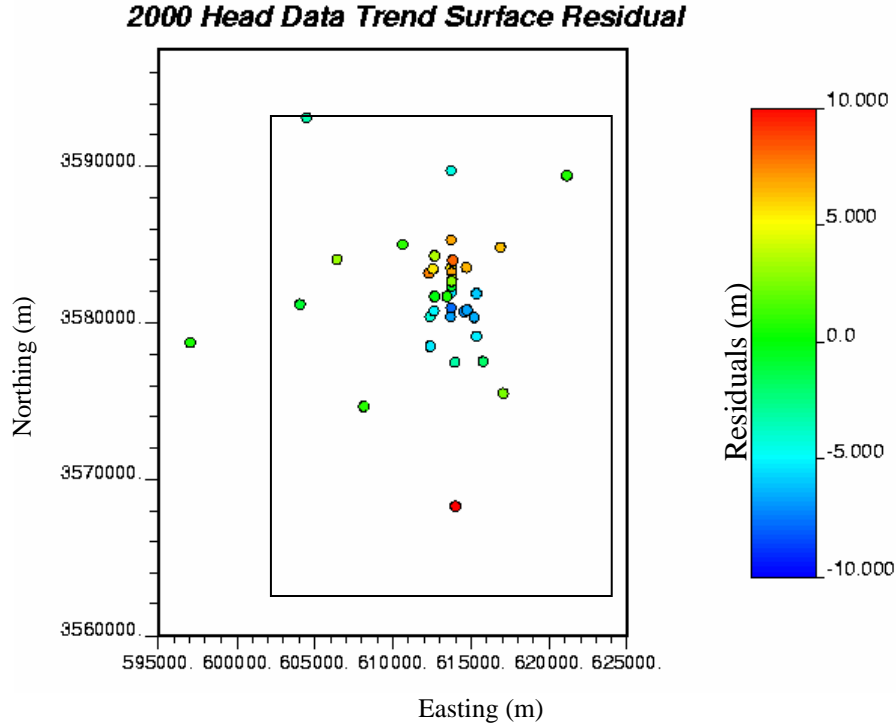
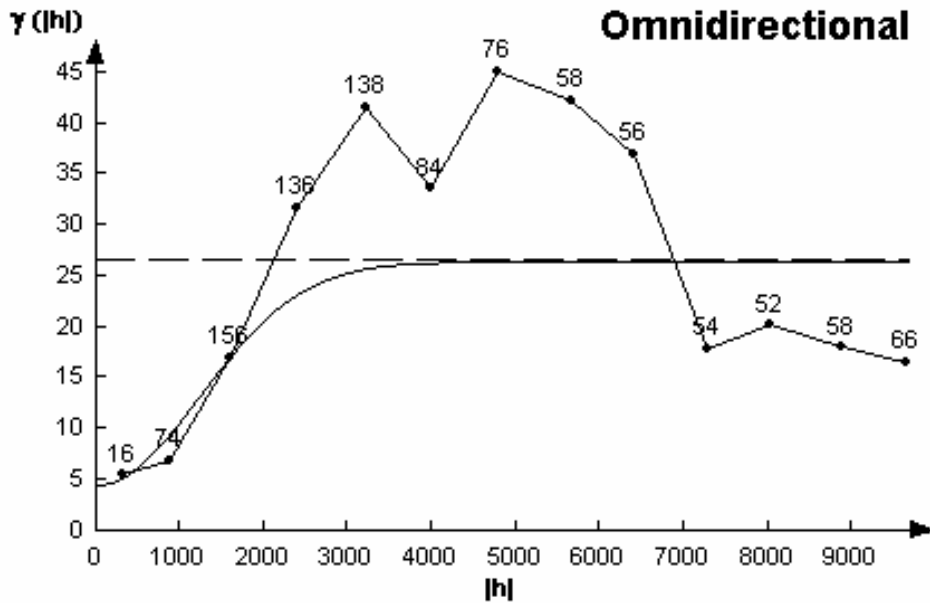


**Figure TFIELD-17. Gaussian Trend Surface Fit to the 2000 Observed Heads**



1  
2  
3  
4  
5

**Figure TFIELD-18. Locations and Values of the Residuals Between the Gaussian Trend Surface Model and the Observed Head Data. The approximate boundary of the flow model is shown as a black rectangle in the image.**



6  
7  
8  
9  
10

**Figure TFIELD-19. Omnidirectional Experimental (Straight-Line Segments) and Model Variograms of the Head Residuals (Curves) for the 2000 Heads. The numbers indicate the number of pairs of values that were used to calculate each point and the horizontal dashed line denotes the variance of the residual data set.**



**Table TFIELD-7. Model Variogram Parameters for the Head Residuals**

Parameter	Value
Sill	22
Range (meters)	3000
Nugget	4.5
Number of Data	37

The experimental variogram calculated on the 2000 data in Figure TFIELD-19 shows a number of points between lags 2,000 and 7,000 m (1.25 and 4.25 mi) that are above the variance of the data set (the horizontal dashed line). This behavior indicates that the Gaussian trend surface model used to calculate the residuals from the measured data did not remove the entire trend inherent in the observed data. A higher order trend surface model could be applied to these data to remove more of the trend, but the Gaussian trend surface model provides a reasonable estimate of the trend in the data.

The GSLIB kriging program kt3d (Deutsch and Journel 1998) was used to estimate the residual values at all points on the grid within the model domain. The Gaussian trend surface was then added to the estimated residual values to produce the final estimates of the initial head field.

### ***TFIELD-6.3* Boundary Conditions**

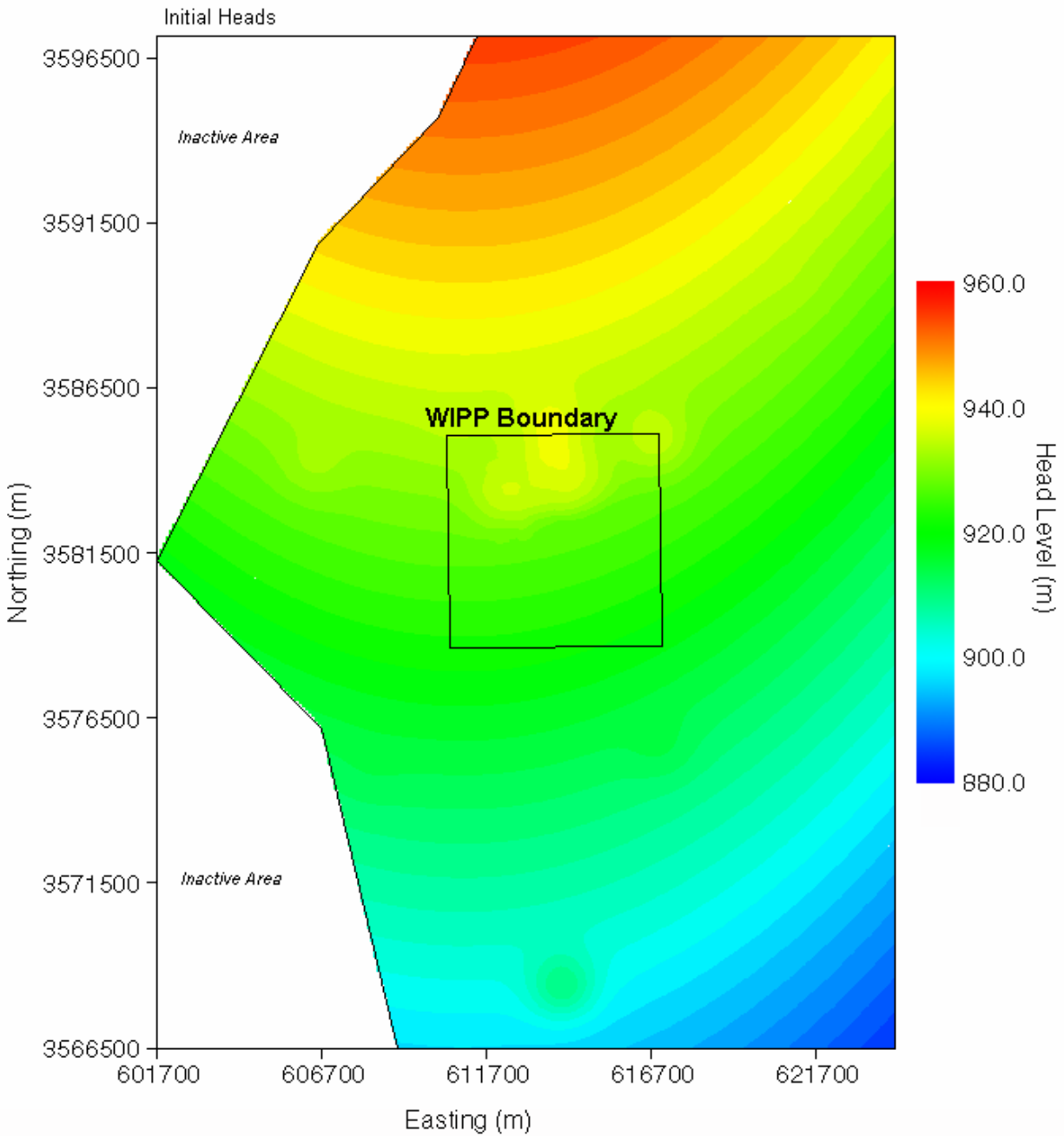
Two types of boundary conditions were specified in MODFLOW-2000: constant-head and no-flow. Constant-head conditions were assigned along the eastern boundary of the model domain, and along the central and eastern portions of the northern and southern boundaries. Values of these heads were obtained from the kriged initial head field. The western model boundary passes through the IMC tailings pond (Laguna Uno) due west of the WIPP site in Nash Draw. A no-flow boundary (a flow line) is specified in the model from this tailings pond up the axis of Nash Draw to the northeast, reflecting the concept that groundwater flows down the axis of Nash Draw, forming a groundwater divide. Similarly, another no-flow boundary is specified from the tailings pond down the axis of the southeastern arm of Nash Draw to the southern model boundary, coinciding with a flow line in the regional modeling of Corbet and Knupp (1996). Thus, the northwestern and southwestern corners of the modeling domain are specified as inactive cells in MODFLOW-2000. The initial (starting) head field is shown in Figure TFIELD-20 and the head values along each boundary of the model domain are shown in Figures TFIELD-21 and TFIELD-22.

### ***TFIELD-6.4* Observed Steady-State and Transient Head Data Used in Model Calibration**

In addition to being used to generate an initial head distribution, the water-level measurements made in 35 wells within the model domain during late 2000 were also used in steady-state model calibration. (Note that Table TFIELD-5 includes data from two wells – WIPP-27 and WIPP-29 – that were used to define model boundary conditions but are outside the area of calibration).

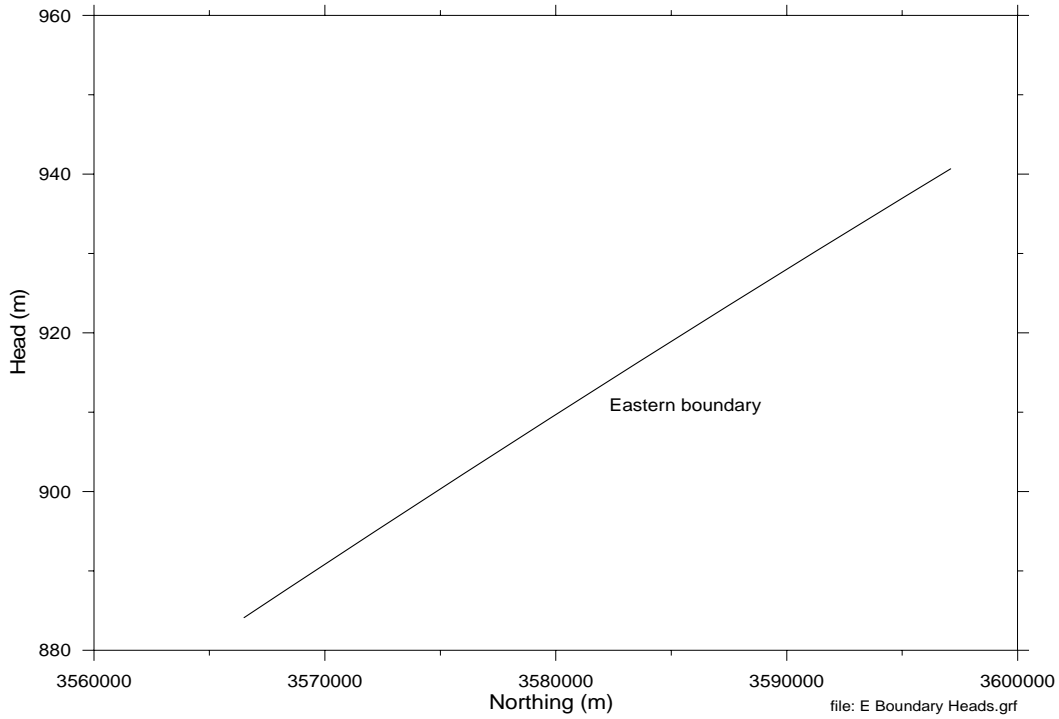
The transient observation data used for the transient calibrations were taken from a number of different sources listed in Beauheim (2003a). Responses to seven different hydraulic tests were employed in the transient portion of the calibration (Table TFIELD-8). Hydraulic responses for each of the seven tests were monitored in three to ten different observation wells depending on the hydraulic test.

1



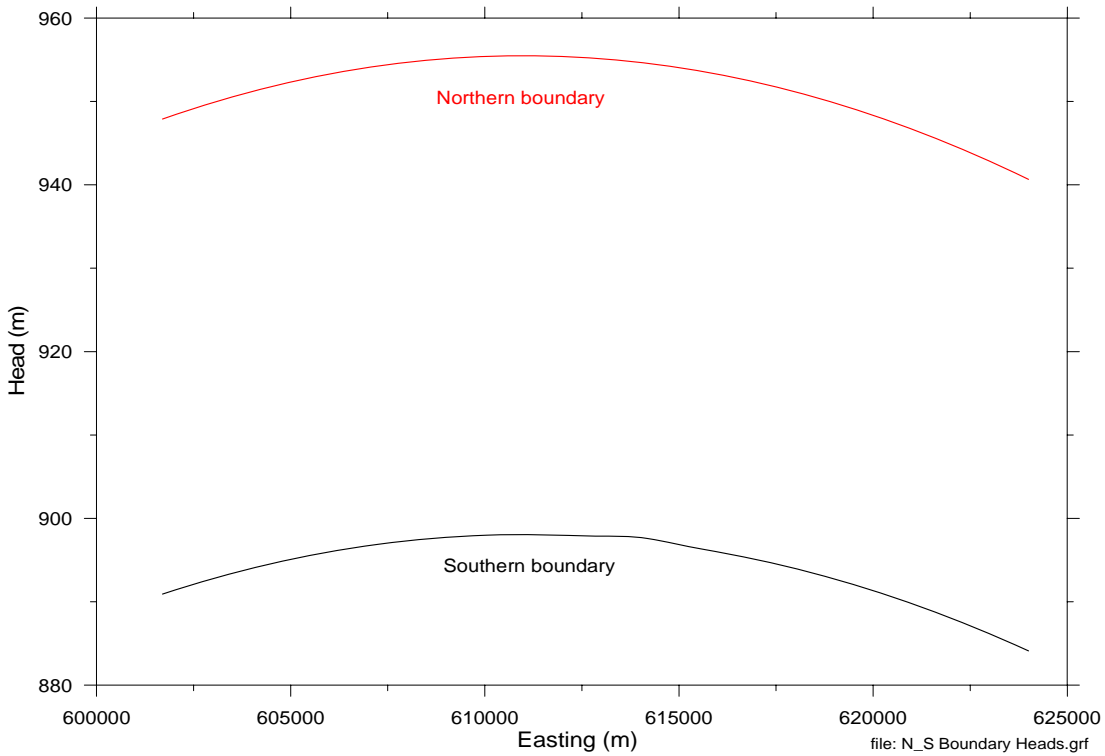
2

3 **Figure TFIELD-20. Map of Initial Heads Created Through Kriging and Used to Assign**  
4 **Fixed-Head Boundary Conditions**



1  
2  
3

**Figure TFIELD-21. Values of Fixed Heads Along the Eastern Boundary of the Model Domain**



4  
5  
6

**Figure TFIELD-22. Values of Fixed Heads Along the Northern and Southern Boundaries of the Model Domain. Note that not all locations along the boundaries are active cells.**

1  
2**Table TFIELD-8. Transient Hydraulic Test and Observation Wells  
for the Drawdown Data**

Stress Point	Observation Well	Observation Start	Observation End	Observation Type
H-3b2	DOE-1	10/15/1985	3/18/1986	Drawdown
	H-1	10/15/1985	4/14/1986	Drawdown
	H-2b2	10/15/1985	4/2/1986	Drawdown
	H-11b1	10/15/1985	4/21/1986	Drawdown
WIPP-13	DOE-2	1/12/1987	5/15/1987	Drawdown
	H-2b2	1/12/1987	5/15/1987	Drawdown
	H-6b	1/12/1987	5/15/1987	Drawdown
	P-14	1/12/1987	5/15/1987	Drawdown
	WIPP-12	1/12/1987	5/15/1987	Drawdown
	WIPP-18	1/12/1987	5/15/1987	Drawdown
	WIPP-19	1/12/1987	5/15/1987	Drawdown
	WIPP-25	1/12/1987	4/2/1987	Drawdown
	WIPP-30	1/12/1987	5/15/1987	Drawdown
P-14	D-268	2/14/1989	3/7/1989	Drawdown
	H-6b	2/14/1989	3/10/1989	Drawdown
	H-18	2/14/1989	3/10/1989	Drawdown
	WIPP-25	2/14/1989	3/7/1989	Drawdown
	WIPP-26	2/14/1989	3/7/1989	Drawdown
H-11b1	H-4b	2/7/1996	12/11/1996	Drawdown
	H-12	2/6/1996	12/10/1996	Drawdown
	H-17	2/6/1996	12/10/1996	Drawdown
	P-17	2/7/1996	12/10/1996	Drawdown
H-19b0	DOE-1	12/15/1995	12/10/1996	Drawdown
	ERDA-9	12/15/1995	12/10/1996	Drawdown
	H-1	12/15/1995	12/10/1996	Drawdown
	H-14	2/7/1995	12/10/1996	Drawdown
	H-15	12/12/1995	12/10/1996	Drawdown
	H-2b2	2/7/1996	12/10/1996	Drawdown
	H-3b2	12/15/1995	12/10/1996	Drawdown
	WIPP-21	1/18/1996	12/9/1996	Drawdown
	WQSP-4	1/1/1996	12/10/1996	Drawdown
WQSP-5	1/18/1995	12/10/1996	Drawdown	
WQSP-1	H-18	1/25/1996	2/20/1996	Drawdown
	WIPP-13	1/25/1996	2/20/1996	Drawdown
	WQSP-3	1/15/1996	2/20/1996	Zero Response
WQSP-2	DOE-2	2/20/1996	3/28/1996	Drawdown
	H-18	2/20/1996	3/28/1996	Drawdown
	WIPP-13	2/20/1996	3/28/1996	Drawdown
	WQSP-1	2/20/1996	3/24/1996	Drawdown
	WQSP-3	2/20/1996	3/24/1996	Zero Response

3

4 A major change in the calibration data set from the CCA calculations is the exclusion of the  
5 hydraulic responses to the excavation of the exploratory (now salt) and ventilation (now waste)  
6 shafts in the current calibration. The responses to the shaft excavations were excluded because:

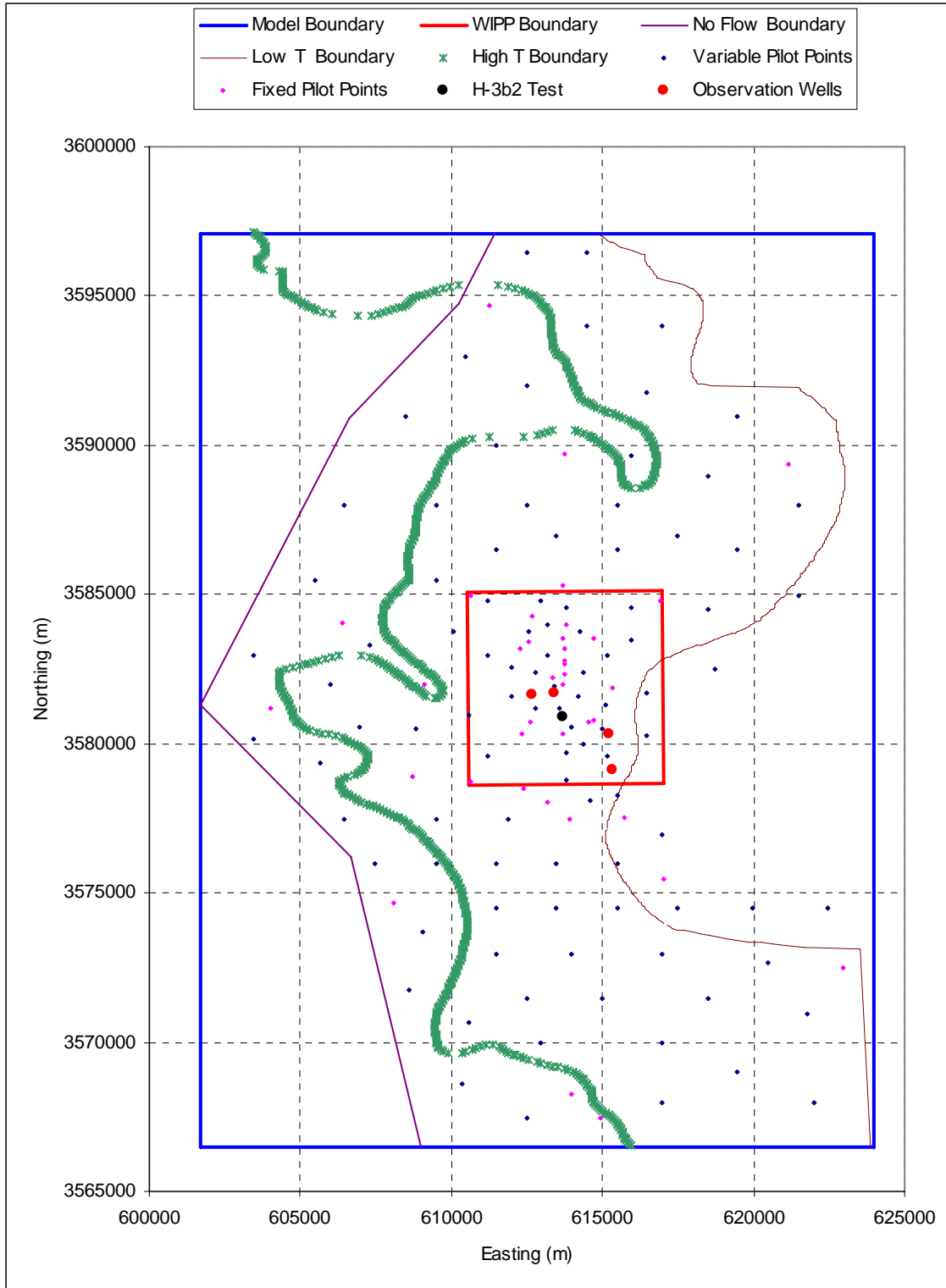
- 1       1. Only two wells (H-1 and H-3) responded directly to the shaft excavations and the areas  
2       between the shafts and these wells are stressed by other hydraulic tests that are included  
3       in the calibration data set (H-3b2, WIPP-13, and H-19b0).
  
- 4       2. It was difficult to model both the flux and pressure changes accurately during the  
5       excavation of the shafts with MODFLOW-2000. This difficulty is due to both the finite-  
6       difference discretization of MODFLOW-2000 that requires each shaft to be modeled as a  
7       complete model cell and some limitations of the data set.
  
- 8       3. The long-term effects of the shafts on site-wide water levels were important for the CCA  
9       modeling because that modeling sought to replicate heads over time. In the current CRA-  
10       2004 calibration effort, shaft effects are not important because drawdowns resulting from  
11       specific hydraulic tests are used as the calibration targets and shaft effects can be  
12       considered as second-order compared to the effects of the hydraulic tests that are  
13       simulated.

14       A small amount of processing of the observed data was necessary prior to using it in the  
15       calibration process. This processing included selecting the data values that would be used in the  
16       calibration procedure from the often voluminous measurements of head. These data were chosen  
17       to provide an adequate description of the transient observations at each observation well across  
18       the response time without making the modeling too computationally burdensome in terms of the  
19       temporal discretization necessary to model responses to these observations. Scientific judgment  
20       was used in selecting these data points. This selection process resulted in a total of 1,332  
21       observations for use in the transient calibration.

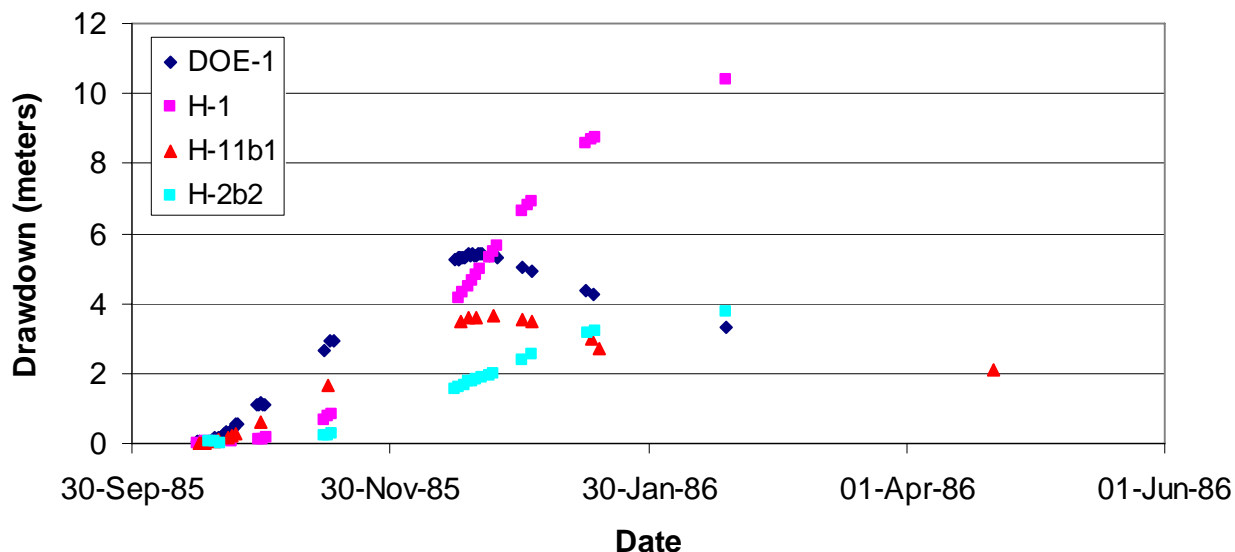
22       Additionally, the modeling of the pressure data is done here in terms of drawdown. Therefore,  
23       the value of drawdown at the start of any transient test must be zero. A separate perl script was  
24       written to normalize each set of observed heads to a zero value reference at the start of the test  
25       with the exception of the H-3 test that is only preceded by the steady-state simulation. The  
26       calculations are such that the resulting drawdown values are positive.

27       In addition to normalizing the measured head data, some of the tests produced negative  
28       drawdown values when normalized. These negative results are due to some of the observations  
29       having heads greater than the reference value. This occurs due to some hydraulic tests that were  
30       conducted at earlier times in the Culebra but were not included in the numerical model. If the  
31       drawdowns from one of these previous tests are still recovering to zero at the start of a  
32       simulation, they can cause negative drawdowns in the simulation as the recovery continues.  
33       Most of these effects were addressed through trend removal in initial data processing (Beauheim  
34       2003a) but some residual effects remain.

35       The resultant transient calibration points are shown in Figures TFIELD-23 through TFIELD-36.  
36       These sets of figures show the location of each hydraulic test and the locations of the observation  
37       wells for that test within the model domain and the time series of drawdown values for each



1  
2 **Figure TFIELD-23. Locations of the H-3b2 Hydraulic Test Well and Observation Wells**



1

2

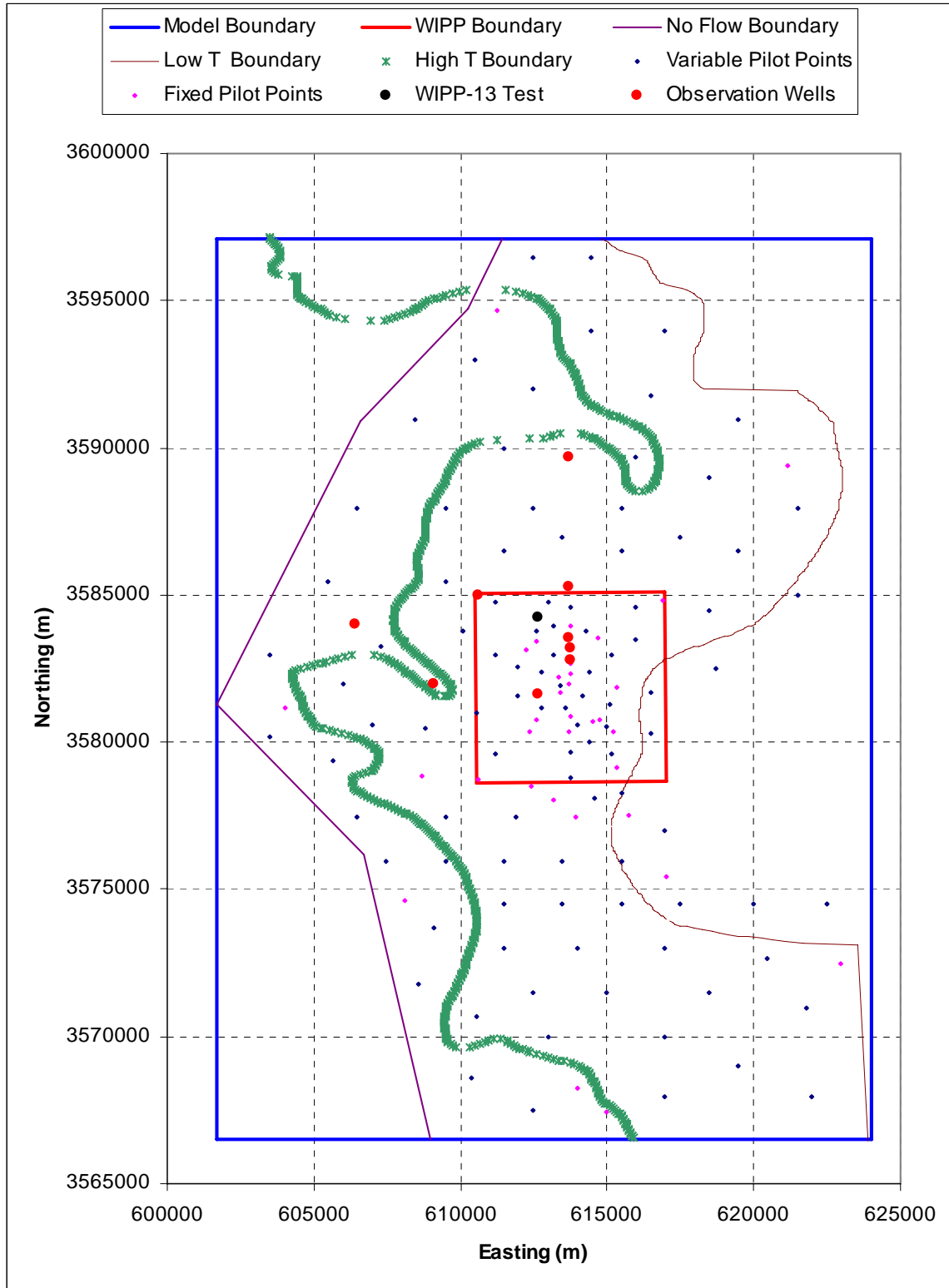
**Figure TFIELD-24. Observed Drawdowns for the H-3b2 Hydraulic Test**

3 observation well. The values of drawdown are in meters where a positive drawdown indicates a  
 4 decrease in the pressure within the well relative to the pressure before the start of the pumping  
 5 (negative drawdown values indicate rises in the water level). For the WQSP-1 and WQSP-2  
 6 tests, well WQSP-3 showed no response. These results are used in the calibration process by  
 7 setting the observed drawdown values to zero for WQSP-3. The maps in Figures TFIELD-23  
 8 through TFIELD-35 also show the locations of the pilot points used in the calibration (these are  
 9 discussed later).

### 10 ***TFIELD-6.5* Spatial Discretization**

11 The flow model was discretized into 68,768 regular, orthogonal cells each of which is 100 m  
 12 (328 ft) × 100 m (328 ft). A constant Culebra thickness of 7.75 m (25.4 ft) was used ( CCA  
 13 Appendix TFIELD.4.1.1, Culebra:Thick). The 100-m (328-ft) grid discretization was selected to  
 14 make the finite-difference grid cell sizes considerably finer, on average, than those used in the  
 15 CCA calculations, but still computationally tractable. In the CCA calculations, a telescoping  
 16 finite-difference grid was used with the smallest cell being 100 m (328 ft) × 100 m (328 ft) near  
 17 the center of the domain. The largest cells in the CCA flow model grid were 800 m (2,625 ft) ×  
 18 800 m (2,625 ft) near the edges of the domain (Lavenue, 1996).

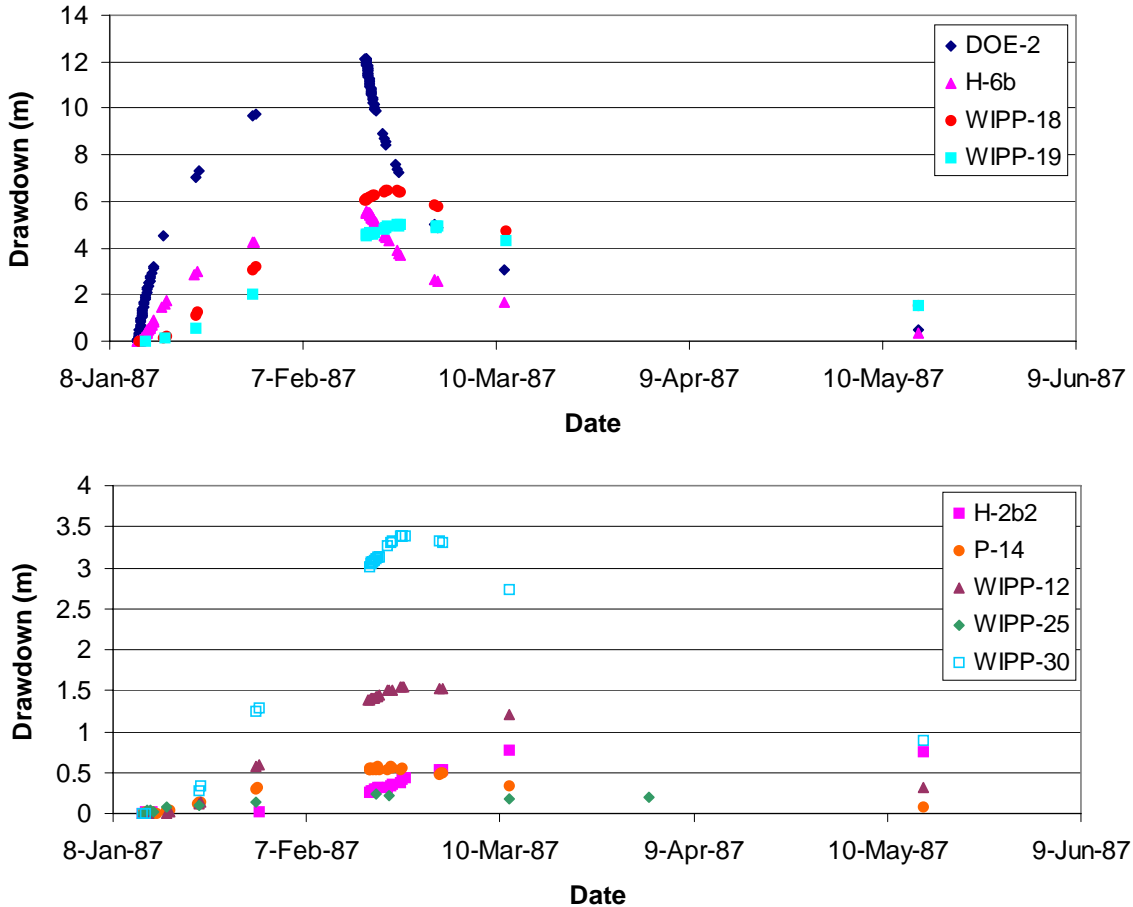
19 The cells in the model domain were assigned elevations based on the digitized version of Figure  
 20 TFIELD-1. Of the 68,768 cells (224 east-west by 307 north-south), 14,999 (21.8 percent) lie to  
 21 the west of the no-flow boundary, so the total number of active cells in the model is 53,769. This  
 22 number is nearly a factor of five larger than the 10,800 (108 × 100) cells used in the CCA  
 23 calculations.



1

2 **Figure TFIELD-25. Locations of the WIPP-13 Hydraulic Test Well and Observation Wells**



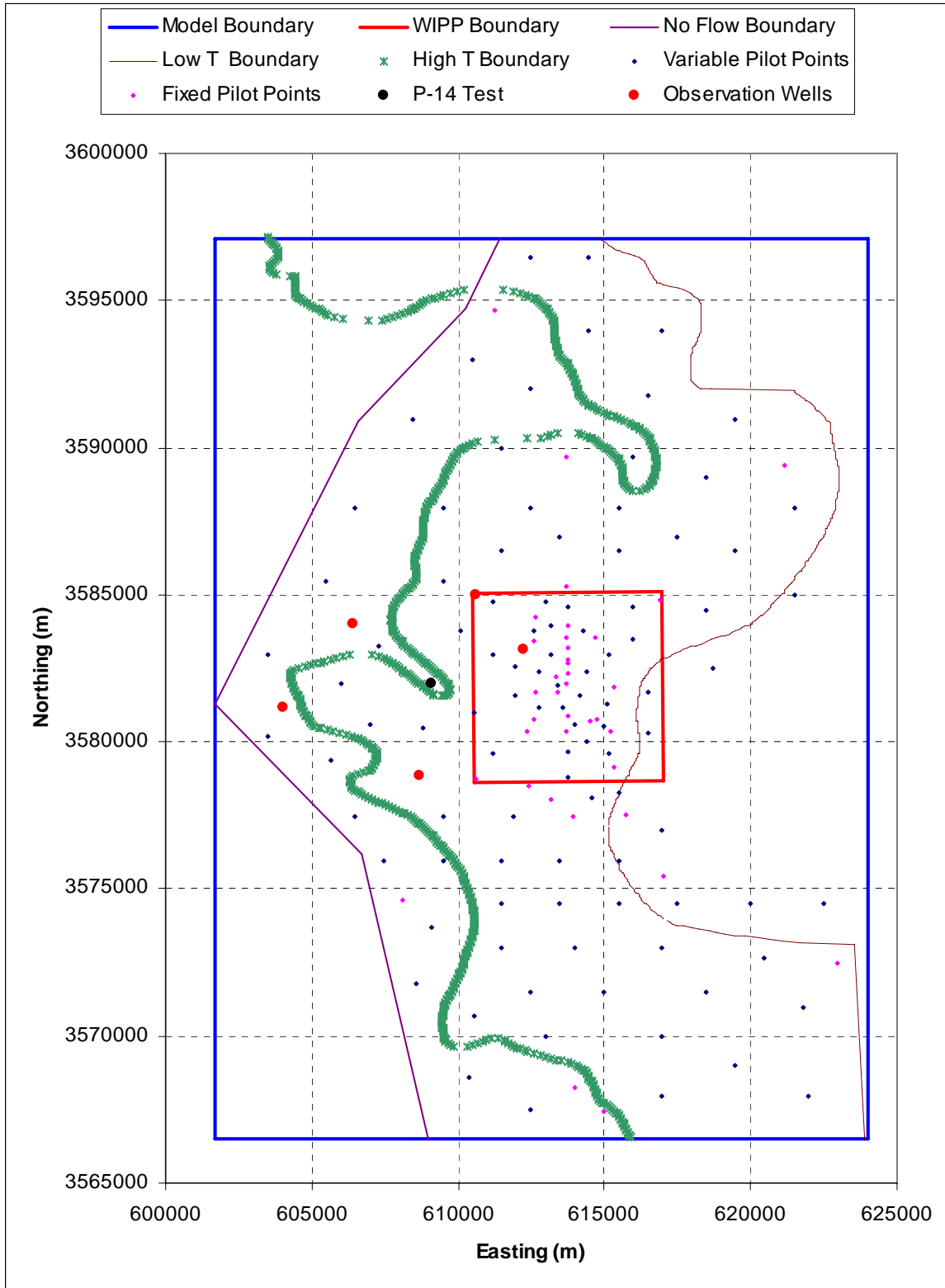


1  
 2 **Figure TFIELD-26. Observed Drawdowns for the WIPP-13 Hydraulic Test. Note the**  
 3 **change in the scale of the Y-axis from the upper to the lower image.**

4 ***TFIELD-6.6 Temporal Discretization***

5 The time period of nearly 11 years and 2 months covered by the transient modeling began  
 6 October 15, 1985 and ended December 11, 1996. Additionally, a single steady-state calculation  
 7 was run prior to the transient modeling. The length of this steady-state time period and the date  
 8 at which it occurs were arbitrarily set to one day (86,400 s) occurring from October 14, 1985, to  
 9 October 15, 1985. These steady-state heads were measured in the year 2000 and were only set to  
 10 these October dates to provide a steady-state solution prior to the start of any transient hydraulic  
 11 events. The responses to the transient events were defined by the amount of drawdown relative  
 12 to the initial steady-state solution. The discretization of this time interval was dictated by the  
 13 pumping history of the different wells used in the hydraulic testing and consideration of the  
 14 additional computational burden required for increasingly fine time discretization.

15 The groundwater flow model, MODFLOW-2000, allows for the discretization of time into both  
 16 “stress periods” and “time steps.” A stress period is a length of time over which the boundary  
 17 conditions and internal stresses on the system are constant. Even though these stresses are  
 18 constant, this does not mean that the flow system is necessarily at steady state during the stress



1  
2 **Figure TFIELD-27. Locations of the P-14 Hydraulic Test Well and Observation Wells**

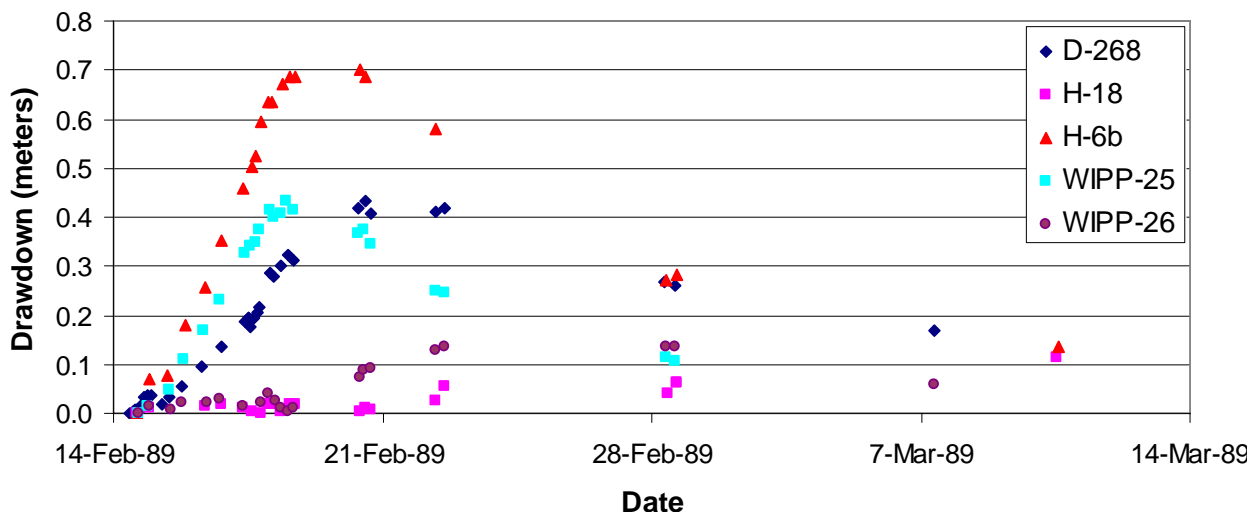
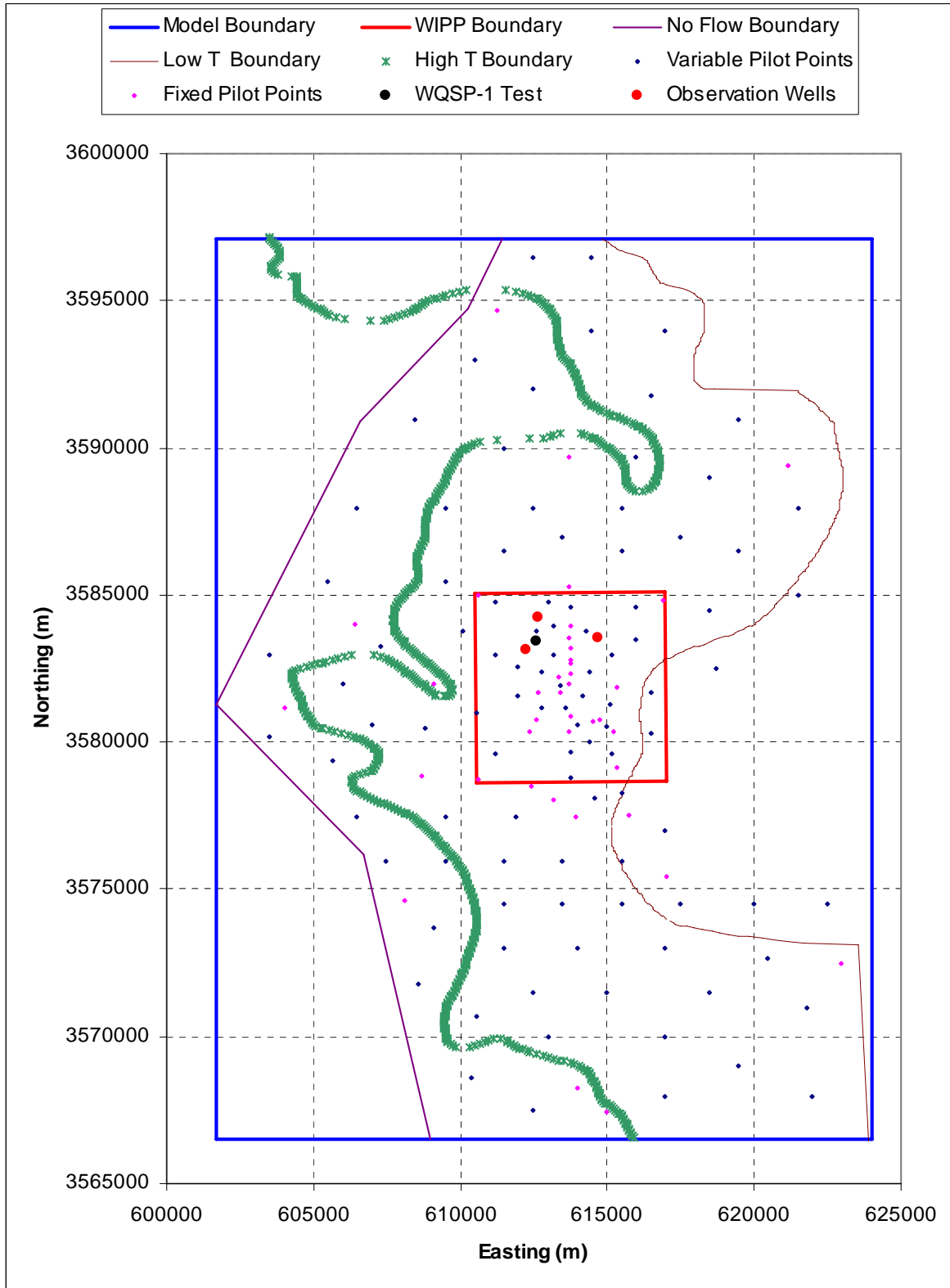


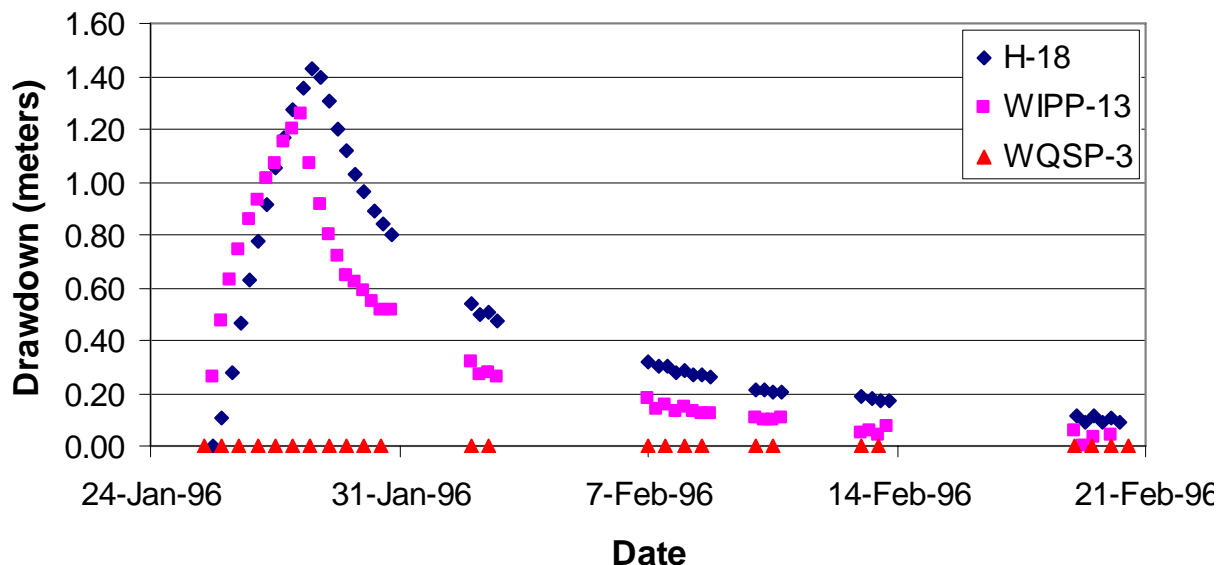
**Figure TFIELD-28. Observed Drawdowns for the P-14 Hydraulic Test**

1  
2  
3 period. A time step is a subdivision of a stress period. System information such as the head or  
4 drawdown values is only calculated at the specified time steps. Each stress period must contain  
5 at least one time step. MODFLOW-2000 allows for the specification of the stress period length,  
6 the number of time steps in the stress period, and a time step multiplier. The time step multiplier  
7 increases the time between successive time steps geometrically. This geometric progression  
8 provides a nearly ideal time discretization for the start of a pumping or recovery period. To save  
9 on computational costs associated with calculating head/drawdown at each time step and with  
10 writing out the heads/drawdowns, the number of time steps in the model was kept to the  
11 minimum number possible that still adequately simulated the hydraulic tests. The time  
12 discretization in MODFLOW-2000 resulted in modeled heads calculated at times that sometimes  
13 differed from the observation times. For this situation, the PEST utility, mod2obs, was used to  
14 interpolate the head, or drawdown, values in time from the simulation times to the observation  
15 times.

16 A summary of the time discretization is given in Table TFIELD-9. There are five separate  
17 MODFLOW-2000 simulations for each complete forward simulation of the transient events.  
18 Each separate call to MODFLOW-2000 has its own set of input and output files. In Table  
19 TFIELD-9, each call to MODFLOW-2000 is separated by a horizontal black line. The first call  
20 is the steady-state simulation. The second, third, and fourth calls to MODFLOW-2000 (H-3,  
21 WIPP-13, and P-14) are all similar in that a single well was pumped. For the H-3 and WIPP-13  
22 calls, there were a total of three stress periods. In the first stress period, the well was pumping at  
23 a constant rate; in the second stress period, the pumped well was inactive and heads were  
24 recovering after the cessation of pumping; and the final stress period was simply a long time of  
25 no pumping activity used to advance the simulation time to be consistent with the calendar time.  
26 The first two stress periods were discretized using eight time steps and the final stress period  
27 with no pumping activity was discretized using the minimum possible number of time steps—  
28 one.



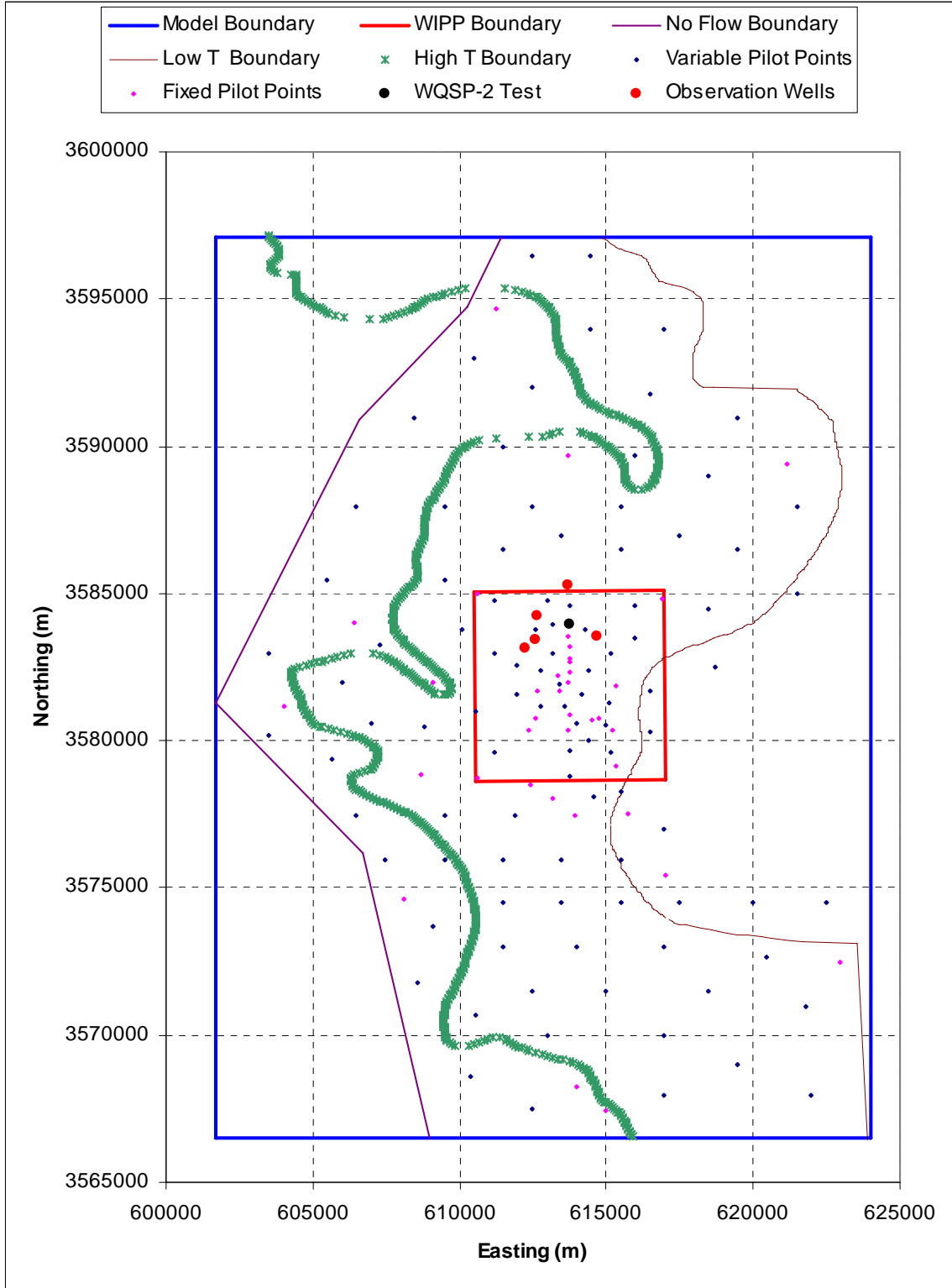
1  
2 **Figure TFIELD-29. Locations of the WQSP-1 Hydraulic Test Well and Observation Wells**



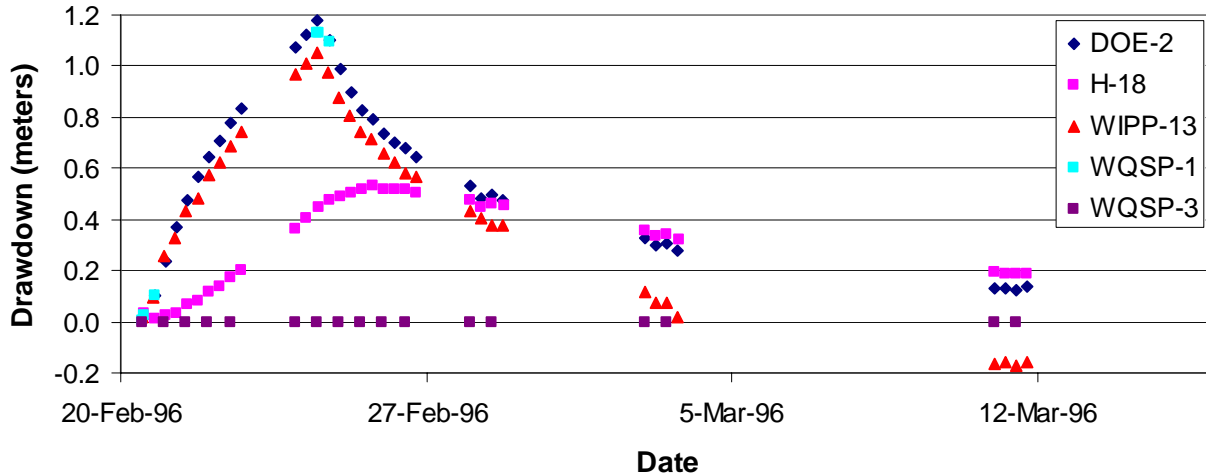
1  
2 **Figure TFIELD-30. Observed Drawdowns for the WQSP-1 Hydraulic Test**

3 The final MODFLOW-2000 call, the H-19 call, was considerably more complicated than the  
4 earlier calls to MODFLOW-2000 and simulated the hydraulic conditions during the H-11, H-19,  
5 WQSP-1, and WQSP-2 hydraulic tests. This final call contained 17 stress periods with as many  
6 as three different wells pumping during any single stress period. The pumping rates of the  
7 different wells in this call to MODFLOW-2000 and the stress periods are shown as a function of  
8 time in Figure TFIELD-37. The first six stress periods in this call simulated pumping in the  
9 H-19 and H-11 wells without any observations (Table TFIELD-9). These pumping periods were  
10 added to the model solely to account for the effects of these tests in observations of later  
11 hydraulic tests and, therefore, these tests could be modeled with a single time step. The pumping  
12 rates shown in Figure TFIELD-37 are given as negative values to indicate the removal of water  
13 from the Culebra following the convention used in MODFLOW-2000.

14 The MODFLOW-2000 simulations could be done using a single call to MODFLOW-2000, but  
15 five separate calls were used here. Each of the five calls created separate binary output files of  
16 drawdown and head that were much smaller and easier to manage than a single output file would  
17 have been. Additionally, the simulated drawdowns at the start of each transient test must be zero  
18 (no drawdown prior to pumping). Because MODFLOW-2000 uses the resulting drawdowns and  
19 heads from the previous stress period as input to the next stress period, a single simulation would  
20 not necessarily start each transient test with zero drawdowns. Calling MODFLOW-2000 five  
21 times allowed the initial drawdowns to be reset to zero each time using shell scripts. The heads  
22 simulated at the end of the final time step in each MODFLOW-2000 call were used as the initial  
23 heads for the next call. The results of all five calls were combined to produce the 1332 model  
24 predictions prior to comparing them to the 1332 selected observation data, thus ensuring that all  
25 steady-state and transient data were used simultaneously in the inverse calibration procedure.



1  
2 **Figure TFIELD-31. Locations of the WQSP-2 Hydraulic Test Well and Observation Wells**

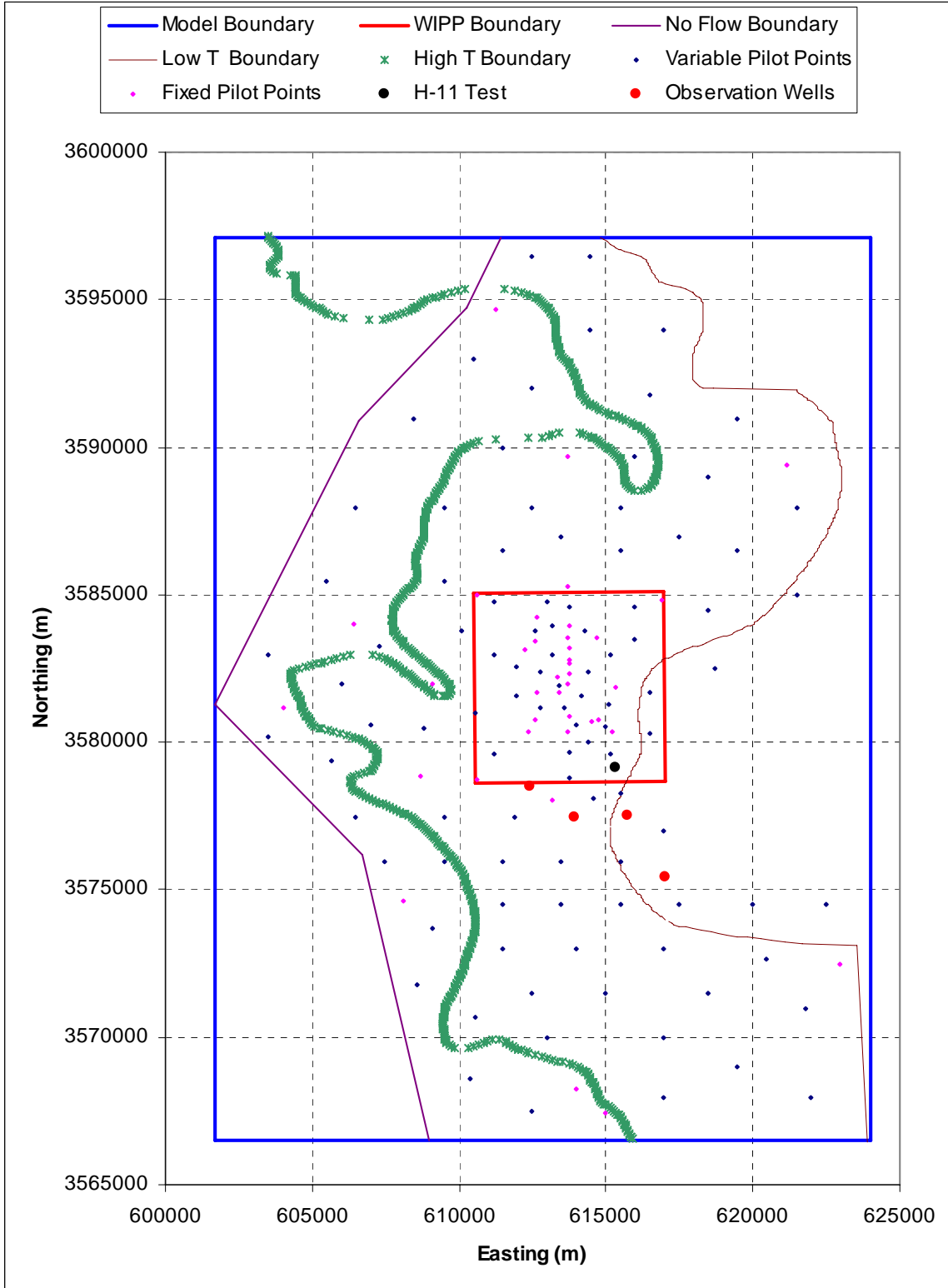


1  
2 **Figure TFIELD-32. Observed Drawdowns from the WQSP-2 Hydraulic Test**

3 ***TFIELD-6.7 Weighting of Observation Data***

4 The observed data for each response to each transient hydraulic test are weighted to take into  
 5 account the differences in the responses across the different tests. The weights are calculated as  
 6 the inverse of the maximum observed drawdown for each hydraulic test. This weighting scheme  
 7 applies relatively less weight to tests with large drawdowns and relatively more weight to tests  
 8 with smaller responses. This weighting scheme was used so that the overall calibration was not  
 9 dominated by trying to reduce the very large residuals that may occur at a few of the observation  
 10 locations with very large drawdowns. Under this weighting scheme, two tests that are both fit by  
 11 the model to within 50 percent of the observed drawdown values would be given equal  
 12 consideration in the calculation of the overall objective function even though one test may have  
 13 an observed maximum drawdown of 10 m (33 ft) and the other a maximum observed drawdown  
 14 of 0.10 m (0.33 ft).

15 The weights assigned in this manner ranged from 0.052 to 20.19. The observed absence of a  
 16 hydraulic response at WQSP-3 to pumping at WQSP-1 and WQSP-2 was also included in the  
 17 calibration process by inserting measurements of zero drawdown that were given an arbitrarily  
 18 high weight of 20. Through trial and error using the root mean squared error criterion of how  
 19 well the modeled steady-state heads fit the observed steady-state heads, a weight of 2.273 was  
 20 assigned to the 35 steady-state observations. This weight is near that of the average of all the  
 21 weights assigned to the transient events and was found to be adequate to provide acceptable  
 22 steady-state matches. It is noted that the steady-state data provide measurements of head while  
 23 all of the transient events provide measurements of drawdown. However, the weights were  
 24 applied to the residuals between the observed and modeled aquifer responses and because both  
 25 heads and drawdowns are measured in meters, there was no need to adjust the weights to account  
 26 for different measurement units.

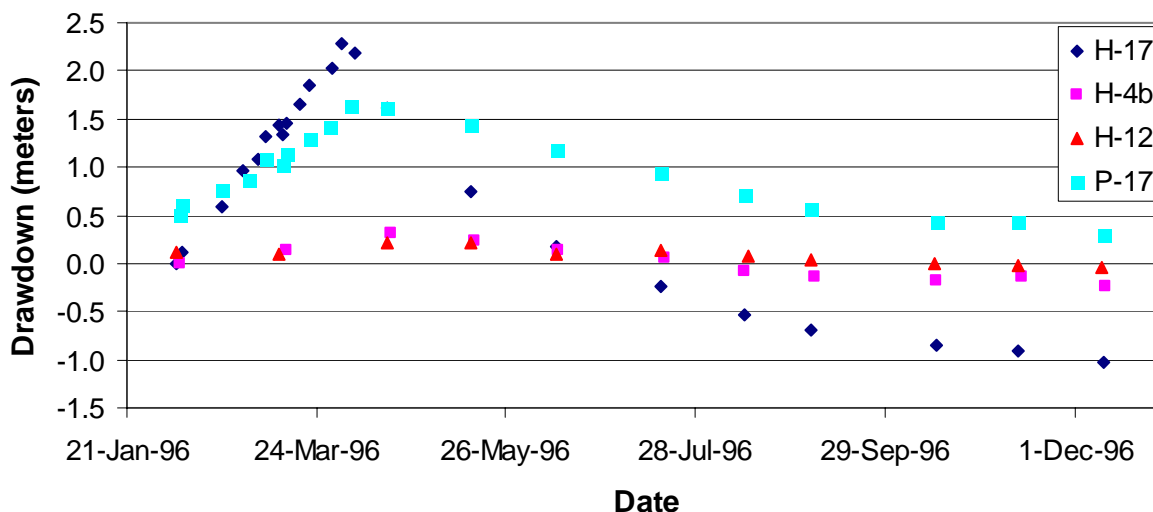


1

2

**Figure TFIELD-33. Locations of the H-11 Hydraulic Test Well and Observation Wells**





1  
2 **Figure TFIELD-34. Observed Drawdowns for the H-11 Hydraulic Test**

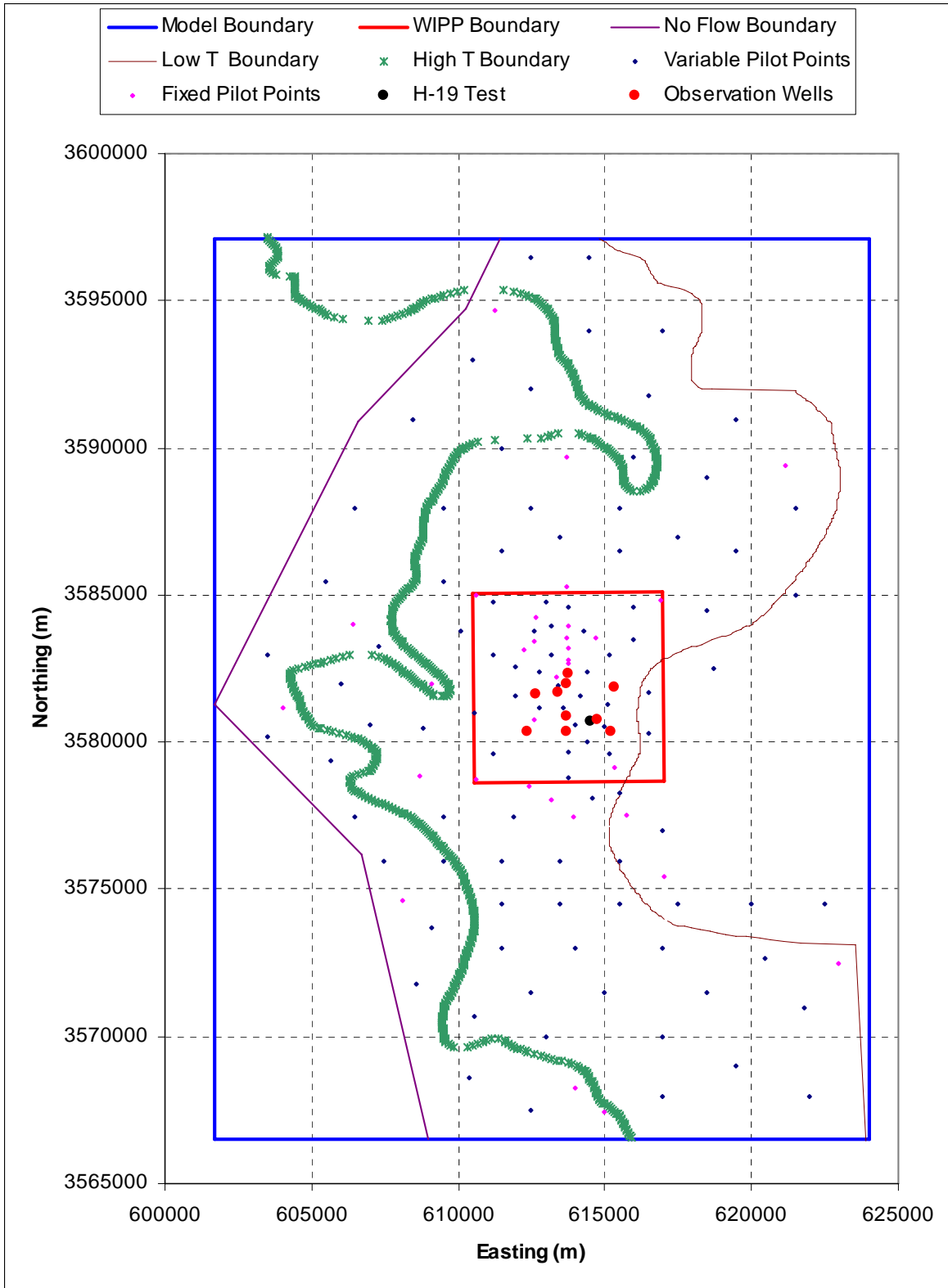
3 The number of measurements used for calibration that were made at individual wells during  
4 individual tests ranged from 6 to 104, and the number of measurements used for calibration that  
5 were made at all wells during a single test ranged from 64 to 410. This means that different well  
6 responses and different tests carried different cumulative weights. The spatially broadest sampling  
7 of transient data possible was used in an effort to get transient coverage of as much of the modeling  
8 domain as possible. In those areas where no transient data are available, the calibration is  
9 dominated by fitting the model to the steady-state measurements. The greatest coverage of  
10 transient data is within the boundaries of the WIPP site, which is also the area of most significance  
11 for radionuclide transport.

12 The maximum observed drawdown, the weight assigned to all the observed test values for each  
13 test, and the total number of observations for each observation well are given in Table  
14 TFIELD-10.

#### 15 ***TFIELD-6.8* Assignment of Pilot Point Geometry**

16 A major development in the field of stochastic inverse modeling that has occurred since the T  
17 fields were constructed for the CCA in 1996 is that inverse techniques are now capable of  
18 simultaneously determining optimal T values at a large number of pilot points. In the T fields  
19 constructed for the CCA, pilot points were added one at a time and each point was calibrated  
20 prior to the addition of the next pilot point. Furthermore, the total number of pilot points was  
21 limited to less than or equal to the total number of T observations to avoid numerical instabilities  
22 in the solution of the inverse problem. With the techniques now available and implemented in  
23 PEST, it is possible to use many more pilot points than there are T observations and to calibrate  
24 these pilot points simultaneously.

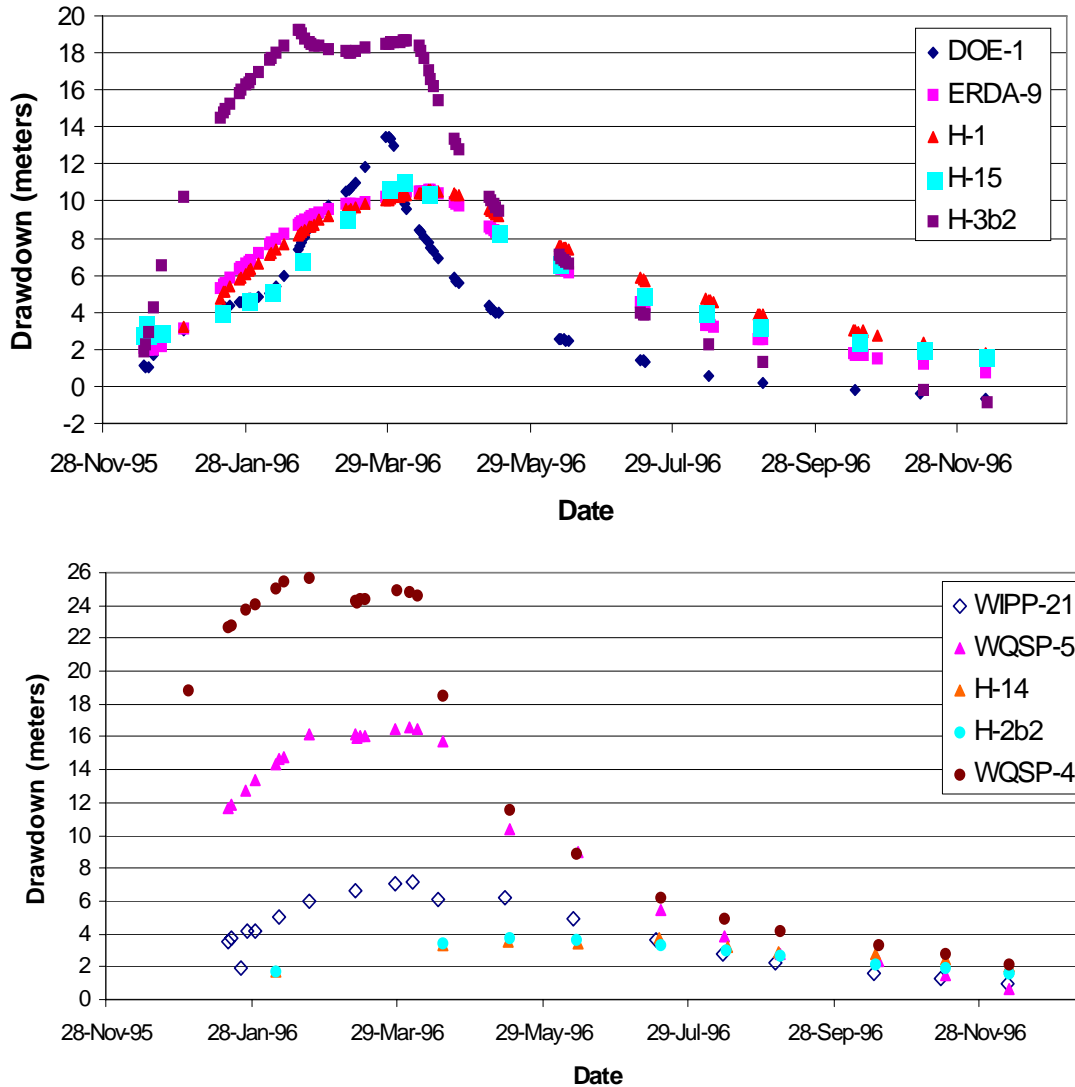
25 The pilot-point locations were chosen using a combination of a regular grid approach and  
26 deviations from that grid to accommodate specific pumping- and observation-well locations



1

2

**Figure TFIELD-35. Locations of the H-19 Hydraulic Test Well and Observation Wells**



1  
2 **Figure TFIELD-36. Observed Drawdowns From the H-19 Hydraulic Test**

3 (Figure TFIELD-38). The goal in these deviations from the regular grid was to put at least one  
 4 pilot point between each pumping well and each of its observation wells. Details of the pilot-  
 5 point locations relative to the pumping and observation wells in the WIPP site area are shown in  
 6 Figure TFIELD-39. This combined approach of a regular grid with specific deviations from that  
 7 grid follows the guidelines for pilot-point placement put forth by John Doherty (the author of  
 8 PEST) as Appendix 1 in the work of McKenna and Hart (2003a). Pilot points located at the T  
 9 measurement locations were held as fixed values during the optimization (fixed pilot points  
 10 shown as magenta squares in Figure TFIELD-38). The variable pilot points (dark blue diamonds  
 11 in Figure TFIELD-38) are those where the T value was adjusted during the calibration  
 12 procedure. A total of 43 fixed and 100 variable pilot points was used in the T-field calibration  
 13 process. The zone option in PEST was employed to limit the influence of pilot points in any one  
 14 zone (e.g., high T or low T) to adjusting only locations that are in the same zone.

**Table TFIELD-9. Discretization of Time into 29 Stress Periods and 127 Time Steps with Pumping Well Names and Pumping Rates**

Event Name	Global Stress Period No.	Internal Stress Period No.	Stress Period Length (s)	No. of Time Steps	Start Date	Stop Date	Pumping Well(s)	Pumping Rate(s) (m <sup>3</sup> /s)
Steady	1	1	86400	1	10/14/859:00	10/15/859:00	0	0
H-3	2	1	5356800	8	10/15/859:00	12/16/859:00	H-3	3.03E-04
	3	2	10892700	8	12/16/859:00	4/21/8610:45	None	0.00E+00
	4	3	22976100	1	4/21/8610:45	1/12/879:00	None	0.00E+00
WIPP-13	5	1	3110400	8	1/12/879:00	2/17/879:00	WIPP-13	1.89E-03
	6	2	7539900	8	2/17/879:00	5/15/8715:25	None	0.00E+00
	7	3	55359360	1	5/15/8715:25	2/14/899:01	None	0.00E+00
P-14	8	1	44928	3	2/14/899:01	2/14/8921:29	P-14	3.92E-03
	9	2	174612	8	2/14/8921:29	2/16/8922:00	P-14	3.64E-03
	10	3	50400	3	2/16/8922:00	2/17/8912:00	P-14	3.37E-03
	11	4	1820396	8	2/17/8912:00	3/10/8913:39	None	0.00E+00
	12	5	193212124	1	3/10/8913:39	4/24/95 19:42	None	0.00E+00
H-19	13	1	148860	1	4/24/9519:42	4/26/95 13:03	H-19b0	2.26E-04
	14	2	4399020	1	4/26/9513:03	6/16/9511:00	None	0.00E+00
	15	3	3614400	1	6/16/9511:00	7/28/95 7:00	H-19b0	2.36E-04
	16	4	1168200	1	7/28/95 7:00	8/10/95 19:30	None	0.00E+00
	17	5	1292700	1	8/10/9519:30	8/25/9518:35	H11	2.44E-04
	18	6	9651300	1	8/25/9518:35	12/15/9511:30	None	0.00E+00
	19	7	2878200	8	12/15/9511:30	1/17/9619:00	H-19b0	2.71 E-04
	20	8	670680	3	1/17/9619:00	1/25/9613:18	H-19b0	2.52E-04
	21	9	238980	3	1/25/9613:18	1/28/96 7:41	H-19b0, WQSP-1	2.52E-04, 4.30E-04
	22	10	872340	3	1/28/96 7:41	2/7/9610:00	H-19b0	2.52E-04
	23	11	1047000	8	2/7/9610:00	2/19/9612:50	H-19b0, H-11	2.52E-04, 2.23E-04
	24	12	81600	3	2/19/9612:50	2/20/9611:30	H-19b0, H-11	1.55E-04, 2.23E-04
	25	13	345600	3	2/20/96 11:30	2/24/9611:30	H-19b0, H-11, WQSP-2	1.55E-04, 2.23E-04, 4.5E-04
	26	14	1395000	8	2/24/96 11:30	3/11/9615:00	H-19b0, H-11	1.55E-04, 2.23E-04
	27	15	1445100	8	3/11/9615:00	3/28/96 8:25	H-19b0, H-11	1.55E-04, 3.76E-04
	28	16	1220700	8	3/28/96 8:25	4/11/9611:30	H-19b0	1.55E-04
	29	17	21074400	8	4/11/9611:30	12/11/969:30	None	0.00E+00

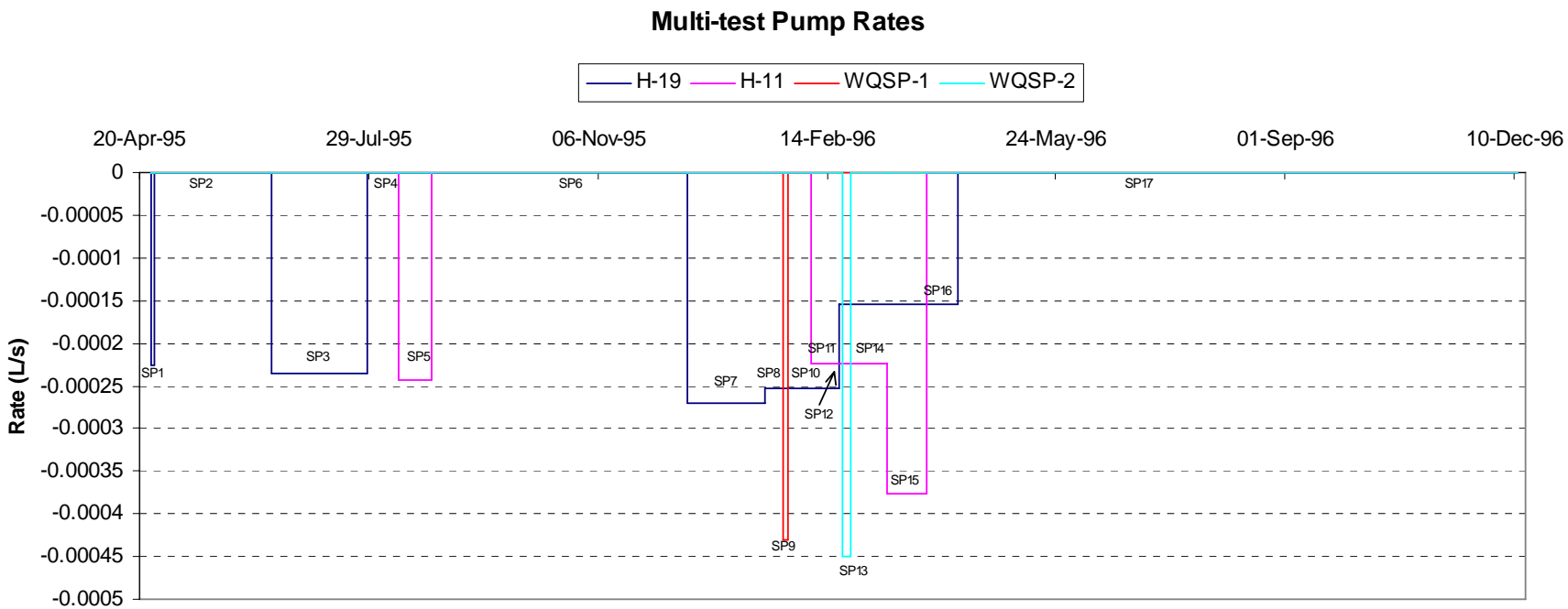
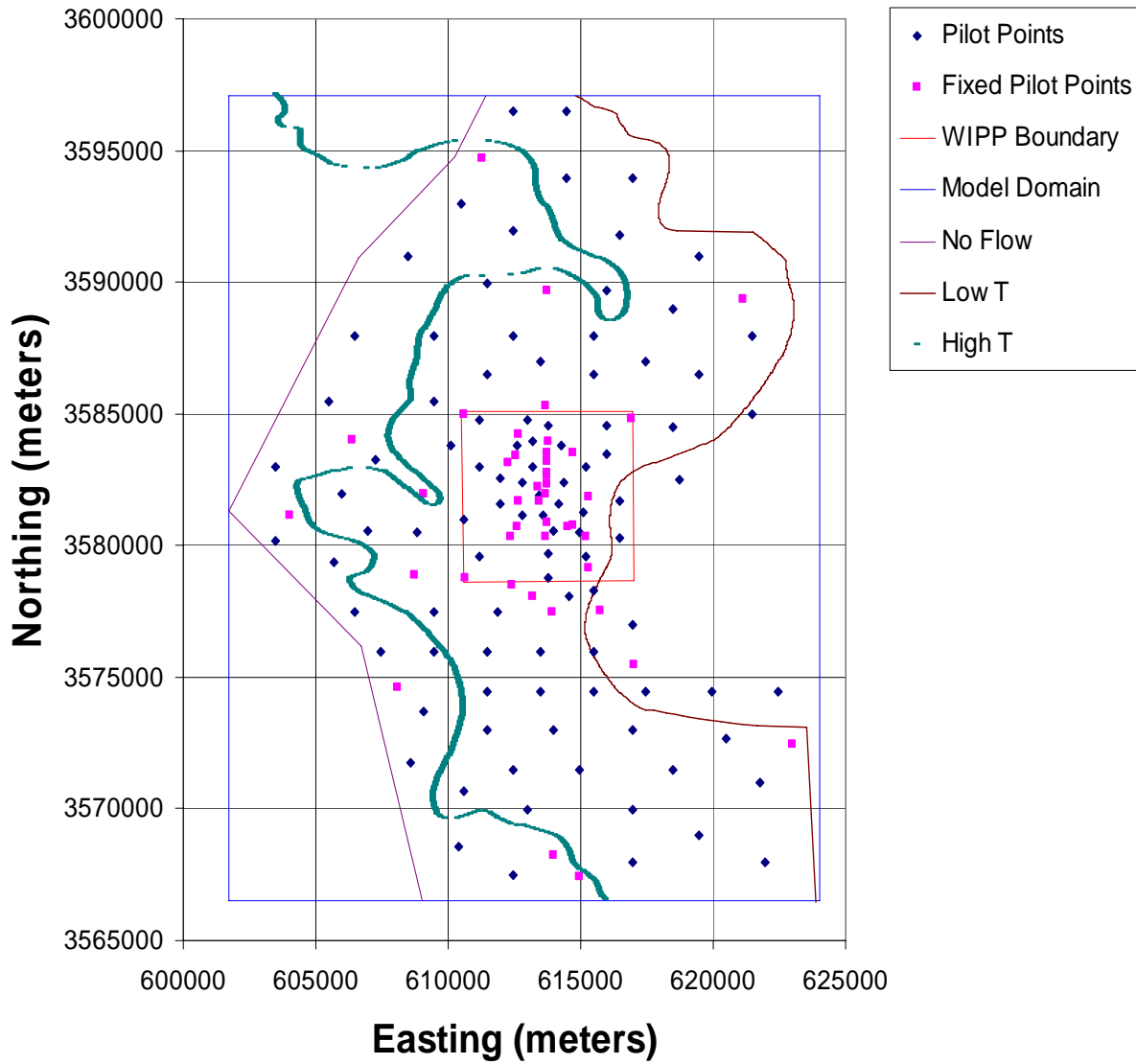


**Figure TFIELD-37. Temporal Discretization and Pumping Rates for the Fifth Call to MODFLOW-2000. A total of 17 stress periods (SPs) are used to discretize this model call.**

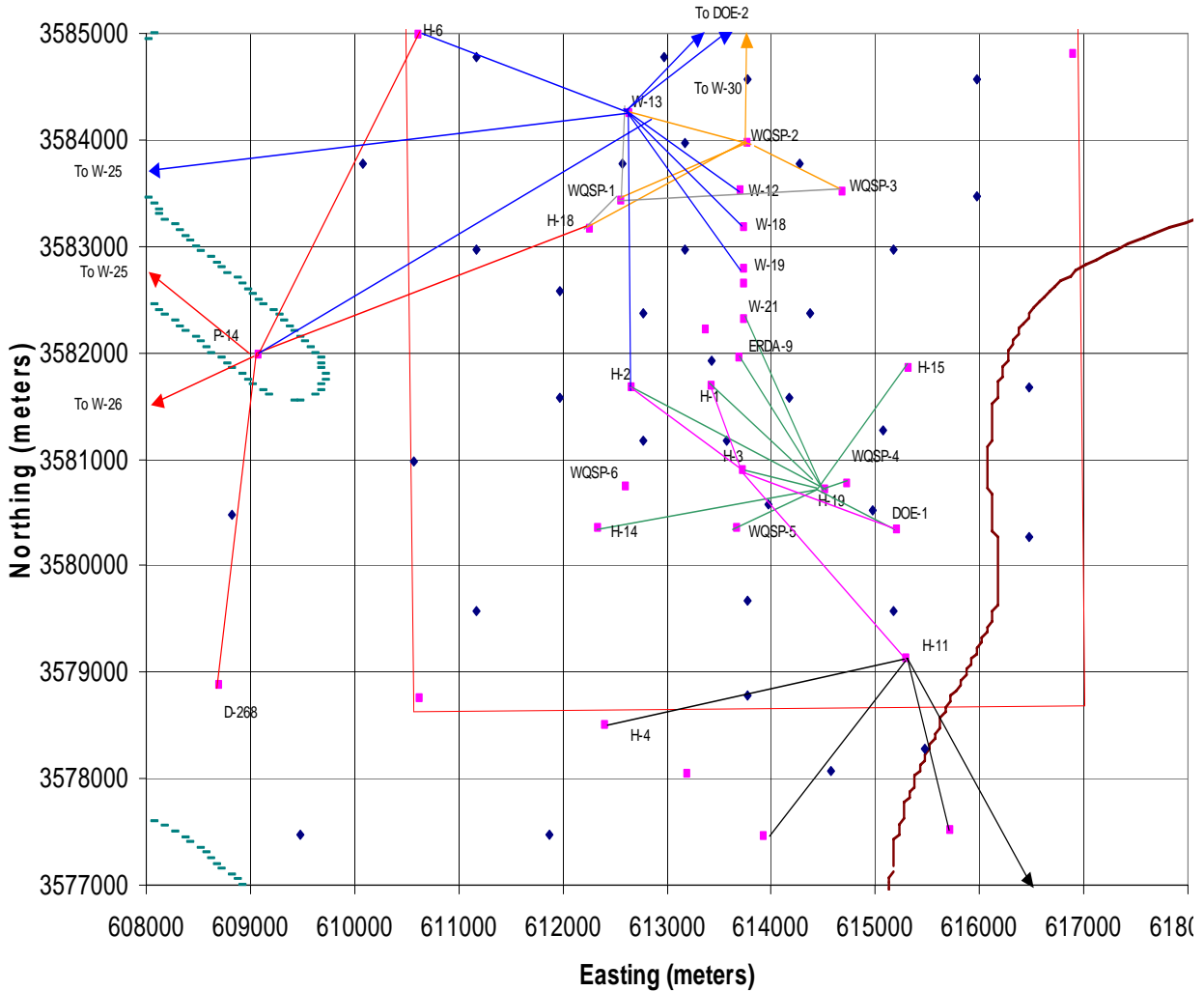
1 **Table TFIELD-10. Observation Weights for Each of the Observation Wells**

Test Well Observation Well	Maximum Drawdown (m)	Weight	Number of Observations
Steady	NA	2.273	35
H3-DOE1	5.426	0.184	57
H3-H1	10.396	0.096	26
H3-H11b1	3.622	0.276	19
H3-H2b2	3.781	0.265	20
W13-DOE2	12.138	0.082	104
W13-H2b2	0.781	1.281	23
W13-H6	5.545	0.180	93
W13-P14	0.570	1.755	38
W13-W12	1.553	0.644	27
W13-W18	6.481	0.154	26
W13-W19	5.048	0.198	22
W13-W25	0.246	4.062	11
W13-W30	3.391	0.295	24
P14-D268	0.432	2.317	38
P14-H18	0.113	8.850	21
P14-H6b	0.701	1.427	21
P14-W25	0.432	2.315	22
P14-W26	0.137	7.310	20
WQSP1-H18	1.431	0.699	47
WQSP1-W13	1.260	0.794	47
WQSP1-WQSP3	0.000	20.000	25
WQSP2-DOE2	1.178	0.849	34
WQSP2-H18	0.529	1.892	35
WQSP2-W13	1.053	0.949	34
WQSP2-WQSP1	1.132	0.884	6
WQSP2-WQSP3	0.000	20.000	18
H11-H17	1.030	0.971	23
H11-H4b	0.232	4.317	11
H11-H12	0.033	20.190	11
H11-P17	1.628	3.304	19
H19-DOE1	13.463	0.074	70
H19-ERDA9	10.571	0.095	80
H19-H1	10.618	0.094	80
H19-H15	11.110	0.090	22
H19-H3b2	19.283	0.052	69
H19-W21	7.153	0.140	19
H19-WQSP5	16.623	0.060	24
H19-H14	3.759	0.602	11
H19-H2b2	3.794	0.608	11
H19-WQSP4	25.721	0.462	24

2



1  
2 **Figure TFIELD-38. Locations of the Adjustable and Fixed Pilot Points Within the Model**  
3 **Domain**



1  
 2 **Figure TFIELD-39. Close-Up View of the Pilot-Point Locations in the Area of the WIPP**  
 3 **Site. The colored (solid) lines connect the pumping and observation wells. The legend for**  
 4 **this figure is the same as that for Figure TFIELD-38.**

5 The variogram model for the residuals between the T measurements and the base field has a  
 6 range of 1,050 m (3,445 ft). Because the pilot-point approach to calibration uses this range as a  
 7 radius of influence, locations of the adjustable pilot points were as much as possible set to be at  
 8 least 1,050 m (3,445 ft) away from other pilot points (adjustable or fixed). For maximum  
 9 impact, all pilot points should be at least 2,100 m (6,890 ft) away from any other pilot point but,  
 10 given the existing well geometry, this distance was not always achievable.

11 **TFIELD-6.9 Stochastic Inverse Calibration**

12 The seed realizations are input to the inverse model using the pilot-point method. The seed  
 13 realizations are calibrated to the steady-state and transient head measurements. The residuals  
 14 and the T-field calculations are done in log<sub>10</sub> space so that a unit change in the residual equates to  
 15 a one order of magnitude change in the value of T. The initial values of the pilot points are equal



1 to the value of the initial residual field at each pilot-point location. The pilot points are  
 2 constrained to have a maximum perturbation of  $\pm 3.0$  from the initial value except for those pilot  
 3 points within the high-T zone in Nash Draw (Figure TFIELD-11) and the low-T zone on the  
 4 eastern side of the model domain that are limited to perturbations of  $\pm 1.0$ . These limits are  
 5 employed to maintain the influence of the geologic conceptual model on the calibrated T fields.

6 Figure TFIELD-11 is updated as Figure TFIELD-40 to show, conceptually, how the addition of  
 7 two pilot points along the cross section can modify the residual field and then update the T field.  
 8 The pilot points are shown as the open circles in Figure TFIELD-40 and are used to modify the  
 9 residual field before it is added to the base T field. Compare the shape of the dashed red and blue  
 10 lines in Figure TFIELD-40 to the same lines in Figure TFIELD-11. The values of the residuals at  
 11 the observation points are held fixed so any adjacent pilot points cannot modify them.

12 At the heart of the calibration process is the iterative adjustment of the residual field at the pilot  
 13 points by PEST and the subsequent updates of the residual field at the locations surrounding the  
 14 pilot points based on the shape of the variogram modeled on the raw residuals. The updated  
 15 residual field is then combined with the base T field (see Figure TFIELD-18) and then used in  
 16 MODFLOW-2000 to calculate the current set of modeled heads. These modeled heads are then  
 17 input to PEST for the next iteration.

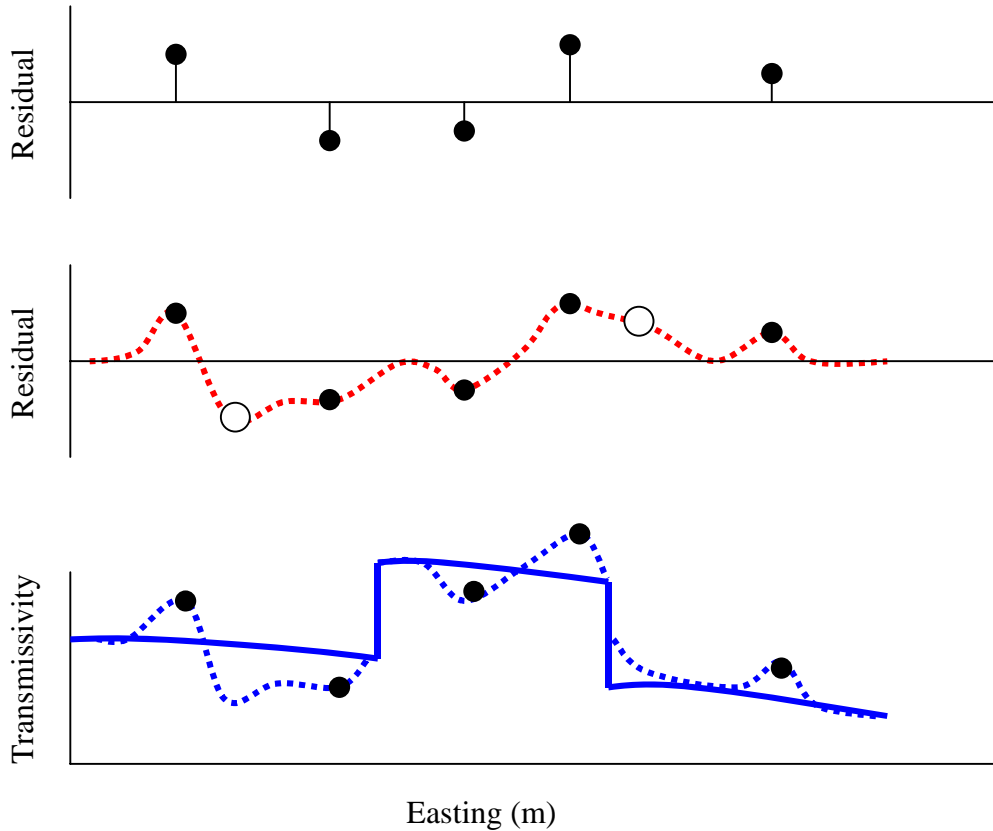
18 The objective function minimized by PEST ( $\phi$ ) is a combination of the weighted sum of the  
 19 squared residuals between the measured and observed steady-state head data, the weighted sum  
 20 of the squared residuals between the measured and observed transient drawdown data, and the  
 21 weighted sum of the squared differences in the estimated T value between pairs of pilot points.

22 Phi is defined as:

$$23 \quad \phi = \sum_{i=1}^{n_{obs}^{SS}} (W^{SS} (H_i^{obs-SS} - H_i^{calc-SS}))^2 + \sum_{i=1}^{n_{wells}^{Tr}} \sum_{j=1}^{n_{obs}^{Tr}} (W_i^{Tr} (D_j^{obs-Tr} - D_j^{calc-Tr}))^2 + \sum_{i=1}^{n_{pp}} \sum_{j=j}^{n_{pp}} W_{ij}^R (PP_i - PP_j) \quad (9)$$

24 where  $n_{obs}$  is the number of head observations,  $n_{wells}$  is the number of wells,  $n_{pp}$  is the number of  
 25 pilot points,  $W$  is the weight assigned to a group of measurements,  $H^{obs}$  and  $H^{calc}$  are the values  
 26 of the observed and calculated heads, respectively,  $D^{obs}$  and  $D^{calc}$  are the values of the observed  
 27 and calculated drawdowns, respectively,  $PP$  refers to the  $\log_{10}$  T value at a pilot point, and  
 28 superscripts  $SS$ ,  $Tr$ , and  $R$  refer to steady-state measurements, transient measurements, and pilot-  
 29 point regularization, respectively. For this work, the weights on the head and drawdown  
 30 observations are as given in Table TFIELD-10. The third weighted sum of squares in the  
 31 objective function is the regularization portion of the objective function. This weighted sum of  
 32 squares involves the difference in T values between each pair of pilot points ( $PP_i - PP_j$ ) and is  
 33 designed to keep the T field as homogeneous as possible and to provide numerical stability when  
 34 estimating more parameters than there are data. The pilot-point regularization weights,  $W_{ij}^R$ , are  
 35 defined by the kriging factors and are a function of the distance between any two pilot points.

36 The stochastic inverse calibration process uses multiple pre- and post-processor codes in addition  
 37 to PEST and MODFLOW-2000. The overall numerical approach to the T-field calibration is  
 38 shown in Figures TFIELD-41 and TFIELD-42 and the details on this approach are documented  
 39

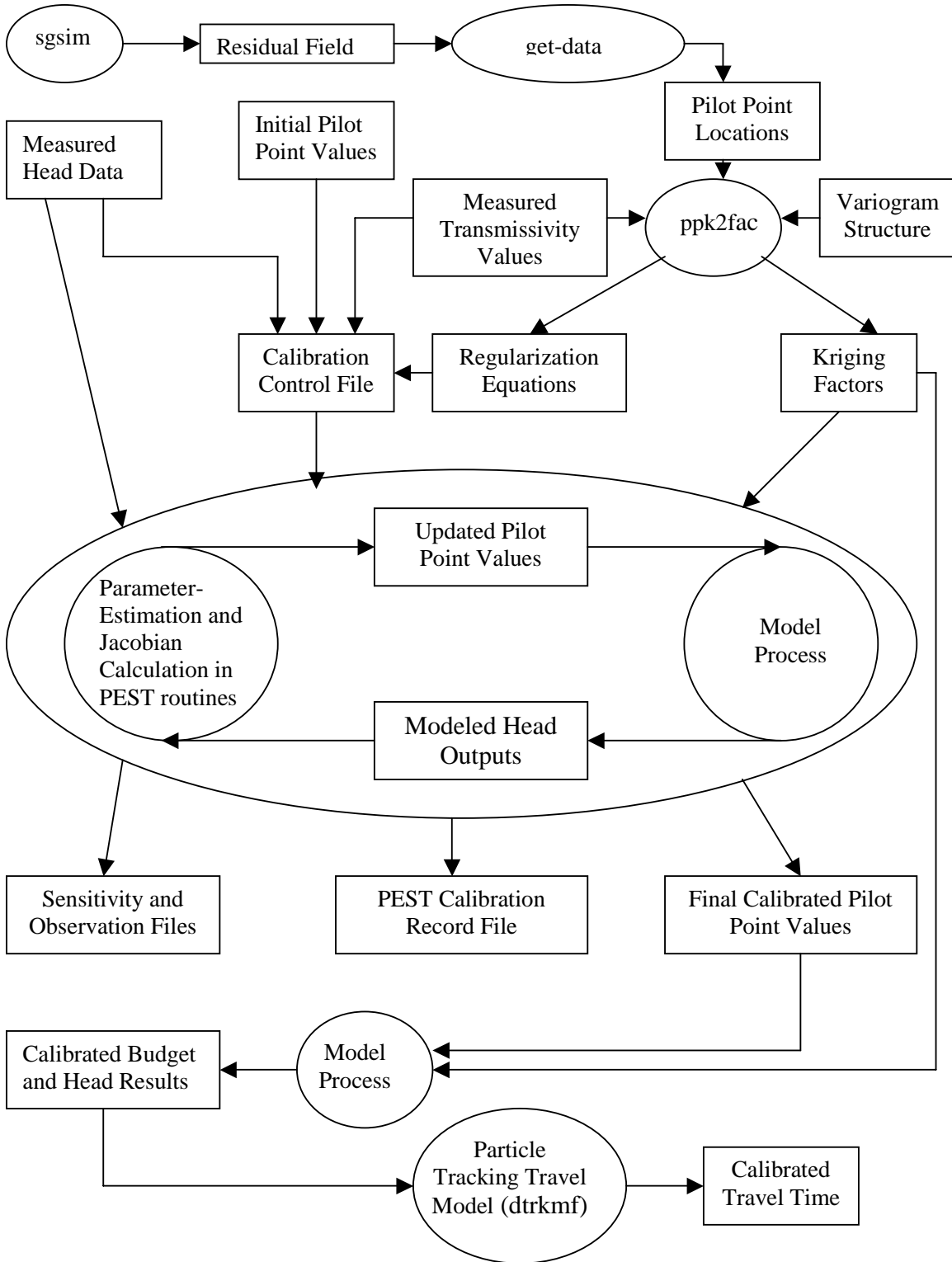


1  
 2 **Figure TFIELD-40. Conceptual Cross-Section Showing the Addition of Pilot Points to the**  
 3 **Optimization Process**

4 in McKenna and Hart (2003a, 2003b). The top of Figure TFIELD-41 shows the pre-processing  
 5 steps. The large oval in the middle of the figure contains the link between MODFLOW-2000  
 6 and PEST. The “model process” portion of the figure is expanded and the details are shown in  
 7 Figure TFIELD-42. The output files and the connection to the particle-tracking code are shown  
 8 in the bottom of Figure TFIELD-41.

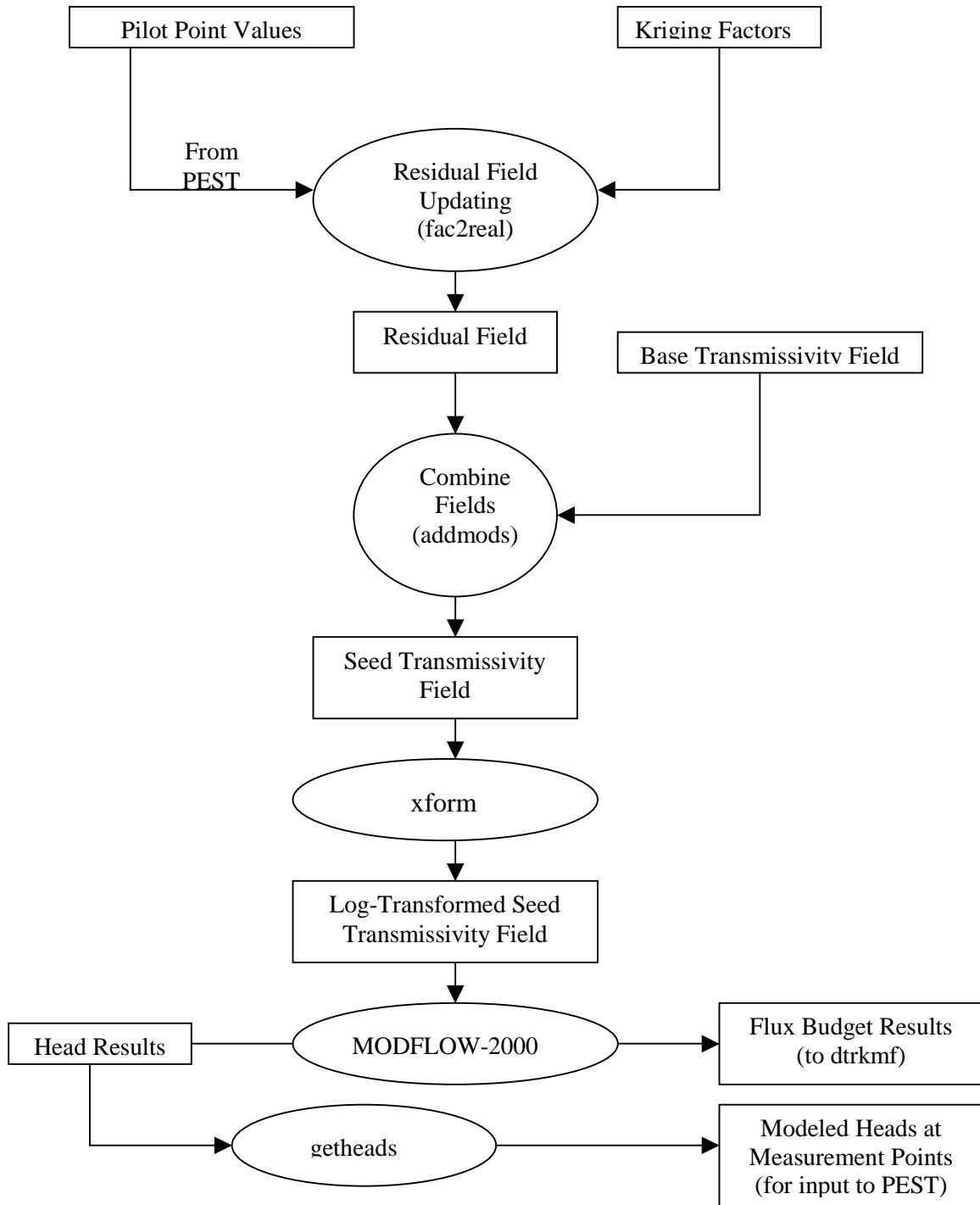
9 The calibration process is run iteratively until at least one of three conditions are met: (1) the  
 10 number of iterations reaches the maximum allowable number of 15; (2) the objective function  
 11 reaches a predefined minimum value of 1,000 m<sup>2</sup>; or (3) the value of the objective function  
 12 changes by less than one percent across three consecutive iterations.

13 At the end of the calibration process, a residual field is created that when added to the base T  
 14 field reproduces the measured T values at the 43 measurement locations and provides a  
 15 minimum sum of squared errors (SSE) between the observed and model-predicted  
 16 heads/drawdowns. An example of the final step in the creation of a calibrated T field is shown in  
 17 Figure TFIELD-43. The computational cost of calibrating to the multiple transient events is  
 18 significant. For comparison, a single forward run of MODFLOW-2000 in steady-state takes on  
 19 the order of 10-15 seconds on a 1.9-GHz Athlon processor, whereas the run time for the  
 20 combined steady-state and transient events is approximately three minutes (a factor of 12-18  
 21 times longer).



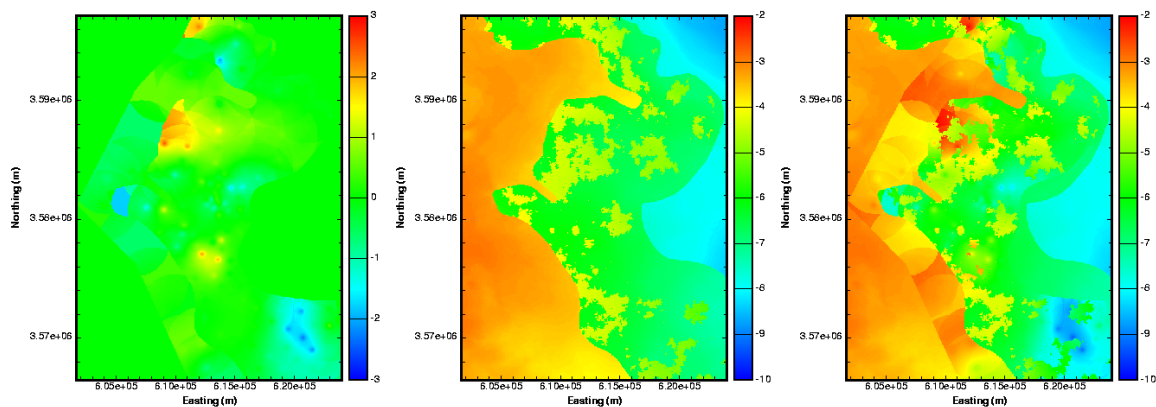
1  
2  
3

**Figure TFIELD-41. Flow Chart of the Stochastic Inverse Calibration Process Used to Create the Final Calibrated Transmissivity Fields**



1  
2  
3

**Figure TFIELD-42. Flow Chart of the Core of the Inversion Process Highlighting the Connection Between PEST and MODFLOW-2000**



1  
2 **Figure TFIELD-43. Example Final Steps in the Creation of a Calibrated T Field. The**  
3 **calibrated residual field (left image) is added to the base T field (middle image) to get the**  
4 **final calibrated T field (right image). All color scales are in units of  $\log_{10} T$  ( $m^2/s$ ).**

5 Due to these longer run times, two separate parallel PC clusters were employed. Each of these  
6 clusters consists of 16 computational nodes running 1.9-GHz Athlon processors with 1 gigabyte  
7 of RAM. One cluster is located in Albuquerque, NM and the other is in the Sandia office in  
8 Carlsbad, NM. Both clusters use the Linux operating system. The total number of forward runs  
9 necessary to complete the calibration process can be estimated as:

10 Total Runs  $\cong$  (# of parameters)  $\times$  (#of PEST iterations)  $\times$  (average runs per iteration)  $\times$  (# of base  
11 T fields).

12 The maximum number of iterations used in these runs was set to 15, although not all fields went  
13 to the maximum number of iterations. Additionally, on average for the first four iterations,  
14 PEST used forward derivatives to calculate the entries of the Jacobian matrix and each entry only  
15 required a single forward model evaluation. For the remaining 11 iterations, PEST used central  
16 derivatives to calculate the Jacobian entries and each calculation required two forward  
17 evaluations of the model (22 total). The average number of model evaluations is  $1.733 = [(4 +$   
18  $22)/15]$ . Therefore an estimate of the maximum possible total number of forward runs is equal  
19 to: 100 pilot points  $\times$  15 iterations/field  $\times$  1.73 runs/iteration  $\times$  150 T fields = 390,000 runs. The  
20 total time necessary to complete these calculations in serial mode on a single processor would be  
21 813 days, or 2.22 years. PEST allows for parallel calculation of the Jacobian matrix, and this  
22 option was used to decrease the total run time significantly relative to the time needed for serial  
23 computation.

24 The model run times, as well as the time necessary to read and write input/output files across the  
25 cluster network, were examined to determine the optimal number of client, or slave, nodes for  
26 each server, or master, node. The optimal number of clients per server was determined to be  
27 eight. More clients per server degraded overall performance due to increased communication  
28 between machines and fewer clients per server resulted in underutilization of the system. By  
29 combining the client and server activities on a single machine using a virtual server setup, four  
30 different base T fields could be calibrated simultaneously on the 32 machines.

**TFIELD-7.0 T-FIELD ACCEPTANCE CRITERIA**

The calibration procedure described in Section 6.0 of this attachment was applied to 150 of the base T fields (the remaining 350 base fields were held in reserve, to be used only if necessary). Not all base T fields yielded a resulting calibrated T field. Four base T fields (d01r03, d01r09, d02r09, and d08r10) encountered numerical difficulties during the first iteration and did not calibrate at all. For each of the remaining 146 T fields, the calibration procedure stopped for one of three reasons:

1. PEST completed the maximum allowed number of iterations (15);
2. PEST was unable to improve the objective function (sum of squared errors of weighted residuals) for three successive iterations; or
3. the optimization became numerically unstable.

Some of the T fields probably could have been calibrated better with more effort and adjustment of some of the PEST input parameters; however, these parameters were set to work across the largest number of fields possible and no calibration process will necessarily be able to make progress on every base field given the same set of parameters.

Because the T-field calibration procedure did not stop when some objective goodness-of-fit target was achieved, criteria had to be established to define what constitutes an acceptable calibration for use in the WIPP CRA calculations. Because the T fields were to be used for calculation of radionuclide transport, the travel times calculated in the T fields for a conservative particle released above the center of the WIPP waste panels (UTM X = 613,597.5 m and Y = 3,581,385.2 m [Ramsey et al. 1996, p. 9]) to reach the WIPP land-withdrawal boundary (LWB) were used in developing acceptance criteria. That is, the sensitivity of the calculated travel-time distribution to potential acceptance criteria was used to identify those criteria that are important. Once the distribution of travel times showed no (remaining) sensitivity to continued refinement of the criteria applied (e.g., a reduction in some metric below a threshold value), all T fields meeting those criteria were considered to be acceptably calibrated.

The travel times discussed herein were obtained using the streamline particle-tracking algorithm implemented in DTRKMF v. 1.0 (Rudeen 2003) assuming a single-porosity medium with a porosity of 0.16. DTRKMF calculates particle tracks in two or three dimensions for steady-state and time-dependent, variably saturated flow fields. The particles are tracked cell-by-cell using a semi-analytical solution. DTRKMF assumes that the velocities vary linearly between the cell faces as a function of the space coordinate and, for time-dependent cases, that the velocities at the faces vary linearly between time planes. It directly reads the cell-by-cell flow budget file from MODFLOW-2000 and uses those values to calculate the velocity field. For each calibrated T field, a final forward run of MODFLOW-2000 was done and the cell-by-cell fluxes from this run were used as input to DTRKMF to calculate the travel time. For each calibrated T field, only a single particle was tracked, providing a single travel time. The MODFLOW-2000 modeling was performed using a 7.75-m (25.4-ft) thickness for the Culebra, whereas transport calculations assume that all flow is concentrated in the lower 4.0 m (13 ft) of Culebra (Meigs and McCord, 1996). Therefore, the travel times obtained from DTRKMF were scaled by multiplying by the

1 factor 0.516 (4/7.75). These scaled travel times were then consistent with the travel times  
 2 calculated and reported by Wallace (1996) for the T fields used in the WIPP CCA (DOE 1996).  
 3 These travel times do not, however, represent the actual predicted travel times of solutes,  
 4 conservative or non-conservative, through the Culebra. Culebra transport modeling treats the  
 5 Culebra as a double-porosity medium with transport through advective porosity (e.g., fractures)  
 6 retarded by diffusion into diffusive porosity (e.g., matrix porosity) and by sorption. The travel  
 7 times presented herein are intended only to allow comparison among T fields.

## 8 ***TFIELD-7.1 Candidate Acceptance Criteria***

9 Four factors were evaluated for their potential to provide T-field acceptance criteria: the root  
 10 mean squared error (RMSE) of the modeled fit to the measured steady-state heads, the agreement  
 11 between the measured and modeled steady-state gradient/heads, the sum of squared weighted  
 12 residuals ( $\phi$ ) for the transient data, and the agreement between the measured and modeled  
 13 transient heads. These factors are not totally independent of one another, but are related in ways  
 14 discussed below.

### 15 ***TFIELD-7.1.1 RMSE Values***

16 The RMSE is a measure of how close MODFLOW-2000/PEST came to matching the measured  
 17 steady-state heads for each T field. The RMSE is defined as:

$$18 \quad RMSE = \sqrt{\frac{\sum_{i=1}^{n_{obs}} (H_i^{obs} - H_i^{calc})^2}{n_{obs}}} \quad (10)$$

19 where  $n_{obs}$  is the number of head observations and  $H^{obs}$  and  $H^{calc}$  are the values of the observed  
 20 and calculated heads, respectively. Previous Culebra T-field calibration exercises (e.g., LaVenue  
 21 and RamaRao 1992) achieved RMSEs less than 3 m (9.5 ft) in most cases when calibration was  
 22 being performed only to steady-state heads. This level of calibration was also achieved by  
 23 McKenna and Hart (2003a) for four different sets of steady-state head measurements. RMSEs  
 24 have not previously been reported for steady-state heads in Culebra T fields calibrated to  
 25 transient heads.

### 26 ***TFIELD-7.1.2 Fit to Steady-State Heads***

27 One measure of how well a T field has matched the steady-state heads can be obtained by simply  
 28 plotting the measured heads versus the modeled heads. If the measured and modeled heads  
 29 match exactly, the best-fit straight line through the data will have a slope of one. Exact  
 30 agreement between measured and modeled heads is not to be expected, so an acceptance  
 31 criterion on the slope of the best-fit line must be established.

32 The steady-state heads are important because the transport calculations performed in  
 33 SECOTP2D rely on the steady-state velocity field provided by MODFLOW-2000. If  
 34 MODFLOW-2000 has not accurately captured the steady-state heads, steady-state gradients and  
 35 the associated steady-state velocities will be in error. With measured head plotted as the  
 36 independent variable (x) and calculated head plotted as the dependent variable (y), a slope of the

1 best-fit line less than unity implies that the calculated gradient is less than the measured gradient.  
2 Low gradients should lead to excessively long travel times. Therefore, it was important to  
3 determine if a threshold value of the steady-state-fit slope exists above which the distribution of  
4 travel times is insensitive.

### 5 ***TFIELD-7.1.3 Phi Values***

6 As shown in Equation (9), phi values have three components:

- 7 • A weighted sum of squared residuals for the steady-state heads,
- 8 • A weighted sum of squared residuals for the transient drawdowns, and
- 9 • A weighted sum of squared differences between T values for each pair of pilot points.

10 The steady-state component of phi is a weighted, squared, and summed expression of the RMSE  
11 given in Equation (10), above, and is not, therefore, meaningful to consider when RMSE is  
12 already being considered. The pilot-point-regularization component of phi relates to the  
13 smoothness of the T field, not to the goodness of fit of the measured and modeled responses.  
14 Hence, only the transient component of phi is considered in the discussion that follows.

15 For reasons discussed in Section 6.7 of this attachment, transient phi values do not provide a  
16 completely unbiased measure of how well a calibrated T field represents the actual T field.  
17 “Measurements” of zero drawdown were given arbitrarily high weights in the calibration  
18 process, the number of measurements used from individual wells during individual tests and the  
19 number of measurements used from all wells during a single test varied, and some parts of the  
20 modeling domain are covered by multiple wells’ responses, while other parts of the domain have  
21 no transient response data. Therefore, no simple numerical value can be established that  
22 represents an average residual of some meaningful value for each transient measurement, such as  
23 the RMSE used to evaluate T-field calibration to steady-state heads alone. Nevertheless, the  
24 transient phi values do provide an indication of how well a T field met the calibration targets as  
25 defined and could be used qualitatively to define acceptable T fields.

### 26 ***TFIELD-7.1.4 Fit to Transient Heads***

27 Evaluating the model match to transient heads is not as straightforward as for the steady-state  
28 heads because the transient match involves both the magnitude and the timing of head changes.  
29 The magnitude and timing of a transient response are governed by both the transmissivity and  
30 storativity (S) of a system, but S was not included as a calibration parameter during the  
31 calibration process. A single S value of  $1 \times 10^{-5}$  ( $\log_{10} = -5$ ) was used during T-field calibration.  
32 As reported by Beauheim (2003a), the apparent storativities obtained from independent analyses  
33 of the test responses used for the calibration range from  $5.1 \times 10^{-6}$  ( $\log_{10} = -5.29$ ) to  $7.3 \times 10^{-5}$   
34 ( $\log_{10} = -4.14$ ). Because the calibration method only allowed PEST to adjust T to try to match  
35 the measured heads, it might actually shift T away from the correct value in trying to compensate  
36 for an inappropriate value of S. Thus, some allowance needed to be made for how close PEST  
37 could actually come to matching the measured responses.



1 To establish the bounds of what might be considered acceptable matches to the transient heads, a  
2 series of well-test simulations using the code nSIGHTS (Roberts 2002) was performed. For  
3 base-case parameter values, a T of  $1 \times 10^{-5}$  m<sup>2</sup>/s and an S of  $1 \times 10^{-5}$  were used. Pumping in a  
4 well was simulated for 5, 25, and/or 50 days, and the responses that would be observed in  
5 observations wells 1, 2, and/or 3 km away were calculated. T and/or S were also varied by  
6 approximately a half order of magnitude upward and downward ( $3 \times 10^{-5}$  and  $3 \times 10^{-6}$ ). The  
7 results of these simulations are shown in Appendix A of Beauheim (2003b).

8 Based on the simulations, a set of guidelines was developed to determine if a modeled response  
9 matched a measured response within a half order of magnitude uncertainty in T and/or S. The  
10 guidelines were structured around the position of the modeled maximum drawdown relative to  
11 the measured maximum drawdown on a linear-linear plot of elapsed time on the x-axis and  
12 drawdown (increasing upward) on the y-axis. The guidelines are as follows:

- 13 • If the modeled peak occurs early and high (relative to the measured peak), S is too low  
14 and the maximum modeled drawdown can be up to three times greater than the maximum  
15 measured drawdown.
- 16 • If the modeled peak occurs early and low, T is too high and the maximum modeled  
17 drawdown can be up to two times lower than the maximum measured drawdown.
- 18 • If the modeled peak occurs late and high, T is too low and the maximum modeled  
19 drawdown can be up to two times higher than the maximum measured drawdown.
- 20 • If the modeled peak occurs late and low, S is too high and the maximum modeled  
21 drawdown can be up to three times lower than the maximum measured drawdown.
- 22 • If the modeled peak occurs at the same time as the measured peak but is high, the  
23 diffusivity (T/S) is correct, but both values are too low and the maximum modeled  
24 drawdown can be up to three times greater than the maximum measured drawdown.
- 25 • If the modeled peak occurs at the same time as the measured peak but is low, the  
26 diffusivity (T/S) is correct, but both values are too high and the maximum modeled  
27 drawdown can be up to three times lower than the maximum measured drawdown.

28 No quantitative criteria were established for how much earlier or later modeled peaks could  
29 occur relative to measured peaks because of the wide range observed in the simple scoping  
30 calculations (calculated peaks occurring a factor of 5 sooner to a factor of 10 later than the  
31 observed peaks) and because of the variability in pumping durations and distances to observation  
32 wells associated with the measured responses.

33 Using these guidelines, plots of each of the 40 transient well responses of each calibrated T field  
34 were evaluated visually to determine if the T field represented that response within a half order  
35 of magnitude uncertainty in T and/or S. A threshold number of well responses that failed this  
36 test was then considered as a possible acceptance criterion for the T fields.

## 1 ***TFIELD-7.2 Application of Criteria to T Fields***

2 The four criteria described above were applied to the calibrated Culebra T fields to determine if  
3 they allowed meaningful discrimination among the fields. Given that travel time is the  
4 performance measure of most concern, the four criteria were evaluated in terms of their effects  
5 on the calculated distribution of travel times from the T fields.

### 6 ***TFIELD-7.2.1 RMSE Values***

7 Steady-state RMSE values for the 146 completed T fields are plotted in Figure TFIELD-44. The  
8 data for H-9b, the southernmost well, were excluded from the RMSE calculation because the  
9 southern model boundary condition consistently caused the modeled H-9b head to be  
10 significantly lower than the measured head, disproportionately affecting the calculation of the  
11 RMSE. The exclusion of the H-9b data should provide a better measure of the accuracy of the  
12 model in the rest of the model domain.

13 All nine RMSE values greater than 20 m (66 ft) correspond to T fields that were not considered  
14 to have been successfully calibrated by McKenna and Hart (2003b). Figure TFIELD-45 shows  
15 the RMSE values plotted against travel time, and shows that the high RMSE values tend to be  
16 associated with long travel times. For RMSE values less than approximately 6 m (20 ft), travel  
17 times tend to cluster below approximately 50,000 years. Applying an RMSE cutoff value of 6 m  
18 (20 ft) would leave 117 T fields, with all but one having travel times less than 102,000 years  
19 (Figure TFIELD-46; the outlier with a travel time of ~241,000 years, d01r06, is not shown).

### 20 ***TFIELD-7.2.2 Fit to Steady-State Heads***

21 Figure TFIELD-47 provides an example plot of measured steady-state heads versus modeled  
22 steady-state heads for one T field, with a unit-slope line shown as a reference. For each plot of  
23 steady-state heads, the slope of the best-fit line through all of the data except for the data for  
24 H-9b was calculated using the Excel SLOPE function. The data for H-9b, the southernmost well,  
25 were excluded from this calculation because the southern model boundary condition consistently  
26 caused the modeled H-9b head to be significantly lower than the measured head. Inasmuch as  
27 the gradient in the extreme southern portion of the modeling domain is unimportant with respect  
28 to transport across the southern half of the WIPP site, the exclusion of the H-9b data should  
29 improve the accuracy of the slope calculation in the area of interest.

30 The slopes of the best-fit lines through the measured vs. modeled steady-state heads are shown  
31 plotted against travel time in Figure TFIELD-48. Steady-state-fit slopes less than 0.5 appear to  
32 lead to significantly longer travel times, consistent with the low hydraulic gradients the low  
33 slopes imply. Of the 116 T fields with steady-state-fit slopes greater than 0.5, all but nine have  
34 travel times less than 50,000 years. Figure TFIELD-49 shows the slopes and travel times for  
35 these 116 fields (the outlier with a travel time of ~241,000 years, d01r06, is not shown), and  
36 indicates that travel time is not sensitive to steady-state-fit slopes above 0.5.

### 37 ***TFIELD-7.2.3 Phi Values***

38 Transient phi values for all the completed T fields are plotted against travel time in Figure  
39 TFIELD-50. As phi values decrease, particularly as they get below approximately 5,000 m<sup>2</sup>

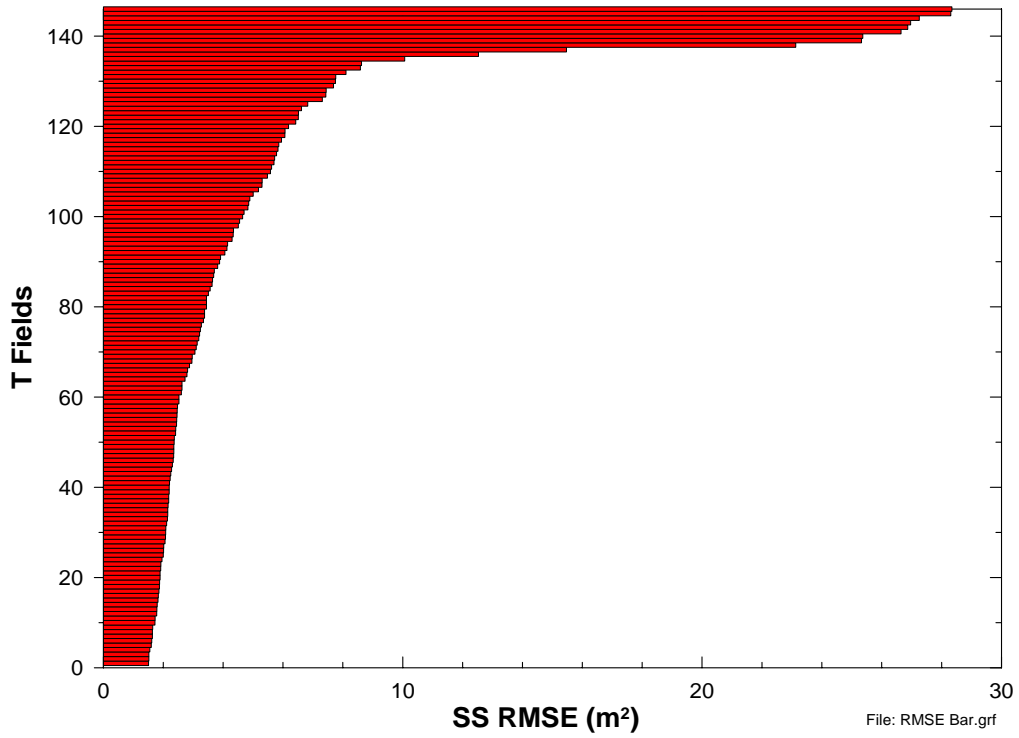


**Figure TFIELD-44. Steady-State RMSE Values for 146 T Fields**

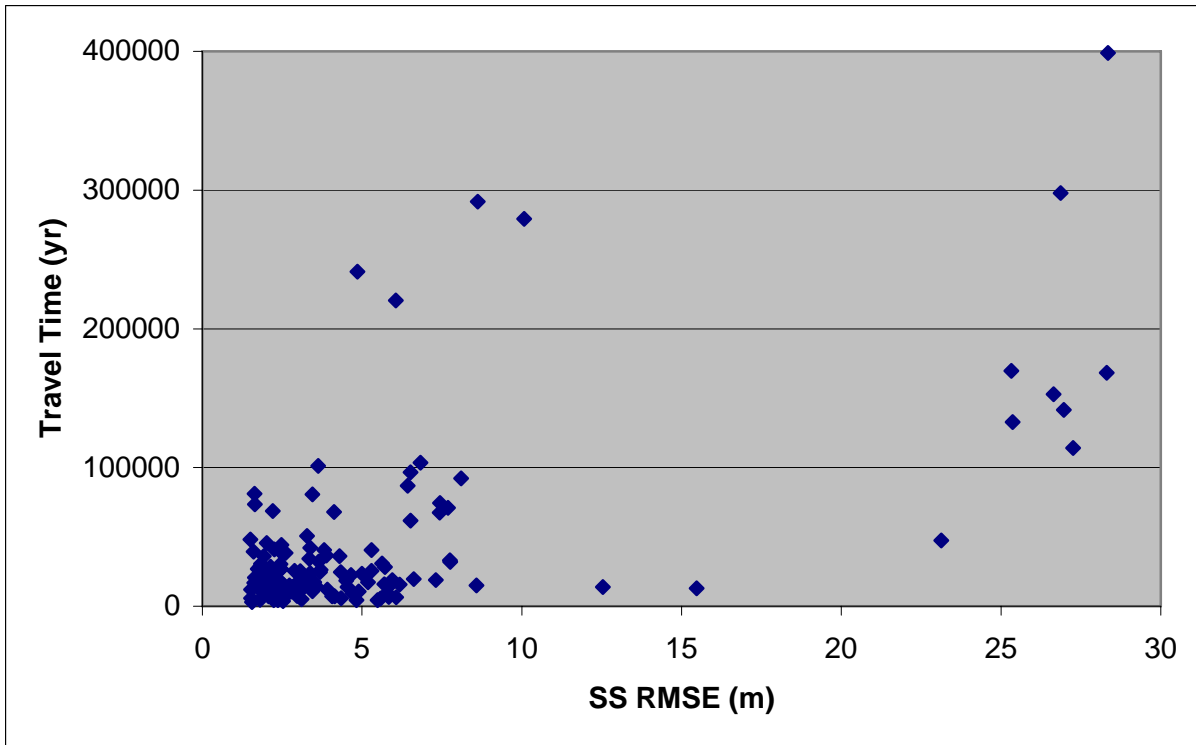
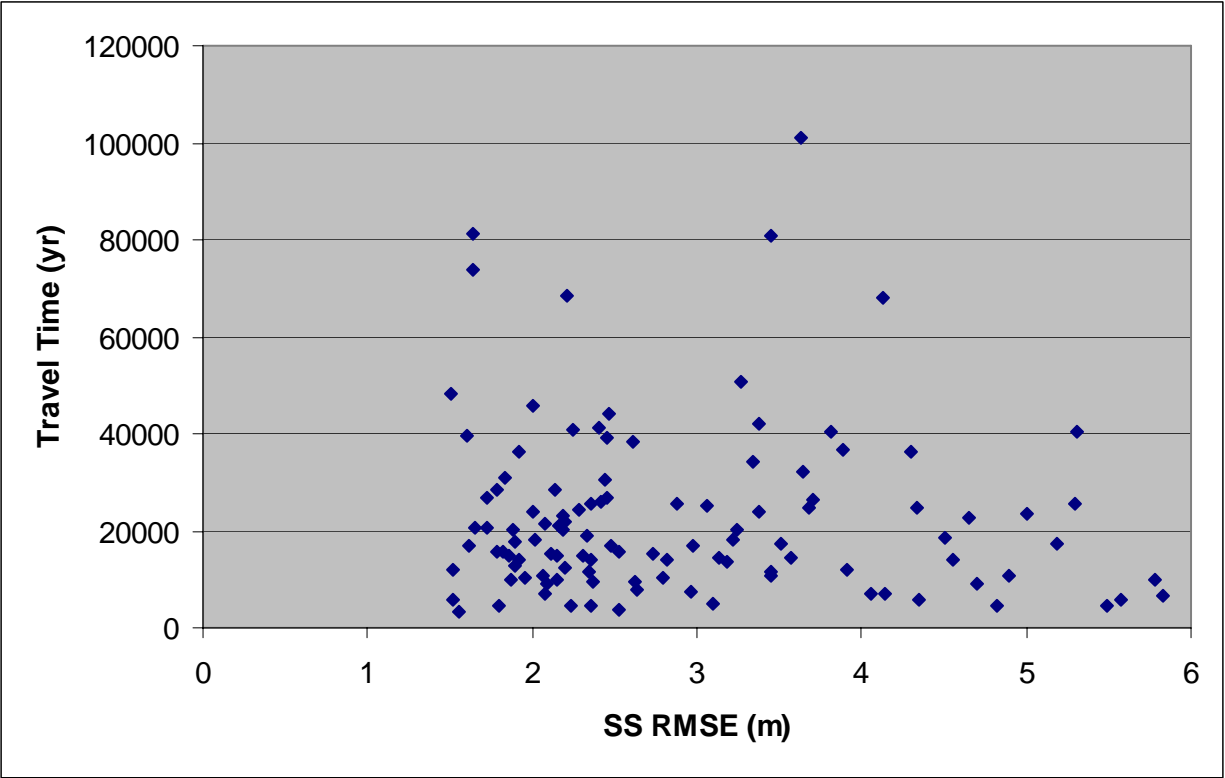


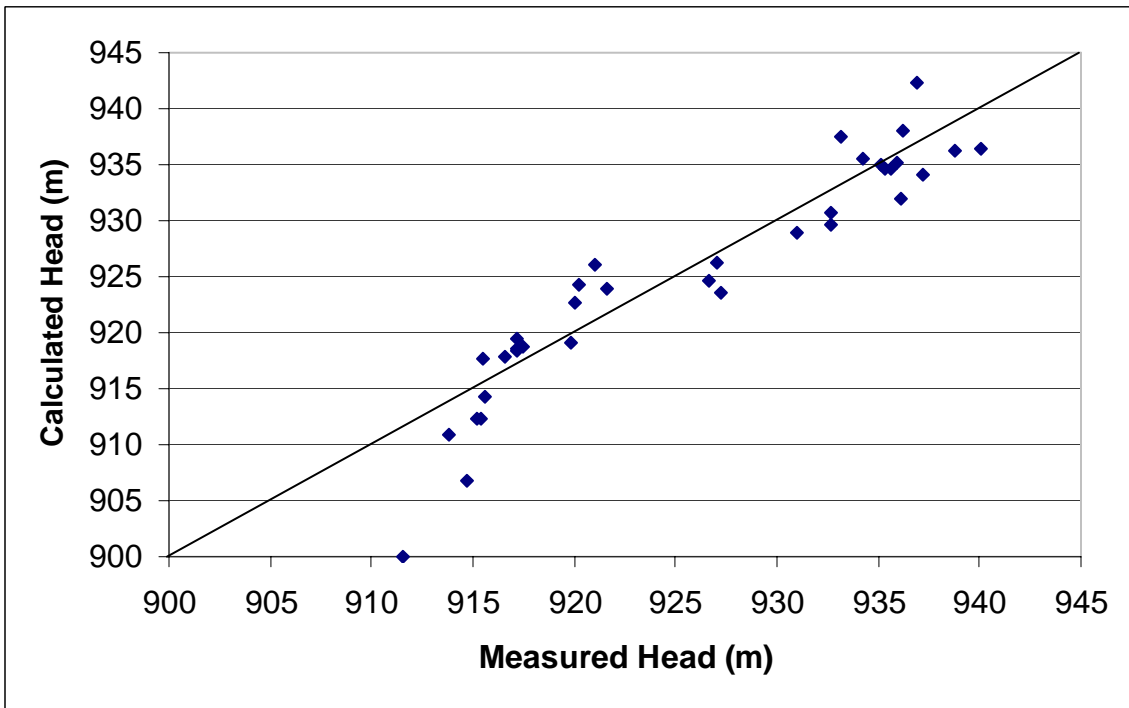
**Figure TFIELD-45. Steady-State RMSE Values and Associated Travel Times**



1

2

**Figure TFIELD-46. Travel Times for Fields with Steady-State RMSE <6 m (20 ft)**



3

4

5

**Figure TFIELD-47. Measured Versus Modeled Steady-State Heads for T Field d21r10**

1 (53,800 ft<sup>2</sup>), travel times tend to cluster below approximately 50,000 years, but little correlation  
2 is seen between transient phi and travel time. Figure TFIELD-51 shows transient phi versus  
3 travel time for the 123 fields with transient phi values less than 8,000 m<sup>2</sup> (86,000 ft<sup>2</sup>), excluding  
4 the five outliers that have travel times greater than 168,000 years. This plot suggests that despite  
5 the clustering of travel times below 50,000 years, the overall range of travel times does not  
6 decrease significantly as phi decreases. Thus, transient phi does not appear to provide an  
7 effective tool for distinguishing among T fields.

#### 8 ***TFIELD-7.2.4 Fit to Transient Heads***

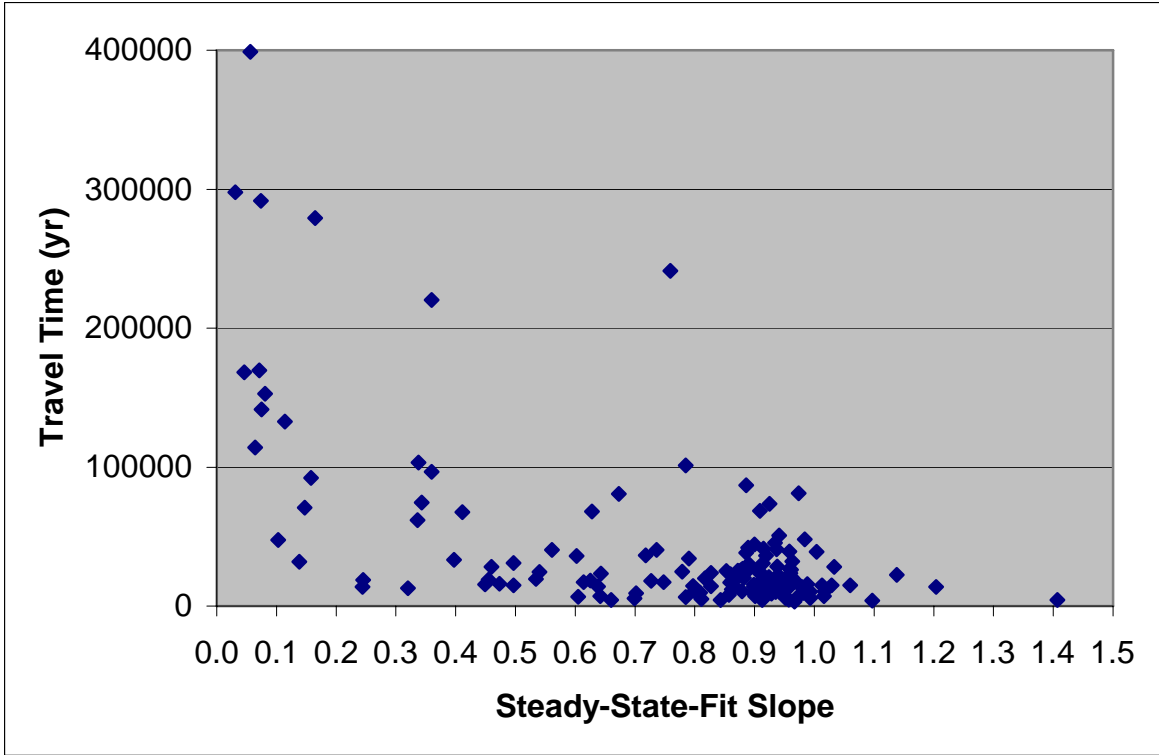
9 In applying the tests described in Section 7.1.4 of this attachment to the well responses simulated  
10 for each T field, it was found that insufficient data (only six measurements) had been included  
11 for the WQSP-1 response to pumping at WQSP-2 to allow any determination of model  
12 adequacy. Thus, this response was eliminated from consideration for all T fields. Figures  
13 TFIELD-52 and TFIELD-53 provide examples from T field d21r10 of well responses that were  
14 judged to PASS and FAIL, respectively, the criteria outlined in Section 7.1.4 of this attachment.  
15 The number of responses that failed for each T field is given in Table TFIELD-11. For the  
16 WQSP-3 responses to pumping at WQSP-1 and WQSP-2 (for which no clear drawdown was  
17 observed and “measured” values of zero were entered), the modeled response was accepted if it  
18 showed no more than 0.25 m (0.82 ft) of drawdown.

19 The number of well responses that fail the tests described in Section 7.1.3 of this attachment  
20 should be related to the transient phi for each T field because both are measures of the match  
21 between the measured and modeled transient heads. Figure TFIELD-54 shows a plot of transient  
22 phi versus the number of failed well responses for all 146 T fields. A definite correlation is  
23 evident up to a phi of approximately 8,000 m<sup>2</sup> (86,000 ft<sup>2</sup>). Beyond that value, the number of  
24 failed well responses simply remains high ( $\geq 14$ ).

25 The number of failed well responses is plotted against travel time in Figure TFIELD-55 for each  
26 of the T fields. The scatter in travel time appears to increase with 14 or more failures, but the  
27 majority of T fields still have travel times in the same range as the fields with less than 14  
28 failures. Thus, the number of failed well responses alone does not appear to discriminate well  
29 among T fields.

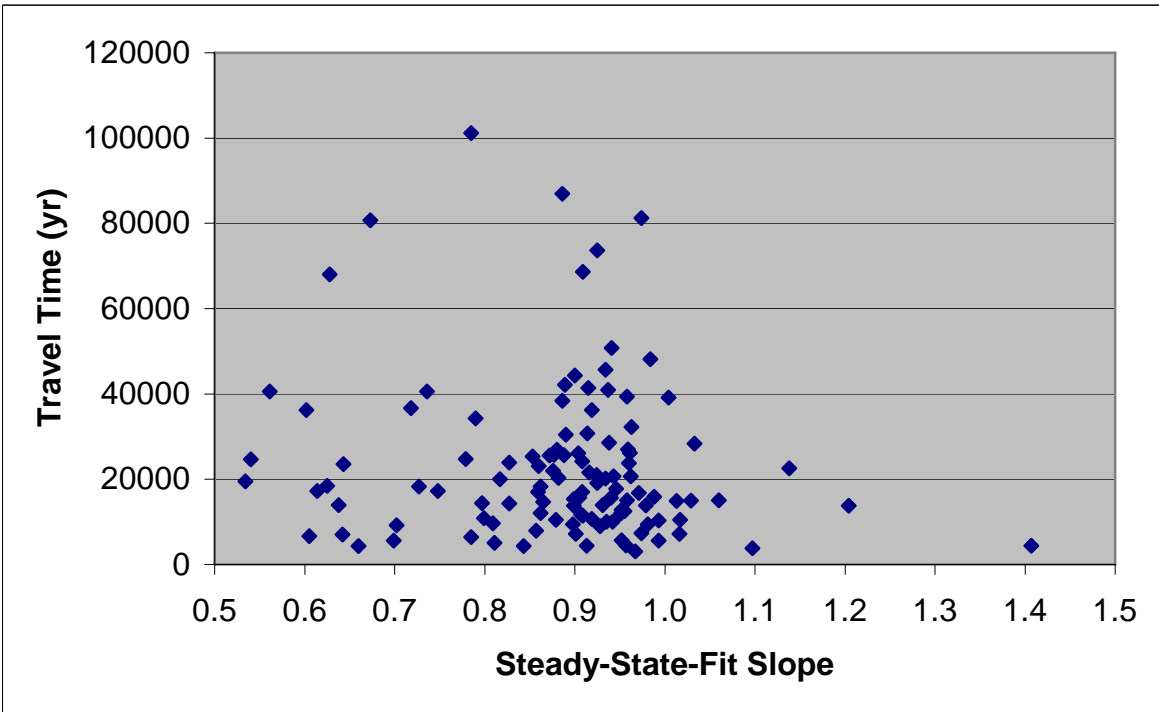
#### 30 ***TFIELD-7.3 Final Acceptance Criteria***

31 Of the criteria discussed above, the two related to the steady-state heads (RMSE and steady-  
32 state-fit slope) appear to be more effective at identifying poorly calibrated T fields than the two  
33 related to transient heads (transient phi and number of failed well responses). The range and  
34 scatter of travel times appears to increase at RMSE values beyond 6 m (20 ft). Applying an  
35 RMSE cutoff of 6 m (20 ft) leaves 117 T fields, all with travel times less than 102,000 years  
36 except one (d01r06). This cutoff also excludes all T fields with steady-state-fit slopes less than  
37 0.45. Steady-state-fit slopes less than approximately 0.5 appear to lead to significantly longer  
38 travel times, consistent with the low hydraulic gradients the low slopes imply. If a simple cutoff  
39 of a minimum steady-state-fit slope of 0.5 is applied, 116 T fields are left, again with travel times  
40 less than 102,000 years (except d01r06), and also with RMSE values less than 8.6 m (28.2 ft).  
41 Five T fields that meet the RMSE less than 6 m (20 ft) criterion fail the steady-state-fit slope



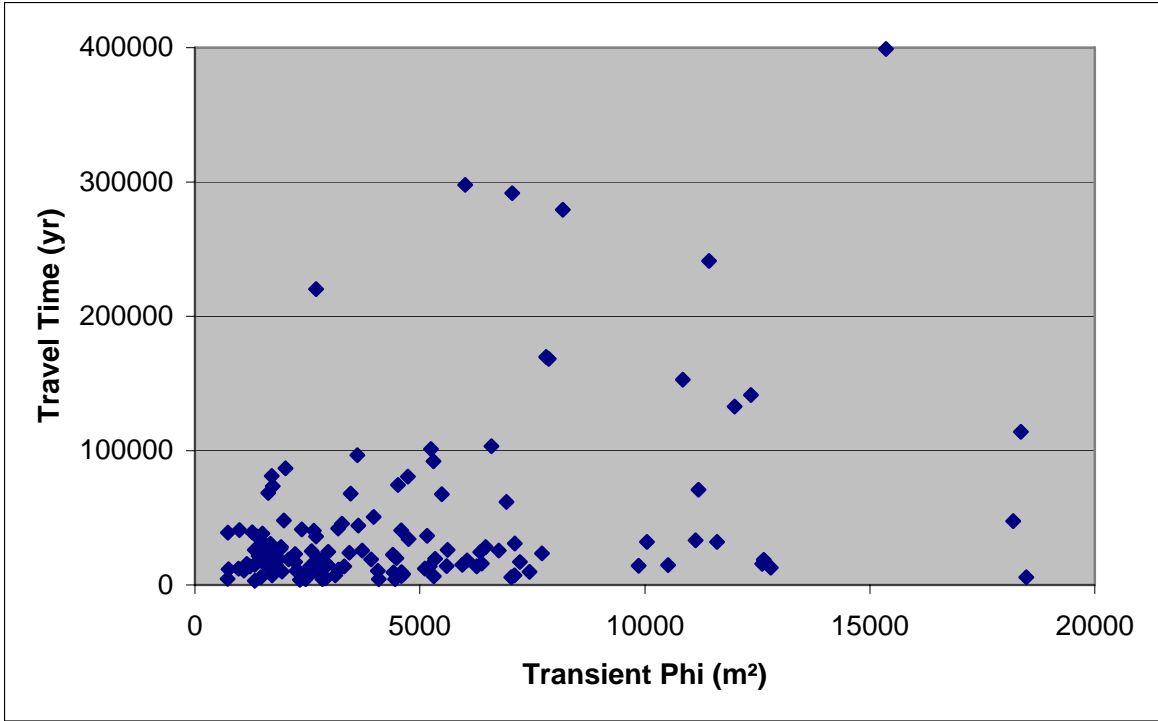
1  
2

**Figure TFIELD-48. Steady-State-Fit Slope Versus Travel Time for All Fields**



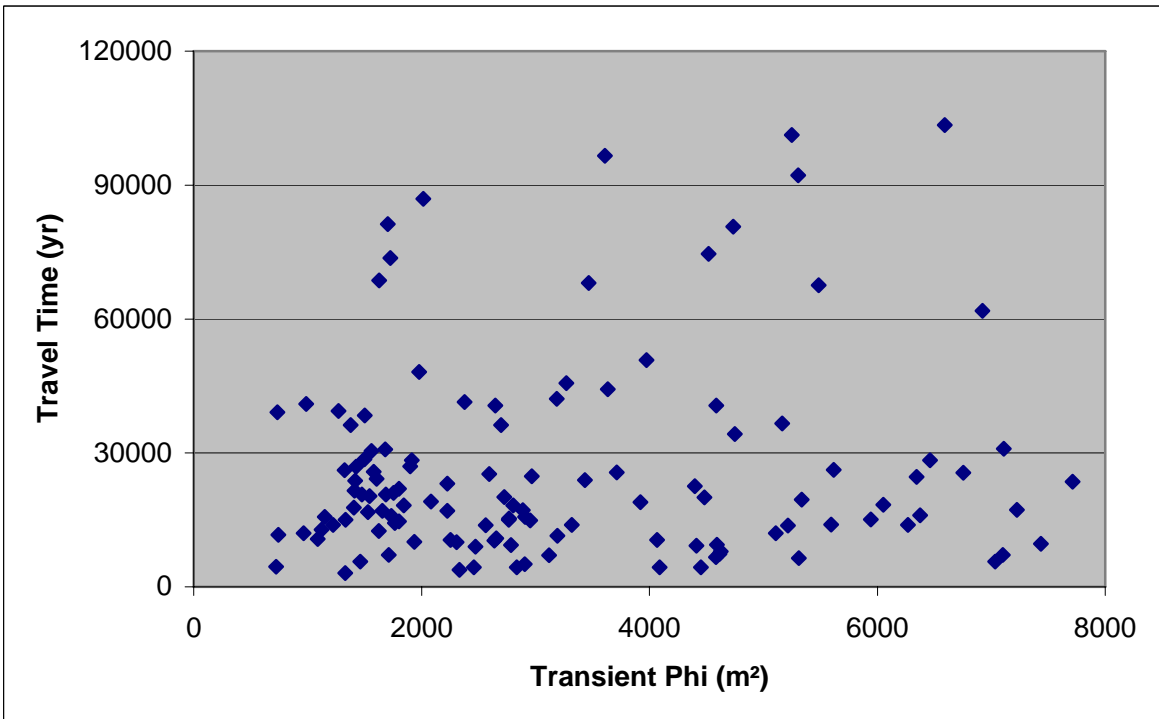
3  
4

**Figure TFIELD-49. Steady-State-Fit Slope Versus Travel Time for Slopes >0.5**



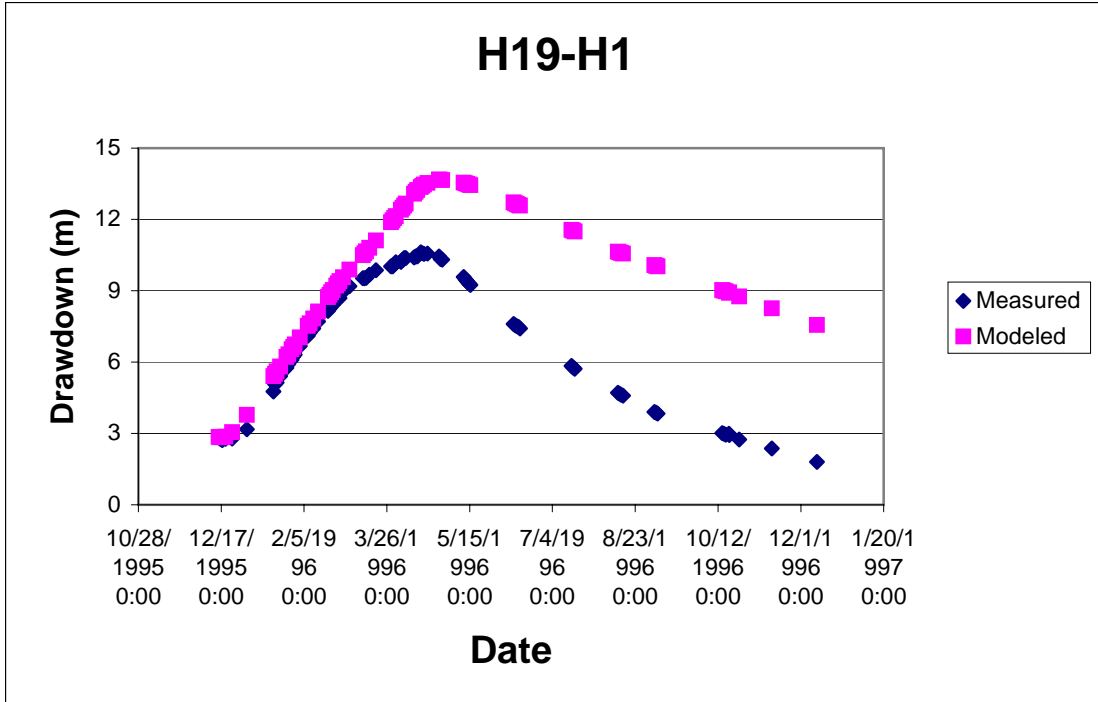
1  
2

**Figure TFIELD-50. Transient Phi Versus Travel Time for All Fields**



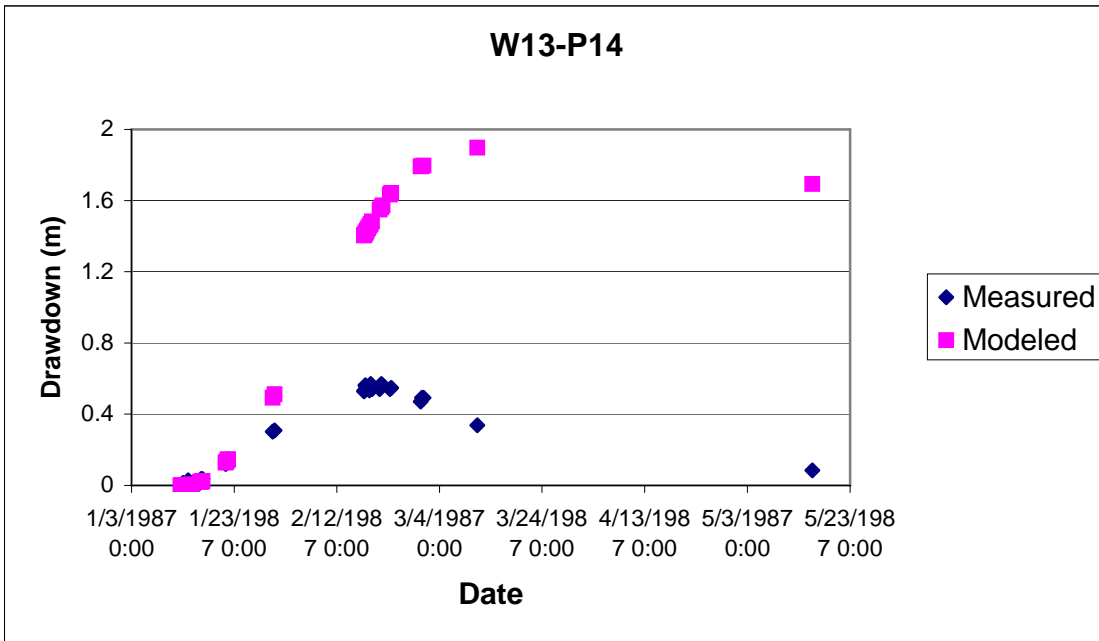
3  
4

**Figure TFIELD-51. Transient Phi Versus Travel Time for Phi <8,000 m²**



1  
2  
3

**Figure TFIELD-52. Example of Passing Well Response from T Field d21r10**



4  
5

**Figure TFIELD-53. Example of Failing Well Response from T Field d21r10**



**Table TFIELD-11. Summary Information on T Fields**

T Field	SS RMSE (m)	SS Phi (m <sup>2</sup> )	Transient Phi (m <sup>2</sup> )	Steady-State-Fit Slope	# of Failed Well Responses	Time to WIPP boundary (yr)
	7.427	10498	5486	0.411	13	67578
<i>d01r02</i>	3.915	3621	5110	0.862	20	12045
<i>d01r04</i>	2.812	2140	2563	1.204	11	13821
	7.313	10245	12643	0.245	16	18886
<i>d01r06</i>	4.856	5006	11426	0.759	15	241211
<i>d01r07</i>	3.377	2851	3187	0.889	9	42123
<i>d01r08</i>	5.484	6122	4091	1.407	14	4399
<i>d01r10</i>	1.646	1094	1476	0.943	9	20685
	26.966	128711	12359	0.075	19	141516
<i>d02r02</i>	3.507	2772	2889	0.748	11	17217
	10.070	18606	8173	0.165	15	279242
	8.104	12482	5305	0.158	12	92235
<i>d02r05</i>	5.184	5577	7224	0.614	17	17255
	25.325	113652	7810	0.071	16	169677
<i>d02r07</i>	3.648	3223	10047	0.963	15	32231
<i>d02r08</i>	5.001	5125	7713	0.643	17	23571
<i>d02r10</i>	6.066	6849	5312	0.785	13	6433
<i>d03r01</i>	4.506	4022	6053	0.625	17	18435
	28.346	142152	15357	0.056	16	398937
<i>d03r03</i>	4.146	3899	7102	1.016	17	7171
	25.367	114006	11991	0.114	14	132833
<i>d03r05</i>	5.836	6873	4585	0.605	13	6638
<i>d03r06</i>	1.729	1208	1899	0.959	13	27006
<i>d03r07</i>	4.655	4740	4399	1.138	13	22599
<i>d03r08</i>	4.550	4250	5593	0.638	17	13942
<i>d03r09</i>	2.352	1574	1580	0.877	7	25757
<i>d03r10</i>	8.584	13811	2766	1.060	13	15054
<i>d04r01</i>	3.447	2370	4736	0.673	17	80690
<i>d04r02</i>	3.818	3175	2647	0.736	12	40593
<i>d04r03</i>	2.352	1659	3317	0.979	12	13888
<i>d04r04</i>	4.298	3692	2697	0.602	13	36245
<i>d04r05</i>	1.507	1059	1980	0.984	9	48168
<i>d04r06</i>	3.705	3146	5618	0.961	16	26199
<i>d04r07</i>	2.183	1397	2226	0.860	10	23105
<i>d04r08</i>	2.444	1759	1560	0.890	11	30470
	27.256	131491	18356	0.064	16	114087
<i>d04r10</i>	3.060	2401	2593	0.853	9	25316
<i>d05r01</i>	6.427	8119	2015	0.886	13	86924
<i>d05r02</i>	5.298	5831	6755	0.872	16	25610
<i>d05r03</i>	3.444	2580	2655	0.799	11	10880
<i>d05r04</i>	5.862	6984	10518	0.497	17	14856
<i>d05r05</i>	4.346	4226	18478	0.952	16	5668
	6.518	8198	3609	0.360	13	96589
<i>d05r07</i>	3.188	2682	5216	0.899	9	13766
	7.686	11242	11194	0.147	16	70896
	26.644	125685	10840	0.081	17	152818
<i>d05r10</i>	5.623	6497	7110	0.497	16	30955
	6.828	9057	6592	0.338	17	103442
<i>d06r02</i>	1.957	1266	2639	0.993	9	10353
<i>d06r03</i>	1.637	1051	1703	0.974	10	81258
<i>d06r04</i>	3.214	2246	2805	0.727	13	18294

1

**Table TFIELD-11. Summary Information on T Fields — Continued**

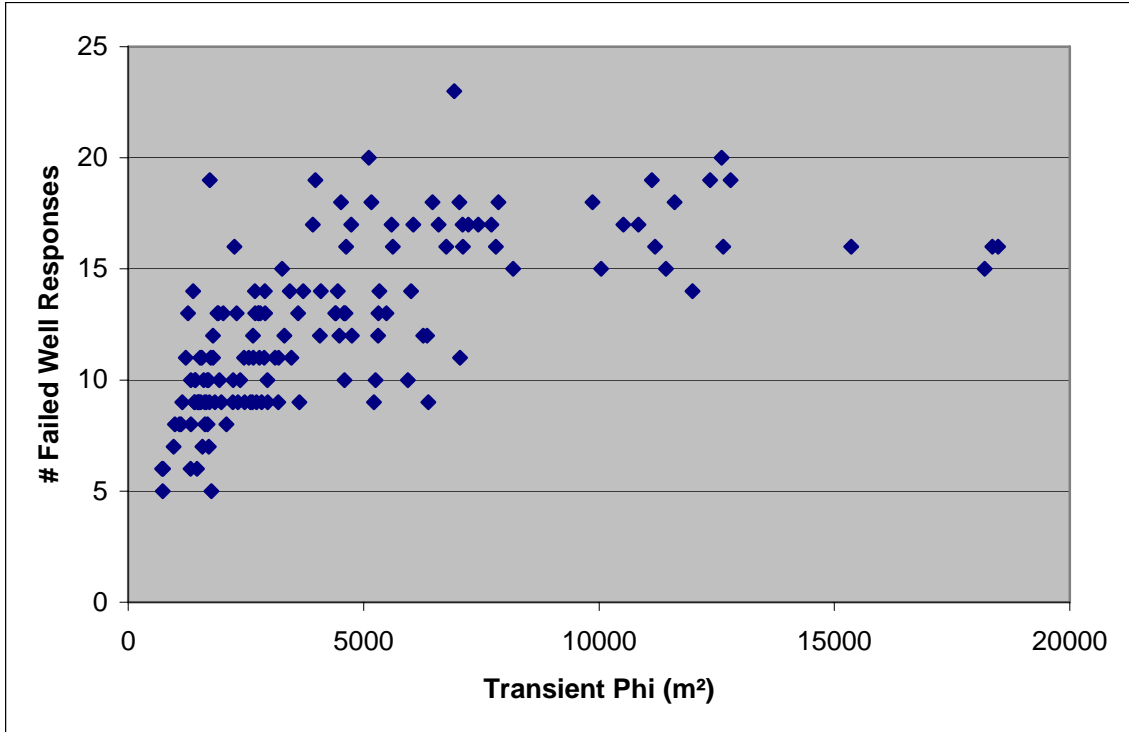
T Field	SS RMSE (m)	SS Phi (m <sup>2</sup> )	Transient Phi (m <sup>2</sup> )	Steady-State-Fit Slope	# of Failed Well Responses	Time to WIPP boundary (yr)
d06r05	3.886	3516	5164	0.718	18	36644
d06r06	2.149	1254	2954	1.013	10	14935
d06r07	1.518	784	965	0.951	7	12035
██████	7.440	10397	4518	0.343	18	74565
██████	28.309	141764	7864	0.046	18	168281
d06r10	2.196	1455	1801	0.876	11	21990
d07r01	3.101	2326	2905	0.811	14	5082
d07r02	2.010	1327	3271	0.934	15	45647
██████	15.470	42986	12795	0.320	19	12919
d07r04	5.579	6230	7033	0.699	18	5638
d07r05	2.727	1705	5942	0.958	10	15097
d07r06	4.334	3927	6345	0.540	12	24641
d07r07	2.477	1737	2225	0.908	9	17038
d07r08	2.232	1097	2836	0.843	9	4355
d07r09	2.207	1239	1628	0.909	8	68629
d07r10	1.782	839	1150	0.940	9	15680
d08r01	2.361	1736	2458	0.913	11	4388
d08r02	2.418	1168	1326	0.904	6	26115
d08r03	2.137	1489	1499	0.938	9	28570
d08r04	3.683	2674	2966	0.779	9	24773
d08r05	2.115	1384	2769	0.899	13	15358
d08r06	1.916	1388	1225	0.931	11	13917
d08r07	1.857	815	1333	1.029	10	15027
██████	12.534	28547	6267	0.244	12	13885
d08r09	5.785	6674	7437	0.809	17	9691
██████	8.621	13909	7050	0.074	11	291623
d09r02	3.243	2418	4482	0.817	12	20048
d09r03	2.252	1337	989	0.937	8	40948
d09r04	1.892	710	1123	0.952	8	12857
d09r05	2.061	954	1088	0.919	8	10726
d09r06	2.794	2313	2253	0.879	16	10509
d09r07	2.629	1676	4591	0.981	10	9472
d09r08	1.895	1030	1406	0.946	9	17741
d09r09	4.826	4945	4453	0.660	14	4359
d09r10	3.273	2790	3976	0.941	19	50791
██████	26.867	127794	6006	0.031	14	297840
d10r02	1.554	589	1330	0.967	8	3111
d10r03	2.201	1474	1626	0.955	9	12533
d10r04	2.527	1788	2334	1.097	9	3799
d10r05	5.722	6646	6463	0.460	18	28390
d10r06	4.702	4644	4412	0.702	13	9210
d10r07	1.870	810	1937	0.935	10	10068
d10r08	2.334	1613	2083	0.925	8	19093
d10r09	4.128	3643	3466	0.628	11	68052
d10r10	1.789	982	1915	1.033	13	28367
d11r01	2.970	2297	1655	0.859	9	17015
d11r02	2.308	1799	1801	0.865	12	14677
d11r03	5.700	6093	6376	0.473	9	16014
██████	6.514	8401	6922	0.336	23	61862
d11r05	5.952	7166	3921	0.455	17	18998
d11r06	2.607	1949	1503	0.886	9	38399

**Table TFIELD-11. Summary Information on T Fields — Continued**

T Field	SS RMSE (m)	SS Phi (m <sup>2</sup> )	Transient Phi (m <sup>2</sup> )	Steady-State-Fit Slope	# of Failed Well Responses	Time to WIPP boundary (yr)
<i>d11r07</i>	1.639	602	1727	0.925	9	73634
<i>d11r08</i>	1.801	1206	723	0.957	6	4520
<i>d11r09</i>	2.073	858	1712	0.901	7	7199
<i>d11r10</i>	3.135	2363	1767	0.827	5	14358
<i>d12r01</i>	3.378	2921	3432	0.827	14	23936
<i>d12r02</i>	2.459	1795	1426	0.880	10	26919
<i>d12r03</i>	1.618	558	1530	0.971	11	16780
██████	6.182	7395	12605	0.449	20	15619
<i>d12r05</i>	1.522	918	1463	0.993	6	5655
<i>d12r06</i>	1.602	539	1271	0.958	13	39399
<i>d12r07</i>	2.016	945	1844	0.862	9	18283
<i>d12r08</i>	2.630	1879	4627	0.857	16	7981
<i>d12r09</i>	2.369	1671	2784	0.898	11	9414
██████	7.762	11431	11606	0.138	18	32059
<i>d13r01</i>	2.163	1061	1753	0.924	11	21032
<i>d13r02</i>	2.881	2054	3715	0.888	14	25639
<i>d13r03</i>	3.444	2580	3192	0.909	11	11493
<i>d13r04</i>	5.302	5856	4588	0.561	13	40601
<i>d13r05</i>	3.343	2671	4750	0.790	12	34247
<i>d13r06</i>	2.410	1441	2377	0.915	10	41400
<i>d13r07</i>	2.280	1395	1606	0.908	10	24211
<i>d13r08</i>	1.879	779	1544	0.882	9	20313
<i>d13r09</i>	1.919	776	1379	0.919	14	36260
██████	6.063	6685	2693	0.360	14	220354
<i>d21r01</i>	2.151	1555	2307	0.942	13	10042
<i>d21r02</i>	2.087	1431	2473	0.928	9	9023
<i>d21r03</i>	2.346	1299	744	0.907	6	11671
<i>d21r04</i>	2.523	1978	2908	0.905	13	15717
<i>d21r05</i>	2.001	932	1417	0.960	10	23750
<i>d21r06</i>	1.721	655	1688	0.962	8	20715
<i>d21r07</i>	2.182	1179	2725	0.934	9	20141
<i>d21r08</i>	6.620	8618	5337	0.534	14	19534
██████	7.750	11501	11124	0.397	19	33308
<i>d21r10</i>	2.959	2226	4615	0.974	13	7384
██████	23.126	94895	18190	0.103	15	47563
<i>d22r02</i>	3.629	3197	5250	0.785	10	101205
<i>d22r03</i>	4.061	3464	3119	0.642	11	7067
<i>d22r04</i>	4.894	5073	4068	1.017	12	10537
<i>d22r05</i>	3.566	3160	9863	0.797	18	14385
<i>d22r06</i>	2.469	1145	3635	0.900	9	44309
<i>d22r07</i>	2.080	999	1413	0.916	9	21589
<i>d22r08</i>	1.837	809	1681	0.914	10	30771
<i>d22r09</i>	1.822	724	1734	0.988	19	15870
<i>d22r10</i>	2.452	1684	735	1.004	5	39116

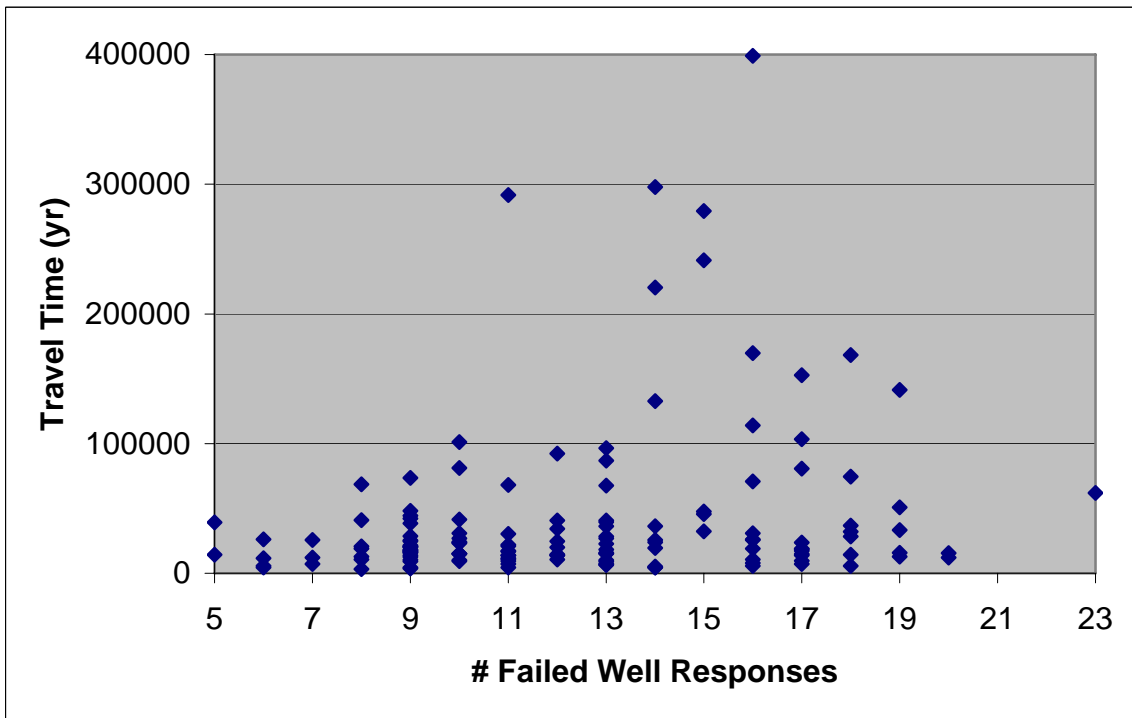
1  
2 ████████ signifies T fields not meeting final acceptance criteria.

3 ***Bold italics*** type signifies 100 final T fields as discussed in Section 7.3 of this attachment.



1  
2

**Figure TFIELD-54. Transient Phi Versus Number of Failed Well Responses**

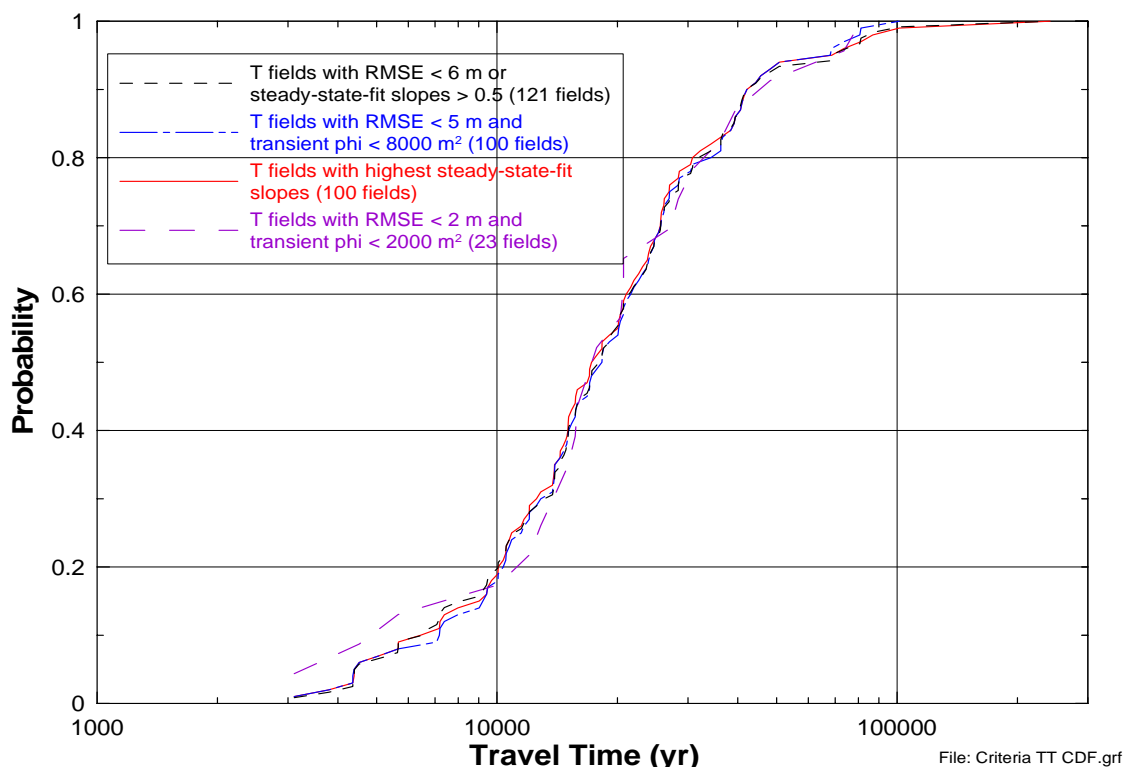


3  
4

**Figure TFIELD-55. Number of Failed Well Responses Versus Travel Time**

1 greater than 0.5 criterion, while four T fields meeting the slope criterion fail the RMSE criterion.  
 2 Thus, 112 T fields meet both criteria while 121 T fields meet at least one of the criteria.

3 Figure TFIELD-56 shows a CDF for the 121 T fields meeting the RMSE and/or steady-state-fit  
 4 slope criteria discussed above. Also shown are curves representing the 100 T fields with RMSE  
 5 values <5 m (16 ft) and transient phi values <8,000 m<sup>2</sup> (86,111 ft<sup>2</sup>), and the 100 T fields with the  
 6 largest steady-state-fit slopes (>0.72). All three CDFs are very similar, the most significant  
 7 difference being that imposing a cutoff value on transient phi eliminates the T field with the  
 8 longest travel time (d01r06). To illustrate the effects of imposing more stringent constraints on  
 9 T-field acceptance, a fourth CDF is shown in Figure TFIELD-56 that represents the 23 T fields



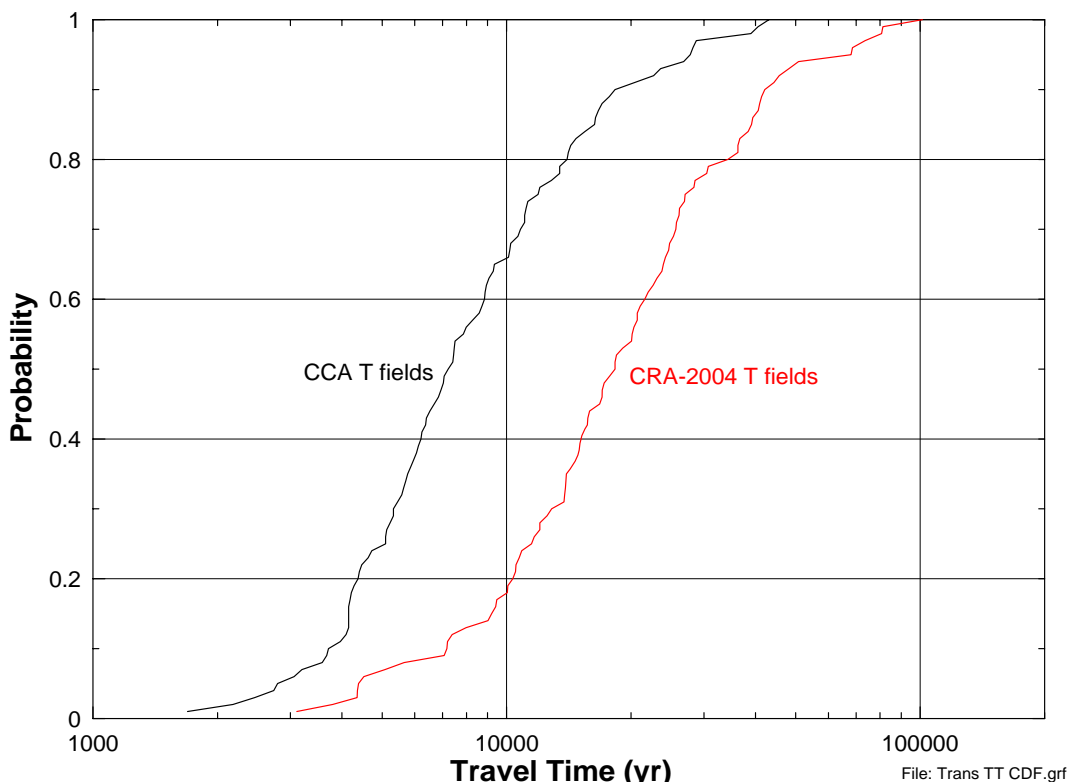
12 **Figure TFIELD-56. Travel-Time CDFs for Different Sets of T Fields**

13 that have RMSE values less than 2 m (7 ft) and transient phi values less than 2,000 m<sup>2</sup> (21,527  
 14 ft<sup>2</sup>). These 23 T fields all have steady-state-fit slopes greater than 0.88. This CDF generally  
 15 shows travel times similar to those of the other CDFs, except at the tails of the distribution which  
 16 are poorly defined because of the relatively small sample size. Thus, because all the CDFs  
 17 shown are similar, all 121 T fields meeting the steady-state-fit slope or RMSE criteria were  
 18 considered to be acceptably calibrated. The T fields that have been rejected are shown in reverse  
 19 type in Table TFIELD-11.

20 Because only 100 T fields were needed, the criteria were refined to eliminate more T fields.  
 21 Given that lower travel times provide a conservative (in terms of leading to increased solute  
 22 transport) way to discriminate among sets of T fields, the 100 T fields with RMSE values <5 m  
 (16 ft) and transient phi values <8,000 m<sup>2</sup> were selected for use in CRA-2004 calculations of

1 radionuclide transport through the Culebra because that set excluded the calibrated T field with  
 2 the longest travel time. These T fields are highlighted in ***bold italicized*** type in Table  
 3 TFIELD-11.

4 For comparison purposes, the CDF of travel times for these 100 T fields is plotted in Figure  
 5 TFIELD-57 with the CDF of travel times for the 100 transient-calibrated T fields used in the  
 6 CCA (Wallace 1996). Generally speaking, travel times are two to three times as long in the  
 7 CRA-2004 fields as in the CCA fields. Considering the degree of uncertainty involved in  
 8 characterizing a geologic medium on the scale of the T fields, a factor of two or three difference  
 9 in travel-time CDFs represents excellent agreement.



10  
 11 **Figure TFIELD-57. Travel-Time CDFs for CCA and CRA-2004 T Fields**

## 12 ***TFIELD-8.0 INVERSE MODELING RESULTS***

13 Some fit statistics (phi, RMSE, etc.) for the 121 T fields that were judged to be acceptably  
 14 calibrated were presented in Section 7.0 of this attachment. Visualizations of the T fields are  
 15 included in Annex A. Additional properties or characteristics of the T fields are given below.

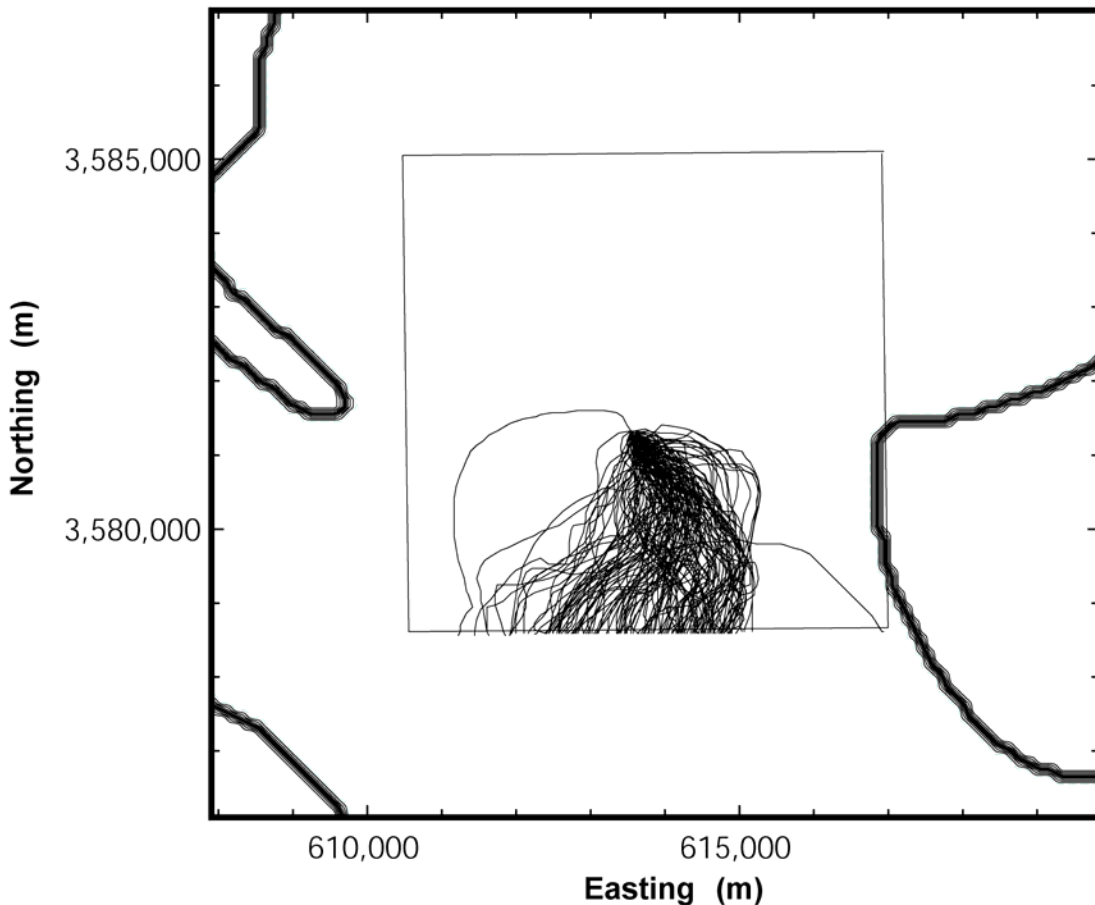
### 16 ***TFIELD-8.1 Particle Tracking***

17 Particle tracking was performed in the 121 calibrated T fields from a point above the center of  
 18 the WIPP disposal panels to both the LWB and the boundary of the model domain, as discussed  
 19 in Section 7.0 of this attachment. The locations of all the particle tracks are shown in Figures  
 20 TFIELD-58 and TFIELD-59. In both figures, the particle tracks are shown using only every 20<sup>th</sup>

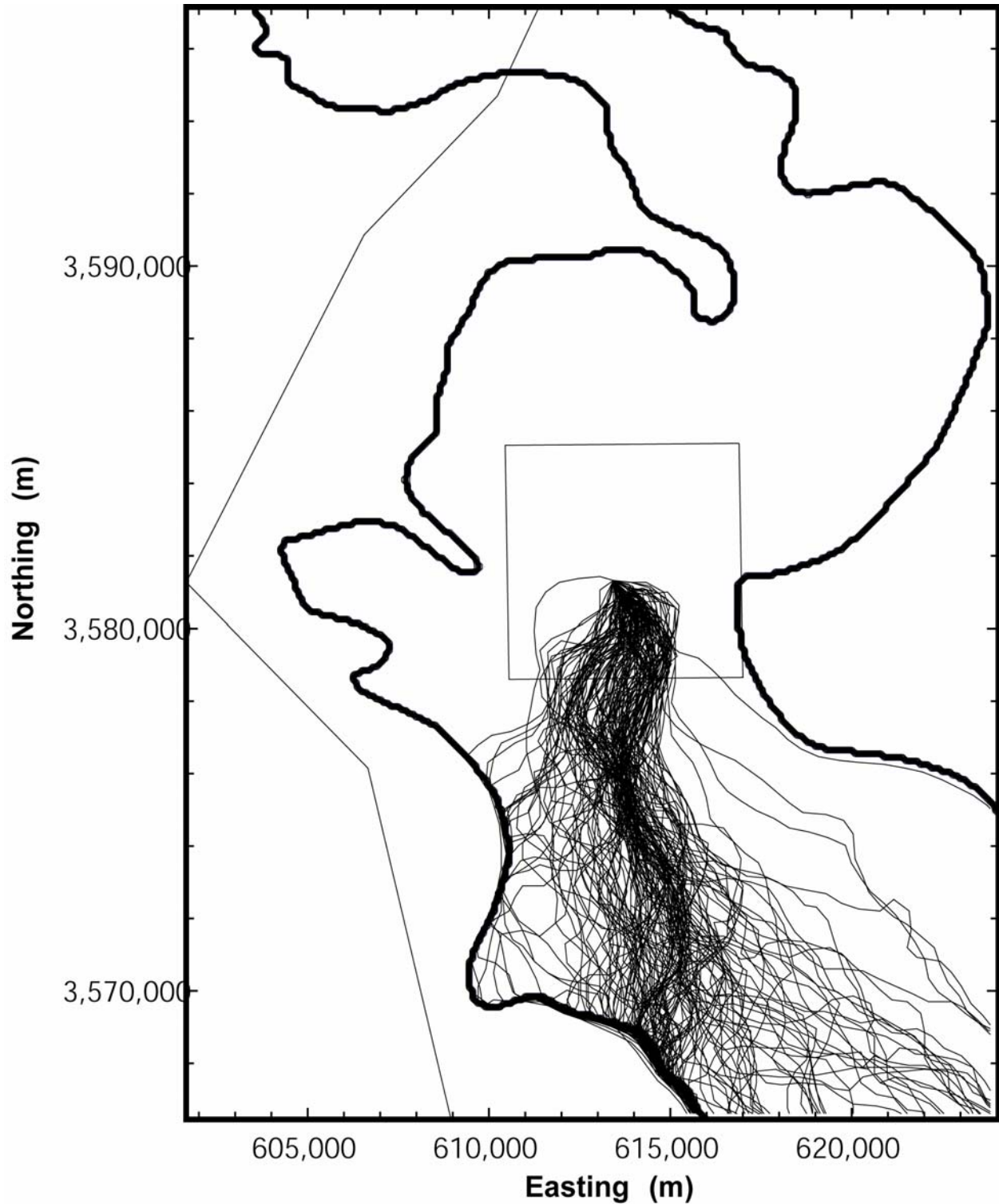
1 point along the track because of a limitation in the graphing software. This filtering leads to the  
 2 particle tracks appearing less smooth than they actually are. Figure TFIELD-58 shows a close-  
 3 up view of the particle tracks within the WIPP LWB. All of the particles exit the southern edge  
 4 of the LWB and the majority of the particles exit the LWB to the southeast of the release point,  
 5 although not as far to the east as the particle tracks for the CCA T fields showed (Ramsey et al.  
 6 1996, p. 49). Figure TFIELD-59 shows the particle tracks within the entire model domain. The  
 7 majority of the particles exit the domain nearly due south of the release point. The particles that  
 8 migrate to the west tend to travel along the boundary of the high-T zone. This result is due to the  
 9 large amount of groundwater flux within the high-T zone creating a streamline at the high-T  
 10 zone boundary.

11 ***TFIELD-8.2 Fit to Steady-State Heads***

12 Some information about how well the calibrated T fields matched the observed steady-state  
 13 heads is given in Sections 7.2.1 and 7.2.2 of this attachment. Additional information is shown in



14  
 15 **Figure TFIELD-58. All Particle Tracks Within the WIPP LWB. The bold lines show the**  
 16 **boundaries of the high-T (left side) and low-T (right side) zones.**



1

2 **Figure TFIELD-59. All Particle Tracks Within the Model Domain. The bold lines show**  
3 **the boundaries of the high-T (left) and low-T (right) zone boundaries. The no-flow and**  
4 **WIPP site boundaries are also shown.**



1 Figures TFIELD-60 and TFIELD-61. Figure TFIELD-60 shows a scatterplot of the modeled  
2 steady-state heads in the 121 calibrated T fields versus the measured heads. Also shown is a  
3 unit-slope line representing perfect agreement between the measured and modeled heads, and  
4 parallel lines showing a 5-m (16-ft) range on either side. Most modeled head values fall within  
5 the  $\pm 5$  m (16 ft) lines, except for the modeled heads for H-9b, the well with the lowest measured  
6 head. As discussed in Section 7.2.1 of this attachment, H-9b is the southernmost well in the  
7 model domain and the southern model boundary condition consistently caused the modeled H-9b  
8 head to be significantly lower than the measured head.

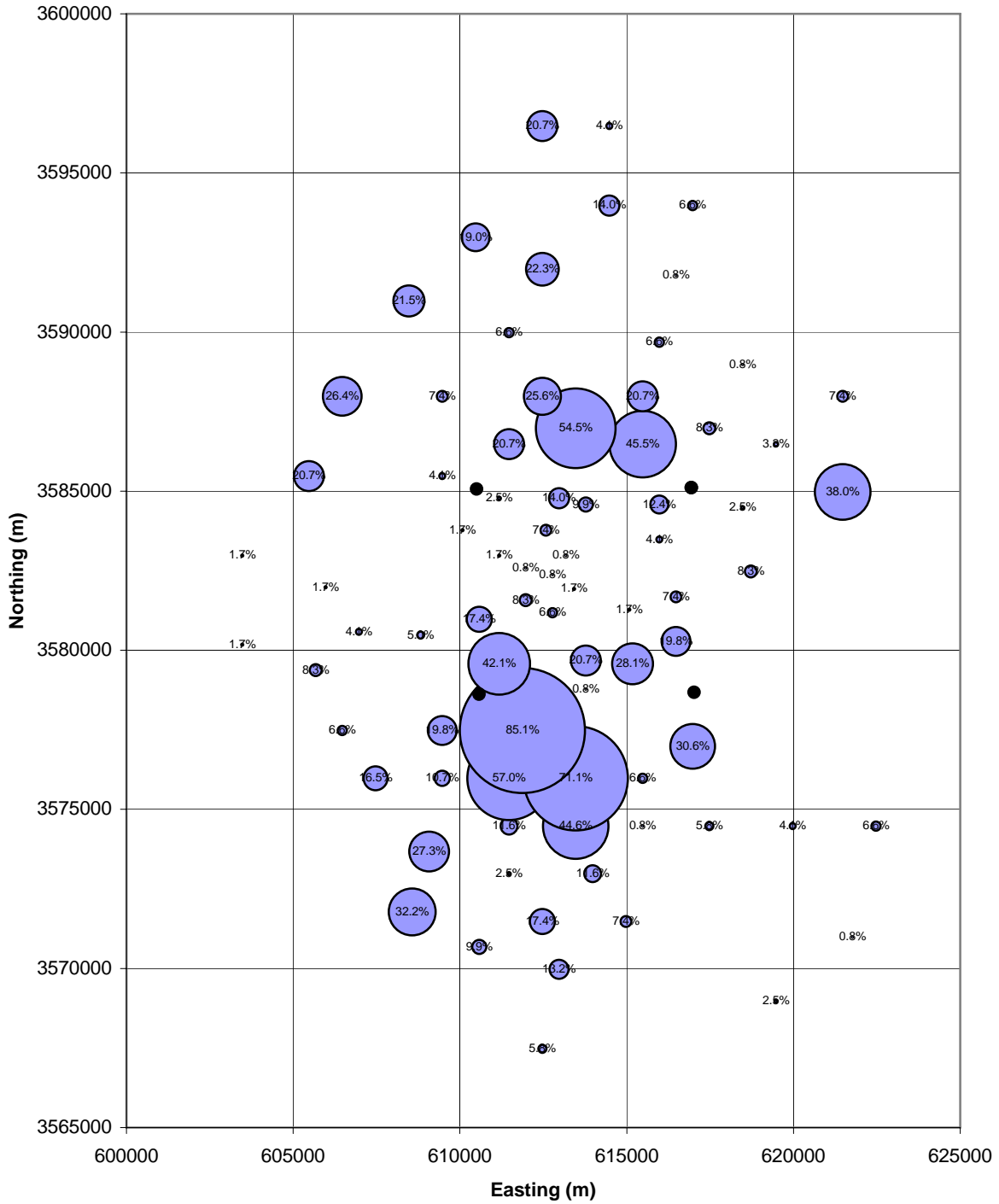
9 Figure TFIELD-61 shows a histogram of the differences between the modeled and measured  
10 heads. The majority of modeled head values more than 8 m (26 ft) lower than the measured  
11 values are associated with H-9b. Excluding the H-9b values, the histogram shows a normal  
12 distribution of errors with 48 percent of the modeled heads within 2 m (7 ft) of the measured  
13 heads, and 79 percent of the modeled heads within 4 m (13 ft) of the measured heads. The fit  
14 between measured and modeled steady-state heads could probably have been improved by  
15 allowing PEST to perform more calibration iterations but, as shown in Section 7.3 of this  
16 attachment, the travel-time distribution for the T fields would be unlikely to be affected.

### 17 ***TFIELD-8.3 Pilot-Point Sensitivity***

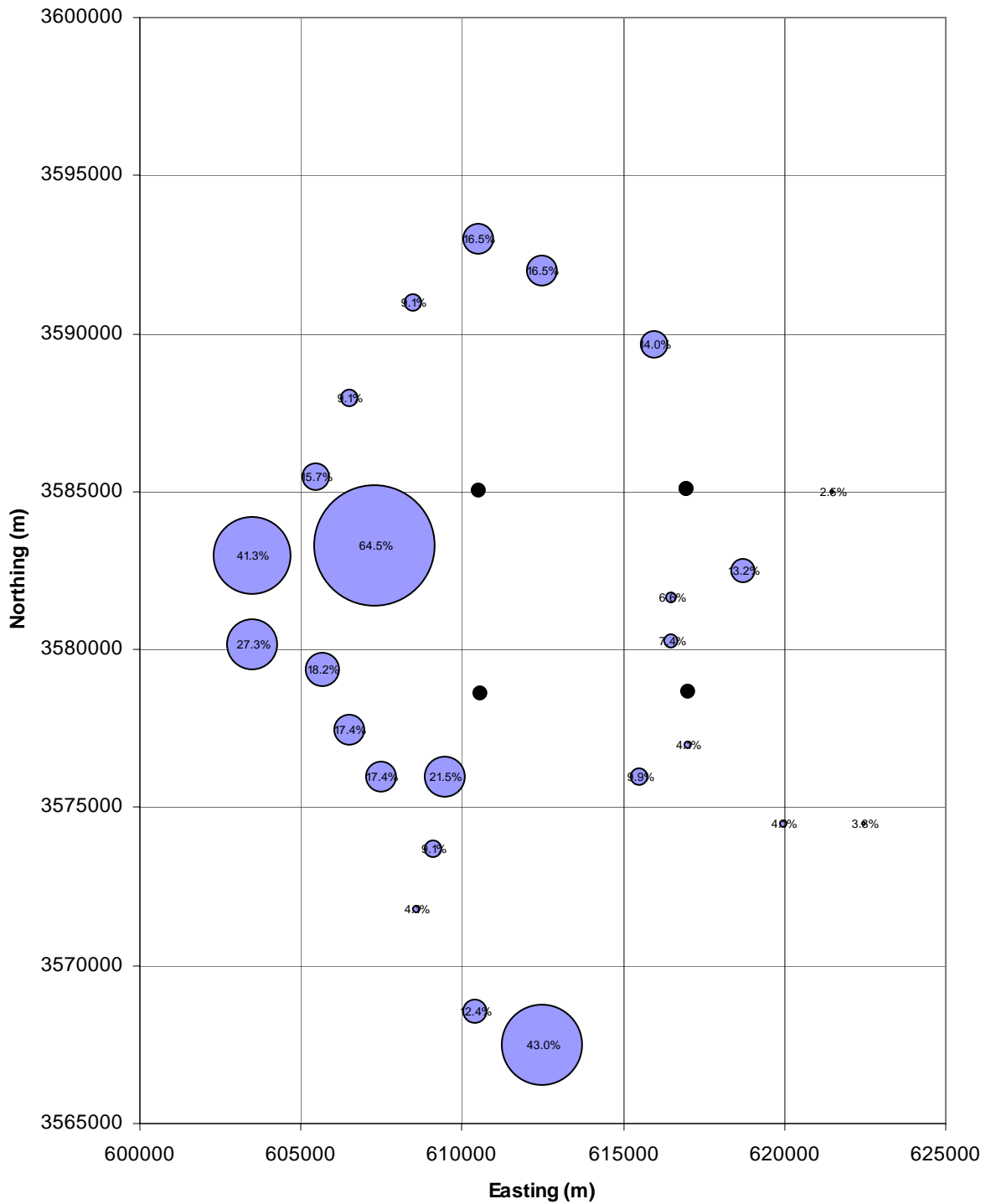
18 Transmissivities at each of the pilot points within the model domain were altered during the  
19 calibration process. The maximum allowable change was  $\pm$  three orders of magnitude in the  
20 middle region of the model domain and  $\pm$  one order of magnitude in the low-T (eastern) and  
21 high-T (western) regions of the model domain. Figures TFIELD-62 and TFIELD-63 show the  
22 percentage of calibrated T fields in which each pilot point hit the maximum and minimum  
23 possible value, respectively. The size of the bubble is proportional to the number of times the  
24 value hits one constraint or the other. Figure TFIELD-62 shows that the pilot points south of the  
25 western portion of the southern LWB were most likely to reach their maximum allowable values,  
26 indicating that the base T fields may have underestimated Ts in this area. Figure TFIELD-63  
27 shows that the pilot point placed in the inferred dissolution reentrant between P-14 and WIPP-25  
28 west of the LWB (see Figure TFIELD-38) was most likely to reach its minimum allowable  
29 value, indicating that this reentrant may not be as hydraulically significant as originally assumed.

### 30 ***TFIELD-8.4 Ensemble Average T Field***

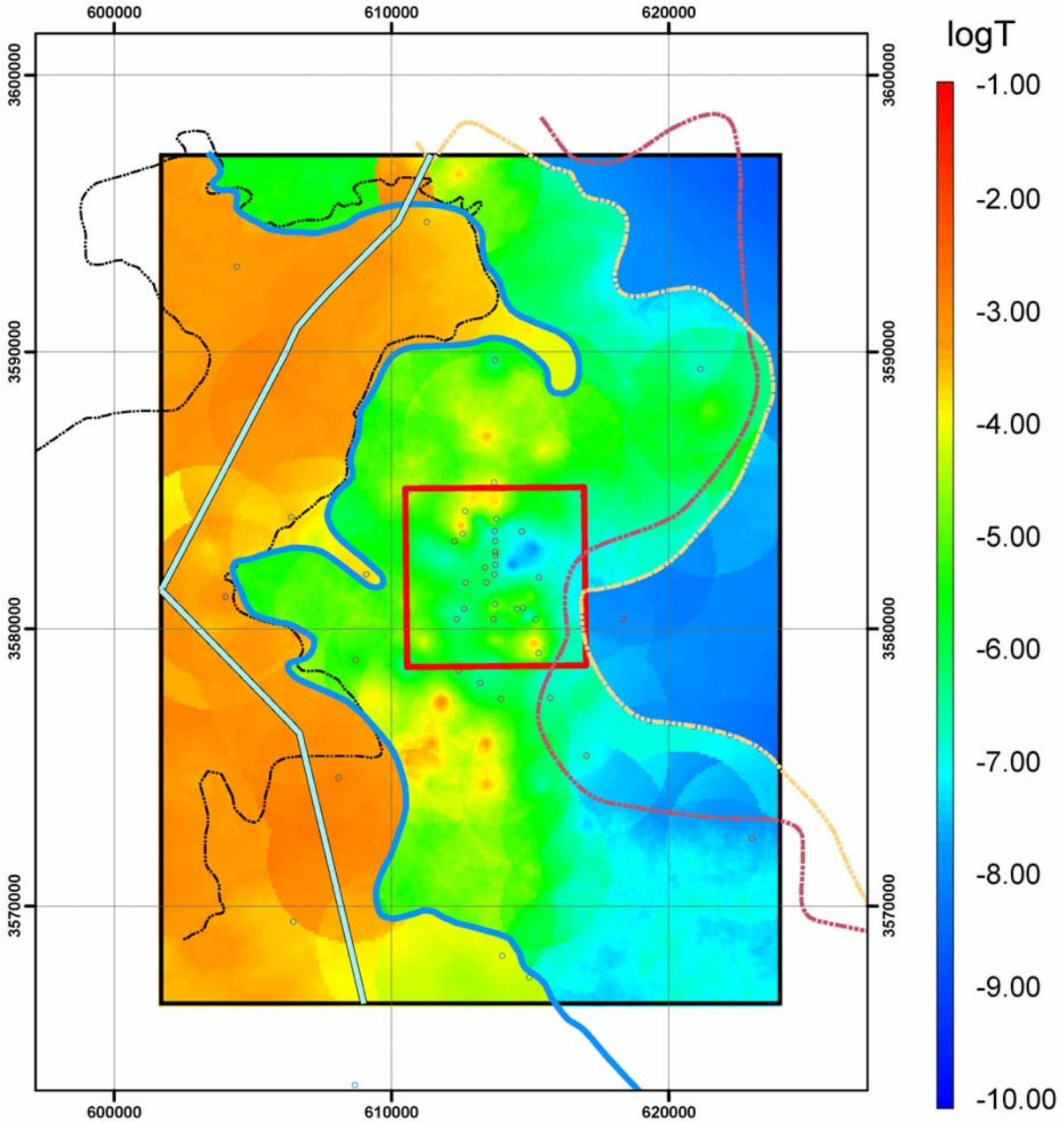
31 The 121 T fields that were acceptably calibrated can be combined into an ensemble average T  
32 field showing the average properties of the T fields (Figure TFIELD-64). The averaging is  
33 performed on a cell-by-cell basis, taking the arithmetic mean of the 121 T values assigned to  
34 each cell. Figure TFIELD-65 shows a close-up view of the ensemble average of the 100 T fields  
35 used for subsequent calculations in the area surrounding the WIPP site, using a different color  
36 scale with T values “binned” by order of magnitude for clarity. This figure does not show a  
37 continuous north-south high-T zone exiting the southeastern portion of the WIPP site, as was  
38 present in the ensemble average T field provided in CCA Appendix TFIELD (Figure 30). It also  
39 shows higher Ts in the southwestern portion of the WIPP site than were present in the CCA  
40 ensemble average field. These differences explain why the travel paths in the CRA-2004 T  
41 fields (Figure TFIELD-58) take a more westerly course, on average, than those in the CCA T



1  
 2 **Figure TFIELD-60. Percentage of T Fields in which Pilot Points Hit Maximum Allowable**  
 3 **Values. Corners of WIPP LWB are shown by unlabeled black dots.**



1  
 2 **Figure TFIELD-61. Percentage of T Fields in which Pilot Points Hit Minimum Allowable**  
 3 **Values. Corners of WIPP LWB are shown by unlabeled black dots.**  
 4



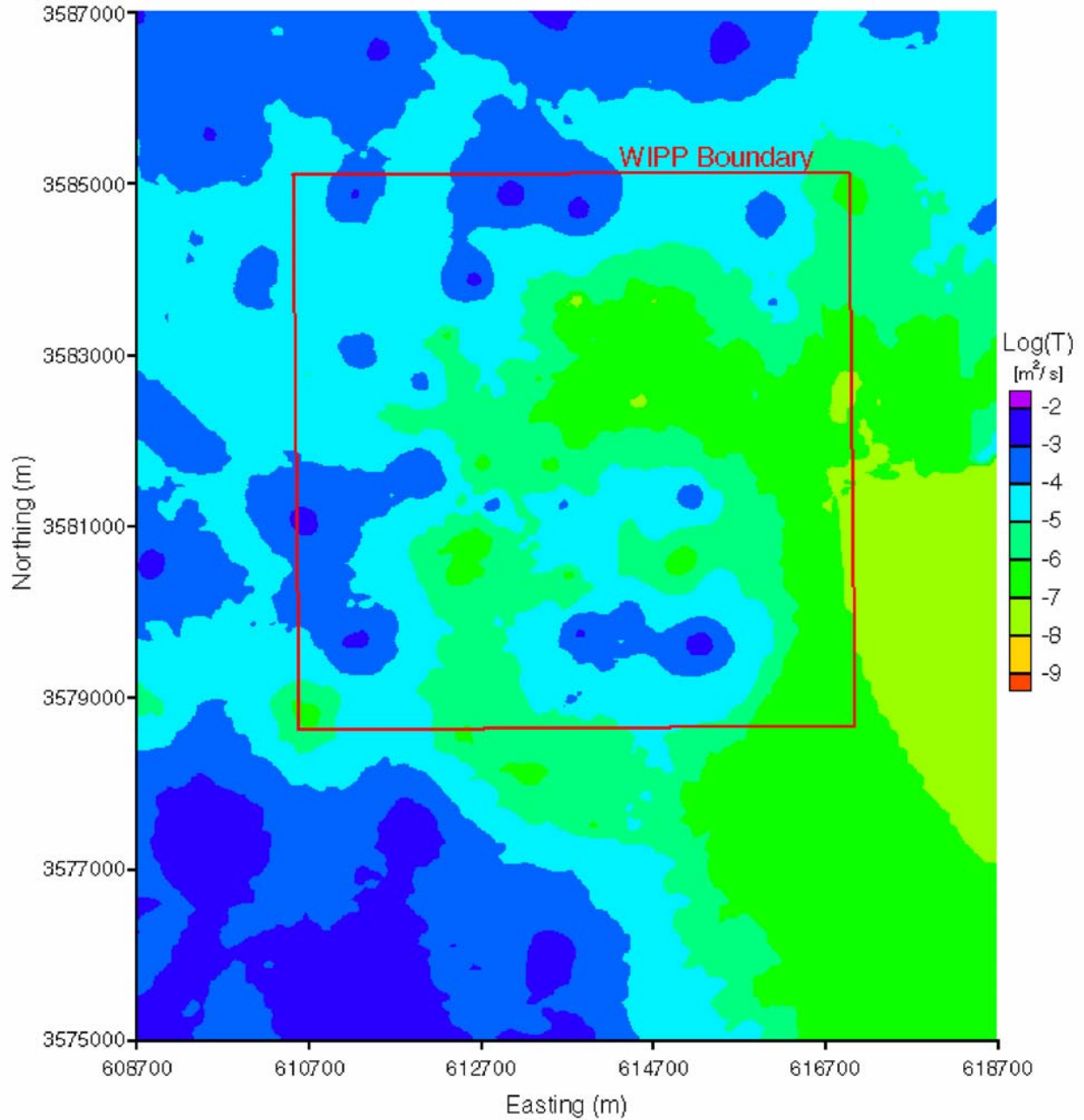
**Explanation**

- |                              |                      |
|------------------------------|----------------------|
| <b>Well (transmissivity)</b> | ----- Nash Draw      |
| ○ Low                        | — Salado Dissolution |
| ○ High                       | □ WIPP Site          |
| ----- Salt Margin m3/h3      | — No Flow Boundary   |
| ----- Salt Margin m2/h2      |                      |



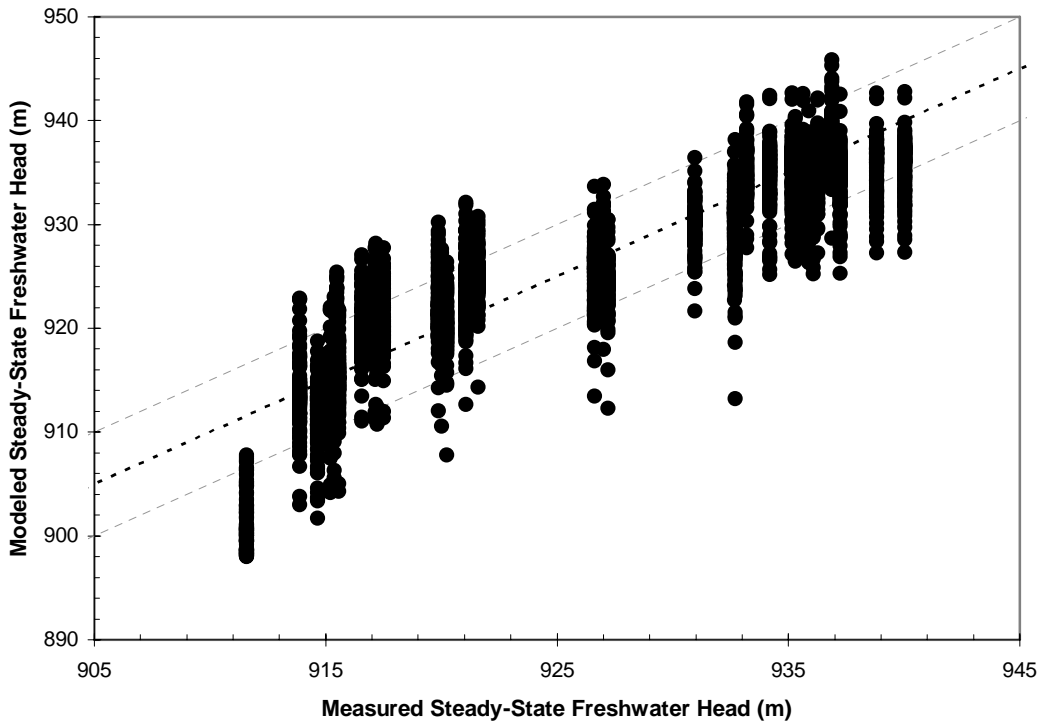
1  
2

**Figure TFIELD-62. Ensemble Average of 121 Calibrated T Fields**



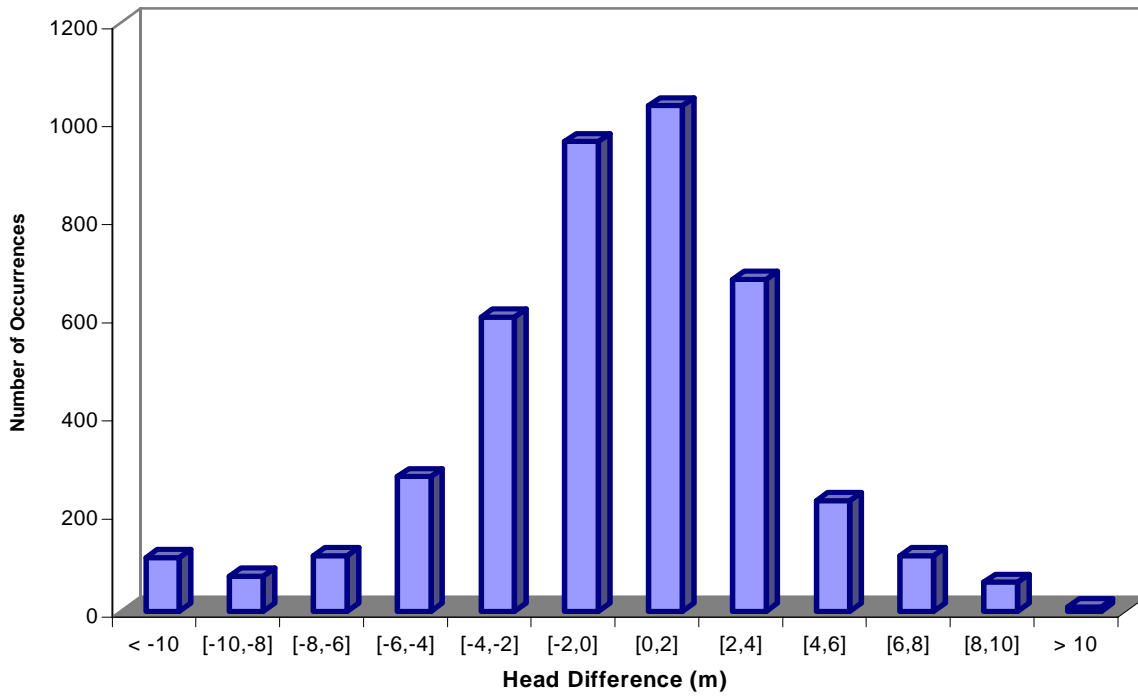
1

2 **Figure TFIELD-63. Close-Up View of the Ensemble Average T Field Near the WIPP Site.**  
3 **Note the different log<sub>10</sub> color scale from Figure TFIELD-62.**



1  
2  
3

**Figure TFIELD-64. Scatterplot of Measured Versus Modeled Steady-State Heads**



4  
5  
6

**Figure TFIELD-65. Histogram of Differences Between Measured and Modeled Steady-State Heads**

1 fields, and why the CRA-2004 travel times are longer than the CCA travel times (Figure  
2 TFIELD-57).

### 3 ***TFIELD-9.0* MODIFICATION OF T FIELDS FOR MINING SCENARIOS**

4 The WIPP site lies within the Carlsbad mining district of southeastern New Mexico. Potash mining  
5 in the WIPP area involves resource extraction below the Culebra in the underlying McNutt potash  
6 zone of the Salado. In the future, potash mining is expected to occur in all areas where  
7 economically extractable ore is present, both outside and inside the WIPP LWB. It is hypothesized  
8 that mining of potash leads to subsidence and fracturing of the Culebra, resulting in increased  
9 Culebra T. This increase in T may change the regional groundwater flow pattern in the Culebra  
10 and affect the transport of any radionuclides entering the Culebra from the WIPP repository.

11 The EPA (1996, p. 5242) guidance for how the potential effects of future mining should be  
12 considered in WIPP PA follows:

13 40 CFR §194.32, Scope of performance assessments.

- 14 (a) Performance assessments shall consider natural processes and events, mining, deep drilling,  
15 and shallow drilling that may affect the disposal system during the regulatory time frame.
- 16 (b) Assessments of mining effects may be limited to changes in the hydraulic conductivity of the  
17 hydrogeologic units of the disposal system from excavation mining for natural resources.  
18 Mining shall be assumed to occur with a one in 100 probability in each century of the  
19 regulatory time frame. Performance assessments shall assume that mineral deposits of those  
20 resources, similar in quality and type to those resources currently extracted from the Delaware  
21 Basin, will be completely removed from the controlled area during the century in which  
22 such mining is randomly calculated to occur. Complete removal of such mineral resources  
23 shall be assumed to occur only once during the regulatory time frame.
- 24 (c) Performance assessments shall include an analysis of the effects on the disposal system of any  
25 activities that occur in the vicinity of the disposal system prior to disposal and are expected to  
26 occur in the vicinity of the disposal system soon after disposal. Such activities shall include,  
27 but shall not be limited to, existing boreholes and the development of any existing leases that  
28 can reasonably be expected to be developed in the near future, including boreholes and leases  
29 that may be used for fluid injection activities.

30 The EPA (1996, p. 5229) further states:

31 In order to consider the effects of mining in performance assessments, DOE may use the location-  
32 specific values of hydraulic conductivity, established for the different spatial locations within the  
33 Culebra dolomite, and treat them as sampled parameters with each having a range of values  
34 varying between unchanged and increased 1,000-fold relative to the value that would exist in the  
35 absence of mining.

36 Accordingly, for PA purposes, the DOE assumes that all economically extractable potash is  
37 mined outside of the WIPP LWB during the 100 years after closure of the WIPP repository  
38 during which active institutional control of the site is maintained. Following that 100-year  
39 period, the DOE assumes there is a one in 100 probability that the potash within the LWB will be  
40 mined during any given century. Therefore, all PA calculations of transport of radionuclides  
41 released to the Culebra through inadvertent human intrusion of the repository assume that all  
42 potash outside the LWB has already been mined (the “partial-mining” scenario) by the time the

1 intrusion occurs. The “full-mining” scenario is invoked when the sampled time of human  
2 intrusion is coincident with or later than the sampled time of mining within the LWB. Under  
3 both scenarios, the hydraulic conductivity (or T) of the Culebra is assumed to be increased by a  
4 random factor between one and 1,000 in the areas affected by mining. The process by which the  
5 calibrated Culebra T fields were modified to account for the effects of mining, and the  
6 characteristics of the resulting modified T fields, are discussed below.

### 7 ***TFIELD-9.1 Determination of Potential Mining Areas***

8 Figure TFIELD-66 shows current potash mines and economically recoverable resources (reserves)  
9 in the known potash lease area around the WIPP site, which are the areas where subsidence  
10 might occur in the future. The map is based on the BLM (1993) map “Preliminary Map Showing  
11 Distribution of Potash Resources, Carlsbad Mining District, Eddy and Lea Counties, New  
12 Mexico.” Whereas the BLM map shows all reserves, Figure TFIELD-66 shows only reserves  
13 that are within existing leases and that are outside the one-quarter to one-half mile (402 to 805  
14 m) exclusion zones around oil and gas wells. Potash reserves outside the current leases will most  
15 likely never be mined because active oil and gas exploration is now underway in those areas.

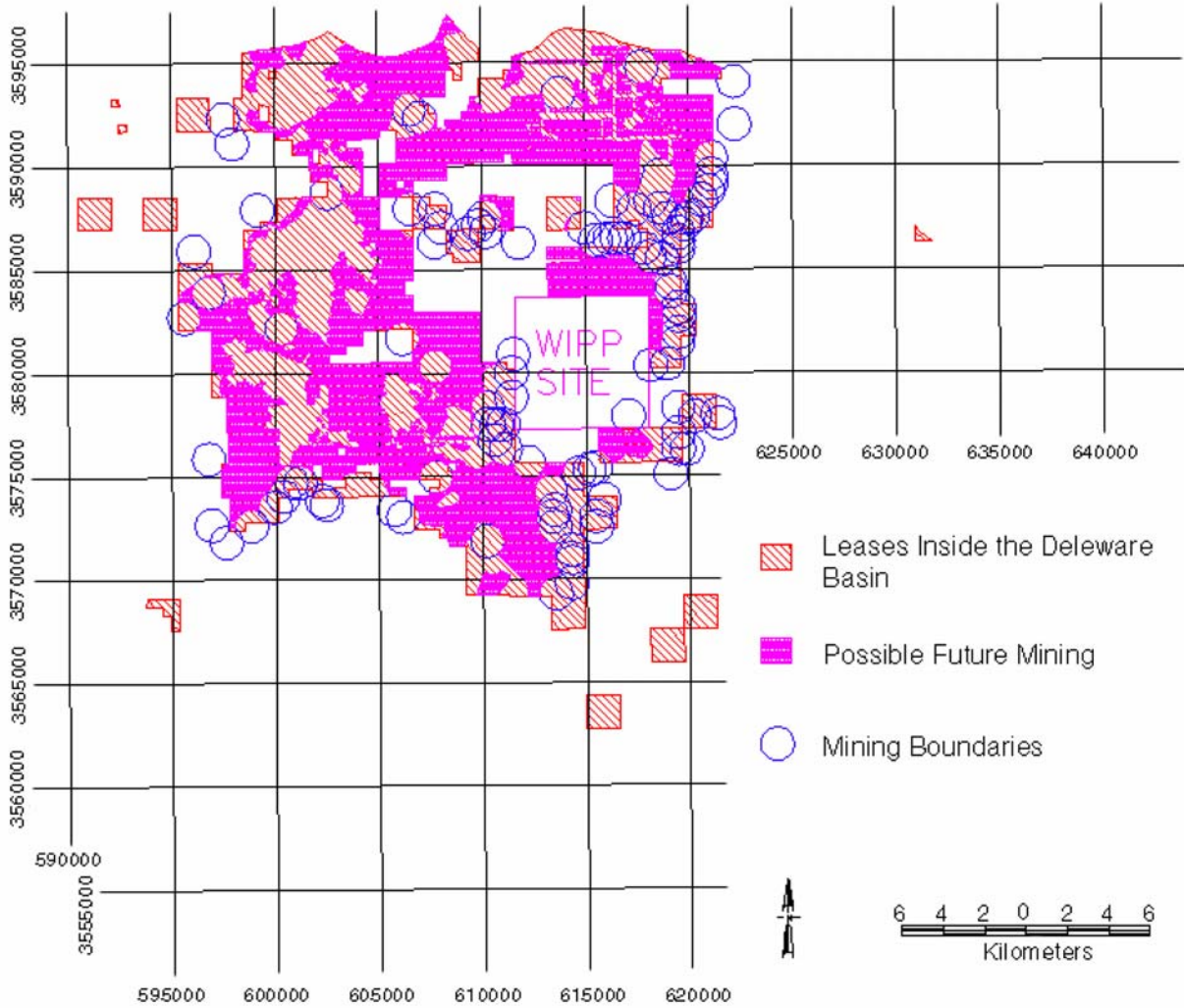
16 This map is periodically updated as part of the Delaware Basin Drilling Surveillance Program. It  
17 also shows the locations of petroleum industry boreholes in the vicinity. The current version of  
18 the map differs from the one used for the CCA calculations in that several areas north of the  
19 LWB have been ruled out as potential mining areas in the updated version due to recent oil and  
20 gas drilling in those areas. Figure TFIELD-67 shows the estimated extent of economically  
21 extractable potash within the WIPP LWB.

22 Because the potash mining horizon is located in the Salado Formation, below the Culebra, the  
23 areas in the Culebra that might be disturbed by the mining activities are larger than shown on  
24 Figures TFIELD-66 and TFIELD-67 due to angle-of-draw effects associated with subsidence.  
25 The rationale for determining the extent of these effects is described in Wallace (1996) with the  
26 final conclusion stating that an additional 253-m (830-ft)-wide “collar” was to be added to the  
27 mining-impacted areas to approximate a 45-degree angle of draw. For the current T fields, a  
28 buffer of three cell widths (300 m [984 ft]) was manually digitized and added to the mining  
29 zones. This new delineation was then compared to the CCA model mining zones to make sure  
30 there were no significant differences outside of those that can be explained by different gridding  
31 of the two model domains and the addition of new data (Figure TFIELD-68). The most notable  
32 difference between the two versions is that the area of potential future mining along the  
33 northeastern boundary of the LWB is no longer directly connected to the northern boundary of  
34 the model domain, which would be expected to decrease flow to the WIPP site.

### 35 ***TFIELD-9.2 Scaling of Transmissivity***

36 For each of the final 100 T fields selected as described in Section 7.4 of this attachment, a  
37 random transmissivity multiplier between 1 and 1,000 was assigned using Latin hypercube  
38 sampling (LHS) (*Long 2004*). That multiplier was then applied to the modeled T values in the  
39 mining-affected areas shown in Figure TFIELD-68 outside of the WIPP LWB to create a partial-  
40 mining T field, and to the modeled T values in mining-affected areas both inside and outside the  
41 LWB to create a full-mining T field. LHS was performed three times to provide three replicates  
42 of 100 full-mining and 100 partial-mining T fields. The purpose of using three replicates is to



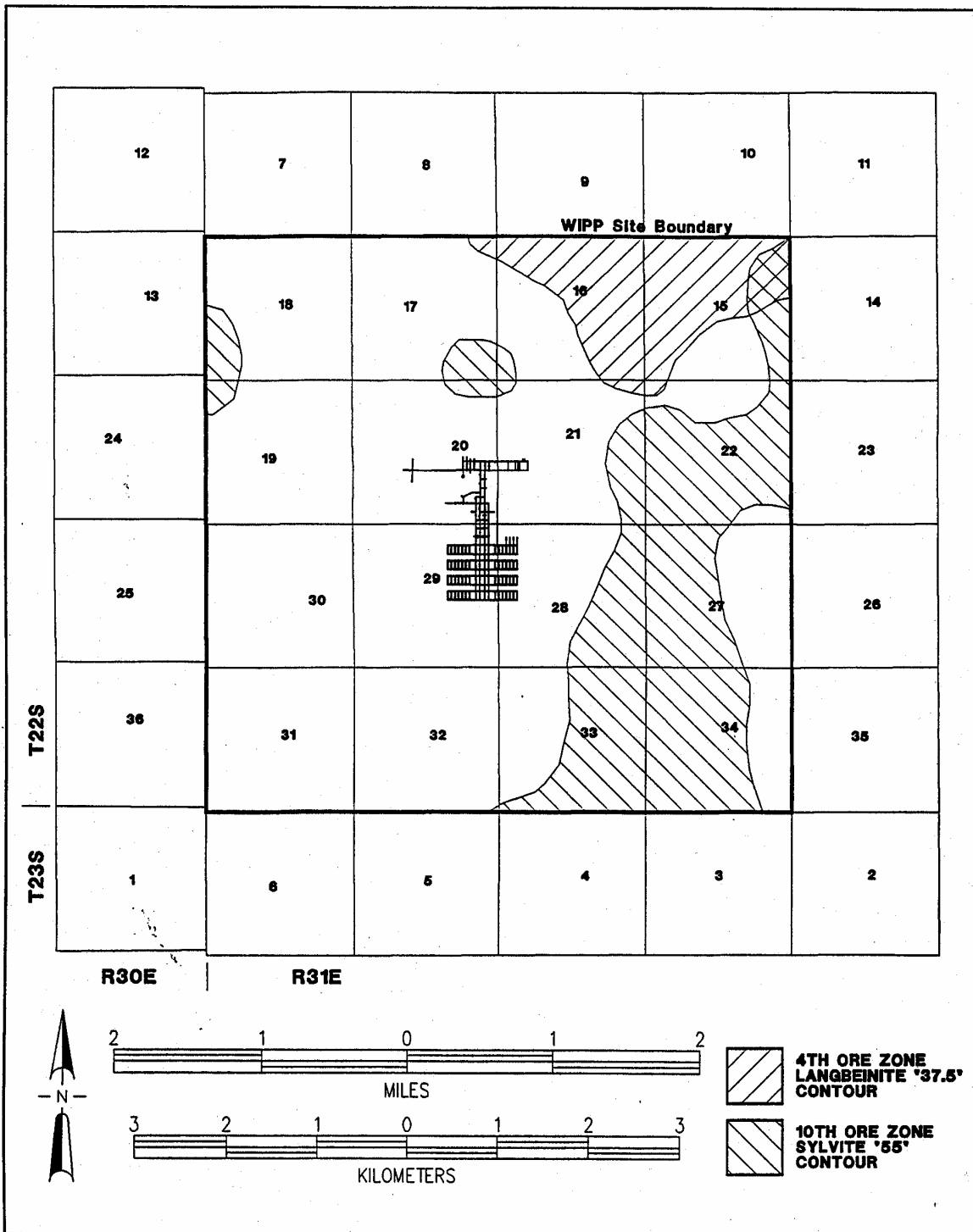


1  
2 **Figure TFIELD-66. Leased Potash Resources Near the WIPP Site**

3 demonstrate that the LHS has adequately captured the uncertainty in the T fields. The  
4 transmissivity multipliers applied to each field for the three replicates are shown in Table  
5 TFIELD-12.

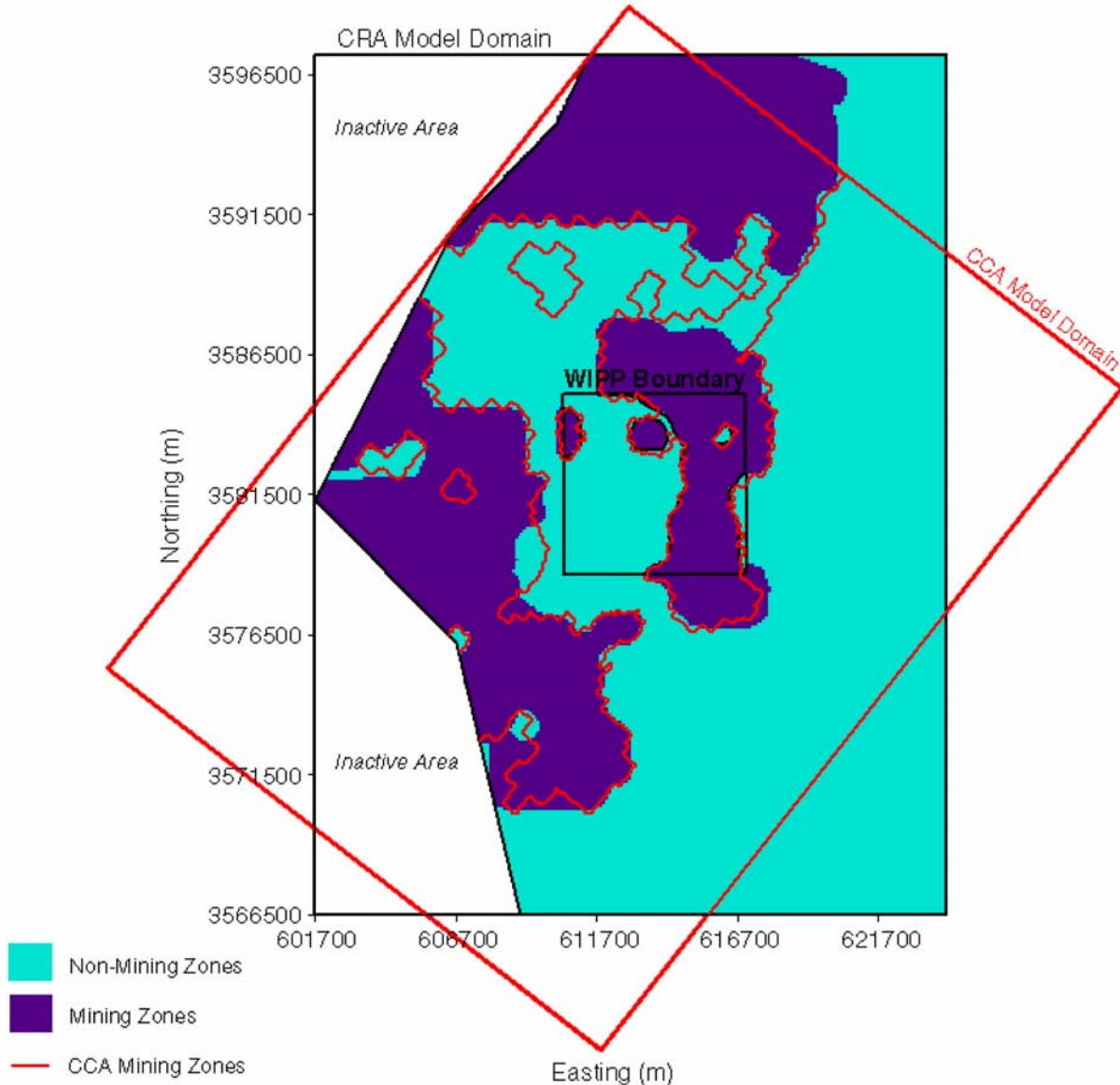
6 ***TFIELD-9.3 Forward Runs***

7 A forward steady-state flow model was run for each of the 100 new T fields under each mining  
8 scenario (full and partial) for the three replicates of transmissivity multipliers, resulting in 600  
9 simulations. Particle tracking was performed using DTRKMF on the modified flow fields to  
10 determine the flow path and groundwater travel time from a point above the center of the WIPP  
11 disposal panels to the LWB. A CDF was produced for each mining scenario (as well as an  
12 undisturbed scenario) that describes the probability of a conservative tracer reaching the LWB at  
13 a given time.



1

2 **Figure TFIELD-67. Potential Potash Distribution Within the WIPP LWB. The repository**  
 3 **excavations are shown in the center.**



1  
2 **Figure TFIELD-68. Comparison of CRA-2004 and CCA Areas Affected by Mining**

3 As was done for the CCA, it was assumed that mining impacts would not significantly change  
4 the boundary conditions used in T-field calibration. Potash mining has already occurred along  
5 the northern boundary of the model domain, and the western model boundary is in Nash Draw  
6 where subsidence and fracturing of the Culebra are already incorporated in the model.

7 ***TFIELD-9.4 Results***

8 ***TFIELD-9.4.1 Travel Times***

9 Figure TFIELD-69 shows CDFs of travel time for the unmodified T fields and for the  
10 Replicate 1 full- and partial-mining T fields. The partial-mining travel times are consistently  
11 longer than the no-mining travel times. The distribution of travel times for the full-mining case

**Table TFIELD-12. T-Field Transmissivity Multipliers for Mining Scenarios**

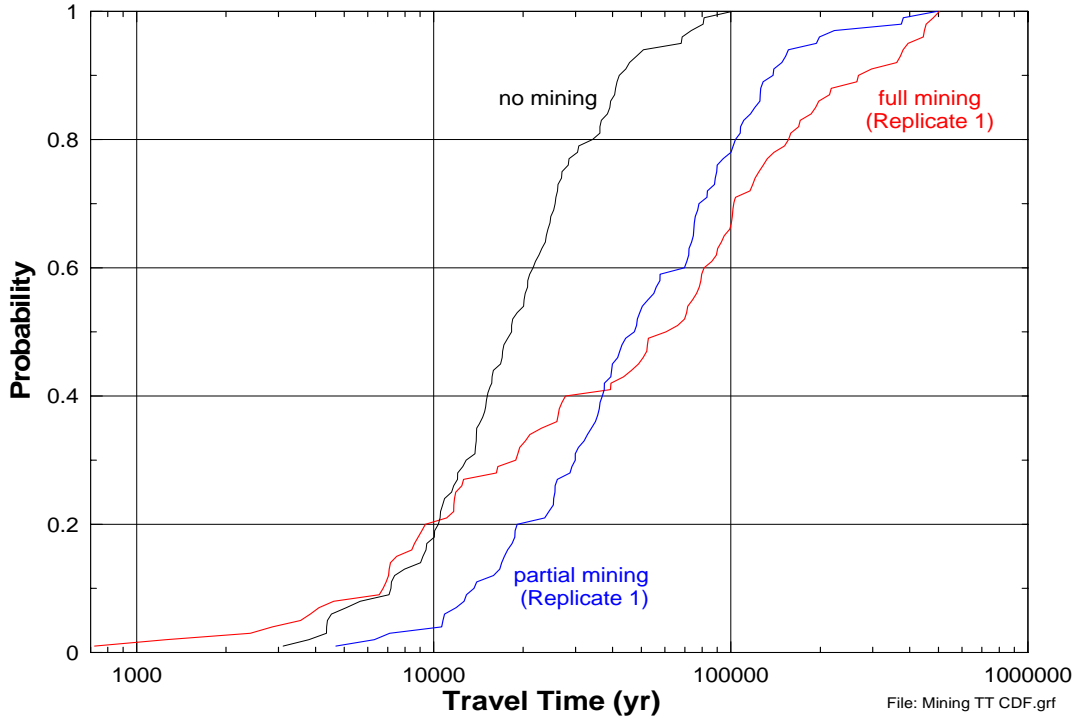
T Field	Replicate 1 Multiplier	Replicate 2 Multiplier	Replicate 3 Multiplier	T Field	Replicate 1 Multiplier	Replicate 2 Multiplier	Replicate 3 Multiplier
d01r02	905.50	32.85	13.54	d09r08	66.07	339.80	327.30
d01r04	508.40	345.10	202.20	d09r09	375.70	806.30	374.20
d01r07	340.30	996.50	936.30	d09r10	521.10	906.90	24.83
d01r10	615.20	828.20	391.80	d10r02	181.60	274.60	651.90
d02r02	575.30	579.30	306.80	d10r03	298.50	796.60	816.70
d03r01	104.00	760.50	955.80	d10r04	705.30	364.70	518.20
d03r03	94.06	514.90	77.79	d10r06	84.20	819.40	690.80
d03r06	913.30	187.60	238.40	d10r07	627.30	728.60	551.20
d03r07	630.50	567.10	725.20	d10r08	403.20	414.80	670.30
d03r08	208.90	475.90	85.67	d10r09	464.20	649.90	885.40
d03r09	769.30	750.00	647.80	d10r10	821.40	607.80	925.70
d04r01	130.20	630.30	478.70	d11r01	307.60	895.10	492.90
d04r02	351.90	453.30	996.70	d11r02	236.50	918.30	364.50
d04r03	46.87	310.90	123.90	d11r06	249.90	159.70	5.43
d04r04	194.60	487.90	217.30	d11r07	543.50	86.78	966.70
d04r05	806.90	923.80	138.30	d11r08	18.75	16.92	973.80
d04r06	264.40	584.00	835.30	d11r09	215.40	618.30	576.30
d04r07	931.50	733.90	802.00	d11r10	73.60	168.90	403.20
d04r08	897.90	51.08	96.80	d12r01	317.40	683.30	756.20
d04r10	32.56	256.50	34.02	d12r02	958.60	204.90	598.10
d05r03	394.10	108.30	159.00	d12r03	686.00	322.00	333.80
d05r07	998.20	535.90	145.50	d12r05	860.70	637.50	589.70
d06r02	790.00	679.40	826.70	d12r06	363.80	359.00	56.05
d06r03	384.10	171.20	261.20	d12r07	660.40	434.90	463.10
d06r04	258.50	860.00	293.90	d12r08	940.20	708.20	312.10
d06r05	432.50	754.10	257.60	d12r09	132.50	464.10	794.60
d06r06	10.02	653.20	172.50	d13r01	983.00	971.30	901.70
d06r07	514.10	221.50	915.60	d13r02	672.80	144.50	224.80
d06r10	282.90	70.11	861.40	d13r03	643.20	849.00	415.20
d07r01	927.30	694.20	625.20	d13r05	425.80	118.60	688.00
d07r02	691.30	864.90	737.80	d13r06	961.10	785.90	385.40
d07r05	738.40	775.30	241.60	d13r07	346.10	282.90	711.40
d07r06	450.20	591.70	548.70	d13r08	838.60	78.26	64.98
d07r07	609.60	447.20	841.00	d13r09	491.00	8.68	458.00
d07r08	557.70	942.30	349.00	d21r01	755.40	307.30	632.40
d07r09	538.60	98.94	285.00	d21r02	172.60	396.20	614.80
d07r10	713.60	379.60	187.30	d21r03	591.50	422.30	45.61

**Table TFIELD-12. T-Field Transmissivity Multipliers for Mining Scenarios  
(Continued)**

T Field	Replicate 1 Multiplier	Replicate 2 Multiplier	Replicate 3 Multiplier	T Field	Replicate 1 Multiplier	Replicate 2 Multiplier	Replicate 3 Multiplier
d08r01	849.30	408.40	194.00	d21r04	322.70	715.50	276.80
d08r02	569.70	989.10	893.90	d21r05	855.70	870.90	105.80
d08r03	419.50	43.16	356.30	d21r06	272.00	501.20	984.40
d08r04	160.00	834.00	857.00	d21r07	652.50	296.70	940.20
d08r05	971.90	881.10	671.60	d21r10	790.50	212.70	562.50
d08r06	118.80	558.90	743.20	d22r02	163.20	527.50	870.60
d08r07	741.30	130.20	706.70	d22r03	812.70	264.30	534.50
d09r02	729.70	497.00	429.30	d22r04	144.70	140.70	526.30
d09r03	483.00	197.30	168.20	d22r06	26.04	962.70	111.70
d09r04	580.60	661.30	766.40	d22r07	870.30	548.10	609.10
d09r05	228.50	240.90	481.90	d22r08	773.60	235.30	771.70
d09r06	474.10	383.50	449.10	d22r09	53.04	937.70	784.10
d09r07	887.20	952.10	503.30	d22r10	460.40	24.35	434.60

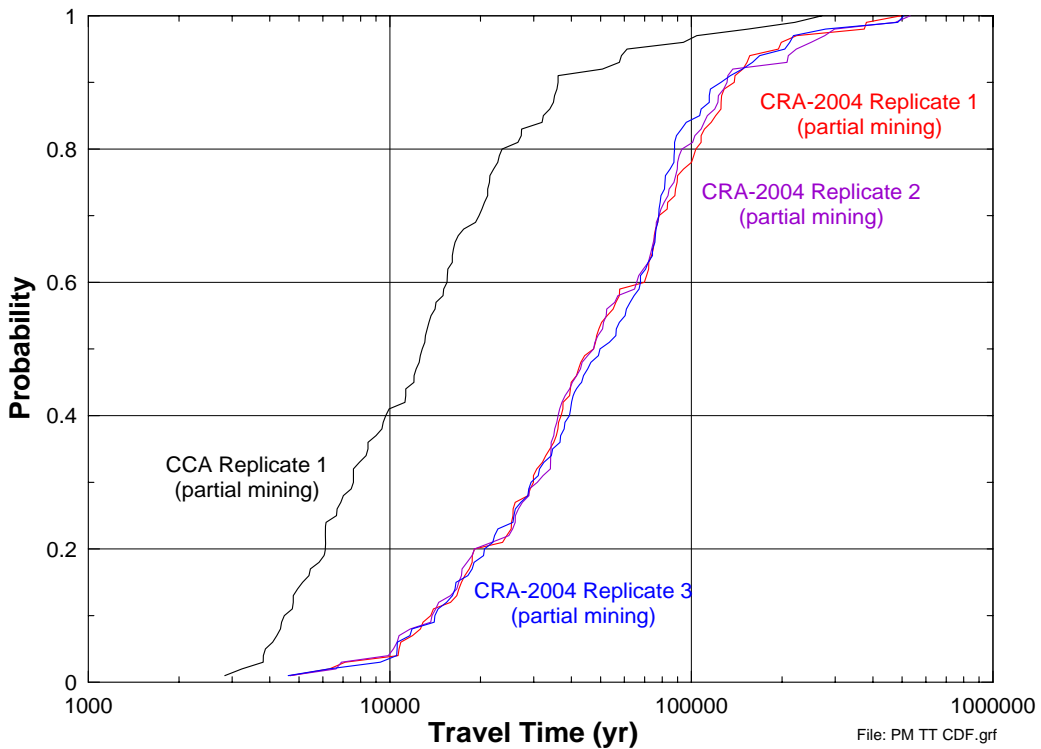
1 is much wider than for the other two cases; some of the full-mining travel times are shorter than  
2 the no-mining times, but most are considerably longer. The median travel times across all three  
3 replicates for the full- and partial-mining scenarios are approximately 3.6 and 2.6 times greater,  
4 respectively, than for the non-mining scenario. Figures TFIELD-70 and TFIELD-71 compare  
5 the CDFs of travel time for all three replicates of the partial- and full-mining cases, respectively,  
6 to the Replicate 1 results from the CCA T fields (Wallace 1996). These plots show, first, that all  
7 three CRA-2004 replicates provided very similar results and, second, that the new travel times  
8 are consistently longer than the CCA travel times. The primary reason for this difference is  
9 probably the absence in the CRA-2004 T fields of the direct, high-T connection between the  
10 WIPP site and the northern model boundary that was present in the CCA T fields and that  
11 provided a source of water to the Culebra within the LWB. As discussed in Section 9.1 of this  
12 attachment, this difference occurs because recent oil and gas exploratory drilling has precluded  
13 potash mining a few kilometers northeast of the LWB (see Figure TFIELD-66).

14 Given the increase in transmissivity due to mining, the increase in travel time may seem counter-  
15 intuitive. However, upon examination of the head contours and flow patterns of the mining  
16 cases, the high-T areas corresponding to the mining zones create preferential pathways through  
17 the system. Figure TFIELD-72 shows the normalized velocity in each cell for the  
18 T field/replicate averaged case for the full-mining scenario. The normalized velocity is the  
19 velocity magnitude in each cell divided by the maximum velocity magnitude across the domain.  
20 Since the velocity magnitudes are highly skewed, the color bands for Figure TFIELD-72 are  
21 nonuniformly scaled at the high end (i.e., a wider range of velocity magnitudes is used to  
22 designate the orange and red bands). This allows for a better qualitative comparison of the  
23 spatial distribution of high and low velocities. "T field/replicate averaged" means the T value for



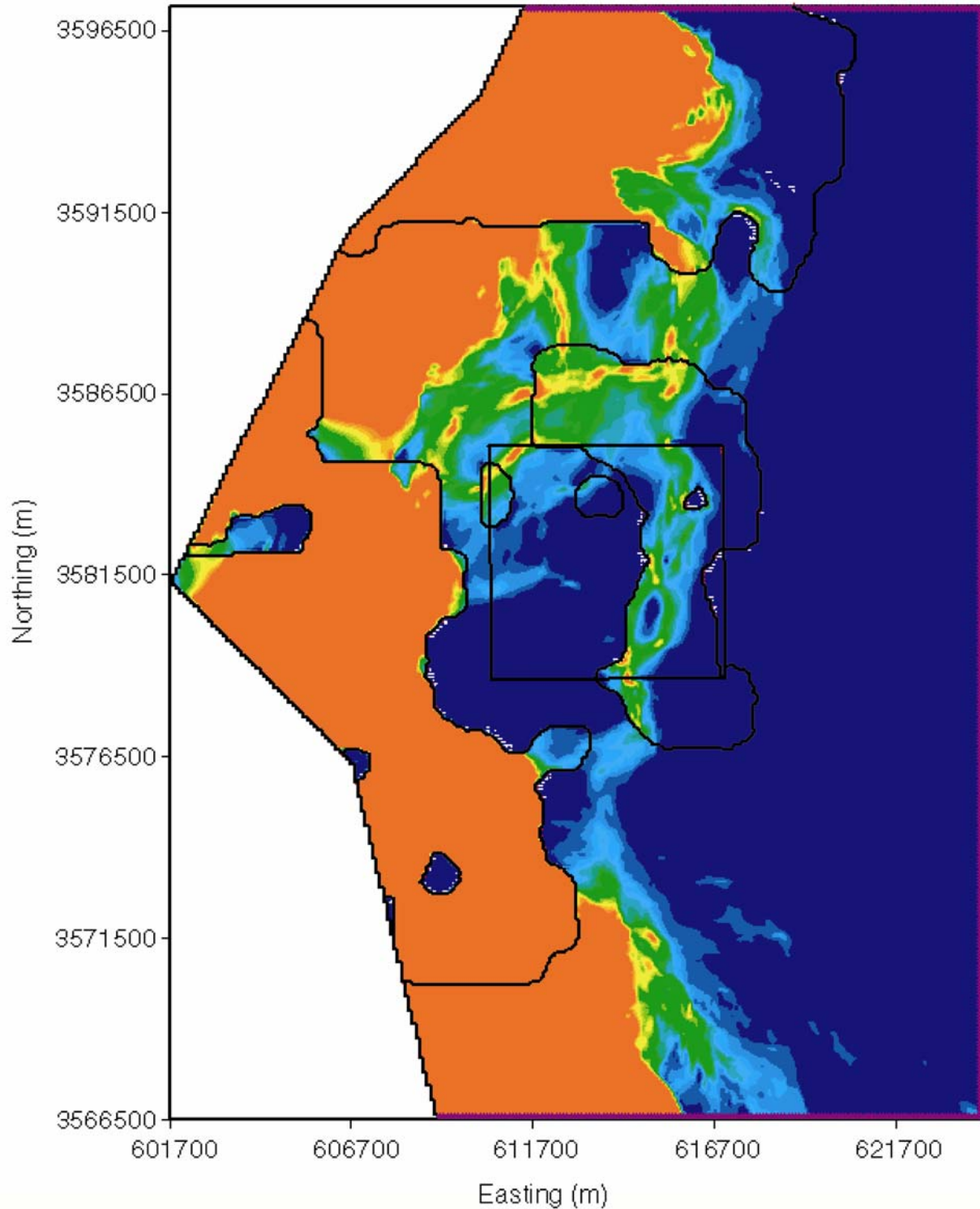
1

2 **Figure TFIELD-69. CDFs of Travel Times for the Full-, Partial-, and No-Mining Scenarios**



3

4 **Figure TFIELD-70. CDFs of Partial-Mining Travel Times for Three CRA-2004 Replicates**  
 5 **and One CCA Replicate**



1  
2 **Figure TFIELD-71. Normalized Pore Velocities for the Full-Mining Case. Red indicates**  
3 **zones of high velocity. The black outline shows the full-mining zones and the red box is the**  
4 **WIPP LWB. The T field used to produce the velocity profile is averaged across all T**  
5 **field/replicate combinations for the full-mining scenario (300 T fields in total).**  
6

1 each cell is the average of the Ts across all T field/replicate combinations for the full-mining  
2 scenario (300 T fields in total). Not surprisingly, it is clear that the areas of high velocities  
3 correspond with the mining zones. The higher velocities and corresponding higher flow rates  
4 through the mining zone areas translate to slower velocities in the nonmining zone areas. In  
5 most cases, the particles for the mining scenarios stay in the lower velocity zones along the entire  
6 pathway to the LWB, which accounts for the higher average travel times. A comparison of the  
7 average, maximum, and minimum values for the full-, partial-, and no-mining scenario travel  
8 times is presented in Table TFIELD-13.

#### 9 ***TFIELD-9.4.2 Travel Directions***

10 The effects of mining also have an impact on the direction of transport, significantly changing  
11 where the particles cross the LWB. This is especially true of the full-mining scenario where  
12 mining within the LWB creates high head along the eastern boundary of the WIPP resulting in a  
13 general flow direction to the westsouthwest. This is in contrast to the partial-mining scenario  
14 where the tracking direction is mainly towards the south, similar to the nonmining scenario. The  
15 particle-track directions for the partial- and full-mining scenarios are illustrated in Figures  
16 TFIELD-73 to TFIELD-78.

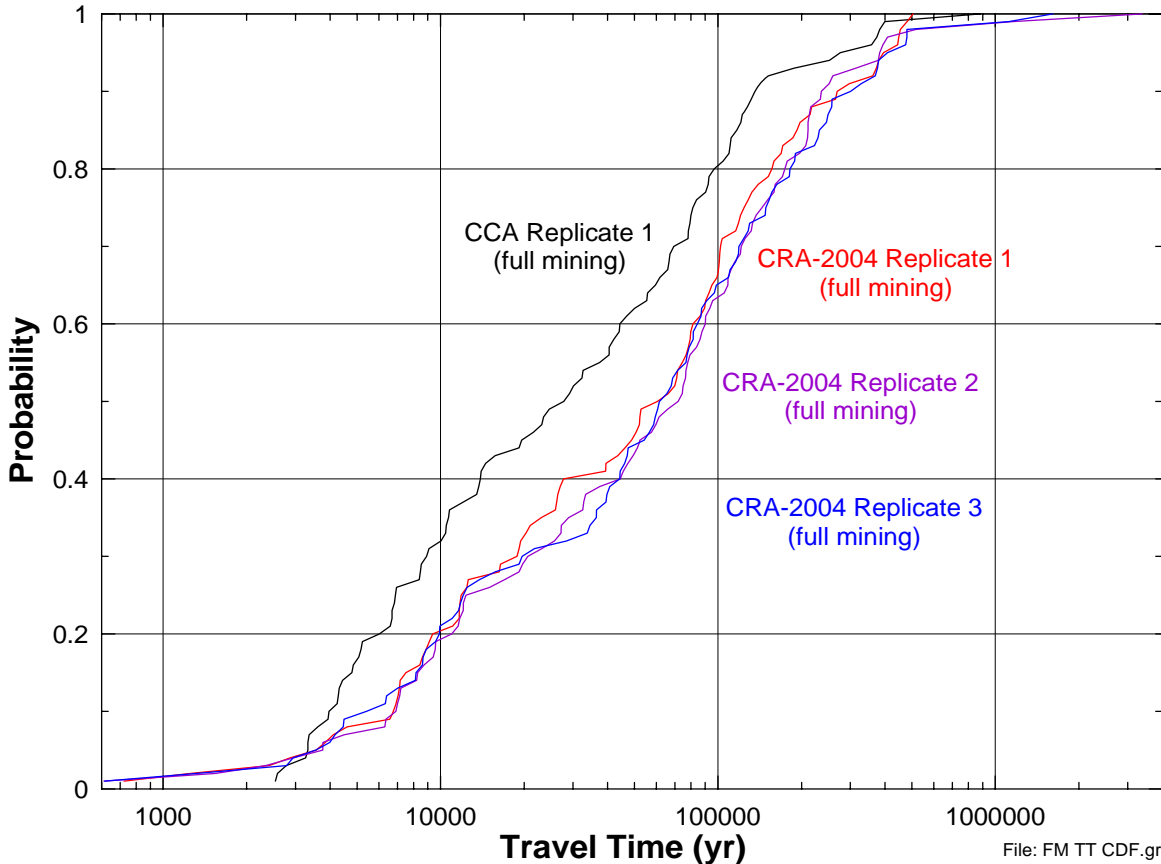
17 There is a strong similarity within each replicate for each scenario. Individual tracks can be  
18 recognized from one replicate to the next, with some slight variations. This indicates that track  
19 directions are determined more by the spatial variation of the calibrated T field than by the  
20 random mining factors. As long as there is some (see below) increase in the mining zone Ts  
21 over that of the nonmining areas, the tracks for each T field will be similar from one replicate to  
22 the next.

23 The partial-mining particle tracks in Figures TFIELD-73 through TFIELD-75 follow paths very  
24 similar to the partial-mining particle tracks through the CCA T fields (Ramsey et al. 1996, Figure  
25 7.12). The full-mining particle tracks in Figures TFIELD-76 through TFIELD-78 show a more  
26 westward component and are generally longer than the full-mining particle tracks through the  
27 CCA T fields (Ramsey et al. 1996, Figure 7.13).

28 The insensitivity of the track directions to the random mining factor also carries over to  
29 insensitivity of the travel time. Correlation analysis shows correlations between travel time and  
30 the random mining factor for the full and partial-mining scenarios as 0.091 and 0.151,  
31 respectively. Thus, like the track directions, travel times are not sensitive to the random mining  
32 factor but rather to the spatial structure of the calibrated T field.

33 This insensitivity to the random mining factor can be explained by recalling that the factor is  
34 applied only to zones deemed as probable mining areas. This means that velocity and flow  
35 increases are limited to the mining zones, with little change in the nonmining areas (assuming  
36 gradients are somewhat constant). Conditions within the nonmining zones are affected most for  
37 cases where the mining zone Ts are close to the non-mining zone Ts. However, the mining  
38 factor ranges uniformly from 1 to 1,000, meaning 99 percent of the T field/replicate  
39 combinations will have multipliers greater than one order of magnitude (for the 300  
40 combinations, only two have multipliers that are less than 10). This translates into small changes  
41 within the non-mining zones for relatively large changes in the mining zones. To illustrate this,

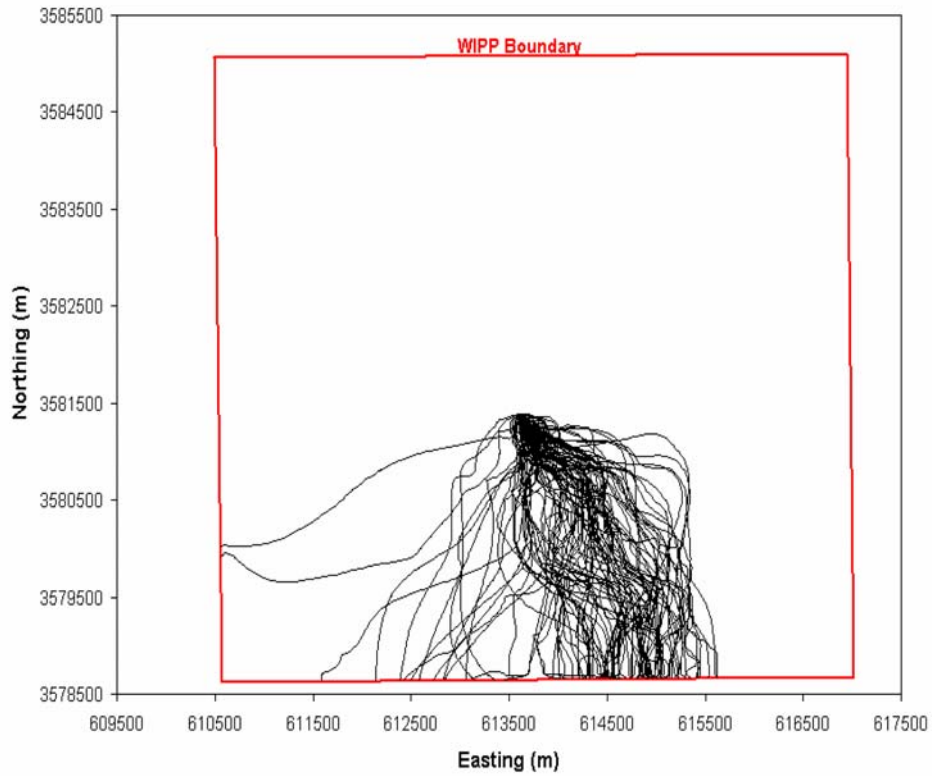




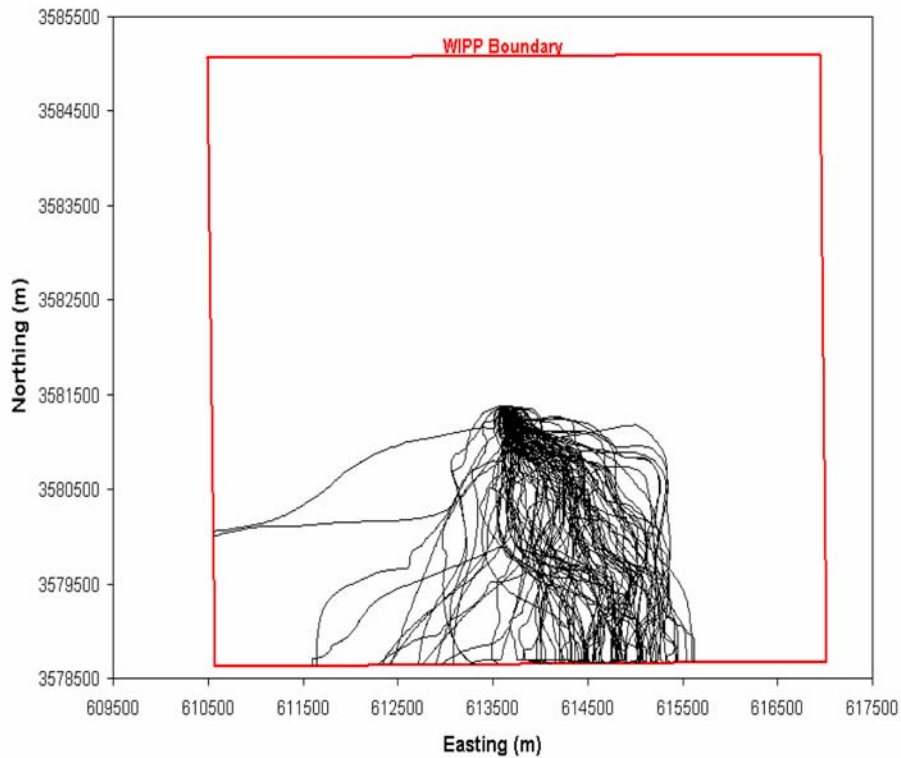
1  
2 **Figure TFIELD-72. CDFs of Full-Mining Travel Times for Three CRA-2004 Replicates**  
3 **and One CCA Replicate**

4 **Table TFIELD-13. Travel Time Statistics for the Full- and Partial-Mining Scenarios as**  
5 **Compared to the No-Mining Scenario**

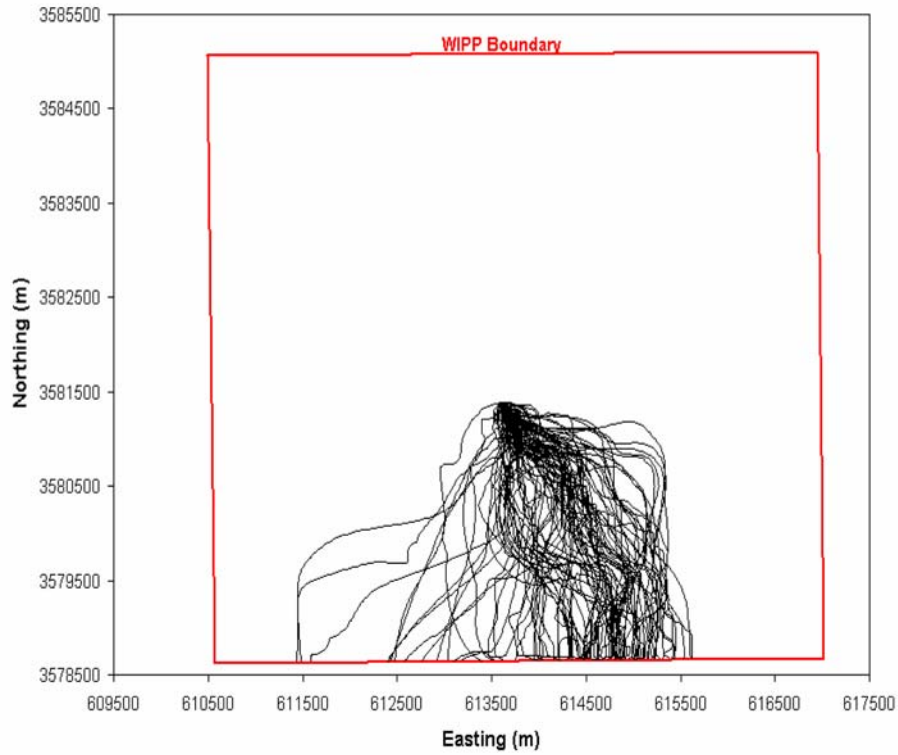
Replicate	Statistic	Full-Mining Travel Time (yr)	Partial-Mining Travel Time (yr)	No-Mining Travel Time (yr)
R1	Median	63,370	47,745	
	Maximum	504,174	494,981	
	Minimum	723	4,684	
R2	Median	73,169	47,651	
	Maximum	3,387,185	531,136	
	Minimum	611	4,654	
R3	Median	63,430	51,622	
	Maximum	1,610,979	506,438	
	Minimum	615	4,603	
Global	Median	66,048	48,290	18,289
	Maximum	3,387,185	531,136	101,205
	Minimum	611	4,603	3,111



1  
2 **Figure TFIELD-73. Particle Tracks for Replicate 1 for the Partial-Mining Scenario**

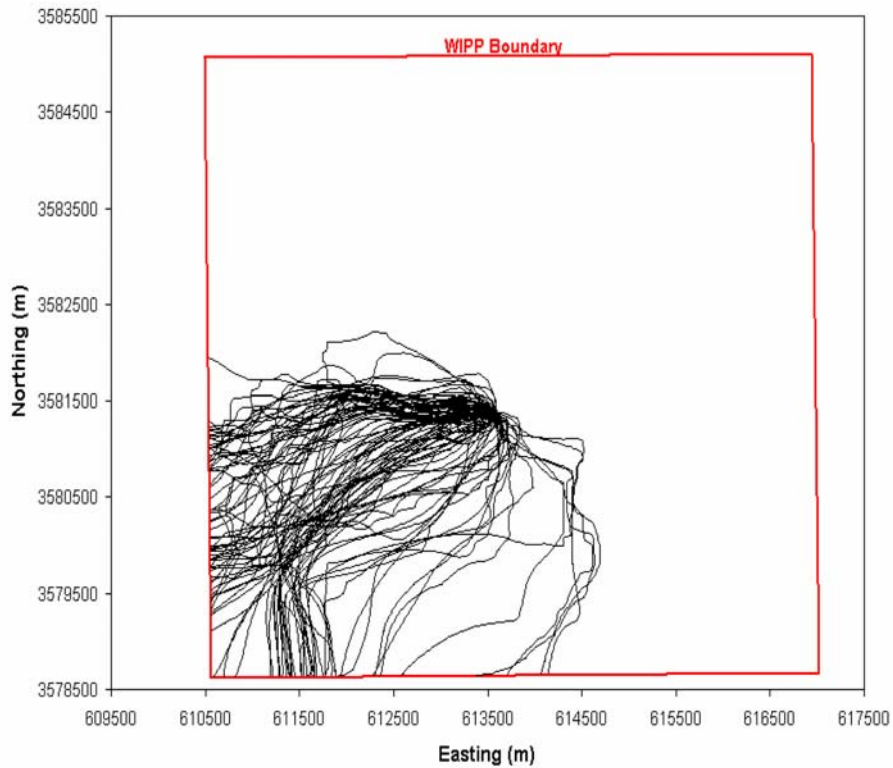


3  
4 **Figure TFIELD-74. Particle Tracks for Replicate 2 for the Partial-Mining Scenario**



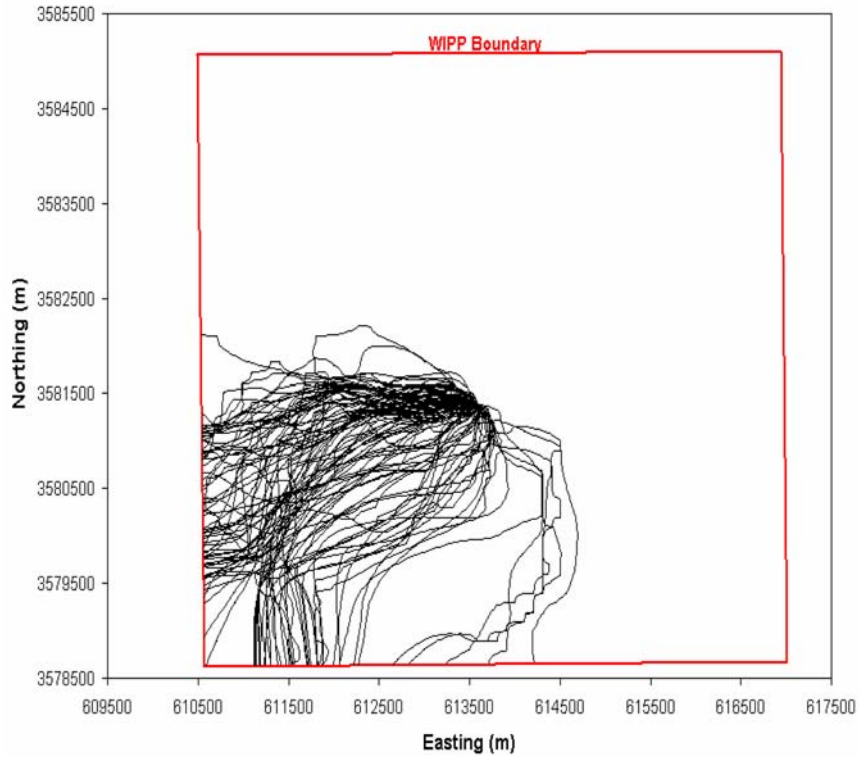
1  
2

**Figure TFIELD-75. Particle Tracks for Replicate 3 for the Partial-Mining Scenario**



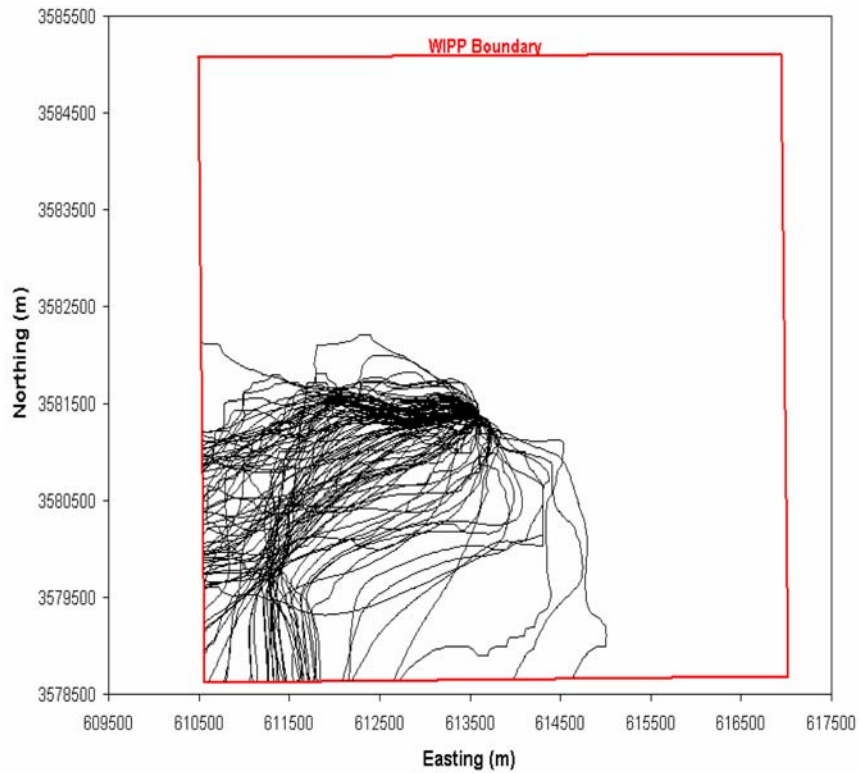
3  
4

**Figure TFIELD-76. Particle Tracks for Replicate 1 for the Full-Mining Scenario**



1  
2

**Figure TFIELD-77. Particle Tracks for Replicate 2 for the Full-Mining Scenario**



3  
4

**Figure TFIELD-78. Particle Tracks for Replicate 3 for the Full-Mining Scenario**

1 Figure TFIELD-79 shows the  $\log_{10}$  travel times versus the random mining factor for the full- and  
2 partial-mining scenarios across all replicates. The high scatter in both the plots is due to the  
3 independence of travel time with regards to the mining factor. This conclusion supports the  
4 mining scenario conceptual model and the use of a random mining factor to model changes in T  
5 due to mining activities. It also indicates that the controlling parameters are the spatial  
6 distribution of the non-mining scenario T field and the delineation of the mining and nonmining  
7 zones.

### 8 ***TFIELD-9.4.3 Extreme Values***

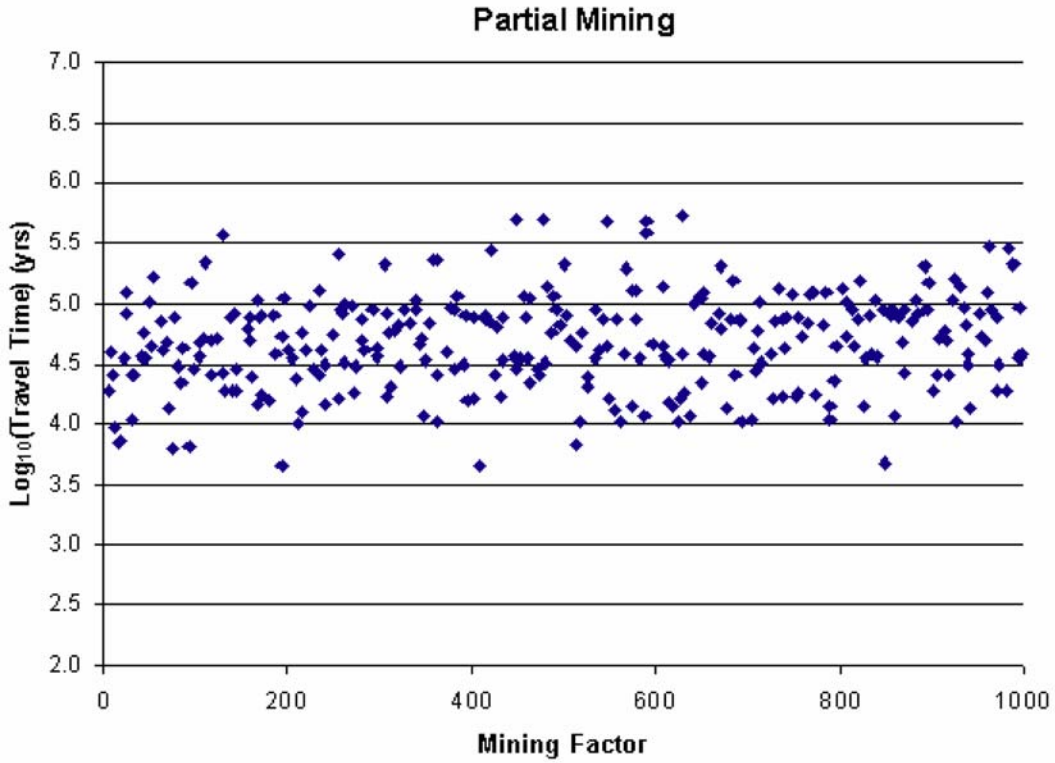
9 Examination of the extreme travel time values and the causes behind those values is useful in  
10 quantifying the range of outcomes given the amount of uncertainty incorporated into the models.  
11 For the partial-mining scenario, T field d04r01 from Replicate 2 had the longest travel time of  
12 531,136 years. In contrast, T field d08r01 from Replicate 3 had the shortest travel time of 4, 603  
13 years. The median travel time is best represented by T field d01r04 from Replicate 1 with a  
14 travel time of 48, 472 years. Figures TFIELD-80 to TFIELD-82 show the head contours for each  
15 of these cases along with the corresponding particle tracks. The particle-tracking directions are  
16 all fairly similar.

17 The full-mining cases (Figures TFIELD-83 to TFIELD-85) have similar characteristics to those  
18 of the partial-mining cases except that the band of high gradient to the northwest is less  
19 pronounced and persistent. For the full-mining scenario, T field d04r01 from Replicate 2 had the  
20 longest travel time of 3, 387,185 years. T field d01r07 from Replicate 2 had the shortest travel  
21 time of 611 years. The median travel time is best represented by T field d10r09 in Replicate 1  
22 (66, 215 years).

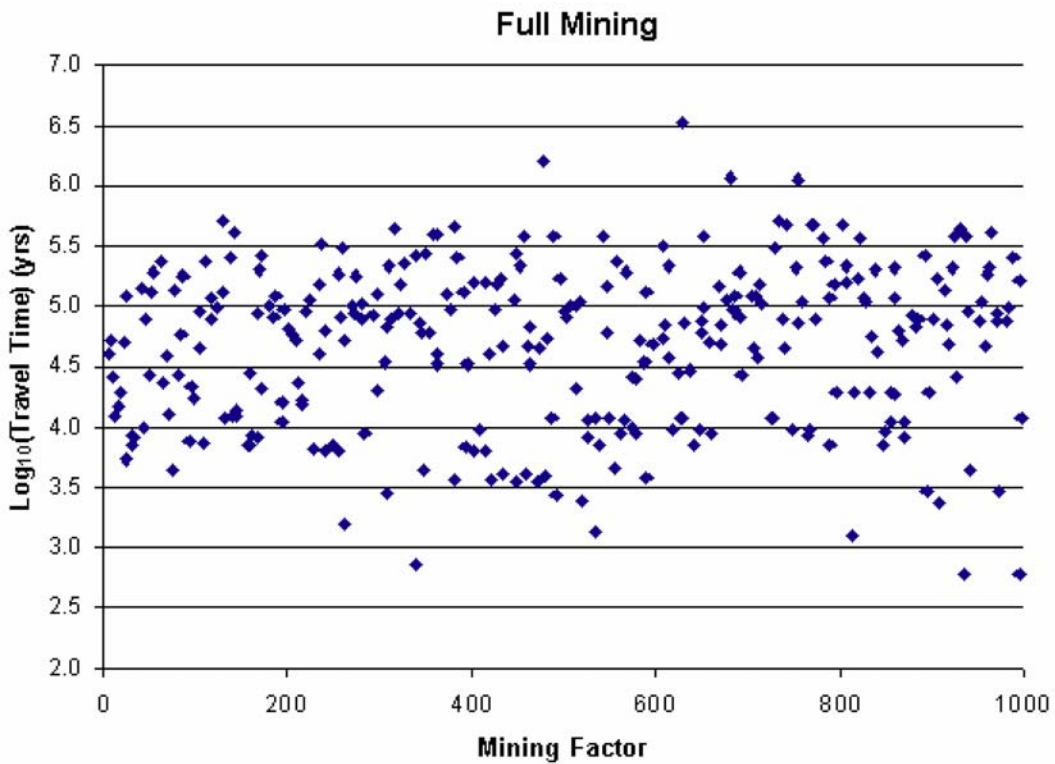
23 Overall, for both the partial- and full-mining scenarios, those T fields that contain higher and  
24 more heterogeneous Ts in the nonmining areas produce the fastest travel times. However, the  
25 partial-mining scenario shows a smaller range of values due to the lack of the large mining zone  
26 in the WIPP area. This smaller range is clearly visible in Figure TFIELD-79. What  
27 distinguishes the plots is the head distribution across the regions. For the slow case (Figure  
28 TFIELD-80), the head contours to the west of the repository are spread far apart, indicating a low  
29 gradient and thus lower groundwater velocities. The fastest case (Figure TFIELD-81) shows a  
30 high-gradient band that originates along the no-flow boundary to the northwest and runs down  
31 the western side of the WIPP site. This high gradient corresponds to higher groundwater  
32 velocities. The median case (Figure TFIELD-82) also shows this high-gradient band, but it is  
33 not as extreme as in the fast case. In all cases, the mining-zone areas look very similar, with  
34 widely spaced head contours and higher velocities relative to the nonmining zones.

### 35 ***TFIELD-10.0 SUMMARY***

36 Observed Culebra T has been related to three deterministic factors: the thickness of overburden  
37 above the Culebra, the presence or absence of dissolution of the upper Salado, and the presence  
38 or absence of halite in units above and below the Culebra. Culebra T is also related to the  
39 occurrence of open, interconnected fractures, which cannot be mapped as easily as the other  
40 three factors and must be treated stochastically. A linear-regression model for Culebra T has  
41 been developed based on these factors that provides an excellent match to the observed data, and

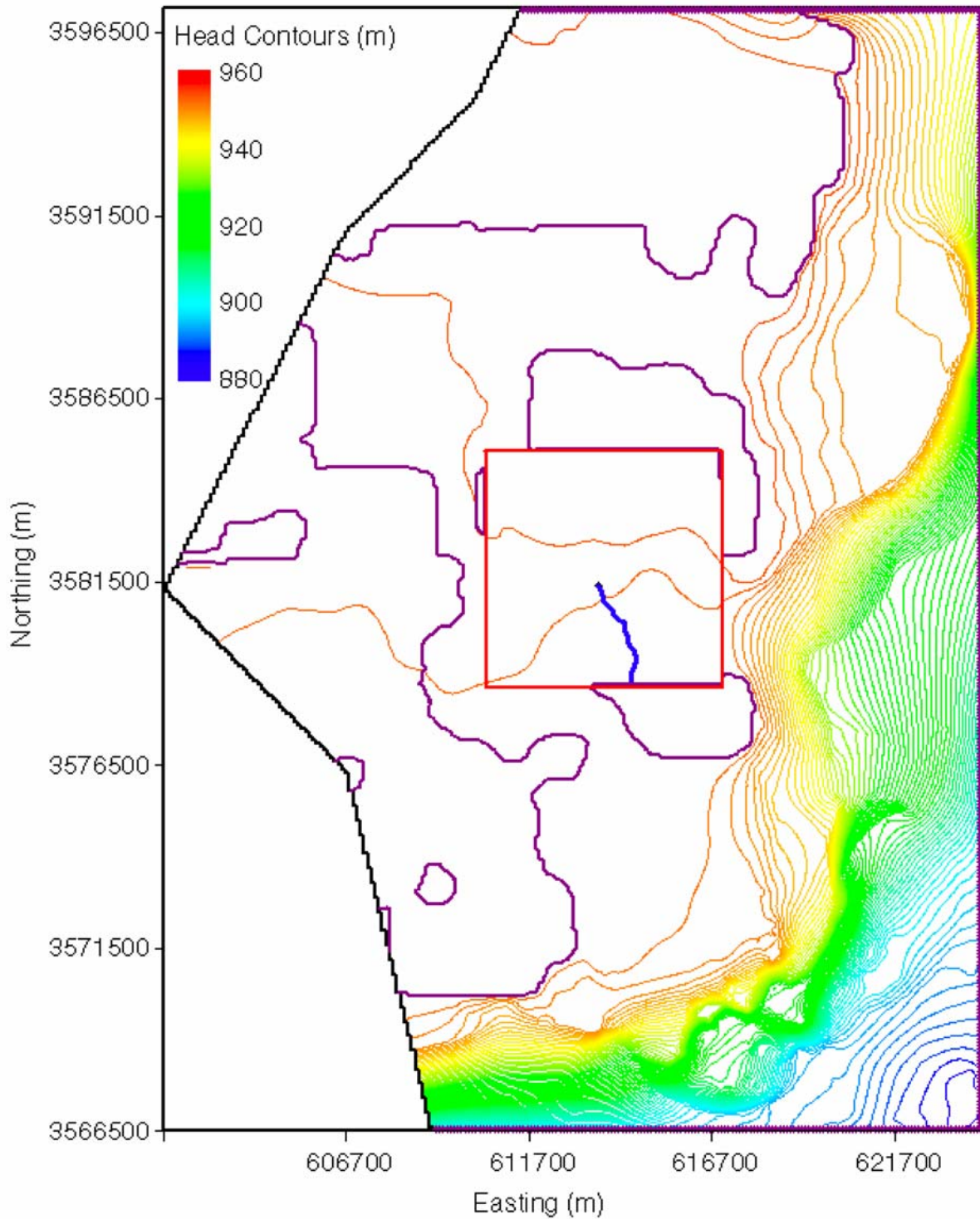


1  
2

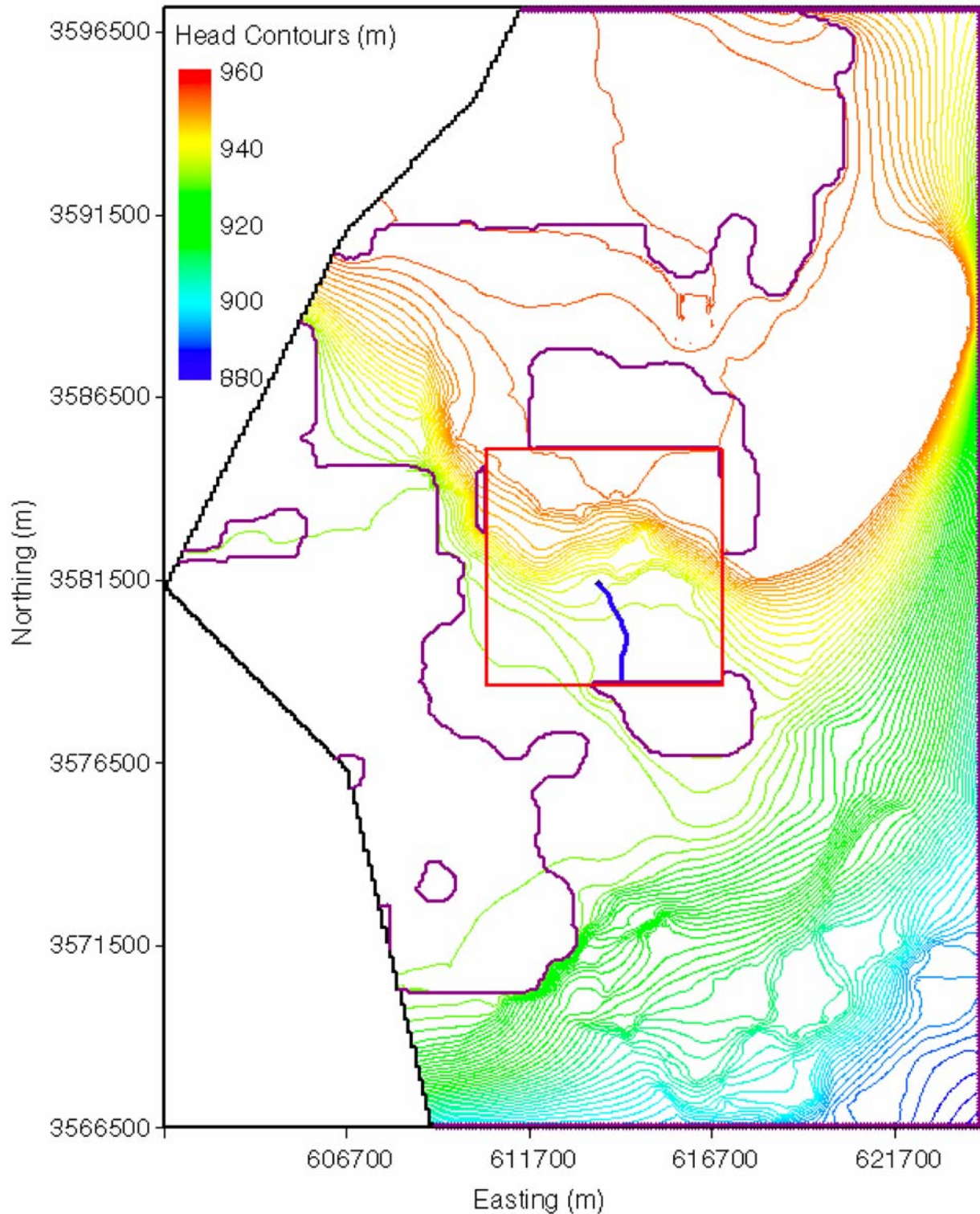


3  
4  
5

**Figure TFIELD-79. Correlation Between the Random Mining Factor and Log<sub>10</sub> of Travel Time**

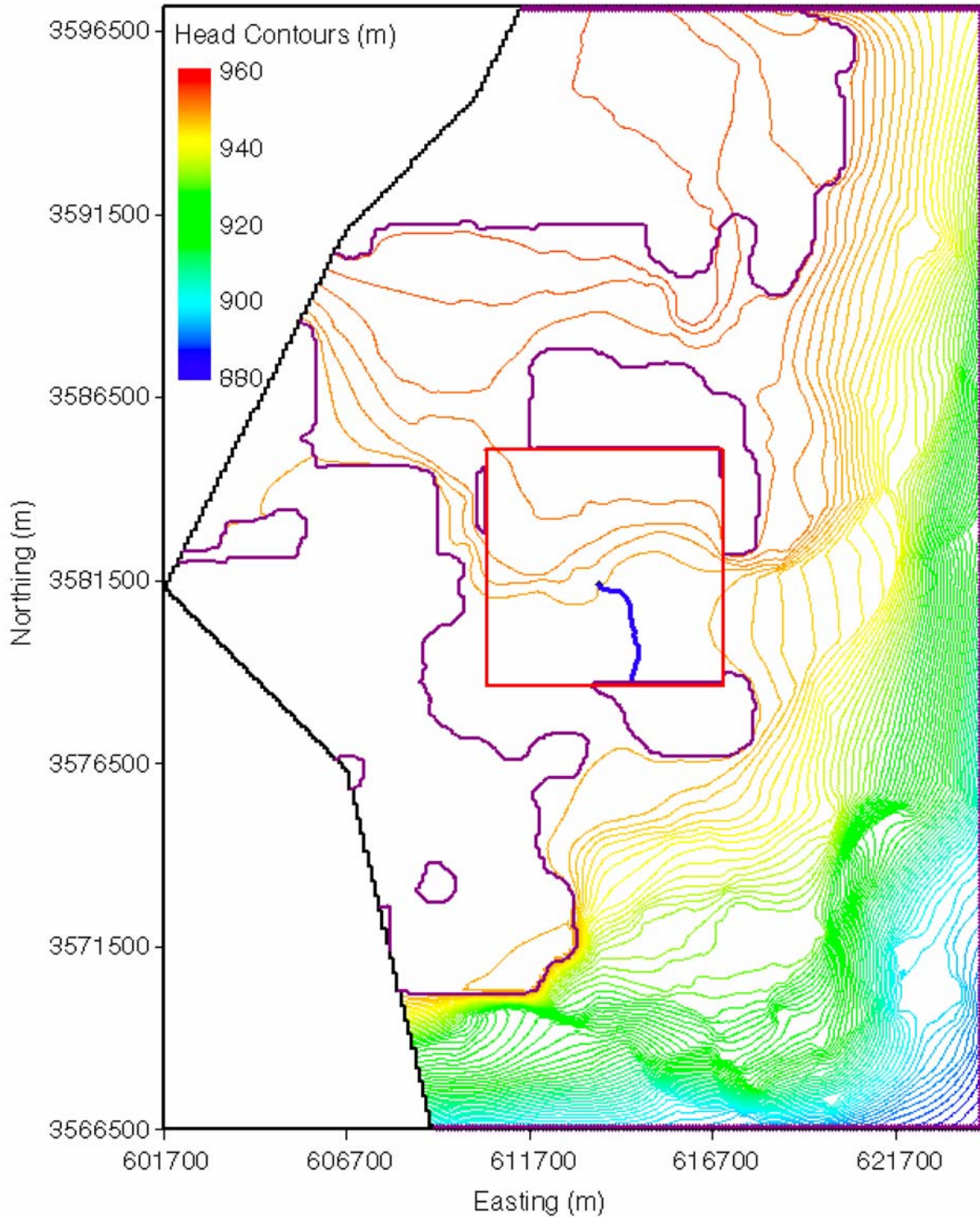


1  
2 **Figure TFIELD-80. Head Contours and Particle Track for the Maximum-Travel-Time T**  
3 **Field (d04r01-R2) for the Partial-Mining Case. The WIPP LWB is the red box in the**  
4 **center of the figure and the particle track is the blue track originating from the**  
5 **approximate center of the WIPP.**



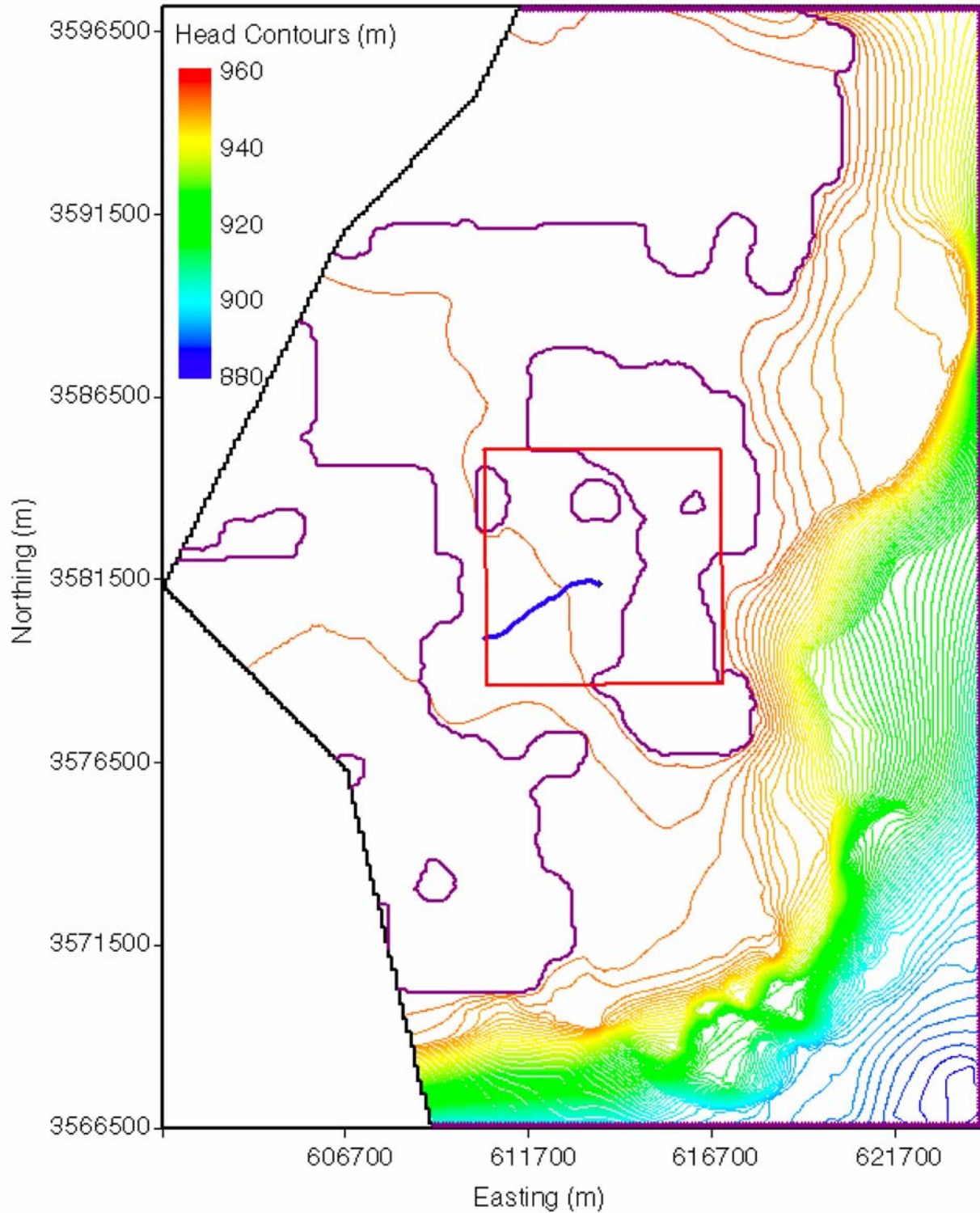
1  
2 **Figure TFIELD-81. Head Contours and Particle Track for the Minimum-Travel-Time T**  
3 **Field (d08r01-R3) for the Partial-Mining Case. The WIPP LWB is the red box in the**  
4 **center of the figure and the particle track is the blue track originating from the**  
5 **approximate center of the WIPP.**





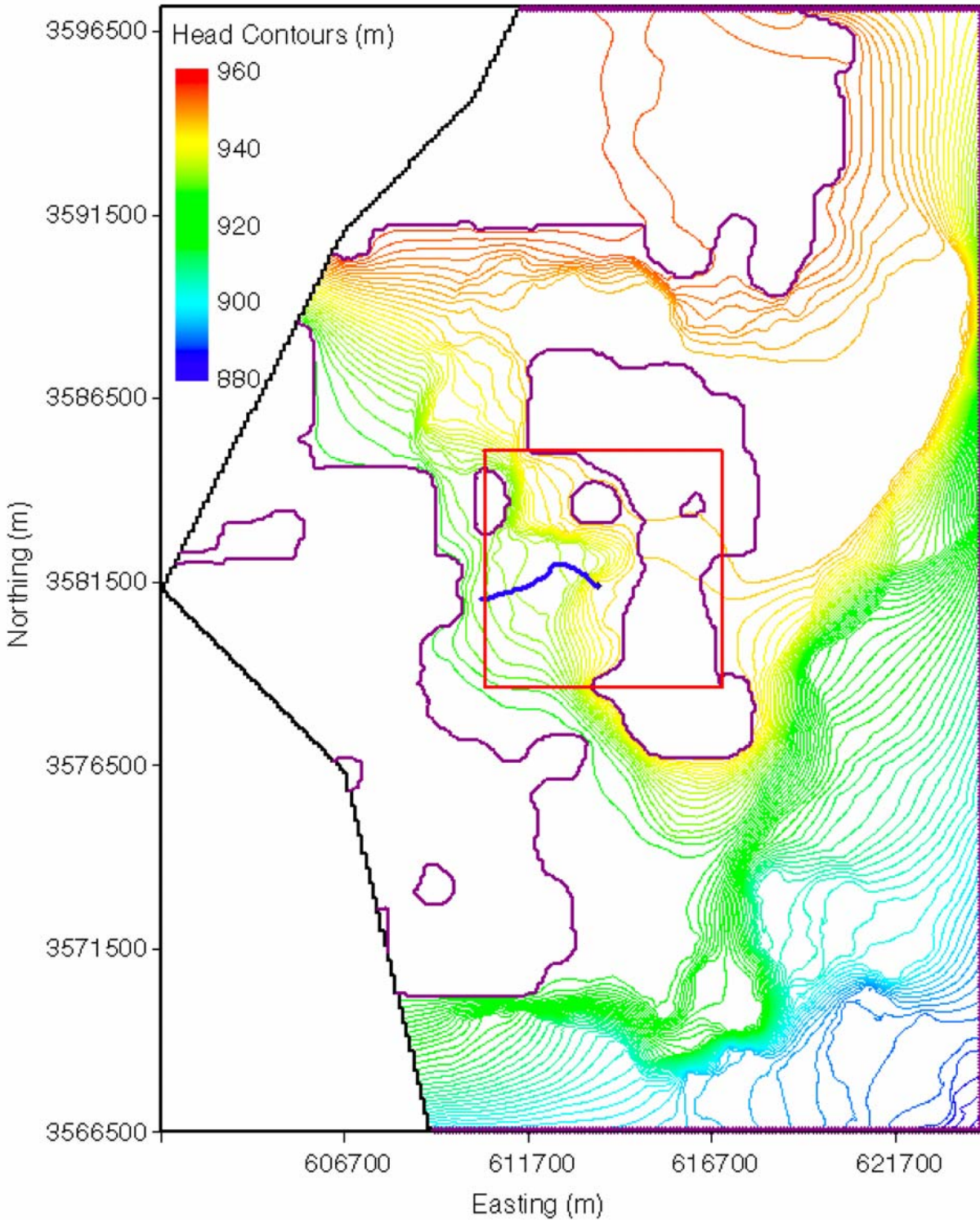
1

2 **Figure TFIELD-82. Head Contours and Particle Track for the Median-Travel-Time T**  
3 **Field (d01r04-R1) for the Partial-Mining Case. The WIPP LWB is the red box in the**  
4 **center of the figure and the particle track is the blue track originating from the**  
5 **approximate center of the WIPP.**



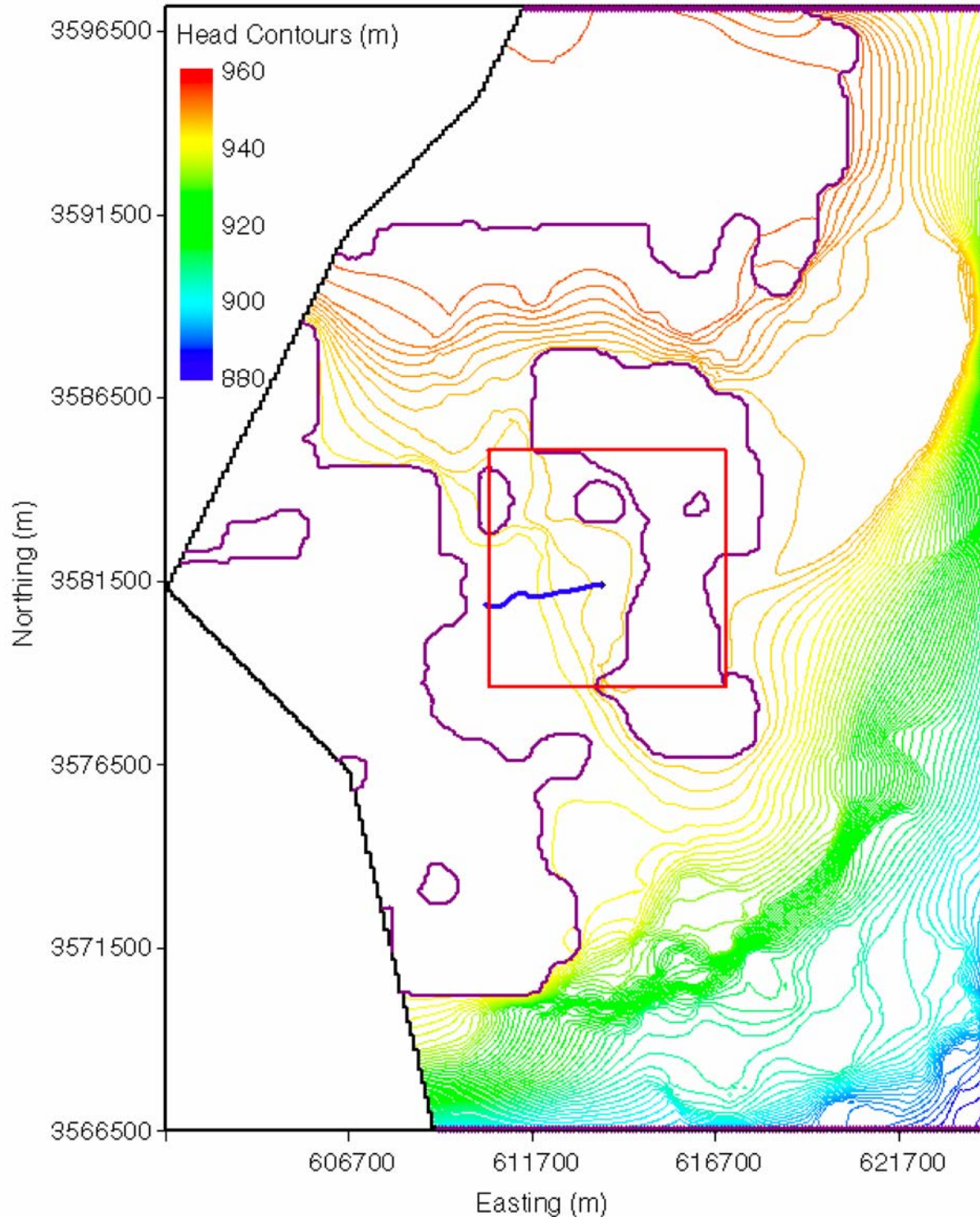
1

2 **Figure TFIELD-83. Head Contours and Particle Track for the Maximum-Travel-Time T**  
3 **Field (d04r01-R2) for the Full-Mining Case. The WIPP LWB is the red box in the center of**  
4 **the figure and the particle track is the blue track originating from the approximate center**  
5 **of the WIPP.**



1

2 **Figure TFIELD-84. Head Contours and Particle Track for the Minimum-Travel-Time T**  
3 **Field (d01r07-R2) for the Full-Mining Case. The WIPP LWB is the red box in the center of**  
4 **the figure and the particle track is the blue track originating from the approximate**  
5 **center of the WIPP.**



1

2 **Figure TFIELD-85. Head Contours and Particle Track for the Median-Travel-Time T**  
3 **Field (d10r09-R1) for the Full-Mining Case. The WIPP LWB is the red box in the center of**  
4 **the figure and the particle track is the blue track originating from the approximate center**  
5 **of the WIPP.**

1 can be tested through the collection of additional data. This model was used to create 500  
2 stochastic realizations of the distribution of Culebra T (“base” T fields) in the vicinity of the  
3 WIPP site.

4 A MODFLOW-2000 modeling domain was defined extending 30.7 km (19.1 mi) north-south  
5 and 22.4 km (13.9 mi) east-west, roughly centered on the WIPP site. This domain was  
6 discretized into 68,768 uniform 100-m (328-ft) by 100-m (328-ft) cells. Water-level  
7 measurements made in 37 wells in late 2000 were used to define “steady-state” head conditions and  
8 constant-head boundary conditions on the northern, eastern, and southern extremes of the model  
9 domain. No-flow boundaries down the arms of Nash Draw, representing flow lines, were used on  
10 the western side of the model domain, reducing the number of active cells to 53,769.

11 MODFLOW-2000 and PEST were used to calibrate 146 of the base T fields to steady-state heads  
12 and transient drawdown responses to seven large-scale pumping tests. This calibration was done  
13 by using 100 pilot points to adjust the T values within the model domain to improve the fit to the  
14 observed heads. The pilot points were used to adjust a residual T field that was combined with a  
15 previously created base T field to yield the final calibrated T field. Of the 146 T fields, 121 were  
16 judged to be adequately calibrated for use in WIPP compliance calculations by virtue of being  
17 from a single population with respect to the CDF of travel times from a point above the center of  
18 the WIPP disposal panels to the LWB. From these 121 T fields, the 100 having the best  
19 objective fit measures were selected for further use.

20 The EPA requires that the potential effects of future potash mining be taken into account when  
21 evaluating the performance of the WIPP disposal system. Accordingly, transmissivities in the  
22 areas within the model domain where current or future mining might affect the Culebra were  
23 scaled by a random multiplier between 1 and 1,000 obtained from LHS. A single multiplier was  
24 used for each T field, applied first to the areas outside the WIPP LWB that might be mined to  
25 create a partial-mining T field, and then to the areas both inside and outside the LWB that might  
26 be mined to create a full-mining T field. The LHS was performed three times to create three  
27 replicates of T fields, leading to a total of 600 T fields. The MODFLOW-2000 water “budget”  
28 files from forward runs of these 600 T fields provided the input to radionuclide-transport  
29 calculations using SECOTP2D.

30 In all cases (no mining, partial mining, and full mining), the particle tracks on the T fields show  
31 travel times that are longer than those calculated for the T fields used in the CCA. In the case of  
32 the T fields unaltered for the effects of mining, the longer travel times are caused by a shift of  
33 relatively high Ts from the southeastern to the southwestern portion of the WIPP site relative to  
34 the CCA T fields. In the case of the T fields altered for full and partial mining, the longer travel  
35 times are the combined result of the westward shift of high Ts discussed above and a change in  
36 the definition of the areas to be mined that resulted in less water entering the Culebra on the  
37 WIPP site.

**REFERENCES**

- 1
- 2 Beauheim, R.L. 1987. *Interpretations of Single-Well Hydraulic Tests Conducted At and Near*  
3 *the Waste Isolation Pilot Plant (WIPP) Site, 1983-1987*. SAND87-0039. Albuquerque, NM:  
4 Sandia National Laboratories.
- 5 Beauheim, R.L. 2002a. Analysis Plan for the Evaluation of the Effects of Head Changes on  
6 Calibration of Culebra Transmissivity Fields, AP-088, Revision 1. ERMS# 524785. Carlsbad,  
7 NM: Sandia National Laboratories, WIPP Records Center.
- 8 Beauheim, R.L. 2002b. Routine Calculations Report In Support of Task 3 of AP-088,  
9 Calculation of Culebra Freshwater Heads in 1980, 1990, and 2000 for Use in T-Field  
10 Calibration. ERMS# 522580. Carlsbad, NM: Sandia National Laboratories, WIPP Records  
11 Center.
- 12 Beauheim, R.L. 2002c. Analysis Package for Interpretation of 1984 H-3 Pumping Tests.  
13 ERMS# 522203. Carlsbad, NM: Sandia National Laboratories, WIPP Records Center.
- 14 Beauheim, R.L. 2003a. Records Package for AP-088 Task 4, Conditioning of Base T Fields to  
15 Transient Heads: Compilation and Reduction of Transient Head Data. ERMS# 527572.  
16 Carlsbad, NM: Sandia National Laboratories, WIPP Records Center.
- 17 Beauheim, R.L. 2003b. Analysis Report for AP-100 Task 1: Development and Application of  
18 Acceptance Criteria for Culebra Transmissivity (T) Fields. ERMS# 531136. Carlsbad, NM:  
19 Sandia National Laboratories, WIPP Records Center.
- 20 Beauheim, R.L., and R.M. Holt. 1990. "Hydrogeology of the WIPP Site," in *Geological and*  
21 *Hydrological Studies of Evaporites in the Northern Delaware Basin for the Waste Isolation Pilot*  
22 *Plant (WIPP), New Mexico*. D. Powers, R. Holt, R.L. Beauheim, and N. Rempe, eds. GSA  
23 Field Trip #14 Guidebook. Dallas, TX: Dallas Geological Society. 131-179.
- 24 Beauheim, R.L., and G.J. Ruskauff. 1998. *Analysis of Hydraulic Tests of the Culebra and*  
25 *Magenta Dolomites and Dewey Lake Redbeds Conducted at the Waste Isolation Pilot Plant Site*.  
26 SAND98-0049. Albuquerque, NM: Sandia National Laboratories.
- 27 BLM (U.S. Bureau of Land Management). 1993. *Preliminary Map Showing Distribution of*  
28 *Potash Resources, Carlsbad Mining District, Eddy & Lea Counties, New Mexico*. Roswell, NM:  
29 U.S. BLM. Copy on file in the Sandia National Laboratories WIPP Records Center, Carlsbad,  
30 NM, as ERMS# 525210.
- 31 Corbet, T.F., and P.M. Knupp. 1996. *The Role of Regional Groundwater Flow in the*  
32 *Hydrogeology of the Culebra Member of the Rustler Formation at the Waste Isolation Pilot*  
33 *Plant (WIPP), Southeastern New Mexico*. SAND96-2133. Albuquerque, NM: Sandia National  
34 Laboratories.
- 35 Currie, J.B., and S.O. Nwachukwu. 1974. "Evidence on Incipient Fracture Porosity in Reservoir  
36 Rocks at Depth," *Bulletin of Canadian Petroleum Geology*. Vol. 22, 42-58.

- 1 Davies, P.B. 1989. *Variable-Density Ground-Water Flow and Paleohydrology in the Waste*  
2 *Isolation Pilot Plant (WIPP) Region, Southeastern New Mexico*. Open-File Report 88-490.  
3 Albuquerque, NM: U.S. Geological Survey.
- 4 Deutsch, C.V., and A.G. Journel. 1998. *GSLIB: Geostatistical Software Library and User's*  
5 *Guide, Second Edition*. New York: Oxford University Press, 369 pp.
- 6 Doherty, J. 2002. Manual for PEST, 5<sup>th</sup> edition. Brisbane, Australia: Watermark Numerical  
7 Computing. Downloadable from [www.sspa.com/pest](http://www.sspa.com/pest).
- 8 Goovaerts, P. 1997. *Geostatistics for Natural Resources Evaluation*. New York: Oxford  
9 University Press, 483 pp.
- 10 Harbaugh, A.W., E.R. Banta, M.C. Hill, and M.G. McDonald. 2000. *MODFLOW-2000: The*  
11 *U.S. Geological Survey Modular Ground-Water Model – User Guide to Modularization*  
12 *Concepts and the Ground-Water Flow Process*. Open File Report 00-92. Reston, VA: U.S.  
13 Geological Survey, 121 pp.
- 14 Holt, R.M. 1997. *Conceptual Model for Transport Processes in the Culebra Dolomite Member,*  
15 *Rustler Formation*. SAND97-0194. Albuquerque, NM: Sandia National Laboratories.
- 16 Holt, R.M., and D.W. Powers. 1988. *Facies Variability and Post-Depositional Alteration*  
17 *Within the Rustler Formation in the Vicinity of the Waste Isolation Pilot Plant, Southeastern*  
18 *New Mexico*. DOE/WIPP 88-004. Carlsbad, NM: U.S. Department of Energy.
- 19 Holt, R.M., and L. Yarbrough. 2002. Analysis Report, Task 2 of AP-088, Estimating Base  
20 Transmissivity Fields. ERMS# 523889. Carlsbad, NM: Sandia National Laboratories, WIPP  
21 Records Center.
- 22 Holt, R.M., and L. Yarbrough. 2003a. Addendum to Analysis Report, Task 2 of AP-088,  
23 Estimating Base Transmissivity Fields. ERMS# 527601. Carlsbad, NM: Sandia National  
24 Laboratories, WIPP Records Center.
- 25 Holt, R.M., and L. Yarbrough. 2003b. Addendum 2 to Analysis Report, Task 2 of AP-088,  
26 Estimating Base Transmissivity Fields. ERMS# 529416. Carlsbad, NM: Sandia National  
27 Laboratories, WIPP Records Center.
- 28 Hunter, R.L. 1985. *A Regional Water Balance for the Waste Isolation Pilot Plant (WIPP) Site*  
29 *and Surrounding Area*. SAND84-2233. Albuquerque, NM: Sandia National Laboratories.
- 30 Lang, W.B. 1935. "Upper Permian Formation of Delaware Basin of Texas and New Mexico,"  
31 *American Association of Petroleum Geologists Bulletin*. Vol. 21, 833-898.
- 32 Lavenue, A.M. 1996. Analysis of the Generation of Transmissivity Fields for the Culebra  
33 Dolomite. ERMS# 240517. Carlsbad, NM: Sandia National Laboratories, WIPP Records  
34 Center.

- 1 LaVenue, A.M., and B.S. RamaRao. 1992. *A Modeling Approach to Address Spatial Variability*  
2 *within the Culebra Dolomite Transmissivity Field*. SAND92-7306. Albuquerque, NM: Sandia  
3 National Laboratories.
- 4 LaVenue, A.M., T.L. Cauffman, and J.F. Pickens. 1990. *Ground-Water Flow Modeling of the*  
5 *Culebra Dolomite, Volume I: Model Calibration*. SAND89-7068/1. Albuquerque, NM: Sandia  
6 National Laboratories.
- 7 Leigh, C., R. Beauheim, and J. Kanney. 2003. Analysis Plan for Calculations of Culebra Flow  
8 and Transport: Compliance Recertification Application, AP-100. ERMS# 530172. Carlsbad,  
9 NM: Sandia National Laboratories, WIPP Records Center.
- 10 Long, J.J. 2004. *Execution of Performance Assessment for the Compliance Recertification*  
11 *Application (CRAI)*, Revision 0. ERMS # 530170. Carlsbad, NM: Sandia National  
12 Laboratories, WIPP Records Center.
- 13 Lowry, T.S. 2003. Analysis Report, Task 5 of AP-088, Evaluation of Mining Scenarios.  
14 ERMS# 531138. Carlsbad, NM: Sandia National Laboratories, WIPP Records Center.
- 15 McKenna, S.A., and D.B. Hart. 2003a. Analysis Report, Task 3 of AP-088, Conditioning of  
16 Base T Fields to Steady-State Heads. ERMS# 529633. Carlsbad, NM: Sandia National  
17 Laboratories, WIPP Records Center.
- 18 McKenna, S.A., and D.B. Hart. 2003b. Analysis Report, Task 4 of AP-088, Conditioning of  
19 Base T Fields to Transient Heads. ERMS# 531124. Carlsbad, NM: Sandia National  
20 Laboratories, WIPP Records Center.
- 21 Meigs, L.C., and J.T. McCord. 1996. "Appendix A: Physical Transport in the Culebra  
22 Dolomite," in Analysis Package for the Culebra Flow and Transport Calculations (Task 3) of the  
23 Performance Assessment Analyses Supporting the Compliance Certification Application,  
24 Analysis Plan 019, Version 00. J.L. Ramsey, M.G. Wallace, and H.-N. Jow. ERMS# 240516.  
25 Carlsbad, NM: Sandia National Laboratories, WIPP Records Center.
- 26 Pannatier, Y. 1996. *VarioWin: Software Spatial Analysis in 2D*. New York: Springer, 91 pp.
- 27 Powers, D.W. 2002a. Analysis Report, Task 1 of AP-088, Construction of Geologic Contour  
28 Maps. ERMS# 522086. Carlsbad, NM: Sandia National Laboratories, WIPP Records Center.
- 29 Powers, D.W. 2002b. Addendum to Analysis Report, Task 1 of AP-088, Construction of  
30 Geologic Contour Maps. ERMS# 523886. Carlsbad, NM: Sandia National Laboratories, WIPP  
31 Records Center.
- 32 Powers, D.W. 2003. Addendum 2 to Analysis Report, Task 1 of AP-088, Construction of  
33 Geologic Contour Maps. ERMS# 525199. Carlsbad, NM: Sandia National Laboratories, WIPP  
34 Records Center.
- 35 Powers, D.W., and R.M. Holt. 1990. "Sedimentology of the Rustler Formation near the Waste  
36 Isolation Pilot Plant (WIPP) Site," in *Geological and Hydrological Studies of Evaporites in the*



- 1 *Northern Delaware Basin for the Waste Isolation Pilot Plant (WIPP), New Mexico*. D. Powers,  
2 R. Holt, R.L. Beauheim, and N. Rempe, eds. GSA Field Trip #14 Guidebook. Dallas, TX:  
3 Dallas Geological Society. 79-106.
- 4 Powers, D.W., and R.M. Holt. 1995. Regional Geologic Processes Affecting Rustler  
5 Hydrogeology. ERMS# 244173. Carlsbad, NM: Sandia National Laboratories, WIPP Records  
6 Center.
- 7 Powers, D.W., and R.M. Holt. 1999. "The Los Medaños Member of the Permian (Ochoan)  
8 Rustler Formation," *New Mexico Geology*. Vol. 21, no. 4, 97-103.
- 9 Powers, D.W., and R.M. Holt. 2000. "The Salt That Wasn't There: Mudflat Facies Equivalents  
10 to Halite of the Permian Rustler Formation, Southeastern New Mexico," *Journal of Sedimentary*  
11 *Research*. Vol. 70, no. 1, 29-36.
- 12 Powers, D.W., R.M. Holt, R.L. Beauheim, and S.A. McKenna. 2003. "Geological Factors  
13 Related to the Transmissivity of the Culebra Dolomite Member, Permian Rustler Formation,  
14 Delaware Basin, Southeastern New Mexico," in *Evaporite Karst and Engineering/  
15 Environmental Problems in the United States*. K.S. Johnson and J.T. Neal, eds. Oklahoma  
16 Geological Survey Circular 109, 211-218.
- 17 Ramsey, J.L., M.G. Wallace, and H-N. Jow. 1996. Analysis Package for the Culebra Flow and  
18 Transport Calculations (Task 3) of the Performance Assessment Calculations Supporting the  
19 Compliance Certification Application (CCA), AP-019. ERMS# 240516. Carlsbad, NM: Sandia  
20 National Laboratories, WIPP Records Center.
- 21 Roberts, R.M. 2002. nSIGHTS User Manual, Document Version 1.0. ERMS# 522061.  
22 Carlsbad, NM: Sandia National Laboratories, WIPP Records Center.
- 23 Rudeen, D.K. 2003. User's Manual for DTRKMF Version 1.00. ERMS# 523246. Carlsbad,  
24 NM: Sandia National Laboratories, WIPP Records Center.
- 25 Snyder, R.P. 1985. *Dissolution of Halite and Gypsum, and Hydration of Anhydrite to Gypsum,*  
26 *Rustler Formation, in the Vicinity of the Waste Isolation Pilot Plant, Southeastern New Mexico.*  
27 Open-File Report 85-229. Denver, CO: U.S. Geological Survey.
- 28 U.S. Department of Energy (DOE). 1996. *Title 40 CFR Part 191 Compliance Certification*  
29 *Application for the Waste Isolation Pilot Plant*. DOE/CAO-1996-2184. Carlsbad, NM: U.S.  
30 DOE, Carlsbad Area Office.
- 31 U.S. Environmental Protection Agency (EPA). 1996. "40 CFR Part 194: Criteria for the  
32 Certification and Re-Certification of the Waste Isolation Pilot Plant's Compliance with the 40  
33 CFR Part 191 Disposal Regulations; Final Rule," *Federal Register*. Vol. 61, no. 28, pp. 5224-  
34 5245, February 9, 1996. Washington, DC: Office of Radiation and Indoor Air.
- 35 Wallace, M. 1996. Records Package for Screening Effort NS11: Subsidence Associated with  
36 Mining Inside or Outside the Controlled Area. ERMS# 412918. Carlsbad, NM: Sandia  
37 National Laboratories, WIPP Records Center.

- 1 WIPP PA (Performance Assessment). 2003. Execution of Performance Assessment for the
- 2 Compliance Recertification Application (CRA1). ERMS# 530150. Carlsbad, NM: Sandia
- 3 National Laboratories, WIPP Records Center.